A novel evaluation of total skin factor and pressure gradients for vertical perforated wells in near-wellbore region

By

Ekhwaiter Abobaker, BEng, MEng

A thesis submitted to the School of Graduate Studies in partial fulfillment of the requirements for the degree of Doctor of Philosophy

Faculty of Engineering and Applied Science

Memorial University of Newfoundland

St. John's, Newfoundland, Canada A1B 3X5.

October 20, 2022

Abstract

The reservoir productivity index relies on fluid flow performance through the near-wellbore and wellbore regions, which itself is highly dependent on wellbore geometry, completion technique, and specific reservoir parameters. The present study aims to present better understanding of fluid flow in the near-wellbore region by evaluating the effect of formation damage, well completion, well geometry as a function of single and two-phase flow rate conditions, thereby expanding industry knowledge about well performance.

An experimental procedure was developed to investigate fluid flow behavior through a cylindrical perforation tunnel and different well completion configurations. The experimental test was carried out using a geotechnical radial flow set-up to measure the differential pressure by injecting the single-phase and the two-phase radially into the core sample. A triaxial experimental set-up was employed in the present work to enable larger scales and high values for parameters (e.g., larger core sample, higher pressure, etc.). The height of the samples used in this study is one foot, the diameter is half a foot, as well as the maximum flow rate reached 4 liter/minute. This set-up also enables different kinds of fluid flow problems to be investigated. Also, the set-up has been appropriately updated to target the monitoring of interaction flows for both well, and near-well areas, including axial well and radial near-well flows. Extensive laboratory testing was conducted to create artificial samples for the perforation tunnel and a cylindrical near-wellbore region that were used in this study. Statistical analysis was coupled with numerical simulation to expand fluid flow investigation in the near-wellbore area that cannot be obtained

experimentally. Design of Experiments (DoE) software was used to determine the numerical simulation runs using the ANOVA analysis with a Box-Behnken Design (BBD) model. Also, ANSYS-FLUENT was used to analyze the numerical simulation for near-wellbore region by applying the single and two-phase flow. The three main investigative procedures of experimental, numerical, and statistical analysis showed a clear view of integrating effects of the skin zone (damaged region), perforation parameters, partial completion, inclination of well, the crushed zone around the perforation, and two-phase flow behavior on the total skin factor and the pressure gradient in the near-wellbore region.

This study presented a novel experimental and numerical approach for studying the combined effects of well completion configurations and fluid flow behavior on the hydrocarbon production by creating a prototype representing the near-wellbore region. This study provided a comprehensive analysis of fluid flow in the near-wellbore region and developed new correlations that calculate completion configurations' effect on the skin factor. The novel correlations that have been produced from this study simplify the skin factor estimation in different well completion types. The comparison demonstrated good agreement between the proposed correlations and available models results within the range of the study's dimensionless parameters. Moreover, this study will help clarify and understand the effect of well completion on well productivity in the near-wellbore region.

This dissertation is dedicated to my parents

Ennamr Rashid Abobaker and Marzieh Hamza Hussein

My wife

Najat Mohmood

&

My kids

Yousuf Abobaker, Sajida Abobaker and Ismail Abobaker for their endless love and support

Acknowledgement

First, I am very grateful to my supervisory committee for their continuous support and insightful guidance during the research period. My duty of gratitude invites me to extend my heartfelt thanks and appreciation to Dr. Faisal Khan for standing by my side during the difficult circumstances after the death of Dr. John Shirkoff and the Covid-19 pandemic and for supervising this study. In this regard, I cannot fail to record a word of thanks and gratitude to Dr. Muhammad Aziz Rahman, whose directives had the most significant impact on setting me on the road to completing this study. Dr. Rahman has many contributions in experimental and numerical procedures development and reviewing and publishing manuscripts. I also extend my thanks and gratitude to Dr. Amer Aborig for all his efforts by providing advice and direct supervision on laboratory experiments and reviewing manuscripts.

Also, I cannot forget the late Dr. John Shirkoff, who provided guidance throughout the beginning stages of the project and financial support to purchase materials for the experiments. It would be impossible to finish the thesis writing up without their uncountable help.

In addition, I acknowledge the Engineering Computing Services (ECS) team for taking advantage of high-performance computing facilities and remote access to the computer lab during the Covid-19 pandemic time. I would like to express my gratitude to Dr. Stephen Butt for providing the experimental setup and reviewing the manuscripts. Further, I do not forget to extend my thanks to Dr. Syed Imtiaz, who provided a place for the experimental setup, and Dr. Edison Sripal, who helped us measure the index properties for artificial samples. Finally, I would like to thank everyone who helped and participated in this work.

Contents

List of Tables

List of Figures

Abbreviations

ANOVA	Analysis of variance
BBD	Box–Behnken design
BIB-SEM	Combining Broad Ion Beam polishing and Scanning Electron Microscopy
CFD	Computational fluid dynamics
DQ	Data acquisition
DoE	Design of experiments
FE-SEM	Field Emission Scanning Electron Microscopy
FIB-SEM	Focused ion beam scanning electron microscopy
EOR	Enhanced oil recovery
IPR	Inflow performance relationship
MIP	Mercury intrusion porosimetry
PD	Perforation by drilling
PR	Productivity Ratio
PSD	Pore size distribution
PTL	Particle Technology Labs
RSM	Response surface methodology
SEM	Scanning electron microscopy

Nomenclature

English letters:

$\vec{B}_f$	Body force
C_2	Inertial resistance factor
D	Diameter of sample
d	Distance between center of perforations and middle of pay zone
d_p	Perforation diameter
$\vec{F}_{pq}^{D}$	Drag force for non-porous flows/region
$\vec{F}_{pq}^{TD}$	Turbulent dispersed force
$\vec{F}_q, \vec{F}_q^L$ *and* $\vec{F}_q^{vm}$	External body, lift and virtual mass exchange forces
$\vec{g}$	Gravitational acceleration
$G(b)$	Function of b (hp/h)
H	Sample height
h	Formation thickness
h_d	Length of the completed interval / formation thickness
h_p	Length of the completed open interval
h_D	Reservoir dimensionless thickness
I_{ani}	Index of anisotropy
J_d	Productivity index for a well with skin factors
J_o	Productivity index for an ideal open hole
K	Absolute permeability
k_d	Permeability of damaged zone
k_{ch}	Horizontal permeability of crushed zone
k_{cv}	Vertical permeability of crushed zone
k_{cz}	Permeability of crushed zone
k_f	Formation permeability
k_h	Horizontal permeability
K_r	Permeability ratio
$K_{r,q}$	Relative permeability
K_S	Skin zone permeability
k_v	Vertical permeability
K_1	Lower layer permeability
K_2	Upper Layer permeability
l	Distance spanning the open interval's top to the formation's top
l_d	Distance spanning the open interval's top to the formation's top / formation thickness
L_d	Damaged zone length
l_p	Perforation length
l_w'	Modified perforation length

$\dot{m}$	Mass flow rate
$\dot{m}_{pq}$	Mass transfers form phase p to phase q
$\dot{m}_{qp}$	Mass transfers form phase q to phase p
n_p	Number of perforations (number of shots per foot)
P	Pressure
p_c	Capillary pressure for wetting phase
p_e	Pressure at the external boundary of reservoir
p_{wf}	Wellbore pressure
P_r	Penetration ratio
p_{wf}	Wellbore pressure
Q	Flow rate
Q_w	Water flow rate
Q_a	Air flow rate
r_{cz}	Radius of crushed zone around perforation
r_{cz}	Radius of crushed zone around perforation
r_d	Wellbore radius / formation thickness
r_e	Formation drainage radius
r_p	Perforation radius
R	Sample Radius
R_r	Ratio of crushed zone to perforation radius
r_r	Ratio of skin zone radius to wellbore radius
r_s	Skin zone radius
r_w	Wellbore radius
$\acute{r_w}$	Modified wellbore radius
$\grave{r_w}(\theta)$	Efficient wellbore radius
S	Mechanical Skin factor
S_{cz}	Skin due to rock crushed around perforations
S_d	Skin due to formation damage
S_D	Difference skin factor
s_{df}	Skin due to hydraulic fracturing
S_h	Horizontal perforation skin factor
S_p	Skin due to ideal perforations
S_{pdc}	Total perforation skin factor
s_{pp}	Skin due to partial penetration
S_t	Total skin factor
S_v	Vertical perforation skin factor
$S_{\emptyset,q}$	Source term
S_{wc}	Wellbore skin factor
S_{wb}	Skin due to wellbore effect
S_{wot}	Skin due to crushed zone without tip
S_{wt}	Skin due to crushed zone with tip
S_θ	Skin due to well inclination
t	Time

$\vec{v}$	Velocity
v_j	Velocity components for x, y and z directions
$\vec{v}_q$	Phase velocity vector
$\vec{v}_{pq}$ *and* $\vec{v}_{qp}$	Relative velocity vectors

Greek letters:

α_q	Volume fraction
Γ_q	Diffusion coefficient
γ	Porosity
γ_s	Porosity of skin zone
γ_f	Porosity of formation zone
γ_{tl}	Porosity of tow-layer reservoir zone
Δ_n	Medium thickness
Δp	Pressure drop
Δp_{pdc}	Pressure drop due to total skin factor
Δp_{woc}	Pressure drop (Ideal perforations without crushed zone)
Δp_{wot}	Pressure drop due to crushed zone without tip
Δp_{wt}	Pressure drop due to crushed zone with tip
θ	Perforation angle
θ_d	Ratio of perforation angle to 180°
θ_D	Ratio of well inclination angle to the maximum inclination angle
θ_m	Maximum angle of the slant
μ	Fluid viscosity
μ_q	Phase viscosity
ρ	Fluid density
ρ_q	Phase density
$\bar{\bar{\tau}}$	Stress tensor related to viscous flow
$\bar{\bar{\tau}}_q$	Phase shear stress
υ	Viscosity of water

Chapter 1

1. Introduction and overview

1.1 Introduction

A hydrocarbon well's productivity is generally considered the standard measure of the well's performance. The productivity of a well depends on several factors, including fluid characteristics, reservoir formation, formation damage, and the kind of completion the well undergoes. To finish a well, an appraisal of the reservoir's quality must be made. The appraisal considers aspects such as the properties of the reservoir rock (e.g., permeability and porosity) as well as saturation and type of interstitial water and hydrocarbon fluids. The process of drilling itself impairs the reservoir rock permeability, decreasing the reservoir's natural productivity. The last stage in well construction is known as well completion, which is also the first stage to move the reservoir toward production status. In near-wellbore regions, fluid flow can be significantly affected by the type of well completion applied. There are several different kinds of well completion. For example, open-hole completion creates a radial flow pattern surrounding the wellbore, leaving a normal trajectory. However, this form of well completion may not in itself be sufficient, in which case other well completion approaches may be necessary. For cased and perforated completion, the well needs to be perforated in order for communication to be enabled between the formation and wellbore. In comparison with ideal open-hole wells, perforated wells can undergo added pressure gains and losses. A perforated well's productivity depends on a number of different factors that interact with each other, such as penetration space, angle, depth, and perforation diameter. Note that during the perforation process, rocks at the perforation tunnels' sites are crushed. In perforation damage, any compaction at the perforation tunnels will lead to reduced permeability, more significant pressure drop, and lower reservoir productivity. Another method that may be used to prevent water and gas coning, isolate or control wellbore fluid entry, or reduce sand production is called partially penetrated completion. Unlike fully penetrated wells, the flow lines of partially completed wells proceed towards the wellbores perpendicularly, while flow pattern distortion due to partially penetrated completion increases pressure loss. The geometrical shape of the well (inclined, undulating, multi-branched, horizontal, and vertical) can also affect the well performance. In addition, when the reservoir pressure drops, two-phase flow occurs in the near-wellbore region, which adds more pressure losses. Overall, perforation total skin factor can be used to represent the combined impacts of reductions in compaction zone permeability near perforation tunnels, ideal perforations, partially penetrated, well inclination, and formation damage caused by drilling and other production operations near wellbores.

1.2 Background

An emerging trend in the hydrocarbon industry is to boost production rates at wells instead of exploring new ones, as new wells are becoming scarcer. However, precisely how the wellbore skin effect may impact completion still needs more investigations. Van Everdingen (1953) and Hurst (1953) first discovered this effect when they noticed that, near the wellbore, there was a greater than anticipated drop during the build-up analysis.

This type of damage typically takes place during production (e.g., drilling, completion, or workover operations) or reservoir engineering (Civan, 2015). In other words, any difference between an actual well's performances compared to that of an ideal vertical open hole is expressed as the total skin factor. A wide range of models (empirical, numerical, experimental, semi-analytical, etc.) have been developed over the past several decades for predicting perforated total skin and for determining the effects of the well completion (Harris 1966; Klotz et al. 1974; Locke 1981; Karakas and Tariq 1991; Yildiz 2006). Perforation is used to connect reservoir formation during hydrocarbon production stages. However, because near-wellbore permeability reduction affects well productivity, any kind of formation damage could negatively impact the overall success of the drilling project. Therefore, to reduce any formation damage effects on the well's productivity, damage mechanisms must be mitigated. This can be best accomplished by attaining a better understanding of fluid flows that occur in the near wellbore during hydrocarbon operations (Rahman et al., 2007a, 2007b; Ahammad et al., 2017, 2018, 2019a, 2019b). In addition, several experimental studies have been completed in recent times related to fluid flow in porous media (Ding et al., 2020, 2021). There are major improvements in computational fluid dynamics (CFD) and computers during the last three decades. The improvements permit the running of significantly larger models and finer meshes for significantly lower cost and time expenditures. As well, the improvements include revisions to field development strategies in relation to horizontal and deviated wells and upgrades to perforating technology in relation to increased penetration depths. Computational fluid dynamics (CFD) technology can easily and quickly model complex interactions flow occurring in near wellbore region (Wood et al., 2020), including formation damage and completion geometry. Several recent studies have used CFD (computational fluid dynamics) for simulating flows in porous media, especially near perforations and wellbore regions, which is becoming more widespread due largely to improvements in computer technology (Byrne et al., 2009, 2010, 2011, 2014; Molina, 2015).

1.3 Research Objectives and Scope

This study's overall objective is to present a better understanding of the fluid flow behavior in the near-wellbore region by evaluating the well completion effects on pressure gradient as a function of single and two-phase flow conditions. Therefore, the work assessed how different completion configurations and other perforation characteristics impact the total skin factor by creating a prototype representing the near-wellbore region conditions. The four main investigative procedures of the samples preparation, experimental method, numerical simulation, and statistical analysis have been used in this study to reach the following objectives:

1. Proposing a technique for preparing artificial sandstone samples that can be applied in this study and the hydrocarbon production research.
2. Studying the effect of damaged zone parameters on the mechanical skin factor value in the vertical open hole well and investigating how skin zone characteristics affect both the cross-flow and pressure distribution of a dual-layer reservoir vertical well.

3. Studying the effect of cased and perforated completion parameters: penetration space, angle and depth, the perforation diameter on the perforation skin factor and pressure gradient in the near-wellbore region,
4. Presenting accurate estimation of the skin factor for partially penetrated wells.
5. Conducting more investigations about the accuracy of available model for crushed skin factor as well as obtaining new correlations may be closer to reality based on some assumptions.
6. Calculating skin effects caused by deviated well slants when considering vertical-to-horizontal permeability anisotropy.
7. Studying the effect of two-phase flow conditions and rock properties (the liquid and gas flow rate, liquid viscosity, permeability, and porosity) on the injection build-up pressure and the time needed to reach a steady-state flow condition.

1.4 The problem statements

In the oil industry, well productivity is paramount, so anything that either interferes with or boosts productivity is worthy of investigation. Therefore, the analysis of fluid flows at the near-wellbore area is critical, as the flow system is not yet entirely understood, despite the majority of well production parameters being impacted by this area. Similarly, the fluid flow behaviors both at and near the well are also not sufficiently understood and involve a number of challenges, including skin zone (damaged region) and different completion configurations. Some of the types of skin damage that may occur at near-wellbore regions include formation plugging skin, flow convergence skin, partial penetration, and drilling-induced skin:

1. For cased and perforated wells, fluids can come into the wellbore via perforation tunnel arrays. The perforations are usually created around the wellbore helically (i.e., shaped like a helix or spiral). The current models used for simulating production flows in perforated vertical wells require a relatively complex process involving tables and equations to calculate skin factor. Aiming to streamline this process by taking advantage of developments in CFD technology and other software, the present work proposes an efficient yet simplistic model for simulating the flows in near well regions with helically and symmetric perforations.
2. The reduced permeability of the crushed zone around the perforation can be formulated in crushed-zone skin factor. For reservoir flow, earlier research studies show how crushed (compacted) zones cause heightened resistance in vertical flows entering perforations. This inflow is known as radially converging vertical flow. However, the effects related to crushed zones on the total skin factor are still a moot point, especially for horizontal flows in perforations. Therefore, the present study investigated the varied effects occurring in crushed zones in relation to vertical and plane flow.
3. The analytical solutions applied to partially penetrating wells take into consideration in their formulations that fluid is admitted at each point or interval along the surface of the completed wellbore. In other words, existing models neglect to include any additional fluid convergence caused by slots or perforations. However, our CFD

model did consider the intrusion of this additional fluid, analyzing its impact as partial penetration parameters.

4. For perforated inclined wells, however, perforations typically deviate from the horizontal plane at angle θ. Simultaneously, the direction of perforations in some completion designs is forced into being a parallel orientation to the bedding plane. More investigations were done about the drawbacks and limitations of the current models in this study.

1.5 Methodology

The four main investigative procedures of samples preparation, experimental method, numerical simulation, and statistical analysis were conducted for more accurate estimation of the total skin factor in the near wellbore region. The experimental approach has been used to validate the numerical model for single-phase and two-phase flow in the artificial samples. Statistical analysis has been coupled with numerical simulation to expand the investigation of fluid flow in the near-wellbore region that cannot be obtained experimentally, due to the limitations of the experimental setup, especially the small sample size.

1.5.1 Samples preparation

As sourcing natural samples can be both expensive and challenging, and because these samples, if found, are often anisotropic (i.e., display various characteristics depending on how they are analyzed), labs tend to rely on models. Therefore, many researchers presented different ways to create artificial samples. Holt et al. (2000) looked at artificial samples for simulating in-situ rock conditions. Their results showed how artificial specimens are interchangeable with the real core in lab tests. In similar work, Butt et al. (1999) investigated samples taken from a mine field in Nova Scotia, Canada, while Ahammad et al. (2018) likewise tested the real and artificial samples in a laboratory. Lab samples are generally prepared according to study specifications and other factors. For our purposes, we investigate the samples using an experimental set-up that has a broad range of applications related to near-wellbore flow phenomena (e.g., formation damage), which occurs at the well completion stage. Our artificial samples have been constructed of waterproof marine epoxy at the Drilling Technology Laboratory, Memorial University, Newfoundland, using genuine sandstone samples originating from Nova Scotia to validate the experimental set-up.

Currently, mercury intrusion porosimetry (MIP) is one of the common techniques used to analyze sandstone samples' main index properties and pore morphologies. The porosimeter uses a specialized pressure chamber as a means to force the mercury to fill porous substrate voids. Being forced by pressure, the mercury intrudes larger pores and then, under increasing pressure, starts intruding smaller pores (Giesche, 2006). Using this approach, it is possible to characterize both intra- and inter-particle pores. MIP was used first to characterize and then analyze the pore morphology and index properties for the artificial samples.

1.5.2 Experimental method

In the present study, the experimental set-up used was initially designed and built by Ahammad et al. (2018 and 2019a) as a radial flow cell (RFC); the RFC was created for the purpose of carrying out experiments under radial flow conditions.

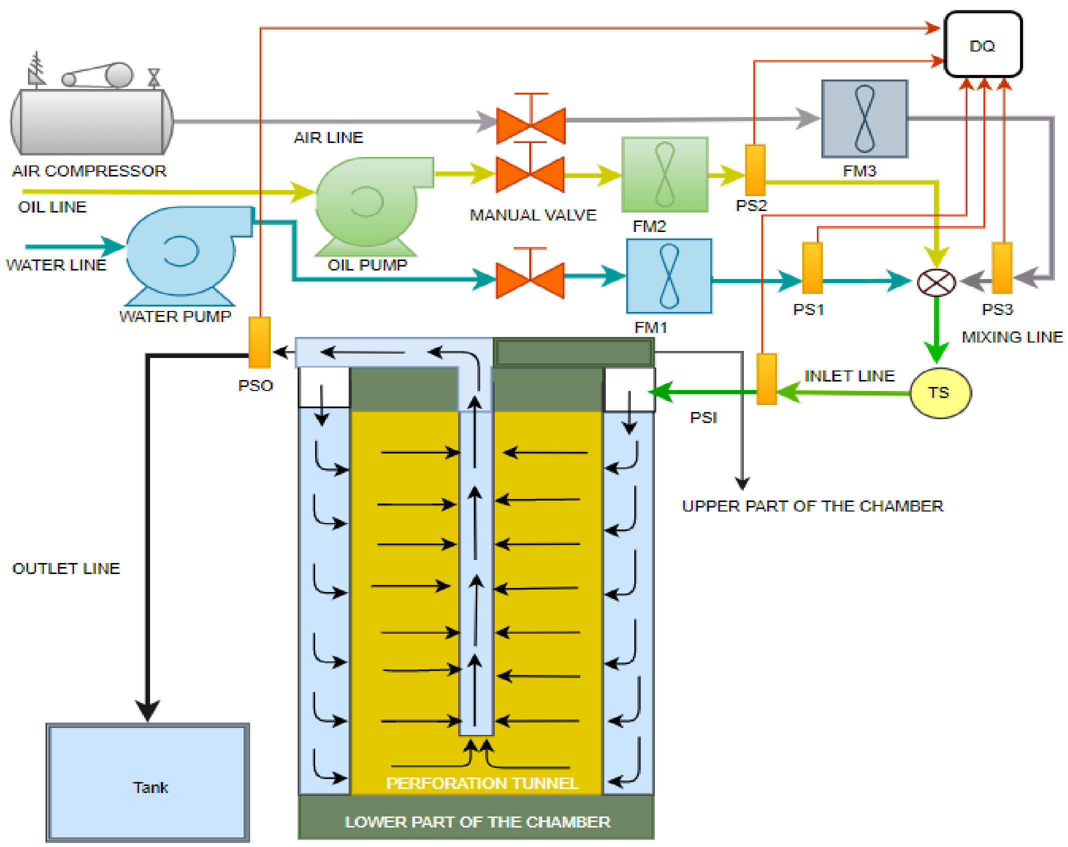

Figure. 1.1: Schematic diagram of the experiment. FM1, FM2, and FM3: Water flow meter, oil flow meter, and airflow meter, respectively; PS1, PS2, and PS3: 3 pressure sensors before mixing point; PSI and PSO: Inlet and outlet pressure sensors, respectively; TS: A temperature sensor; and DQ: Data Acquisition system

Figure 1.1 shows the RFC set-up, which features the three following main sections: flow lines extending from inlet to outlet; an inner chamber for holding samples with axial loads; and a Data Acquisition (DQ) system. Experiments carried out on perforation methods have primarily relied on rather simplistic assumptions, such as those presented by Rahman et al. (2007a, 2007b). Moreover, as a result of laboratory constraints, most experimental investigations have neglected key reservoir characteristics, such as thermal effects, drawdown pressure, and actual reservoir pressure.

In the experimental portion of this work, a measured volume of a single-phase (water) or two-phase (air/water) was injected into the core samples. As well, the geotechnical radial flow test set-up was used to measure the differential pressure and flow rate for perforated samples, with both air and water being radially injected into the core samples in single and the two-phase flow cases within the following boundary conditions: The outer side of the sample is considered an inlet while the perforation surface is an outlet. Furthermore, both inlet/outlet pressures were measured for cylindrical samples using specified fluid flow rates.

1.5.3 Numerical simulation method

In this study, ANSYS FLUENT was used for numerical simulations through a perforation tunnel and well completion samples. ANSYS FLUENT is a high-performance simulation tool that has been applied to solve a wide range of fluid flow problems with reliable and accurate solutions. The main target is to present a single-phase fluid flow simulation for a reservoir described as three-dimensional, vertical, and cylindrically layered. Hence, we can apply the conditions and assumptions enumerated below in developing our model:

1. The medium is anisotropic and porous, of uniform thickness, and is constantly permeable (i.e., features constant vertical permeability that is non-zero).
2. The flow through the reservoir can be described as single-phase water, and either radial-vertical laminar or Darcy's flow.
3. Any flux proceeding into the well features uniform distribution across perforated intervals.
4. Thermal effects are ignored.

In the numerical work, a measured volume of water was injected into the cylindrical sample. The conservation equations for mass and momentum describing single-phase flow in a porous region could be expressed, respectively, as

$$\frac{\partial \gamma\rho}{\partial t} + \nabla.(\gamma\rho\vec{v}) = 0 \tag{1.1}$$

$$\frac{\partial}{\partial t}(\gamma\rho\vec{v}) + \nabla.(\gamma\rho\vec{v}\vec{v}) = -\gamma\nabla p + \nabla.(\gamma\bar{\bar{\tau}}) + \gamma\vec{B}_f - \left(\frac{\mu}{k}\vec{v} + -\frac{C_2}{2}\rho|\vec{v}|\vec{v}\right) \tag{1.2}$$

The last term in Equation (1.2) represents the viscous and inertial loss imposed by the porous media on the fluid. The laminar flows in porous media generally feature a pressure drop proportional to permeability (k) and velocity (v). By ignoring out an inertial loss term, we can reduce the porous media model to Darcy's law, as expressed in Equation:

$$\nabla p = -\frac{\mu}{k}\vec{v} \tag{1.3}$$

The uniform mesh and cut mesh methods were used to generate high quality mesh. This configuration contributed to the production of a high mesh density to capture the significant pressure gradients in the border regions.

1.5.4 Statistical analysis method

Design of Experiments (DoE) was used in this study to conduct statistical analysis procedure. DoE refers to several different strategies that determine how various parameters can help alter results in controlled experiments. DOE methodologies can streamline systems while also determining how different factors may impact complex models through interactive, linear, or polynomial behaviors. A principal advantage of the DOE approach is that it requires fewer runs for researchers to gain a good grasp of the experimental results. Fewer runs translate to more cost-effective experimental procedures. In general, DOE functions by altering multiple factors during individual runs rather than changing them one factor per run, as is done in conventional approaches. DOE then applies statistical analysis in order to develop a model that accurately reflects the experiment results, for both simple and complex scenarios. Additionally, DOE can determine how variables will interact, which cannot be done in single factor runs.

Nowadays, advanced experimental design is employed across a number of different engineering fields, aiming to provide an optimal understanding of the experiments being conducted. However, very few studies have yet investigated how response surface techniques can be applied to determine the significance of wellbore parameters with regard to reservoir productivity. DOE's streamlined modeling approach represents a new way of conducting experiments, which means the results of this technique will provide novel insights into the research field. Of the several features that make DOE successful are its ability for randomization and comparison.

These features are discussed below. Randomization requires that runs be random for Design of Experiments analysis, as randomization ensures random distribution of any systematic errors that may happen during the course of an experiment. The random distribution of the errors lowers the likelihood that they will be included in the analysis. In contrast, replication means that runs are repeated at identical factor levels in order to obtain a sense of natural variances occurring in the experiment. Although replication may be important in laboratory experiments, it is not required in numerical/computer experiments, where no errors arising from external sources can occur. The present work focuses on numerical simulations, so there is no need to use replication here.

Comparison, however, is needed and is also a key feature of DOE, as it assesses the relative importance of the factors being considered. The ANOVA process employs this technique, with the mean square being used for estimating a factor's variance and the P-value then being calculated based on that estimate to determine the significance level at which the null hypothesis fails. In cases where the value is lower than the significance level chosen, the factor is deemed to be statistically significant.

The statistical analysis procedure includes the following steps:

1. The first step identifies independent factors or variables that can impact the outcome, followed by the identification of dependent factors or variables. Typically, these experiments run according to a variety of levels or factor values (Davim, 2016). Every experimental or numerical run represents a different combination of specific levels (or factor values) under investigation.

2. The second step includes determining the appropriate design for the numerical run. The Box-Behnken design (BBD) is one of the common design models, and it is a response surface methodology (RSM) design that only requires three levels for experimental or numerical runs. For the proposed study, Design-Expert® DoE software with BBD was used to design the necessary runs for the statistical analysis (Box and Cox., 1960, 1964).
3. The design model generates a number of runs based on the determined parameters and levels (design range). Each numerical run conducts and lists for the following analysis.
4. Once the numerical results are collected and listed, the next step determines the fitting model (linear, 2FI, quadratic, etc.) based on the response. The model will be statistically validated using variance (ANOVA). The statistical process includes determining which significant parameters that clearly affect outcomes and producing a model based on these parameters. The obtained model must show the normal distribution of numerical results with a constant variance of features.

1.6 Impact of research

This work will be contributed to improving hydrocarbon production by understanding how the fluid flow dynamics of the completion technique can affect well production in the near-wellbore region, thereby expanding industry knowledge about well performance.

1.7 Contributions and Novelties

In this study, the main contributions are to present a novel experimental technique by creating prototype artificial samples that mimic near-wellbore conditions and a numerical model that can predict the total skin factor more accurately. Earlier techniques to predict the total skin factor remain relatively impractical from an applicability perspective when considered for use in different reservoir types. This lack of practical applicability is caused by issues around computational accuracy and geometrical effects. More specifically, these aspects have persistently lacked sufficient accuracy and/or need to be processed through an elaborate transient numerical simulator. Therefore, this study provided a comprehensive analysis of fluid flow in the near-wellbore region and find new correlations that calculate completion configurations' effect on the skin factor and pressure gradient. The novel correlations have been produced from the current study that simplifies the estimation of the skin factor for vertical wells in many completion and damage cases:

1. Cased and completed perforated completion.
2. Partially penetrating wells.
3. Crushed zone around the perforation.
4. Inclined wells.

1.8 Industrial applications

Well completion is the final stage in a well construction that helps connect reservoir formations to wellbore during hydrocarbon production. The successful well completion method maximizes the reservoir productivity index due to less formation damage. This can be best accomplished by attaining a better understanding of fluid flows at near-wellbore regions during oil and gas operations. An understanding of the pressure gradient and fluid flow dynamics in perforations and casing and determining how important design is in flow distribution near a wellbore is significant for petroleum engineering applications (e.g., drilling, completion, multiphase production system and enhanced oil recovery method).

1.9 Organization of the thesis

This thesis has nine chapters. The first chapter describes the introduction, background, the objectives and scope, the problem statements, methodology, impact of research, contributions and novelties, industrial applications and organization of the thesis.

In chapter 2, artificial sandstone samples were created by mixing sand and epoxy glue; these samples were used in this work and can be used in hydrocarbon production projects. Mercury intrusion porosimetry (MIP) and scanning electron microscopy (SEM) have been used first to characterize and then analyze the pore morphology and index properties for the artificial samples. The results of this study were published in an article in the Canadian Society for Mechanical Engineering International Congress, June 27-30, 2020, Charlottetown, PE, Canada.

In chapter 3, computational fluid dynamics (CFD) simulation was presented to investigate the effect of damaged zone parameters on the mechanical skin factor value in vertical open hole well by using ANSYS Fluent platform 18. Also, the numerical model was used to investigate how skin zone characteristics affect both the cross flow and pressure distribution of a dual-layer reservoir vertical well. The work results were published in an article in the 5-6th Thermal and Fluids Engineering Conference (TFEC), Virtual Conference, May 26–28, 2021.

In chapter 4, the four main investigative procedures of samples preparation, experimental, numerical, and statistical analysis were conducted for more accurate estimation of the skin factor for perforated wells. The work results were published in an article in the Journal of Petroleum Exploration and Production Technology, 2021.

In chapter 5, the study investigated the varied effects occurring in crushed zones around the perforations in vertical and plane flow. The results of this study were published in an article in the Geofluids Journal, 2021.

In chapter 6, the study presented experimental work, numerical simulation model and statistical analysis for more accurate estimation of the skin factor for partially penetrated wells. The study results were published in an article in the Journal of Petroleum Exploration and Production Technology, 2021.

In chapter 7, the research employed computational fluid dynamics (CFD) software for simulating production flows in inclined wells through the injection of Darcy and single-phase flows using 3D geometric formations. The work results were published in an article in the Energies Journal, 2021.

In chapter 8, three main investigative procedures of experimental, numerical, and statistical analysis were presented to investigate the behavior of two-phase flow boundary conditions (liquid and gas flow rate, liquid viscosity) and effect of rock properties (permeability, and porosity) through a cylindrical perforation tunnel. The work results were published in an article in the ASME 40th International Conference on Ocean, Offshore and Arctic Engineering OMAE, Virtual Conference: June 21 – June 30, 2021.

1.10 Co-authorship statement

I, Ekhwaiter Abobaker, hold a primary author status for all the Chapters in this dissertation, and I carried out most of the experimental and numerical data collection and analysis. I have drafted the manuscripts and included the comments of the supervisory committee and other co-researchers. However, all manuscripts are co-authored by my supervisor and other co-researchers; their contributions have facilitated the completion of this study, as summarized below.

In the Chapter 2, I am the primary author and, I have analyzed the index properties data of the artificial samples and drafted the manuscript for review and comments. As co-author, Abadelhalim Elsanoose helped collect, sieve, and create artificial samples. Dr. Amer Aborig contributed to determining the required quantities of sands and reaching the sample's optimal shape through supervision and follow-up. Dr. Edison Sripal helped in measuring the index properties (permeability, porosity, etc.) of the artificial samples. Dr. Mohammad Azizur Rahman and other co-authors supported in developing the idea and reviewing the draft manuscript.

In the Chapters 3-8. I am the primary author, and I have 80%- 90% contributions in all chapters. The experimental facility used in most chapters initially was designed and built by Ahammad et al. (2017) as a radial flow cell (RFC); it was updated in this work with the collaboration of Abadelhalim Elsanoose. Also, Abadelhalim helped in conducting experiment runs and validating the numerical results. Dr. Mohammad Azizur Rahman has many significant contributions in conducting the experimental procedure and setting up the numerical simulation modeling. Drs. Faisal Khan, Mohammad Azizur Rahman, Amer Aborig, and other co-authors supported in developing the idea and reviewing the draft manuscript and provided valuable comments that contributed to improving and enriching the manuscripts.

References

Ahammad, M. J. Rahman, M. A., Butt, S. D., & Alam, J. M. (2017). Numerical simulation of two-phase flow in porous media using a wavelet based phase-field method. Chemical Engineering Science, 173, 230-241.

Ahammad, M. J. Rahman, M. A., Butt, S. D., & Alam, J. M. (2019b). A computational fluid dynamics investigation of the flow behavior near a wellbore using three-dimensional Navier–Stokes equations. Advances in Mechanical Engineering, 11(9), 1–12. doi:1687814019873250

Ahammad, M. J., Rahman, M. A., Butt, S. D., & Alam, J. M. (2019a). An experimental development to characterise the flow phenomena at the near-wellbore region. ASME 2019 38th International Conference on Ocean, Offshore and Arctic Engineering. Glasgow, Scotland, UK: Volume 8: Polar and Arctic Sciences and Technology; Petroleum Technology.

Ahammad, M., Rahman, M., Zheng, L., Alam, J., & Butt, S. (2018). Numerical investigation of two-phase fluid flow in a perforation tunnel. Journal of Natural Gas Science and Engineering, 55, 606-611.

Box, G. E., & Behnken, D. W. (1960). Some new three level designs for the study of quantitative variables. Technometrics, 2(4), 455-475.

Box, G. E., & Cox, D. R. (1964). An analysis of transformations. Journal of the Royal Statistical Society: Series B (Methodological), 26(2), 211-243.

Butt, S. (1999). Development of an apparatus to study the gas permeability and acoustic emission characteristics of an outburst-prone sandstone as a function of stress. International Journal of Rock Mechanics and Mining Sciences, 36(8), 1079-1085.

Byrne, M. T., Jimenez, M. A., & Chavez, J. C. (2009). Predicting well inflow using computational fluid dynamics - closer to the truth? the 8th European Formation Damage Conference. Scheveningen- Netherlands.

Byrne, M. T., Jimenez, M. A., Rojas, E. A., & Chavez, J. C. (2010). Modelling well inflow potential in three dimensions using computational fluid dynamics. the SPE International Symposium and Exhibition on Formation Damage Control. Louisiana, USA.

Byrne, M., Djayapertapa, L., Watson, K., & Goodin, B. (2014). Complex completion design and Inflow Prediction enabled by detailed numerical well modeling. the SPE International Symposium and Exhibition on Formation Damage Control. Lafayette, Louisiana, USA.

Byrne, M., Jimenez, M. A., Rojas, E., & Castillo, E. (2011). Computational fluid dynamics for reservoir and Well fluid Flow Performance Modelling. the SPE European Formation Damage Conference. Noordwijk-Netherlands.

Civan, F. (2015). Reservoir formation damage. Gulf Professional Publishing.

Davim, j. P. (2016). Design of experiments in production engineering. Cham: Springer.

Ding et al., (2020). Estimation of Local Equilibrium Model Parameters for Simulation of the Laboratory Foam-Enhanced Oil Recovery Process Using a Commercial Reservoir Simulator. ACS Omega, 5(36), 23437-23449.

Ding et al., (2021). An experimental investigation of the foam enhanced oil recovery process for a dual porosity and heterogeneous carbonate reservoir under strongly oil-wet condition. Fuel, 122684.

Giesche, H. (2006). Mercury porosimetry: A general (practical) overview. Particle & Particle Systems Characterization, 23(1), 9-19. doi:10.1002/ppsc.200601009

Harris, M. (1966). The effect of perforating oil well productivity. Journal of Petroleum Technology, 18(04), 518-528.

Holt, R., Brignoli, M., & Kenter, C. (2000). Core quality: Quantification of coring-induced rock alteration. International Journal of Rock Mechanics and Mining Sciences, 37(6), 889-907.

Karakas, M., & Tariq, S. (1991). Semianalytical productivity models for perforated completions. SPE Production Engineering, 6(01), 73-82.

Klotz, J., Krueger, R., & Pye, D. (1974). Effect of perforation damage on well productivity. Journal of Petroleum Technology, 26(11), 1303-1314.

Locke, S. (1981). An advanced method for predicting the productivity ratio of a perforated well. Journal of Petroleum Technology, 33(12), 2481-2488.

Molina, O., & Tyagi, M. (2015). A computational fluid dynamics approach to predict pressure drop and flow behavior in the near wellbore region of a frac-packed gas well. ASME 2015 34th International Conference on Ocean, Offshore and Arctic Engineering, 10. St. John's, Newfoundland, Canada.

Rahman, M., Mustafiz, S., Biazar, J., Koksal, M., & Islam, M. (2007a). Investigation of a novel perforation technique in petroleum wells—perforation by drilling. Journal of the Franklin Institute, 344(5), 777-789.

Rahman, M., Mustafiz, S., Koksal, M., & Islam, M. (2007b). Quantifying the skin factor for estimating the completion efficiency of perforation tunnels in petroleum wells. Journal of Petroleum Science and Engineering, 58(1-2), 99-110.

Van Everdingen, A. (1953). The Sktn Effect and Its Influence on the Productive Capacity or a Well. Journal of Petroleum Technology, 5(6), 171-176. doi:10.2118/203-g

Wood, B. D., He, X., & Apte, S. V. (2020). Modeling turbulent flows in porous media. Annual Review of Fluid Mechanics, 52(01), 171-203.

Yildiz, T. (2006). Assessment of total skin factor in perforated wells. SPE Reservoir Evaluation & Engineering, 9(1), 61-76. doi:10.2118/82249-pa

Chapter 2

2. Investigating the effect of mixing grain size and epoxy glue content on index properties of synthetic sandstone sample

Investigating the effect of mixing grain size and epoxy glue content on index properties of synthetic sandstone sample

Ekhwaiter Abobaker[1], Abadelhalim Elsanoose[1], Mohammad Azizur Rahman[2], Amer Aborig[1], Yan Zhang[1] , Edison Sripal[1]

Corresponding author: Ekhwaiter Abobaker; email: eera48@mun.ca

The Canadian Society for Mechanical Engineering International Congress, 2020, Charlottetown, PE, Canada

Abstract: Evaluating petroleum reserves requires an initial investigation of the relevant petrophysical characteristics of a target area's sandstone. In general, the most common type of host rocks represented in hydrocarbon reservoirs are sedimentary rocks, which include sandstone. This paper presents a technique for preparing four homogenous synthetic sandstone samples that can be applied in hydrocarbon recovery projects. The approach involves mixing sand with epoxy glue and can be employed to create and evaluate synthetic sandstone samples characteristics and then compared with a carbonate sample. The study conducted extensive laboratory tests to create synthetic sandstone samples using four sandstone grain sizes. Three synthetic sandstone samples were made from different sandstone grain sizes, and one sample was a mixture of two different grain sizes with various amounts of epoxy. Mercury intrusion porosimetry (MIP) and scanning Electron microscopy (SEM) were used to first characterize and then analyze the pore

---

[1] Faculty of Engineering and Applied Science, Memorial University of Newfoundland, St. John's, NL, A1C 5S7, Canada

[2] Petroleum Engineering, Texas A&M University at Qatar, Doha, 23874, Qatar.

morphology and index properties of the synthetic samples. The index properties included permeability, porosity, median pore diameter, tortuosity, and pore size distribution. The experimental results indicated that weak solidified sandstone index characteristics are strongly affected by both mixing and grain size. In addition, SEM map images revealing pore morphologies and homogenous grain distribution of the tested samples indicate that grains that undergo reductions in size require additional epoxy glue content, likely due to binder distribution of glue among the small grains.

Keywords-component; homogenous synthetic sandstone samples; mixing grain size ; epoxy glue content

2.1 Introduction

Investigations into the properties of reservoirs necessitate the quantitative study of the surrounding rock formations. As a sedimentary rock class, sandstones are well-known as typical host rocks in hydrocarbon reservoirs, and the characteristics of sandstones have a significant effect on the development and success of drilling projects. Accordingly, it is important to understand the characteristics not only of sandstones but of their interrelationships with the immediate drilling environment. The characteristics of sandstone have economic significance, which means that knowledge about these characteristics is needed to determine a reservoir's potential and capacity for hydrocarbon production.

Over the years, enhanced oil recovery (EOR) experiments have been performed at various oil laboratories using different kinds of rocks commonly found in reservoir areas.

These rocks include but are not limited to Botucatu, limestone and Berea sandstones (Cardoso and Balaban, 2015). As sourcing natural samples can be both expensive and challenging, and because these samples, if found, are often anisotropic (i.e., display various characteristics depending on how they are analyzed), labs tend to rely on models (Marques et al., 2011; Fattahpour et al., 2014). To develop a pore model, the topology and geometry must be known, along with the properties of the pore space. As explained by Xiong et al. (2016), finding the properties of pore space usually involves the use of mercury intrusion porosimetry, gas adsorption, and direct imaging. These researchers also looked at development methods for primary pore networks. Furthermore, Xiong et al. (2016) found that pore network models can be invaluable tools in the prediction of mesoscale phenomena such as the linking of single pore processes. The current state of the technique uses mercury intrusion porosimetry (MIP) and scanning electron microscopy (SEM) for analyzing the main index characteristics and pore morphologies in sandstones that are weakly solidified. Both MIP and SEM are employed in the quantitative and qualitative assessments of pore structural features in various types of rock samples. In the hydrocarbon field, SEM-based imaging techniques have typically been employed to visually characterize pore systems of reservoir rocks at the nanoscale. The high-resolution FE-SEM techniques have been applied by Yang et al. (2016) and Sun et al. (2016) to study nanoscale pore features in organic-rich Wufeng-Longmaxi shale and the Lower Cambrian Niutitang shale, respectively. Loucks et al. (2012) also used SEM and FE-SEM to examine and analyze pore type as well as lithologic composition in shale and mudstone. Klaver et al. (2012) employed BIB-SEM and focused on pore space morphology for their Posidonia shale study. In related work, Jiao et al.

(2014) and Zhou et al. (2016) used FIB-SEM to explore 2D and 3D nano pore properties, respectively, in Longmaxi gas shales.

Using MIP, pore structure properties are examined more indirectly, providing a broader overview of pore information, including porosity, distribution, and permeability. MIP, which has been used for decades in various industries, utilizes capillary pressure measurements to characterize pore structure in a variety of porous media (Giesche, 2006; Vavra et al., 1992). The main advantages of using the MIP technique are that it is time-saving, easy to operate, and features wide pore-throat sizes that typically measure from 3 nm to 250 µm. Numerous researchers have investigated the pore structure for different reservoir rocks using MIP. For example, Zhang et al. (2016) used data from MIP measurements to examine pore structure properties and permeability in several different deep sedimentary rocks, including sandstone, coarse sandstone, medium sandstone, fine sandstone, siltstone, mudstone, sandy mudstone, and conglomerate. Yang et al. (2017) investigated the various qualities in pore systems of Longmaxi shales and organic-rich Wufeng by applying a few complementary strategies along with MIP. Also, Lai and Wang (2015) explored pore fractal features prevalent in tight gas sandstones by employing high-pressure mercury intrusion methods. In acknowledgment of previous work done in the field, the present study seeks to obtain homogenous synthetic sandstone samples from mixing sand and epoxy glue to be used in this study. It also further explores and defines microscale pore structure characteristics, along with the porosity and permeability of synthetic samples, utilizing both SEM and MIP in combination. These findings will then serve as a basis for comparison with natural carbonate samples.

2.2 Experimental Methods

2.2.1 Samples preparation

In the laboratory experiments, four highly permeable synthetic sandstone samples were prepared. The four cylindrical samples were made of sand particles measuring 0.18 to 0.85 mm, as shown in Figure 2.1. To begin the preparations and experiments, sieve analysis was conducted in order to quantitatively gauge the size of the sandstone samples' grains or particles. The aggregate samples were then dried inside a hot-air oven (thermostatically controlled) at temperatures between 105° C and 110° C. The samples were oven-dried for 24 hours and then sieved. Following the sieving, an analysis was conducted for aggregate samples obtained after using a 0.85 mm and smaller sieve net.

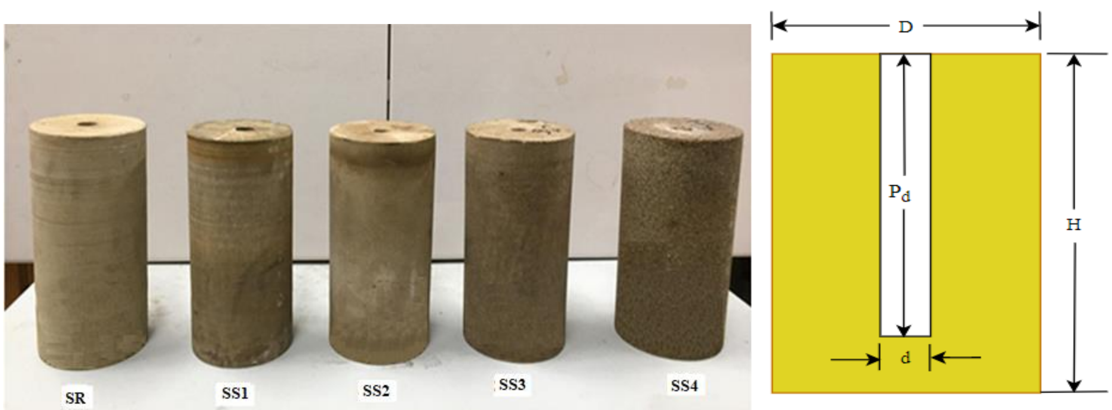

Figure 2.1: The shape and dimensions of the carbonate (SR) and four synthetic samples (SS1-SS4)

The synthetic sandstone samples have been created using sandstones of various sizes or by mixing two different sizes in the 0.18 mm to 0.85 mm range after sieving using waterproof marine epoxy glue. The sandstone and epoxy glue were mixed in different quantities (depending on the size of the sand) by using an electric mixer for 10 minutes.

The mixture is then placed in a plastic container over the course of four different stages, using an electric vibrator to ensure the distribution of grain with epoxy glue. The samples measure 12 inches high (H), with a diameter (D) of 6 inches and hole (d) in the center of the sample of 0.50 inch (at the center-point of the diameter), as explained in Figure 2.1. Initially, the samples were created without a hole (P_d) in the center of the sample. Then, a hole was made in the middle of the sample measuring 0.5 inch (radius) by 10 inches (depth). The large samples will be used to study the fluid flow behavior in the porous media, and the cores taken from the large samples were used in this study to obtain petrophysical properties of the samples. The weight of the sand and the amount of epoxy glue in each sample are presented in Table 2.1.

Table 2.1: The four samples preparation details

Sample name	**The weight of the sand and the amount of epoxy glue**			
	Sieving pan, NO	**Grain Size (mm)**	**Glue to Grain Percentage**	**Note**
SS1	80	< 0.18	950 ml to 8.025 kg	
SS2	60+80	(0.25-0.425) +0.18	850 ml to 8.025 kg	Mix of 60 and 80
SS3	60	0.25- 0.425	850 ml to 8.025 kg	
SS4	40	0.425 - 0.85	750 ml to 8.025 kg	

2.2.2 Methods for determining index properties

2.2.2.1 Mercury intrusion porosimetry (MIP)

Mercury intrusion porosimetry (MIP) can be used to obtain a variety of petrophysical properties or index properties, such as permeability, porosity, median pore diameter, average pore diameter, and bulk density. The porosimeter uses a specialized pressure chamber as a means to force the mercury to fill porous substrate voids. Being forced by pressure, the mercury intrudes into larger pores and then, under increasing pressure, starts intruding into smaller pores. Using this approach, it is possible to characterize both intra- and inter-particle pores.

MIP utilizes the Washburn Equation to find the relation of applied pressure and pore diameter, applying the mercury's physical characteristics (Giesche , 2006). These main characteristics are surface tension and the contact angle between the material and the mercury. In the Particle Technology Labs (PTL), various instrumentation and equipment are used that enable work to be carried out requiring pressures between around 1 psi and 60,000 psi. This range correlates well with pore measurements of between approximately 250 µm and 0.003 µm (3 nm).

Another consideration is the suitability of the mercury's contact angle in relation to the material being tested. If the contact angle cannot be measured or otherwise provided, default values are given for analysis. How much mercury enters the sample is monitored by volume, using a penetrometer. A section of the penetrometer holds the sample. In this case, the sample size must be around 1.5 cm wide and 2.5 cm long. The MIP tests in the present study were conducted using the carbonate sample and four synthetic sandstone samples. Throughout the course of the tests, pressure analyses are carried out. The results of the pressure testing show that the lowest and highest pressures are, respectively, one psia and 60,000 Psia. These readings relate well with the largest and smallest pore-throat diameters, respectively.

2.2.2.2 Scanning Electron Microscopy

As mentioned earlier, data related to pore throat size distribution is typically found by employing mercury intrusion porosimetry. When this option is not available or is unsuitable, we can use scanning electron microscope (SEM) images instead. SEM is able to examine microstructural pore characteristics at a nanoscale so that the distribution, morphology, and various types of nanopores can be explored and determined. Microscale images for one carbonate sample and four synthetic sandstone samples were taken using SEM. Prior to launching the imaging procedure, a surface from every sample is perpendicularly broken. The rock samples are 15 mm long, 5 mm high, and 10 mm wide. The perpendicular breakage of the samples results in undamaged surfacing that reveals each sample's pore structure. As a final step, the samples are digitally imaged using a through-the-lens detector (TLD) mode.

2.3 Results and discussion

2.3.1 MIP Measurements

In testing for permeability, measurements for the carbonate sample indicated a low permeability value of only 6.4133 mD, whereas the measurements for the four synthetic sandstone samples indicated high values (between 2035.9545 and 26151.7250 mD). In testing for porosity, the measurement results given for the synthetic samples using MIP indicated relatively large porosity compared to the real carbonate sample. We can describe pore structure properties (e.g., amount and size) quantitatively by employing parameter sets derived from the MIP experiments. Table 2.2 shows the pore structure parameters for the investigated samples obtained from MIP. These parameters include permeability, porosity, tortuosity, and median pore diameter.

Table 2.2: Parameters of pore-system structure measured by MIP

Sample name	Index properties for the samples			
	Permeability (mD)	**Porosity (%)**	**Tortuosity**	**Median pore diameter (μm)**
SR	6.5965	13.092	18.3575	0.0403
SS1	2035.954	33.3	3.19	32.14
SS2	6292.662	26.22	2.27	60.6101
SS3	8127.038	25.6	2.1	81
SS4	26151.72	25	1.7765	181.7485

How well a reservoir formation can store hydrocarbons is in large part determined by the reservoir rock’s porosity. Because porosity is such a key index characteristic, its characterization's accuracy in relation to sandstone’s textural properties is crucial. For sandstone, porosity represents the ratio of void volume (between the grains) to total rock volume. Compared to other rocks, sandstone generally has a broad porosity range. We found in our conducted tests that porosity in the four synthetic sandstone samples ranged between 25% and 33%, for an average value of around 28%. Natural sandstone, however, typically has a porosity of 10% to 25%. Suppose we plot the porosity and tortuosity from our test results against median grain-size particles. The average or median grain size was calculated for each range of sieving pan. In that case, we can see that synthetic fine-grain samples show higher porosity compared to coarse-grain samples (see Figure 2.2). A clear relationship emerges, showing porosity reduction in response to median grain size increases, and the results of tortuosity show a similar trend with median grain size. The results also demonstrate that this relationship is not linear. These test results agree with those found in previous studies, where porosity reduced when grain sizes increased for very well-sorted sands (Pryo, 1973; Bell, 1980; Fang 1991; Selle, 2000 and Ogolo et al., 2015). Their results showed that the density of packing decreases with reducing grain size depending on the grain shape. This means more space or pore volume between particles with decreasing grain size.

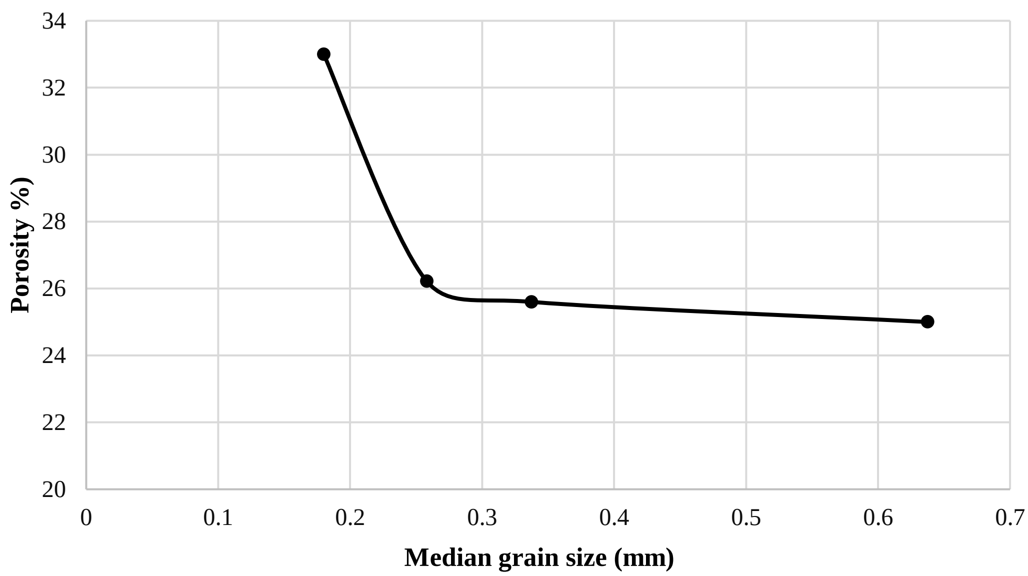

Figure 2.2: Effect of median grain size on porosity

Conversely, mixing two-grain size ranges indicates a different trend, where both the permeability and porosity for the synthetic sandstone are reduced. The primary cause leading to the reduction in porosity is that smaller particles intrude into large voids. Porosity generally depends on the size of particles when there are uniform spheres and fixed bulk volumes (i.e., ideal system). However, a real system features differently sized particles, in which case the smaller particles cause a decrease in porosity by intruding into any empty space between large particles. Hence, we can see from this that particle size determines porosity to a very great extent. Furthermore, the results reveal that systems that contain uniform particles (ideal systems) show that particle size and porosity are intimately related. This can be seen in cases SS1, SS3, and SS4. In the carbonate sample (SR), however, where there are differently sized particles, porosity is reduced because of the smaller particles intruding into porous spaces. Other factors that decreases porosity in the carbonate sample is the inclusion of different grain sizes, cementation, and compaction. The empty spaces are intruded by cementitious materials, reducing the pore percentage for the solid sample. An important factor tested in our experiments is permeability, which is the capacity for fluid in rock pores to move through reservoir rock. Permeability is directly related to the sample's particle size as well as to its cementation and consolidation. In general, permeability is reduced when solid feature pores are interconnected. This is because the empty spaces are intruded by smaller particles, in addition to cementation and compaction. Hence, in our tests, one sample (SS2) using two distinct sand sizes that were mixed in order to appropriately represent a real reservoir environment. A rock's dry bulk density can be defined as mass per unit volume. This parameter is highly affected by both the amount of pore space between grains and grain composition: more pore space leads to reduced density.

Furthermore, because grain size affects pore space, grain size also affects permeability and density. Figures 2.3 and 2.4 illustrate the test samples' interrelationships of permeability and median pore diameter vs. median grain size, clearly indicating a direct relationship caused by reduced pore space due to increased grain size.

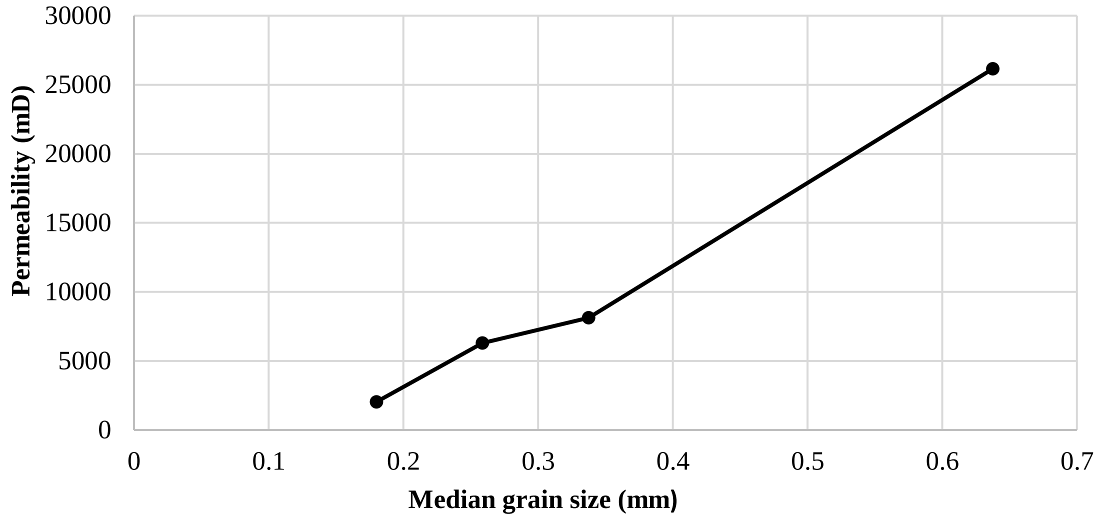

Figure 2.3: Effect of median grain size on permeability.

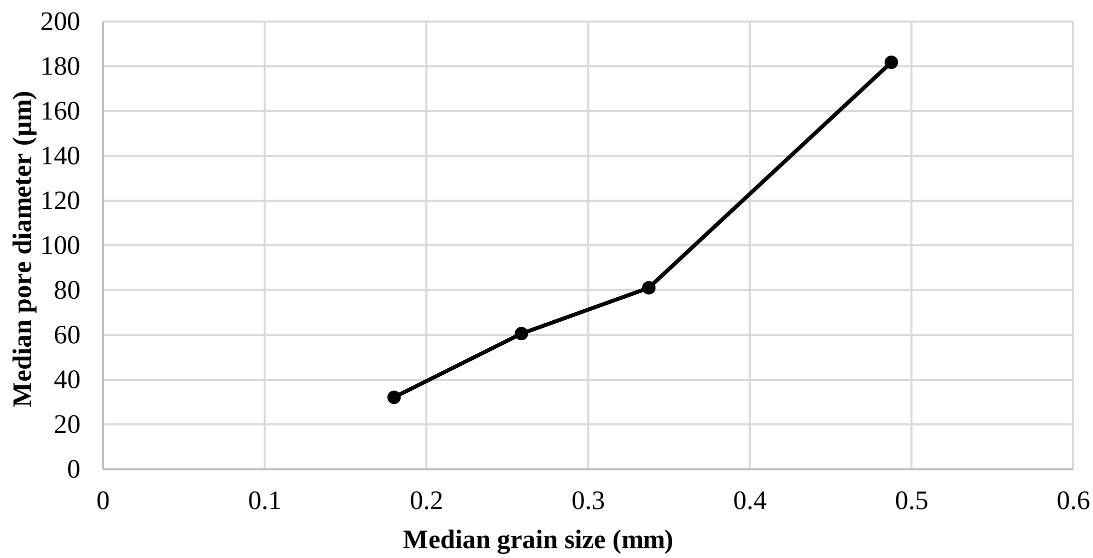

Figure 2.4: Relationship between median grain size and median pore diameter

Using MIP experimental data, Figures 2.5 and 2.6 show the pore size distribution (PSD) curves as pore throat diameter vs. dV/dlogD pore volume for both the carbonate sample and the synthetic sandstone samples. As can be seen, the samples for both carbonate and synthetic sandstone samples reveal PSD curves with the single-peak distribution. Moreover, pore sizes are mainly in the range of 0.03 to 350 mm. Loucks et al. (2012) reported pore size classification schemes for fine-grain samples. In referring to their work, we can see that our fine-grain samples' dominant pores can be classified as micropore (0.03 μm ≤ d < 62.5 μm). Also, using Loucks et al. (2012) as a reference, the PSD curves of the four synthetic sandstone samples in our study show single peaks, which means that the synthetic sandstone samples have homogenous pore size distributions.

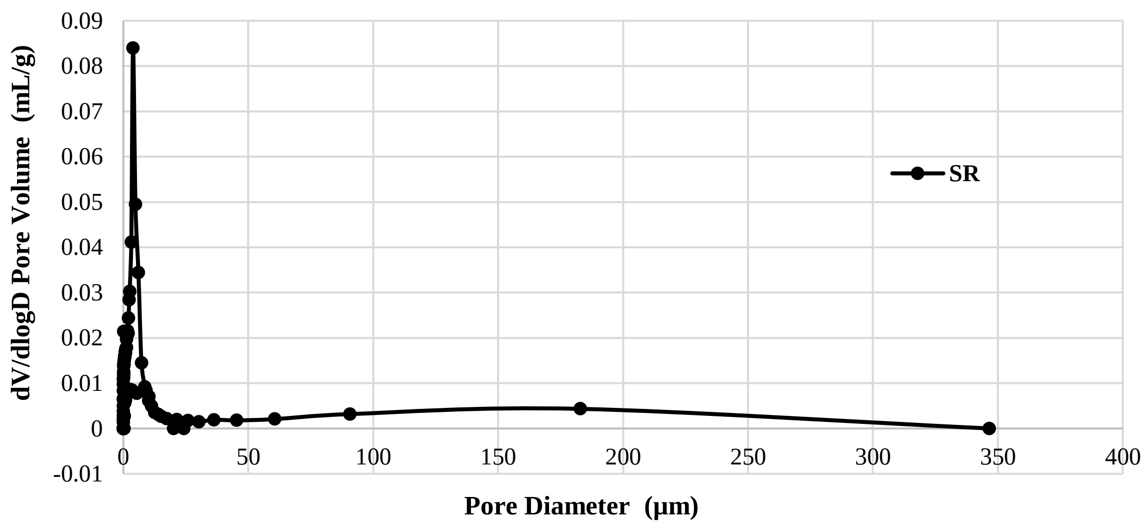

Figure 2.5: Pore size distribution (PSD) curves of carbonate sample

Figure 2.6 shows PSD curves from synthetic samples of differently sized grains (i.e., SS1, SS2, SS3 and SS4) as measured with MIP. As can be seen, there is a rise in cumulative porosity in samples of the same grain size as well as those for mixing grain size samples. Although this increase is not significant in pore throat sizes below 30 μm, most of the pores from the synthetic sandstone samples are 30 µm or larger and feature pore size distribution that is homogenous. In any case, the two figures show a similar PSD curve trend between the carbonate sandstone sample (SR) and the synthetic sandstone samples (SS1, SS2, SS3 and SS4), other than for variations in the pore size due to the samples' differently sized grains.

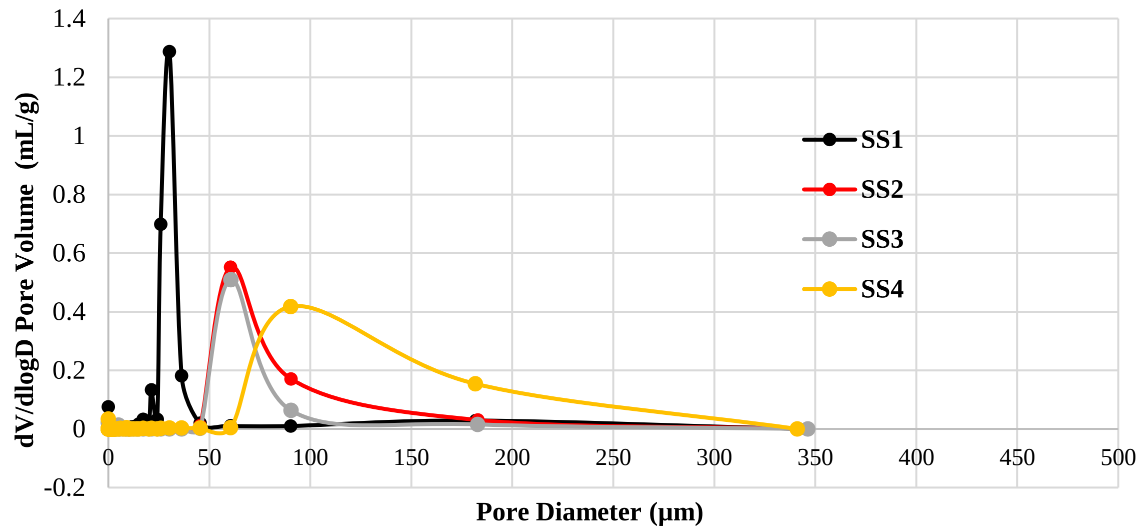

Figure 2.6: Pore size distribution (PSD) curves of the four synthetic sandstone samples

2.3.2 SEM Measurements

By investigating and analyzing pore structure, we can better understand the fluid transport mechanism in sandstone. We proposed a quantitative approach for characterizing the distribution of pore sizes in synthetic sandstone and carbonate samples, using scanning electron microscopy (SEM). Following an initial SEM scan, we chose specific SEM images we considered representative among dozens of images. The main aim was to best showcase the samples' micro-morphology. As SEM image magnification can affect the quality and type of information it relays, choosing appropriate magnification parameters is crucial. Following several attempts to obtain accurate representations of the needed data, we chose SEM images from the identical scanned area and from the identical operating voltage (30 kV), but showing different magnifications. These differences in magnification revealed the images' meso-morphology features for the samples, as depicted by Figures 2.7 and 2.8. Having chosen these SEM images, we could clearly observe the pores, grains and glue content, along with the material and structural morphology of the samples. The left side of the SEM images depicts grayscale pictures (predominantly grey and black), with the grey portions indicating grain matrix and the black portion possibly denoting the pore. In addition, the transition zone (black to white) could indicate an interface existing between the grain matrix and the pore.

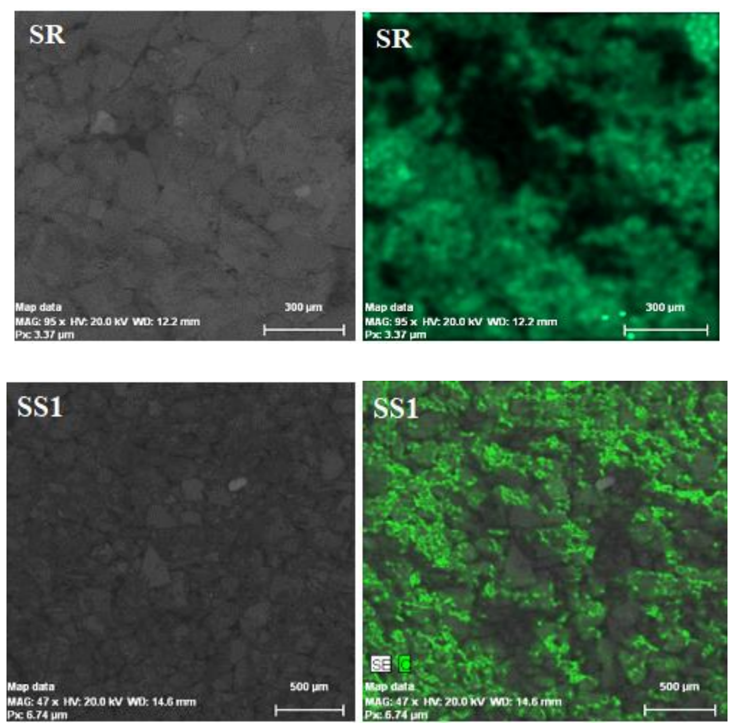

Figure 2.7: The SEM images of synthetic sandstone sample (SS1) and carbonate sample (SR).

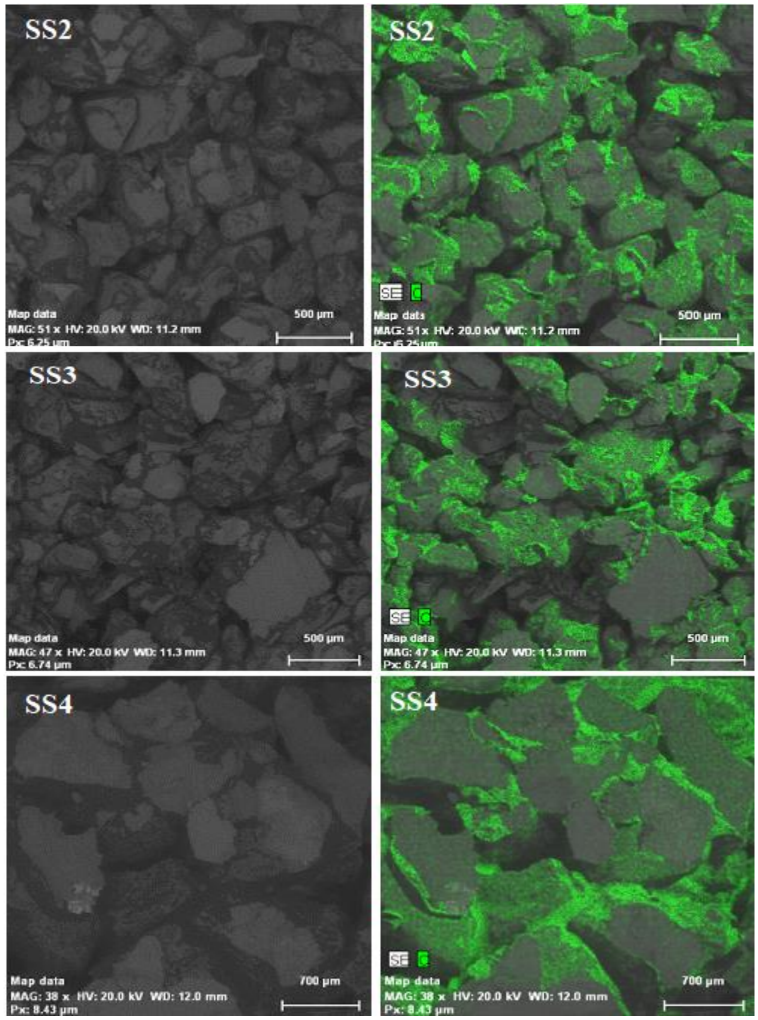

Figure 2.8: The SEM images of synthetic sandstone samples (SS2, SS3 and SS4)

Also, the green map images reveal the distribution of epoxy glue content among the grains. From the map, we can see SEM images showing how reductions of grain sizes require additional epoxy glue content because when the grain size is smaller, more glue is needed. As depicted, the glue is located at the contact area of the grain. It creates binder bonds that grow harder and join sand particles when sintered. Hence, as the number of bonds and extensions increases, so does the glue. During this process, particles become involved, intruding empty spaces and causing decreases in permeability and porosity. The SEM imagery ultimately indicated similar pore size distribution, similar pore orientation, similar pore shape, and similar microstructure. All of which points to the porosity and mineralogy in the four artificial samples being homogenous. Finally, we saw that areas within the SEM imagery showed connecting pore throats among the sandstone matrix pores. As demonstrated in Figure 2.8, the pore throats exhibited nearly the same diameters, indicating that pores can be characterized as pervasive in addition to being interconnected with the glue matrix.

2.4 Conclusion

This work presents a technique for preparing homogenous synthetic sandstone samples that can be applied in this study and hydrocarbon recovery projects. Mercury intrusion porosimetry (MIP) and scanning electron microscopy (SEM) have been used to first characterize and then analyze the pore morphology and index properties for the synthetic sandstone samples. The following conclusions can be summarized:

1. The experimental results indicated that weak solidified sandstone index characteristics are strongly affected by both mixing and grain size:

   a) The results exhibited an inverse relation between the samples' porosity and the grain size, with porosity experiencing a non-linear reduction with increases in grain size.

   b) The results also showed direct relationships between grain size and other properties such as permeability and median pore diameter. In this case, permeability levels rose with increases in median grain size. This tendency appears to have an indirect relation with reductions in porosity, considering median grain size as a function.

c) The results point to reductions in both permeability and porosity when two different grain sizes are mixed. The primary cause for the initial reduction in permeability and porosity appears to be the infilling of larger-sized voids with smaller-sized particles.

2. The PSD curves showed homogenous pore size distributions and trend similarity between the carbonate sample and the synthetic sandstone samples.

3. Furthermore, SEM map images of the pore morphologies and grain distribution of the tested samples indicate that grains that undergo reductions in size require additional epoxy glue content, likely due to binder distribution of glue among the small grains.

References

Bell, F. G., (1983). Fundamentals of Engineering Geology, Pp. 219.

Cardoso, O. R., & Balaban, R. d. (2015). Comparative study between Botucatu and berea sandstone properties. Journal of South American Earth Sciences, 62, 58-69. doi:10.1016/j.jsames.2015.04.004.

Fang, Hsai-Yang. (1991). Foundation Engineering Handbook. Second Edition, USA, Pp.118.

Fattahpour, V., Baudet, B. A., Moosavi, M., Mehranpour, M., & Ashkezari, A. (2014). Effect of grain characteristics and cement content on the unconfined compressive strength of artificial sandstones. International Journal of Rock Mechanics and Mining Sciences, 109-116. doi:10.1016/j.ijrmms.2014.09.008

Giesche, H. (2006). Mercury porosimetry: A general (practical) overview. Particle & Particle Systems Characterization, 23(1), 9-19. doi:10.1002/ppsc.200601009.

Jiao, K., Yao, S., Liu, C., Gao, Y., Wu, H., Li, M., & Tang, Z. (2014). The characterization and quantitative analysis of nanopores in unconventional gas reservoirs utilizing FESEM–fib and image processing: An example from the lower silurian Longmaxi Shale, Upper Yangtze Region, China. International Journal of Coal Geology, 128-129, 1-11. doi:10.1016/j.coal.2014.03.004

Klaver, J., Desbois, G., Urai, J., & Littke, R. (2012). Bib-SEM study of the pore space morphology in early mature Posidonia Shale from the Hils area, Germany. International Journal of Coal Geology, 103, 12-25. doi:10.1016/j.coal.2012.06.012.

Lai, J., & Wang, G. (2015). Fractal analysis of tight gas sandstones using high-pressure mercury intrusion techniques. Journal of Natural Gas Science and Engineering, 24, 185-196. doi:10.1016/j.jngse.2015.03.027.

Loucks, R. G., Reed, R. M., Ruppel, S. C., & Hammes, U. (2012). Spectrum of pore types and networks in mudrocks and a descriptive classification for matrix-related mudrock pores. AAPG Bulletin, 96(6), 1071-1098. doi:10.1306/08171111061

Marques, L. C., Appoloni, C. R., & Fernandes, C. P. (2011). Porosity study of synthetic sandstones by non-destructive nuclear techniques. Materials Research, 14(3), 394-402. doi:10.1590/s1516-14392011005000048

Ogolo, Naomi A., Akinboro, Olorunmbe G., Inam, Joseph E., Akpokere, Felix E., and Mike O. Onyekonwu. (2015). Effect of Grain Size on Porosity Revisited. Paper presented at the SPE Nigeria Annual International Conference and Exhibition, Lagos, Nigeria. doi: https://doi.org/10.2118/178296-MS

Pryo, Wayne A. (1973). Permeability-Porosity Patterns and Variations in Some Holocene Sand Bodies. *AAPG Bulletin* , 57 (1), 162–189. doi: https://doi-org.qe2a-proxy.mun.ca/10.1306/819A4252-16C5-11D7-8645000102C1865D

Selle, Richard C. (2000). Applied Sedimentology. Second Edition, Academic Press Pp. 74.

Sun, M., Yu, B., Hu, Q., Chen, S., Xia, W., & Ye, R. (2016). Nanoscale pore characteristics of the Lower Cambrian Niutitang Formation Shale: A Case Study from well yuke #1 in the southeast of Chongqing, China. International Journal of Coal Geology, 154-155, 16-29. doi:10.1016/j.coal.2015.11.015.

Vavra, C., Kaldi, J., & Sneider, R. (1992). Geological applications of capillary pressure: A review. AAPG Bulletin, 76. doi:10.1306/bdff88f8-1718-11d7-8645000102c1865d.

Xiong, Q., Baychev, T. G., & Jivkov, A. P. (2016). Review of pore network modelling of Porous Media: Experimental Characterisations, network constructions and applications to reactive transport. Journal of Contaminant Hydrology, 192, 101-117. doi:10.1016/j.jconhyd.2016.07.002

Yang, R., Hao, F., He, S., Guo, X., Yi, J., Hu, H., . . . He, C. (2017). Experimental investigations on the geometry and connectivity of pore space in organic-rich Wufeng and Longmaxi shales. Marine and Petroleum Geology, 84, 225-242. doi:10.1016/j.marpetgeo.2017.03.033

Yang, R., He, S., Yi, J., & Hu, Q. (2016). Nano-scale pore structure and fractal dimension of organic-rich Wufeng-Longmaxi Shale from Jiaoshiba area, Sichuan Basin: Investigations using Fe-SEM, gas adsorption and helium pycnometry. Marine and Petroleum Geology, 70, 27-45. doi:10.1016/j.marpetgeo.2015.11.019.

Zhou, S., Yan, G., Xue, H., Guo, W., & Li, X. (2016). 2D and 3D nanopore characterization of gas shale in Longmaxi Formation based on FIB-SEM. Marine and Petroleum Geology, 73, 174-180. doi:10.1016/j.marpetgeo.2016.02.033.

Zhang, N., He, M., Zhang, B., Qiao, F., Sheng, H., & Hu, Q. (2016). Pore structure characteristics and permeability of deep sedimentary rocks determined by Mercury intrusion porosimetry. Journal of Earth Science, 27(4), 670-676. doi:10.1007/s12583-016-0662-z.

Chapter 3

3. Quantifying the mechanical skin factor effect on the pressure gradient and cross flow behavior in vertical oil wells

Quantifying the mechanical skin factor effect on the pressure gradient and cross flow behavior in vertical oil wells

Ekhwaiter Abobaker[1], Abadelhalim Elasnoose[1], Faisal Khan[1], Mohammad Azizur Rahman[2], Amer Aborig[1]

5-6th Thermal and Fluids Engineering Conference (TFEC), Virtual Conference, 2021

Abstract: One of the most common factors determining the permeability in the near-wellbore region is the mechanical skin factor, leading to increase pressure drop during hydrocarbon production. This type of damage typically takes place during production (e.g., drilling, completion, or workover operations). To boost productivity, engineers employ a range of optimization procedures at wellbore completion, depending on conditions, as a way to lower the skin value. Computational fluid dynamics (CFD) simulation was presented to investigate the effect of damaged zone parameters on the mechanical skin factor value in the vertical open hole well by using ANSYS Fluent platform 19. The numerical model was also used to investigate how skin zone characteristics affect both the cross-flow and pressure distribution of a dual-layer reservoir vertical well. The study has analyzed each investigated parameter's effect by conducting a single-phase flow through the cylindrical near wellbore region. The cross-flow behavior and pressure responses have been observed in three cases (positive, zero, and negative) for mechanical skin factor at a constant flow rate. The results showed the

---

[1] Faculty of Engineering and Applied Science, Memorial University of Newfoundland, St. John’s, NL, A1C 5S7, Canada

[2] Petroleum Engineering, Texas A&M University at Qatar, Doha, 23874, Qatar.

numerical model's ability to simulate real conditions of the near-wellbore region, and the comparison results demonstrated good agreement between the numerical model and Hawkins equation results. In addition, the cross-flow and pressure distribution appear to be affected by interactions occurring between the various characteristics of the skin zone and the reservoir layers. This work will help to simulate and understand the effects of various skin zone properties on the pressure drop in the near-wellbore region.

3.1 Introduction

The formation damage typically takes place during production (e.g., drilling, completion, or workover operations) (Yuan and Wood, 2018). The process of drilling itself impairs the reservoir rock permeability, decreasing the reservoir's natural productivity. One of the main contributing factors to well components is skin factor, which may significantly affect productivity. Therefore, production engineers should strive to design the best possible completion for each individual project and also focus on the completion's implementation. In general, most reservoirs have numerous layers with a wide range of physical characteristics. Separating the layers is the formation of shale or silt that are usually thin and have low permeability. Accurately estimating the properties of these layers (e.g., thickness, porosity, permeability, etc.) is critical for effective drilling procedures. However, for the purpose of simplicity, many reservoirs are considered either as a compilation of many layers or as a mass of one layer that is mostly uniform. The inaccurate appraisal of these layers' characteristics can lead to problems during drilling, as each of the layers affects the others via interlayer cross-flow in the reservoir. Hence, a less simplistic and more accurate treatment of the layers is essential. One of the many factors impacting fluid flow across permeable layers is when the flow moves in a perpendicular direction to the bulk flow. Such a cross-flow could result from one or more of four forces affecting fluid flow within permeable media, namely concentration, gravity, capillarity, and viscous forces. Also, well productivity has been documented as being affected by a number of interacting elements, including the formation damage zone, perforation methods, and boundary flow conditions. In the wellbore skin effect, the near-wellbore experiences a pressure drop; Van Everdingen (1953) and Hurst (1953) first discovered this effect when they noticed that, near the wellbore, there was a greater than anticipated drop during the buildup analysis. The altered zone permeability can be used to determine the skin effect, which may have either a positive or negative effect, depending on whether the altered zone's permeability is larger or smaller in comparison to that of the reservoir (Hawkins, 1956):

$$S = \left(\frac{K_f}{K_d} - 1\right) \ln\left(\frac{r_s}{r_w}\right) \tag{3.1}$$

Since then, despite the skin concept becoming a standard feature of oil and gas research when quantifying well conditions, very few researchers have examined wellbore skin values in relation to different kinds of completion designs. An ongoing issue that occurs across the various branches of the hydrocarbon industry is formation damage (Civan, 2015). Formation damage can impact the near-wellbore region as well as further down the formation itself (VasheghaniFarahani et al., 2014). In the drilling and completion stages, the damage usually results from fluids entering the pay zone or perforations, causing rock compaction (Ezeakacha et al., 2017). However, because near-wellbore permeability reduction affects well productivity, any kind of formation damage could negatively impact the drilling project's overall success. Therefore, to reduce any formation damage effects on the productivity of the well, damage mechanisms must be mitigated. This can be best accomplished by attaining a better understanding of fluid flows that occur in the near-wellbore during hydrocarbon operations (Rahman et al., 2006, 2007a, 2007b and 2008; Ahammad et al., 2018, 2019a). This work presented a numerical model in order to expand the investigation of the skin region effect on the pressure distribution and cross-flow in a vertical well with a single and a two-layer reservoir.

3.2 Methodology

ANSYS fluent (3D) 18.1 was used for numerical simulations through a near wellbore region with a single and two-layer reservoir. In the first stage, the cylindrical geometry, including the skin and formation zones were used to present near-wellbore conditions, as shown in Figure 3.1. The single-phase (1 liter /minute water) was injected radially through the cylindrical near-wellbore region. The inlet was specified as the outer formation zone surface, and the outlet was specified as the interior surface of the wellbore, as exhibited in Figure 3.2. The pressure at the outlet was imposed to be equal to gauge pressure. The two dimensionless parameters have been investigated, including the ratio of skin zone radius to wellbore radius and the permeability ratio.

$$r_r = \frac{r_s}{r_w} \tag{3.2}$$

$$k_r = \frac{K_f}{K_s} \tag{3.3}$$

The dimensions and the index properties of vertical near wellbore region included permeability and porosity, as shown in Table 3.1.

Table 3.1: The dimensions and the index properties of the near wellbore region.

Dimensions and properties of the sample	**Values (units)**
Sample height (H)	182.88 cm
Diameter of sample (D)	193.04 cm
Wellbore radius (r_w)	10.16 cm
Skin zone radius range (r_s)	15.24 -60.96 cm
Permeability of skin zone range (K_s)	$2*10^{-14}$ –10^{-15} m^2
Porosity of skin zone (γ_s)	16 %
Permeability of formation zone (K_f)	10^{-14} m^2
Porosity of formation zone (γ_f)	20 %

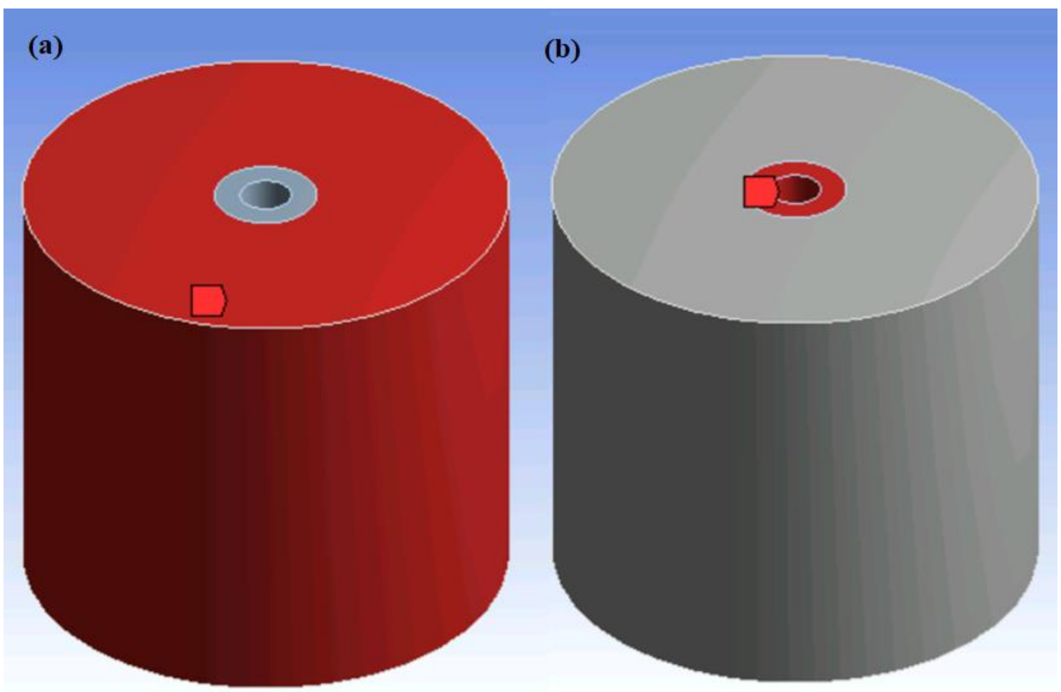

Figure 3.1: The formation zone (a), and the skin zone (b)

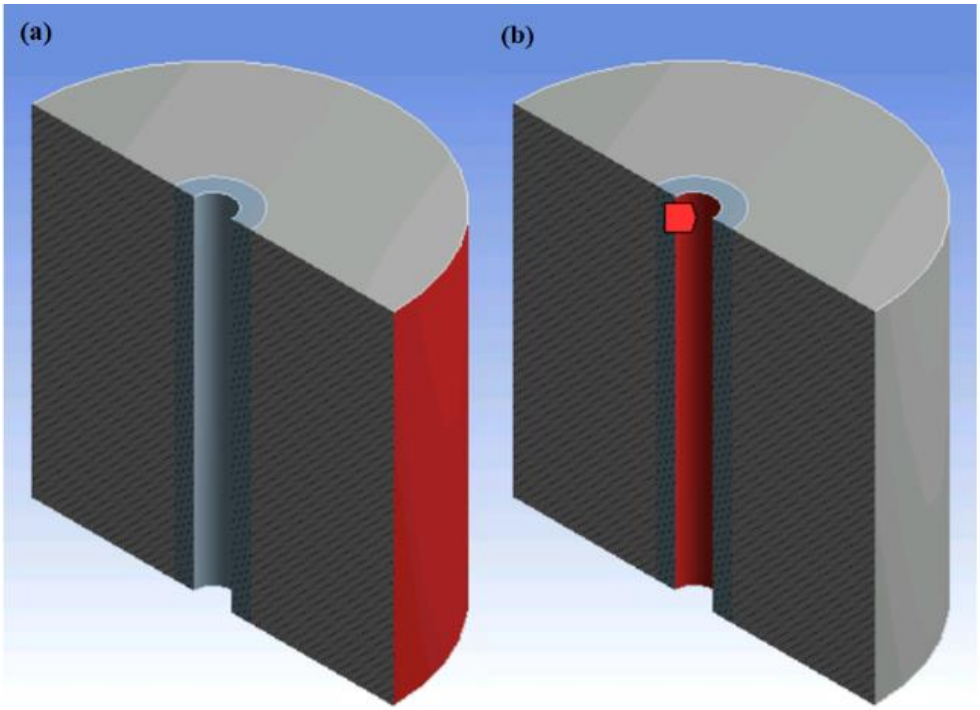

Figure 3.2: Vertical section for inlet (a) and outlet (b)

In the second stage, a two-layer reservoir was used to present near-wellbore conditions, which comprises two parallel layers with different permeability, are contiguous, and have no flow barriers on the boundary between them, as shown in Figure 3.3. Furthermore, each layer was assumed to be isotropic and has the same thickness. The layers also feature constant properties with regard to porosity, permeability, compressibility, etc., and the wellbore storage and gravity force impacts were assumed to be negligible. The single-phase (5 liter /minute water) was injected radially through the two cylindrical layers with formation damage around the well in three cases (positive, zero, and negative) for mechanical skin. The dimensions and the index properties of the two-layer reservoir with skin zone, as shown in Table 3.2.

Table 3.2: The dimensions and the index properties of the two-layer reservoir

Dimensions and properties the sample	**Values (units)**
Sample height (H)	365.76 cm
Diameter of sample (D)	10 m
Wellbore Radius (r_w)	10.16 cm
Skin Zone Radius (r_s)	50.8 cm
Positive Skin Zone Permeability (K_s)	10^{-15} m^2
Negative Skin Zone Permeability (K_s)	10^{-12}m^2
Lower Layer Permeability (K_1)	10^{-14}m^2
Upper Layer Permeability (K_2)	10^{-13}m^2
Porosity of Skin Zone (γ_s)	16 %
Porosity of Tow-layer Reservoir Zone (γ_{tl})	20 %

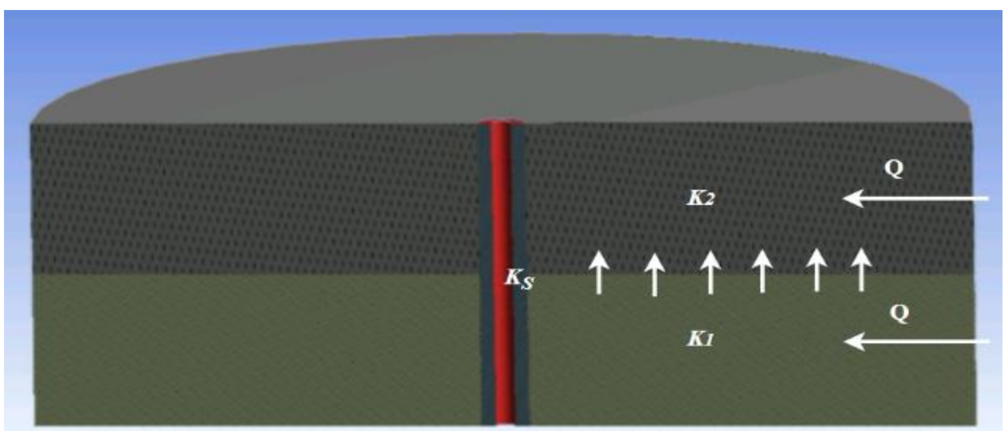

Figure 3.3: The two layers of the reservoir that parallel and contiguous with different formation permeability and a similar skin zone.

The cut mesh and uniform mesh strategies were used for generating high-quality mesh, as shown in Figure 3.4. This configuration helped to predict a good quality and high density mesh to capture localized great flow gradients in the border regions.

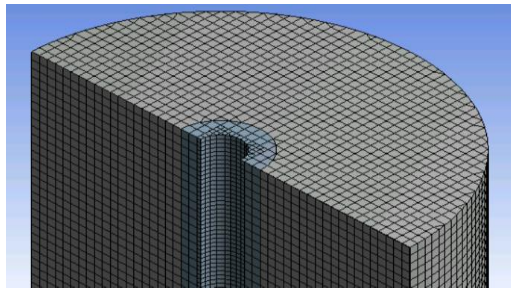

Figure 3.4: The shape of uniform configuration mesh that used in CFD simulations

The flow rate for a vertical well in a cylindrical near wellbore region with isotropic permeability and Darcy flow perpendicular to the wellbore is expressed as:

$$Q = \frac{2\pi K_f h(p_e - p_{wf})}{\mu\left[ln\left(\frac{r_e}{r_w}\right) + S\right]} \tag{3.4}$$

The skin factor can be obtained after the pressure drop is calculated from the simulation:

$$S = \frac{2\pi K_f h(p_e - p_{wf})}{Q\mu} - ln\left(\frac{r_e}{r_w}\right) \tag{3.5}$$

3.3 Results and discussion

In the first stage, the results of numerical investigations showed that CFD simulation was able to predict the effect of formation damage on the pressure gradient in the vertical near-wellbore region, as shown in Figure 3.5. The results showed the specific effects of two dimensionless parameters (the ratio of skin zone radius to wellbore radius r_r and the permeability ratio k_r) on the mechanical skin factor and the pressure gradient in the vertical near-wellbore region, and the comparison results demonstrated good agreement between the numerical model and Hawkins equation results. The results indicated that the increase of the ratio skin zone radius to wellbore radius has significant effects on the injection pressure, as exhibited in Figure 3.6. A rise in pressure drop is caused by higher resistance in a larger skin zone radius, as shown in Figure 3.7.

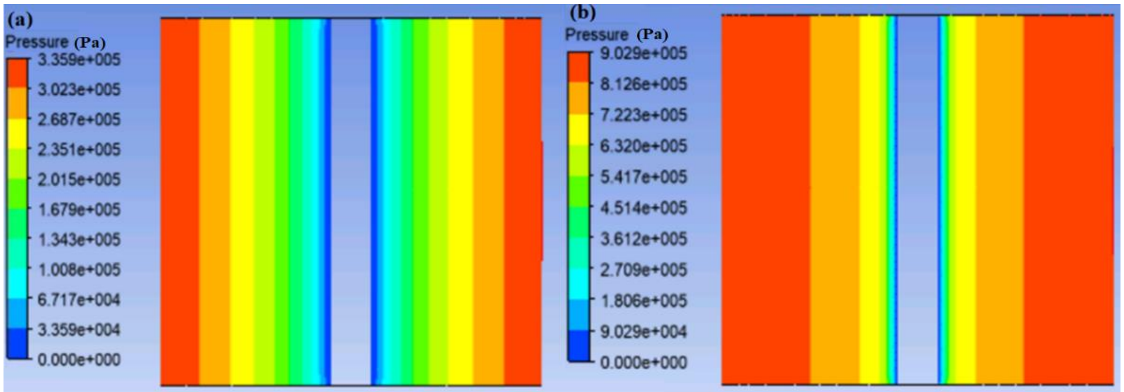

Figure 3.5: Numerical results of the pressure gradient through the near wellbore region without skin zone (a) and with skin zone (b) at Q = 1 liter/minute, r_r = 1.5 and k_r =10

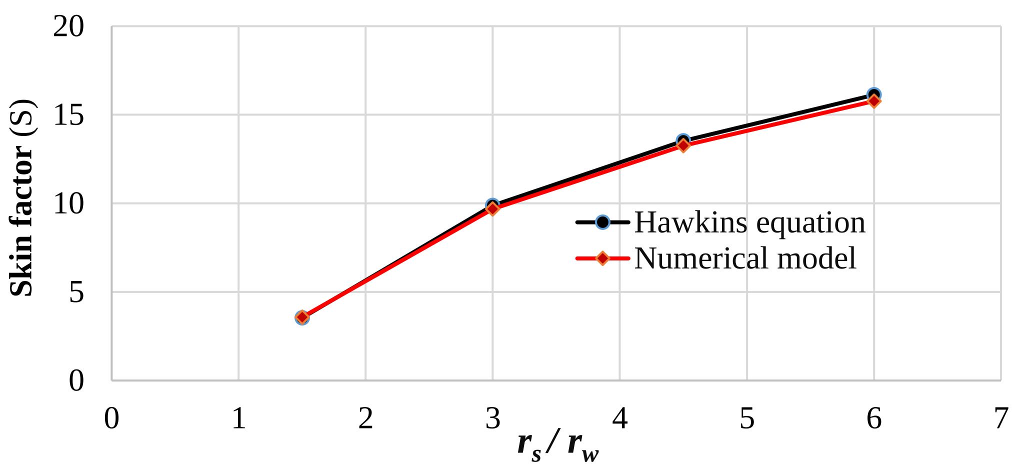

Figure 3.6: The comparison between the numerical model and Hawkins equation results for a single-phase flow at a water flow rate (1 liter/minute) and the ratio of skin zone radius to wellbore radius r_r (1.5 -6).

Also, the ratio of formation permeability to skin zone permeability has a great effect on mechanical skin factor with regard to the well productivity, as exhibited in Figure 3.8. If the ratio between the permeability of formation and skin zone is high, the rise in pressure drop will be higher, as shown in Figure. 3.9.

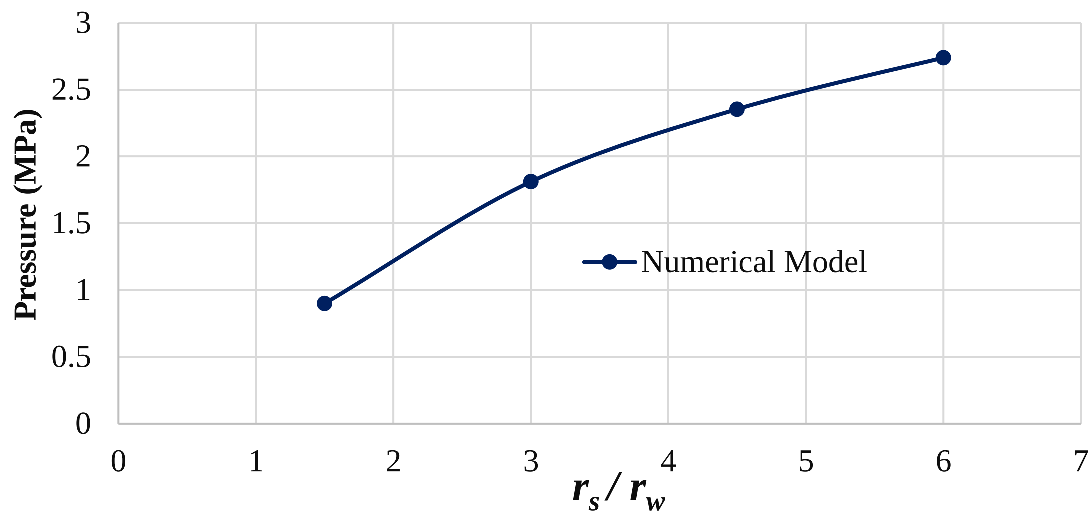

Figure 3.7: The numerical model result of pressure drop for a single-phase flow at the flow rate (1 liter/minute) and the ratio of skin zone radius to wellbore radius r_r (1.5 -6)

In this case, due to high resistance, higher energy consumption would be necessary in order to inject the required volume through the near-wellbore region. Therefore, using the optimal completion and drilling method reduces the mechanical skin factor and increases the production rate.

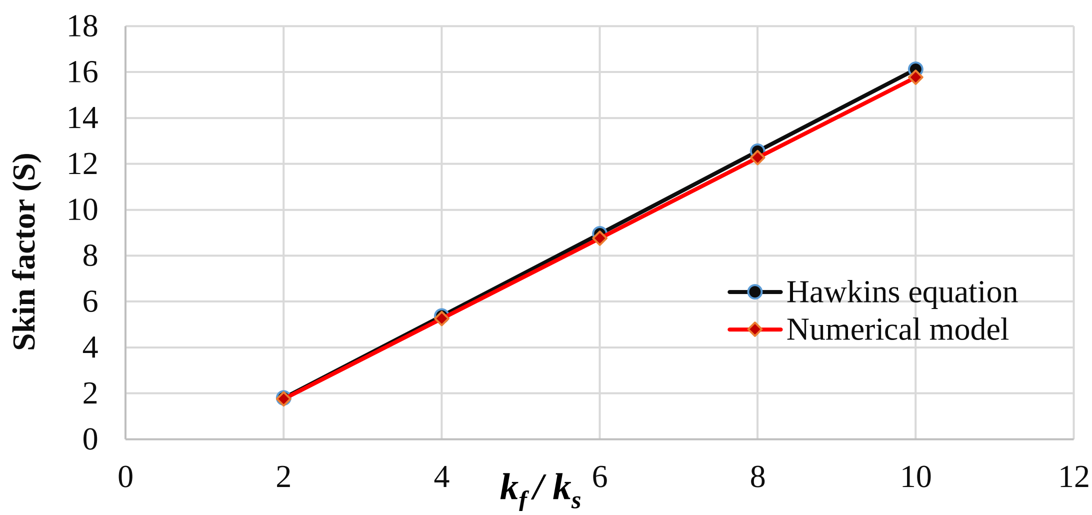

Figure 3.8: The comparison between the numerical model and Hawkins equation results for a single-phase flow at a flow rate (1 liter/minute) and a permeability ratio k_r (2 -10)

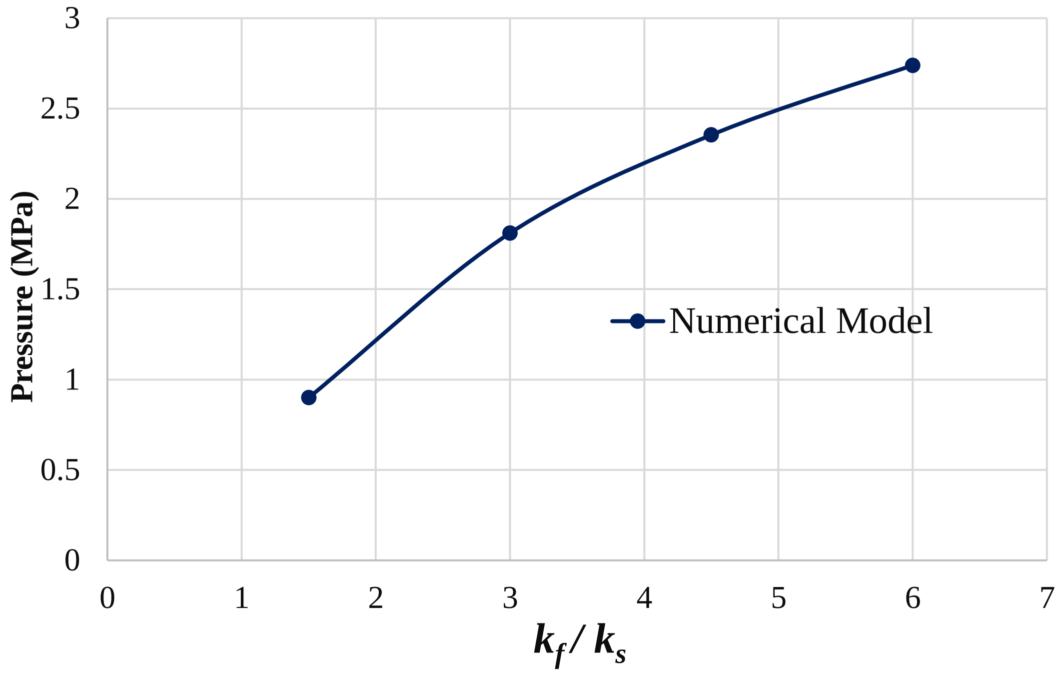

Figure 3.9: The numerical model result of pressure drop for a single-phase flow at flow rate (1 liter/minute) and range of permeability ratio k_r (2 -10)

The results provide a highly accurate estimation of cross-flow and pressure response behavior for the three examined cases. Moreover, as can be seen from the results, the layers' cross-flow and pressure distribution behavior were strongly affected by skin zone characteristics and permeability ratios, as shown in Figure 3.10. This is because the vertical pressure gradients, which develop due to different degrees of resistance, cause the fluids to flow between layers during vertical communication. However, the amount of cross-flow and the pressure gradient is mainly determined by vertical transmissibility.

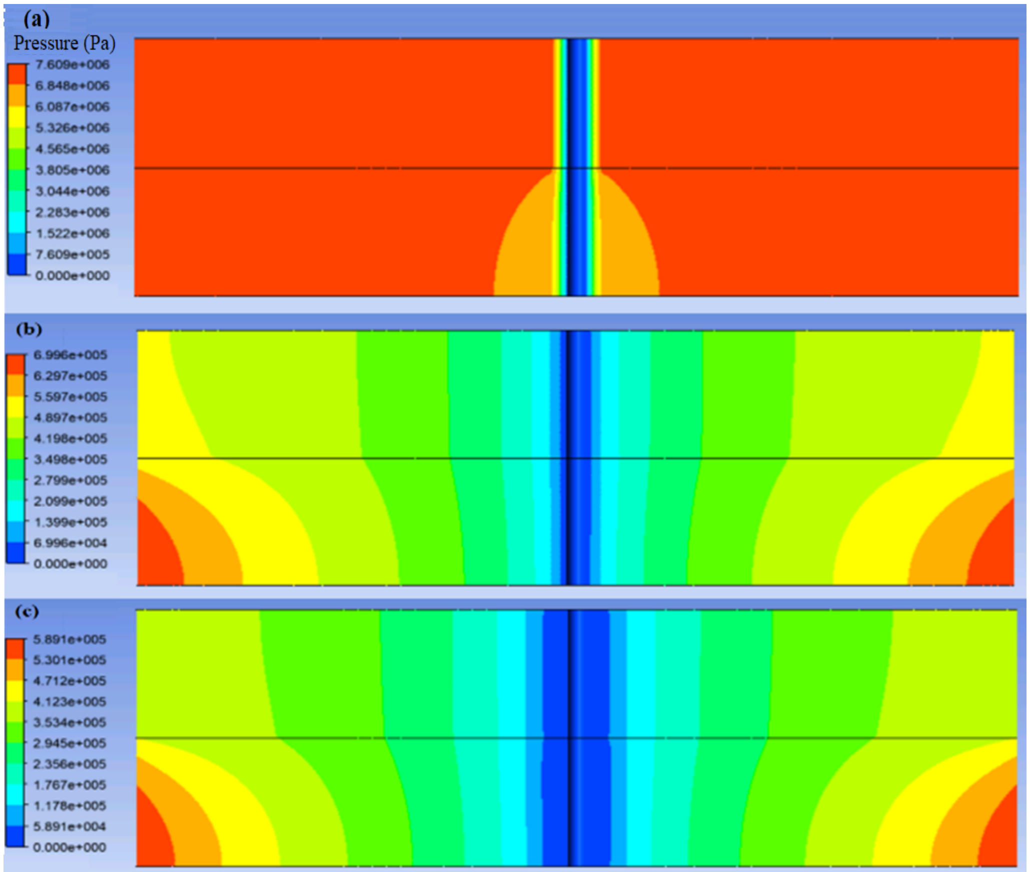

Figure 3.10: Numerical results of the pressure gradient through the two-layer reservoir for three cases: with positive skin factor (a), zero skin factor (b), and negative skin factor (c)

An important observation in this study is that when the skin factor has the same index properties in two layers, the skin zone appears to have control over the cross-flow behaviour. This observation is particularly relevant for a positive skin case. Thus, the skin zone serves as a dam, thus effectively lowering the cross-flow and redistributing the pressure more or less equally to the layers. On the other hand, in zero or negative skin factors case, there is an increase in the cross-flow between the layers and an increase in the pressure gradient. This increase results in a restriction of production to be through one of the layers with an increase in velocity fluid, as shown in Figure 3.11.

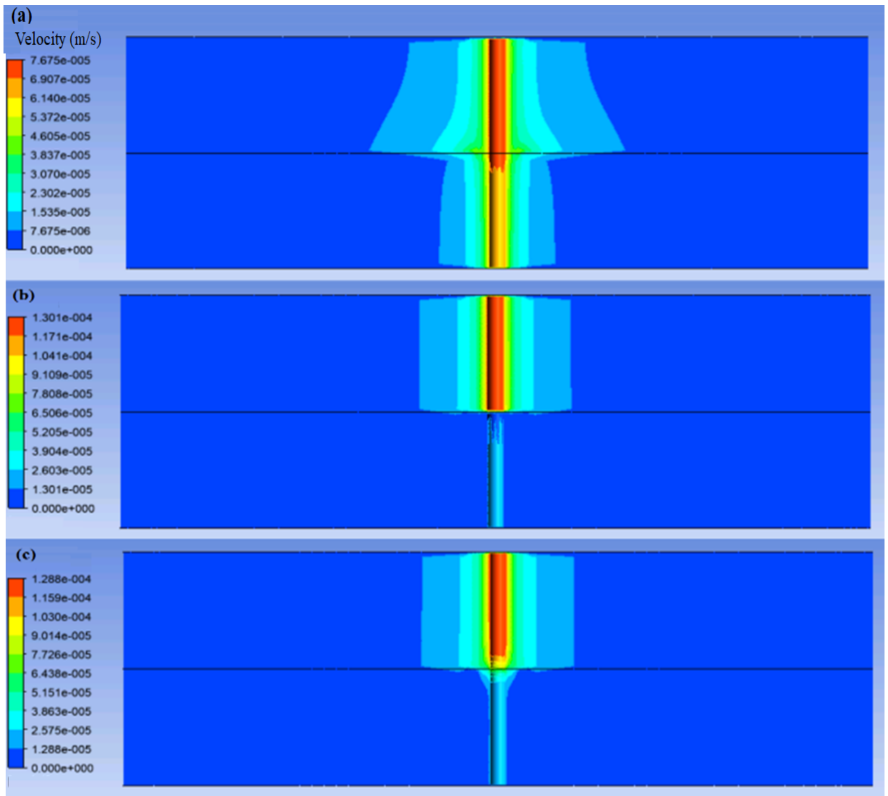

Figure 3.11: Numerical results of the cross flow or velocity distribution through the two-layer reservoir in three cases: with positive skin factor (a), zero skin factor (b), and negative skin factor (c).

3.4 Conclusions

The work has been conducted in order to expand the investigation about formation damage or skin zone and distribution of pressure gradient in vertical near wellbore region. Based on numerical analyses, the following conclusions can be summarized:

1. The numerical investigations showed a clear view of the two dimensionless parameters' effect on the mechanical skin factor and pressure gradient in the near-wellbore region. The results showed that the ratio of skin zone radius to wellbore radius and the permeability ratio significantly affect the mechanical skin factor and pressure drop in the near-wellbore region.
2. The comparison results demonstrated good agreement between the numerical model and Hawkins equation results.
3. The positive skin factor with the same properties for two-layer is effectively lowering the cross-flow and redistributing the pressure more or less equally to the layers.
4. The zero and negative skin factors increase the cross-flow between the layers and increase the pressure gradient.

In future work, the mechanical skin factor's effect on the pressure response and cross-flow behavior will be studied in multi-formation layers, including perforations and gravity effect.

References

Ahammad, M. J., Rahman, M. A., Butt, S. D., & Alam, J. M. (2019a). An experimental development to characterise the Flow phenomena at THE Near-Wellbore Region. *ASME 2019 38th International Conference on Ocean, Offshore and Arctic Engineering*. Glasgow, Scotland, UK: Volume 8: Polar and Arctic Sciences and Technology; Petroleum Technology.

Ahammad, M., Rahman, M., Zheng, L., Alam, J., & Butt, S. (2018). Numerical investigation of Two-phase fluid flow in a perforation tunnel. *Journal of Natural Gas Science and Engineering, 55*, 606-611.

Civan, F. (2015). *Reservoir formation damage.* Gulf Professional Publishing.

Ezeakacha, C. P., Salehi, S., & Hayatdavoudi, A. (2017). Experimental study of drilling fluid's filtration and mud cake evolution in sandstone formations. *Journal of Energy Resources Technology, 139*(2), 1-8.

Hawkins, M. F. (1956). A note on the skin effect. *Journal of Petroleum Technology, 8*(12), 65-66. doi:10.2118/732-g

Hurst, W. (1953). Establishment of the Skin Effect and Its Impediment to Fluid-Flow into a Well Bore. *Pet. Eng., 25,* B-6.

Rahman, M. A. (2008). Scale-up of perforation process from laboratory model to bottom hole dimensions. *Journal of Porous Media, 11*(1), 19-34.

Rahman, M. A., Heidrick, T., Fleck, B., & Koksal, M. (2006). Enhancement of the completion efficiency of perforation tunnels in petroleum wells. *ASME 2006 2nd Joint U.S.-European Fluids Engineering Summer Meeting Collocated With the 14th International Conference on Nuclear Engineering.* Miami, Florida, USA.

Rahman, M., Mustafiz, S., Biazar, J., Koksal, M., & Islam, M. (2007a). Investigation of a novel perforation technique in petroleum wells—perforation by drilling. *Journal of the Franklin Institute*, *344*(5), 777-789.

Rahman, M., Mustafiz, S., Koksal, M., & Islam, M. (2007b). Quantifying the skin factor for estimating the completion efficiency of perforation tunnels in petroleum wells. *Journal of Petroleum Science and Engineering, 58*(1-2), 99-110.

Van Everdingen, A. (1953). The Sktn Effect and Its Influence on the Productive Capacity or a Well. *Journal of Petroleum Technology, 5*(6), 171-176. doi:10.2118/203-g

VasheghaniFarahani, M., Soleimani, R., Jamshidi, S., & Salehi, S. (2014). Development of a dynamic model for drilling fluid's filtration: Implications to prevent formation damage.

Yuan, B., & Wood, D. A. (2018). A comprehensive review of formation damage during enhanced oil recovery. *Journal of Petroleum Science and Engineering*, *167*, 287-299.

Chapter 4

4. A New assessment of perforation skin factor for vertical perforated wells in near-Wellbore Region

A new assessment of perforation skin factor for vertical perforated wells in near-wellbore region

Ekhwaiter Abobaker[1], Abadelhalim Elsanoose[1], Faisal Khan[1], Mohammad Azizur Rahman[2], Amer Aborig[1], Khalid Noah[3], Stephen Butt[1]

Corresponding author: *Ekhwaiter Abobaker; email: eera48@mun.ca*

Journal of Petroleum Exploration and Production Technology, 2021

Abstract: The perforating technique is one of the well completion methods and a final stage that helps connect reservoir formation to wellbore during hydrocarbon production. The present work aimed to determine the effect of the perforated casing completion on the pressure gradient and perforation skin factor in the vertical near-wellbore region. This work presented a novel experimental approach for studying the effect of perforation parameters on hydrocarbon production by creating a prototype representing the near-wellbore region. The study conducted extensive laboratory testing to create two prototype artificial samples for a cylindrical near-wellbore region, open hole, and perforated casing sample. An experimental test was carried out using a geotechnical radial flow set-up to measure the differential pressure in the two samples; the single-phase (water) was radially injected into the core sample within the same flow boundary conditions. Numerical simulation and statistical analysis were used to expand the investigation of the

1 Faculty of Engineering and Applied Science, Memorial University of Newfoundland, St. John's, NL, A1C 5S7, Canada
2 Petroleum Engineering, Texas A&M University at Qatar, Doha, 23874, Qatar.
3 Faculty of Engineering, University of Tobruk, Tobruk, Libya.

effect of the dimensions and distribution of perforations on the perforation skin factor and the pressure gradient in the cylindrical near-wellbore region. The results showed a clear view of the effect of the perforations' parameters on the pressure gradient in the vertical near-wellbore region. In addition, two novel correlations were produced from statistical analysis that simplified the estimation of the perforation skin factor in the perforated casing completion. This study will help to clarify and understand the effect of perforation parameters on well productivity.

Keywords Radial flow cell. Artificial sandstone sample. Near wellbore region. Perforation skin factor.

4.1.Introduction

The last stage in well construction is known as well completion, which is also the first stage to move the reservoir toward production status. To finish a well, an appraisal of the reservoir's quality must be made. The appraisal considers aspects such as the properties of the reservoir rock (e.g., permeability and porosity) as well as saturation and type of interstitial water and hydrocarbon fluids. Therefore, the production engineer must have a variety of tools available for designing an appropriate completion plan in accordance with reservoir fluid characteristics, the production rate for casing, and rock formation type. Because the process of well completion is costly, the majority of these wells must be able to quickly produce large amounts of hydrocarbon to ensure an attractive and rapid return on investment. However, the process of drilling itself impairs the reservoir rock permeability, decreasing the reservoir's natural productivity. This phenomenon is called "formation damage" and is mainly caused by the completion process, drilling, stimulation, and other activities (Yuan & Wood, 2018). One of the main contributing factors to well components is formation damage, which may significantly affect productivity. In general, well productivity has been documented as being affected by a number of interacting elements, including the diameter of the casing entrance hole, the depth and density of perforations, and boundary flow conditions. Perforations are used to connect reservoir formation to wellbore during hydrocarbon production stages. Although the primary purpose of using perforation is to boost production, its application can also cause issues with virgin reservoirs (Renpu, 2011). Perforations can be created using a variety of methods (Behrmann, Hughes, Johnson, & Walton, 2002), and their success is related to a number of characteristics, including radius, phasing angle, density, and length (Economides, 2013). Here, a flow path is generated between the wellbore and pay zone that affects the efficiency of the well's operation (Economides & Nolte, 2000). For the mentioned factors (radius, phasing angle of perforations, etc.), the total and combined effect can typically be attributed to one parameter only, which is the total skin factor. In general terms, the total skin factor measures the productivity of a well. Skin factor may also provide a measure for pressure drop in perforated completion in comparison to the ideal pressure drop that is predicted using the radial flow theory for similar flow rates. Perforation skin models for vertical wells have been presented in various studies for more than 50 years (Harris 1966; Klotz et al. 1974; Locke 1981; Karakas and Tariq 1991; Yildiz 2006). Klotz et al. (1974) employed a 2-D finite element model to examine how perforations and formation damage at the crushed zone affect well productivity, while Locke (1981) looked at a novel way (nomograph) to estimate skin for perforated completions. Nomographs can take skin factors into account by considering rock compaction and formation damage at perforation tunnels. Using a finite element simulator, Karakas and Tariq (1991) formulated several empirical equations for predicting total skin factor at fully perforated vertical wells. Yildiz (2006) proposed a novel way to assess total skin factor that accounted for a large number of other factors, including compaction zone skin, perforation skin, drill-damaged skin, and the impact of partial formation perforation. In particular, the model of Karakas and Tariq (1991) have been commonly used in the industry for the past three decades.

There have been significant improvements in computational fluid dynamics (CFD) and computers during the last two decades. The improvements permit the running of significantly larger models and finer meshes for significantly lower cost and time expenditures. As well, the improvements include revisions to field development strategies in relation to horizontal and deviated wells and upgrades to perforating technology in relation to increased penetration depths. Several recent studies have used CFD for simulating flows in porous media, especially near perforations and wellbore regions, which is becoming more widespread, due largely to improvements in computer technology. CFD technology can easily and quickly model complex interactions' flow occurring in a near-wellbore region (Wood et al. 2020), including formation damage and completion geometry. Using CFD, the well's completion is expedited by formatting the well as a grid and dealing with each small section individually. Reservoir heterogeneity and formation damage can also be captured for a well, which allows for a significantly more detailed examination of the well and near-wellbore area, resulting in improved estimations for inflow performance. For example, Byrne et al. (2009) used CFD to model well inflow at a perforated vertical well. Also, Byrne et al. (2010 and 2011) demonstrated how CFD could resolve asymmetric distribution formation damage near the well and capture the cross flow in the layered reservoir with a heterogeneous. A few years later, the same researchers developed a model for a perforated horizontal well (Byrne, et al. 2014). Additionally, Molina and Tyagi (2015) applied CFD on a near-well model to examine how a perforated gas well performs, looking in particular at various types of completion techniques and how these strategies might have erosive effects at the wellbore. This study is an extension of the works (Zheng, et al. 2016; Ahammad, et al. 2018; Ahammad, et al. 2019; Abobaker et al. 2021a, 2021b) for investigating single fluid flow occurring in perforated porous substances numerically and experimentally. The researchers' model was able to predict the pressure gradients of petrophysical characteristics within perforation tunnels and the near-wellbore regions. The present research attempts to determine how the dimensions and distribution of perforations affect skin factor by conducting a combination of experimental, numerical, and statistical procedures. Also considered in this work is how skin factor and other completion characteristics affect the productivity ratio. The experimental and numerical studies were carried out to present a better understanding of the fluid flow dynamics in both perforations and casing and determine the effect of well-completion design on pressure gradient in the near-wellbore region. This approach allows for pressure drop in various completion configurations to be studied and analyzed and allows flow convergence-affected corresponding skin to be measured. In addition, the study also develops simple correlations for predicting the perforation skin factor for perforated vertical wells and compares the validity of the correlations with the available model of Karakas and Tariq (1991) for the specified reservoir and perforating parameters.

4.2. Methodology

In porous media, fluid flow at low velocities typically obeys Darcy's law. As the flow velocity increases, however, a non-Darcy flow regime begins to develop, caused by the increasingly non-linear relationship between the local pressure gradient and in-situ fluid velocity. Open-hole well completion is both the simplest and most popular completion strategy used in the oil and gas hydrocarbon industry today. Constructing a productivity model of vertical open holes is likewise relatively straightforward. Through integrating the relevant data with Darcy's equation, a well-productivity model can be built that describes open-hole well production in steady-state flows.

$$Q = \frac{2\pi kh(p_e - p_w)}{\mu ln\left(\frac{r_e}{r_w}\right)} \tag{4.1}$$

The flow rate (Q) for a vertical well in a cylindrical near-wellbore region with perforations, anisotropy permeability and Darcy flow perpendicular to the wellbore is expressed as (Economides, 2013):

$$Q = \frac{2\pi kh(p_e - p_w)}{\mu\left[ln\left(\frac{r_e}{r_w}\right) + S_p\right]} \tag{4.2}$$

Hydrocarbon wells can be affected by a number of skin factors. These effects include perforation skin factor (S_p); any difference between an actual well's performances compared to that of an ideal vertical open hole is expressed as the perforation skin factor.

The perforation skin factor can be obtained after the pressure drop is calculated from the equation:

$$S_p = \frac{2\pi kh(p_e - p_w)}{Q\mu} - ln\left(\frac{r_e}{r_w}\right) \tag{4.3}$$

To better understand how skin factors can affect the productivity of a well, the productivity index for an ideal open hole (J_o) is compared to that for a well with skin factors (J_d) (Economides, 2013):

$$\Delta p = \frac{Q\mu}{2\pi kh}\left[\ln(r_e/r_w) + S_p\right] \tag{4.4}$$

$$J_d = \frac{Q}{\Delta p} = \frac{2\pi kh}{\mu\left[\ln(r_e/r_w) + S_p\right]} \tag{4.5}$$

To quantify the comparison, the productivity ratio (PR) is applied, as expressed in eq:

$$PR = \frac{J_d}{J_o} = \frac{\ln(r_e/r_w)}{\ln(r_e/r_w) + S_p} \tag{4.6}$$

In the literature, some studies calculate the total skin factor by adding together all of the above-mentioned skin factors. Karakas and Tariq's model is commonly applied when estimating how a well's productivity is influenced by perforation .There are two scenarios: the perforation tunnel exceeds the formation damaged zone, or the perforations remain within the formation damaged zone. Karakas and Tariq (1991) developed a procedure to calculate the perforation skin factor. The perforation skin factor is a combination including the horizontal flow effect(S_h), the vertical converging effect (S_v) , and the wellbore effect, (S_{wb}).

Hence

$$S_p = S_h + S_v + S_{wb} \tag{4.7}$$

The horizontal perforation skin factor, S_h, is given by

$$S_h = \ln\left(\frac{r_w}{\grave{r_w}(\theta)}\right) \tag{4.8}$$

where $\grave{r_w}(\theta)$ is the efficient wellbore radius and is a function of the perforation angle θ

$$\grave{r_w}(\theta) = \begin{Bmatrix} l_p/4 & if\ \theta = 0 \\ \alpha\theta(r_w + l_p) & otherwise \end{Bmatrix} \tag{4.9}$$

where l_p is the perforation's length, and αθ is phase dependent on variables obtain from Table 4.1.

Table 4.1: Dependency of $\grave{r_w}(\theta)$ on phasing

Perforating phasing	**Phase ($\boldsymbol{\alpha\theta}$)**
0° (360°)	0.25
180°	0.5
120°	0.648
90°	0.726
60°	0.813
45°	0.860

The vertical perforation skin effect is then given by Karakas and Tariq (1991):

$$S_v = 10^a {h_d}^{b-1} {r_{pd}}^b \tag{4.10}$$

where h_d, r_{pd}, *a* and *b* are given by

$$h_d = \frac{h_p}{l_p}\sqrt{\frac{k_h}{k_v}} \tag{4.11}$$

$$r_{pd} = \frac{r_{per}}{2h_p}\left(1 + \sqrt{\frac{k_v}{k_h}}\right) \tag{4.12}$$

$$a = a_1 \log(r_{pd}) + a_2 \tag{4.13}$$

$$b = b_1 r_{pd} + b_2 \tag{4.14}$$

Finally, the wellbore skin effect, S_{wb}, can be obtained by

$$S_{wb} = c_1 e^{c_2 r_{wd}} \tag{4.15}$$

where r_{wd} is given by

$$r_{wd} = \frac{r_w}{l_p + r_w} \tag{4.16}$$

The constants a_1, a_2, b_1, b_2, c_1 and c_2 are given in Table 4.2 as functions of the perforation angle, θ.

Table 4.2: Vertical and wellbore skin correlation coefficients

Perforating phasing (θ)	a_1	a_2	b_1	b_2	c_1	c_2
0° (360°)	-2.091	0.0453	5.1313	1.8672	1.6x 10-1	2.675
180°	-2.025	0.0943	3.0373	1.8115	2.6x 10-2	4.532
120°	-2.018	0.0634	1.6136	1.7770	6.6x 10-3	5.320
90°	-1.905	0.1038	1.5674	1.6935	1.9x10-3	6.155
60°	-1.898	0.1023	1.3654	1.6490	3.0x10-4	7.509
45°	-1.788	0.2398	1.1915	1.6392	4.6x 10-5	8.791

Karakas and Tariq (1991) suggested using a modified perforation length l'_w and the modified wellbore radius r'_w when the perforation tunnel exceeds the formation damaged zone.

$$r'_w = r_w + \left(1 - \frac{k_d}{k}\right) L_d \tag{4.17}$$

$$l'_w = l_p - \left(1 - \frac{k_d}{k}\right) L_d \tag{4.18}$$

Using Karakas and Tariq's (Karakas & Tariq, 1991) semi-analytical model as a foundation and reference point, the present study aims to compare and extend the investigations in near-wellbore region flow, thereby expanding industry knowledge about well performance. This study is an extended work, conducting the four main investigative procedures of samples preparation, experimental, numerical, and statistical analysis for more accurate estimation of the perforation skin factor for perforated wells. The experimental approach has been used to validate the numerical model for single-phase flow through the two perforation samples. Statistical analysis has been coupled with numerical simulation to expand the investigation of fluid flow in the near-wellbore region that cannot be obtained experimentally, due to the limitations of the experimental setup, especially the small sample size.

4.2.1. Samples preparation

Prototype artificial samples have been created that mimic a near-wellbore region, utilizing two zones with different levels of permeability. The model features cylindrical geometry as a means to enable radial flow towards the borehole, while the boundary condition has been set to a constant mass flow rate to help monitor any pressure changes occurring at/near the wellbore. As sourcing natural samples can be both expensive and challenging, and because these samples, if found, are often anisotropic (i.e., display various characteristics depending on how they are analyzed), labs tend to rely on models. Therefore, many researchers have presented different ways to create artificial samples. Holt et al. (2000) looked at synthetic samples for simulating in-situ rock conditions. Their results showed how synthetic specimens are interchangeable with the real core in lab tests. In similar work, Butt (1999) investigated samples taken from a mine area in Nova Scotia, Canada, and also Ahammad et al. (2018) tested real and artificial samples in a laboratory. Lab samples are generally prepared according to study specifications and other factors. For our purposes, we investigate the samples using an experimental set-up that has a broad range of applications related to near-wellbore flow phenomena (e.g., formation damage), which occurs at the well completion stage. Our synthetic samples have been constructed of epoxy glue at the Drilling Technology Laboratory, Memorial University, Newfoundland, using genuine sandstone samples originating from Nova Scotia to validate the experimental set-up. In the laboratory experiments, two highly permeable synthetic sandstone samples have been prepared. The two cylindrical samples were made of sand particles measuring 0.18 to 0.85 mm.

The study conducted extensive laboratory testing to create two prototype samples for a cylindrical near wellbore region. Each synthetic sample has been created from two different sandstone grain sizes. The fine grain size (S1) was used to create a skin zone region around the wellbore and the coarse grain size (S2) used to create a formation reservoir zone. The sandstone particles and epoxy glue were mixed in different quantities (depending on the size of the sand) using an electric mixer for 10 minutes. The mixture was then placed in a plastic container throughout four different stages, using an electric vibrator to ensure the distribution of grain with epoxy glue. Each sample was constructed in two stages; the skin zone was created and then perforated in the first stages, and the formation zone was created by putting the mixture of coarse grains (S2) around the skin zone. The first sample was not perforated (open hole), the second one cased and perforated (8 perforations). The dimensions of the two samples included perforation parameters, as shown in Table 4.3. The perforation by drilling (PD) technique was used to create the perforations in this study. This technique has been used by Rahman et al. (2006, 2007a, 2007b and 2008), as it does not create any transient shockwaves at the perforation tunnel during drilling. They found only small amounts of very fine particles were produced, with negligible redistribution and little damage. This is the result of the nature of the drilling process, and most of the damage was confined to the perforated tunnel, causing only a slight blockage of flow. Therefore, we assumed that the created samples were ideal perforations and did not have a crush zone around the perforation. The shape and dimensions of two well completion sandstone samples are explained in Figures. 4.1 and 4.2.

Table 4.3: The dimensions of synthetic samples

Dimensions and properties the sample	Values (units)
Sample height (H)	1 ft
Diameter of sample (D)	0.5 ft
Wellbore radius (r_w)	0.5 in
Skin zone radius (r_s)	2 in
Perforation diameter (d_p)	0.11811 in
Perforation length (l_P)	1.5 in
Perforation space h_p	1.5 in (8/ft)
Perforation angle (θ)	90°

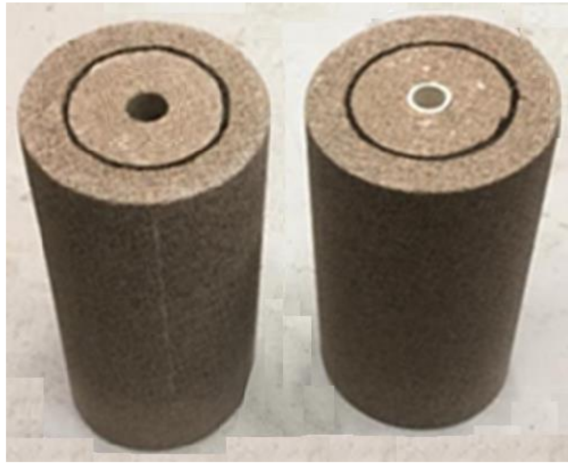

Figure 4.1: The shape of two well completion sandstone samples

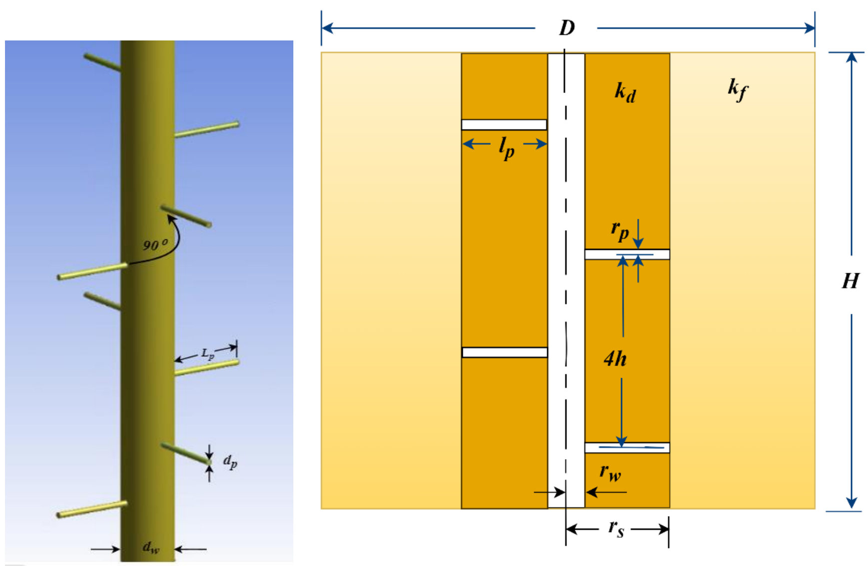

Figure 4.2: The dimensions of perforated well completion sandstone sample with 8 perforations

Currently, mercury intrusion porosimetry (MIP) is one of the common techniques used to analyze sandstone samples' main index properties and pore morphologies. The porosimeter uses a specialized pressure chamber as a means to force the mercury to fill porous substrate voids. Being forced by pressure, the mercury intrudes larger pores and then, under increasing pressure, starts intruding smaller pores (Giesche, 2006). Using this approach, it is possible to characterize both intra- and inter-particle pores. MIP was used first to characterize and then analyze the pore morphology and index properties for the two zones in the samples.

4.2.2. Experimental procedure

In the present study. Our work investigates a specific liquid volume that was injected into the samples in order to determine the differential pressure of these samples under a variety of tested boundary conditions. Figure 4.3 shows the set-up, which features the following three main sections: flow lines extending from inlet to outlet, an inner chamber for holding samples with axial loads, and a Data acquisition (DQ) system.

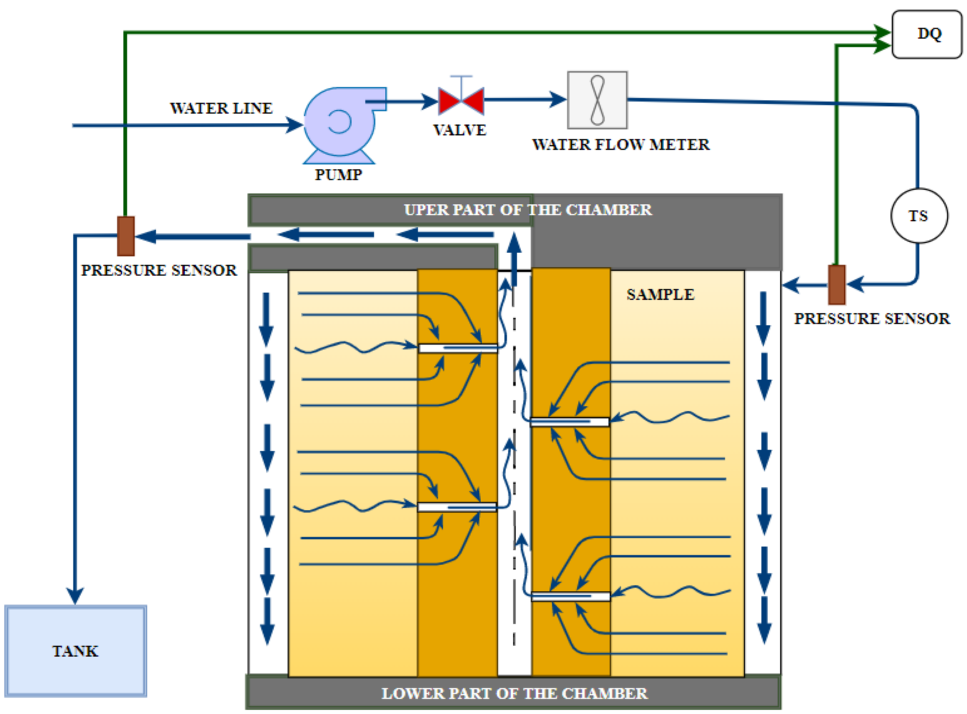

Figure 4.3: The Schematic diagram of the radial flow cell for single phase water

The three value flow rates (1, 2, and 3 liter/minute) for water were injected through each sample within Darcy's flow range. Water was used instead of oil as water does not cause permanent damage to the samples. The radial flow test set-up has been used to measure the differential pressure and phases flow rates for two synthetic samples, with the water being radially injected into our core sample in the single flow within the different flow boundary conditions.

4.2.3. Numerical simulation procedure

In the present work, we used ANSYS FLUENT 18.1 for our computational fluid dynamics (CFD) model. Our aim was to present a single-phase fluid flow simulation for a reservoir described as three-dimensional, vertical, and cylindrically layered. We created a sample that is vertical with single layer of uniform thickness. Next, we assumed the well was centrally located and had a drilled radius (r_w) throughout the formation. Further, the well was perforation completed and it also had a horizontal-to-vertical permeability ratio ($\frac{k_h}{k_v}$). Although perforation skin has been considered in the present research, other skin factors have not. The perforations are assumed to be ideal without formation damage and a crushed zone.

In the numerical work, we injected a measured volume of liquid into the cylindrical sample. The outer side of the sample was considered an inlet and the wellbore surface was an outlet in open hole completion case, while the perforations' surface was taken as an outlet in the perforated casing completion case. The uniform mesh and cut mesh method have been used to create high quality mesh, as shown in Figure 4.4. This arrangement helped to predict a good quality and high density mesh close to borders.

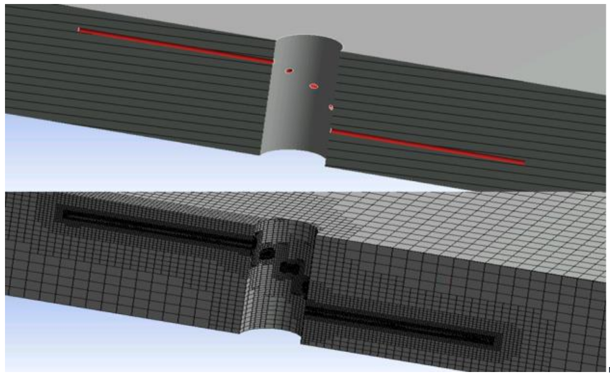

Figure 4.4: Vertical section for the outlet and the shape of uniform configuration mesh.

Furthermore, both the inlet and outlet pressures were measured for our cylindrical samples at constant and laminar flow rates.

4.2.4. Statistical procedure

In statistical procedure, four dimensionless parameters are investigated, including the penetration ratio (P_r), radius ratio (R_r) permeability ratio (K_r) and the ratio of perforation angle to 180° (θ_d):

$$P_r = \frac{l_p}{h_p} \tag{4.22}$$

$$R_r = \frac{r_p}{r_w} \tag{4.23}$$

$$K_r = \frac{k_h}{k_v} \tag{4.24}$$

$$\theta_d = \frac{\theta}{180} \tag{4.25}$$

Two boundary points were selected, and one midpoint was determined by BBD for the intervals of the parameters, as presented in table (4.4). Statistical analysis has been applied to determine the impact of the dimensionless parameters on the perforation skin factor value in two cases. In the first case, the effect of three dimensionless parameters ($P_r,\ R_r\ and\ K_r$) on the perforation skin factor has been analyzed at the perforation angle (360°). In the second case, the same procedure was followed as in the first case with a range of perforation angles (60° -180°). Thirty-six numerical runs in two cases were performed to obtain a suitable statistical analysis using the ANOVA analysis with the BBD model.

Table 4.4: The range dimensionless parameters

Dimensionless parameters	Range
Penetration ratio (Pr)	1.333-8
Ratio of perforation radius to wellbore radius (Rr)	0.025-0.2
Permeability ratio (Kr)	1-10
Ratio of perforation angle to 180° (θ_d)	0.33-1

4.3.Results and discussion

The four investigative methods of samples preparation, experimental, numerical, and statistical analysis were used to analyze the interaction among the perforations' parameters and their effect on the pressure gradient in the near-wellbore region. For the samples' preparation, MIP technique was used to obtain the main index properties (permeability and porosity) and to make sure the artificial samples were homogeneous. MIP measurements of the two artificial sandstone zones (S1 and S2) showed high values for permeability and porosity, as illustrated in Table 4.5.

Table 4.5: The main index properties of the samples

Index properties of the samples (S1 and S2)	Values (units)
Permeability of Skin Zone (K_d)	6.3 Darcy
Porosity of Skin Zone (γ_s)	26%
Permeability of Formation Zone (K_f)	26.6 Darcy
Porosity of Formation Zone (γ_f)	21%

Using MIP experimental data, Figure 4.5 shows the pore size distribution (PSD) curves as pore throat diameter vs. pore volume (dV/dlogD) for the two artificial sandstone zones. The two artificial sandstone zones' PSD curves show single peaks, which means that the two sandstone samples have homogeneous pore size distributions. Moreover, pore sizes are mainly in the range of 50 to 350 µm.

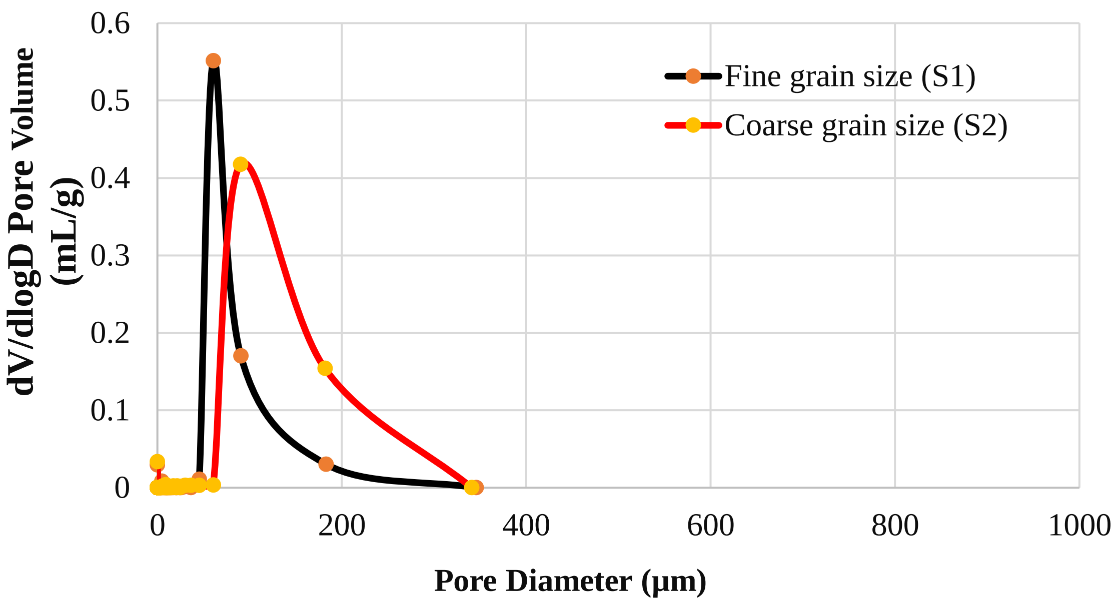

Figure 4.5: Pore size distribution (PSD) curves of the two artificial sandstone zones

The statistical analysis was coupled with numerical simulation to expand fluid flow investigation in the near-wellbore region and analyze the results.

For perforated wells, fluids can come into the wellbore via perforation tunnel arrays. The perforations are usually created around the wellbore helically (i.e., shaped like a helix or spiral). The CFD simulation results have been validated with experimental data for the injection build-up pressure through the open hole sample and the perforated casing sample at the same flow boundary conditions (Table 4.6). The comparison between the experimental data and numerical results for the single-phase flow (water) through the two artificial samples is shown in Figures 4.6 and 4.7. The results of validation showed a good agreement between the numerical results and experimental data.

Table 4.6: Dimensionless parameters of two artificial samples and flow boundary conditions

Dimensionless parameters and flow boundary conditions	Values (units)
Penetration ratio (P_r)	1
Ratio of perforation radius to wellbore radius (R_r)	0.11811
Permeability Ratio (K_r)	1
Ratio of perforation angle to 180° (Θ_d)	0.5
Three water flow rates (Q_w)	1, 2 and 3 liter/minute
Viscosity of water (μ)	0.00095 kg/m-s

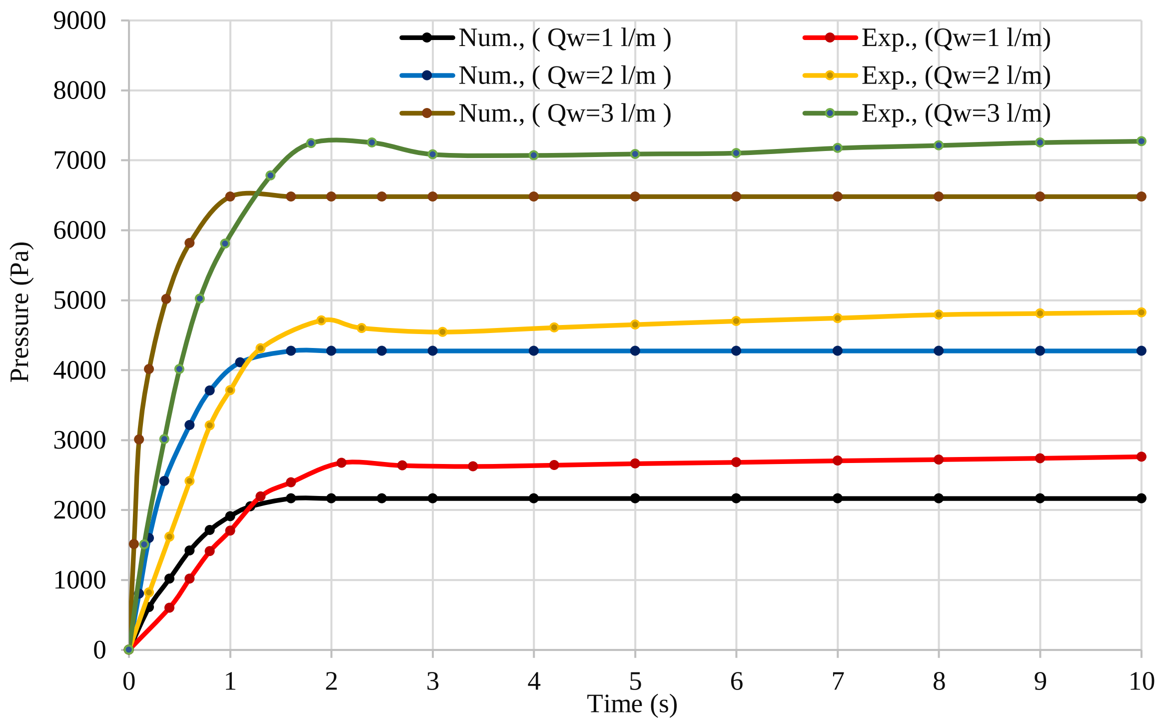

Figure 4.6: The comparison between experimental data and numerical simulation results for a single phase (water) flow at the different flow rates through the open hole well completion sample

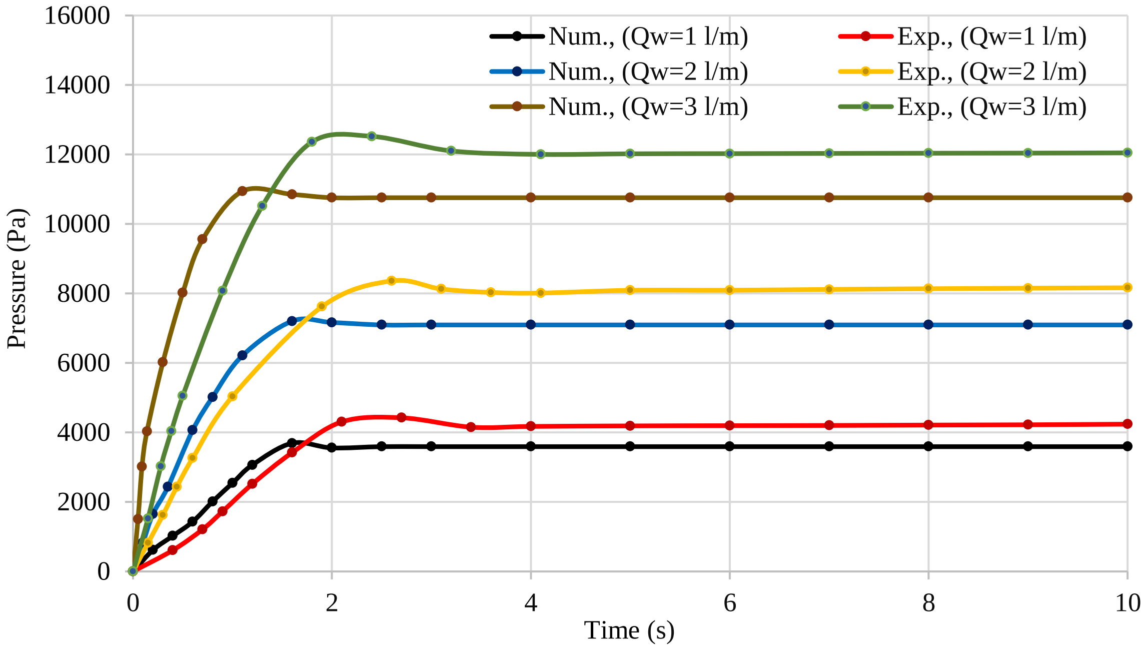

Figure 4.7: The comparison between experimental data and numerical simulation results for a single phase (water) flow at the different flow rates through the casing perforated sample

The comparison results showed that the perforated sample strongly affects the injection pressure build-up, due to the casing resistance, by forcing the flow to pass only through the perforations. Also, the results exhibited that the pressure build-up takes a short time to reach steady-state condition; this time decreases with increasing water flow rate (Q). In the low flow rate cases, the required time for reaching steady-state conditions is longer than the high flow rate case due to the samples' large storage capacity; a high portion of the fluid will pass through the perforations, and a small portion will be stored within the pores. In addition, the results show a slight deviation between the experimental and numerical results that appear in higher flow rate cases. This may be related to the resistance of small damage or amounts of very fine particles around the perforations produced by the PD technique.

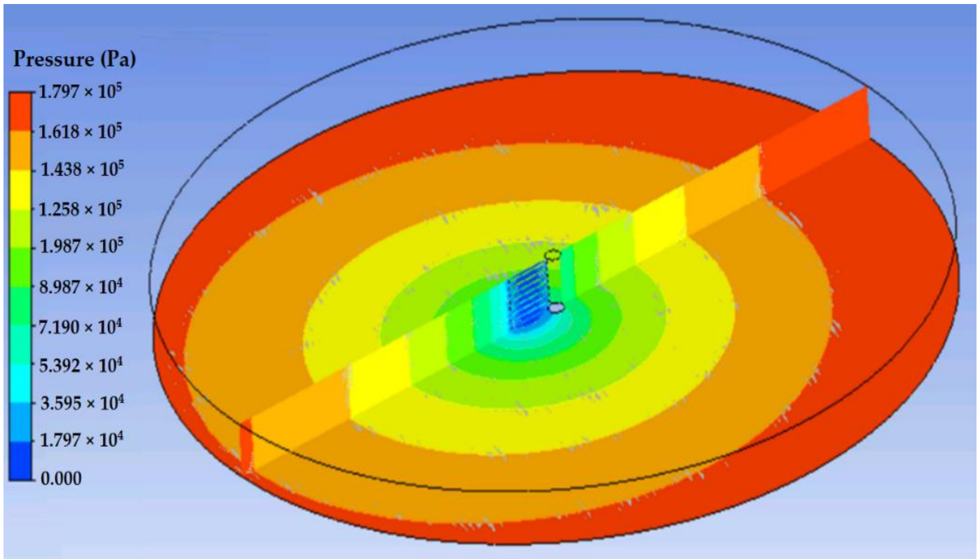

Figure 4.8: Numerical results of the pressure gradient contour for perforated completion case at boundary conditions (Q_w= 1 l/m, μ = 0.001003 kg/m-s, r_e= 32.8 ft, r_w= 0.33 ft, γ=*20 %*, P_r =8, R_r=0.1125, K_r=1, and Θ =360°).

The perforation skin factor was obtained from the difference for pressure drop results between the two completion samples in both experimental and numerical methods. The numerical results exhibit a clear view of the effect of perforation parameters on the value and distribution of pressure gradient for the single flow water at the same flow boundary condition. For example, the perforation skin factor value for one of the numerical run cases was calculated; it was close to zero due to the similar pressure gradient results in both cases (an open hole and perforated sample), as shown in Figures 4.8 and 4.9.

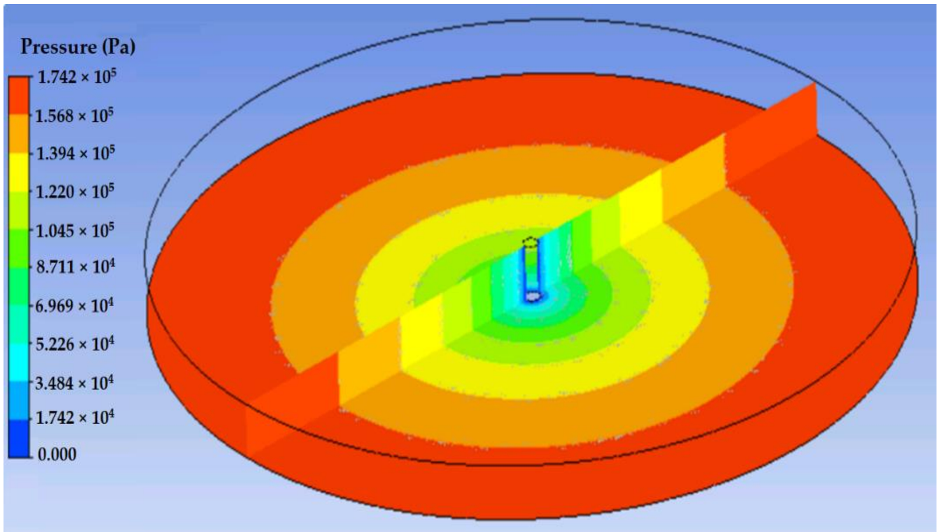

Figure 4.9: Numerical results of the pressure gradient contour for open hole completion at boundary conditions (Q_w= 1 l/m, μ = 0.001003 kg/m-s, r_e= 32.8 ft, r_w = 0.33 ft, γ=20 %, k_v=10.13 md, and k_h=101.3 mD)

The present study provides an in-depth analysis of perforated well completion productivity. As part of the analysis, dimensionless groups are identified that control flows within the perforations, along with the effects of these groups on wells' productivity. Furthermore, using numerical and statistical analyses, a series of results are obtained that highlight the examined well's perforation skin factor. The statistical analysis results show a clear view of the interaction effect among the four dimensionless parameters ($P_r,\ R_r,\ K_r\ and\ \Theta_d$) on the perforation skin factor (S_p) for two perforation angle cases (360° and 60°- 180°), as illustrated in Figures. (4.10 and 4.11). The results indicate that the increasing penetration ratio (P_r) decreased the perforation skin factor due to the high radial flow rate. This means that if the perforations are long and the distance between them is short, the well productivity will be significantly increased. If the penetration ratio is low, the rise in perforation skin factor will be higher. In this case, due to high resistance, higher injection pressure would be necessary to inject the required volume in the core sample. Therefore, long perforations, together with high perforation density, will decrease the perforation skin factor's value and increase the radial flow in the near-wellbore region.

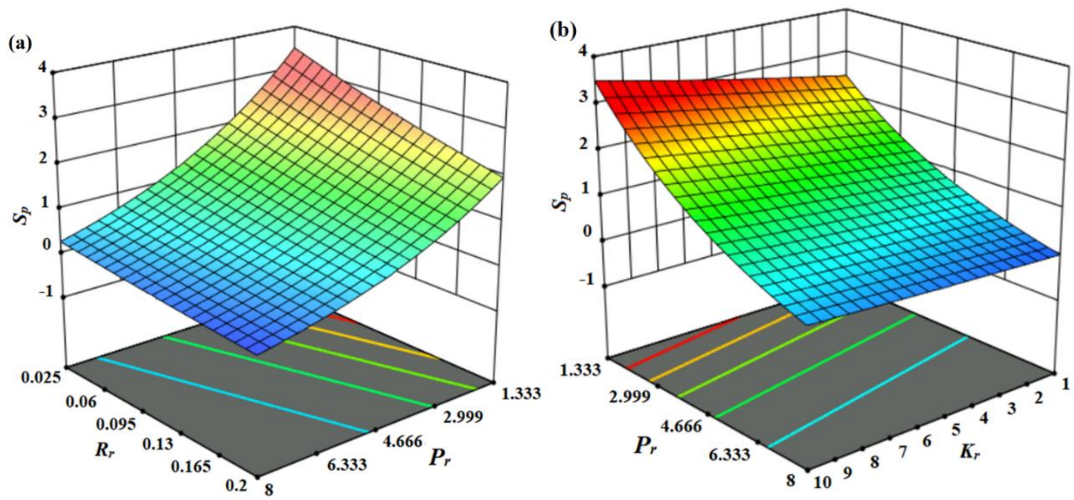

Figure 4.10: Interaction of the three dimensionless parameters $(P_r\ ,\ R_r\ and\ K_r)$ and their effects on the perforation skin factor (S_p) at perforation angle $\theta = 360°$: (a) Interaction between the two dimensionless parameters $(P_r\ and\ \ R_r)$ with constant value for the dimensionless parameter $(R_r\ = 0.025)$; (b) Interaction between the two dimensionless parameters $(P_r\ and\ K_r)$ with constant value for the dimensionless parameter $(R_r\ = 0.025)$

In addition, the ratio of perforation radius to wellbore radius (R_r) and permeability ratio (K_r) have a moderate effect, while the ratio of perforation angle (θ_d) has quite a low impact on the perforation skin factor value. The results also show the perforation radius to wellbore radius ratio as a moderate contribution to productivity, which indicates that perforation aperture widening for enhancing bottom flow accomplishes relatively little. For vertical wells, the reservoir anisotropy's effect on productivity ratio is also tested in this work, showing that the productivity ratio generally declines with increasing the horizontal-vertical-permeability ratio (k_h/k_v). The skin factor for different penetration angles is reduced when the inflow angle decreases, whereas maximum value is achieved at a penetration angle of 360°, as illustrated in Figure 4.10.

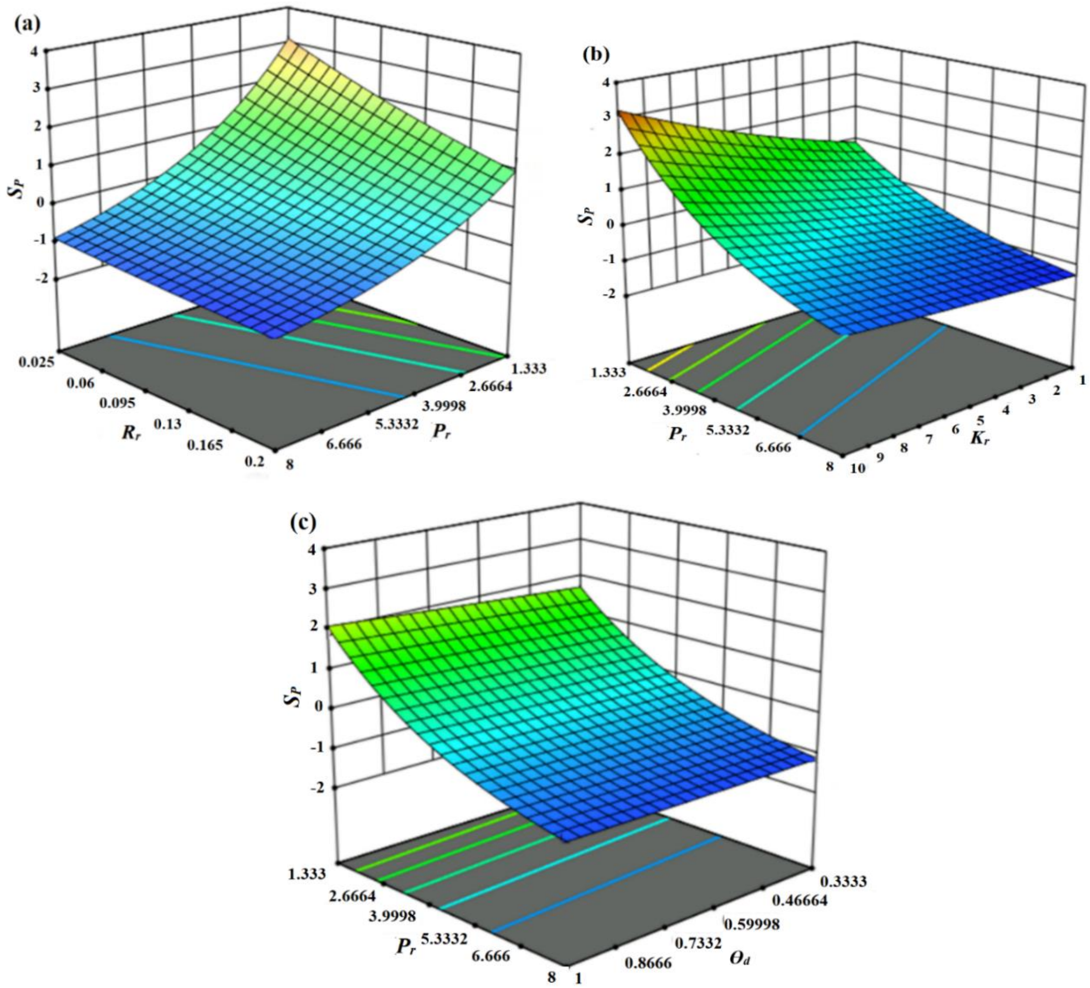

Figure 4.11: Interaction of the three dimensionless parameters $(P_r\,,\ R_r\,, K_r \; and \; \Theta_d)$ and their effects on the perforation skin factor (S_p) at perforation angles $\theta = 60° - 180°$:(a) Interaction between the two parameters $(P_r \; and \;\; R_r)$ with constant value for $K_r = 5.5$ and $\Theta_d = 0.666$; (b) Interaction between the two parameters $(P_r \;\; and \, K_r)$ with constant value for $R_r = 0.1125$ and $\Theta_d = 0.666$; (c) Interaction between the two parameters $(P_r \; and \;\; \Theta_d)$ with constant value for $R_r = 0.1125$ and $K_r = 5.5$

We can learn the effect of each perforation parameter from these results and, based on the results, choose the design that is optimal. This means choosing the best perforation technique that will lead to a high flow rate, as well as choosing the best density and dimensions for the perforation as a means to accelerate radial inflow. The overall outcome of these informed choices is an increase in the productivity index.

The current correlations used for simulating production flows in perforated vertical wells require a relatively complex process involving tables and equations to calculate perforation skin factor. Aiming to streamline this process, the present work proposed efficient and simple correlations for simulating the flows in the near-wellbore region that have helical and symmetrical perforations. Two correlations were obtained from the statistical analysis based on the experimental and numerical results in two cases:

$$S_p(360^\circ) = 10^{(0.65-0.08756P_r-1.069R_r+0.01312K_r)} - 0.85 \tag{4.26}$$

$$S_p(60^\circ - 180^\circ) = 10^{(0.655-0.1123P_r-1.428R_r+0.0302K_r+0.0703\theta_d)} - 1.75 \tag{4.27}$$

The two correlations are used to determine the effect of the four dimensionless parameters on the perforation skin factor value. For example, the perforation skin factor value for the perforated sample used in the comparison of experimental and numerical results can be calculated from the proposed correlation (4.27), and its value is 1 at the same perforation parameters shown in Table 4.6. The perforation skin factor value was equal to the results that have been obtained from the experimental and numerical procedures for three flow rate cases.

A comparison of perforation skin factor results for obtained correlations and results of the available model (Karakas and Tariq (1991)) was performed to verify their computational accuracy and efficiency, as shown in Figures. (4.12-4.15). The comparison results demonstrated good agreement between the current correlations and Karakas and Tariq's semi-analytical model results within the range of dimensionless parameters (see Table 4.4). In addition, two novel correlations have been produced from the current study that simplify the estimation of the perforation skin factor in perforation wells compared to the available model. The correlations can be used to calculate the perforation skin factor by integrating the horizontal-flow effect, the vertical converging effect, and the wellbore effect.

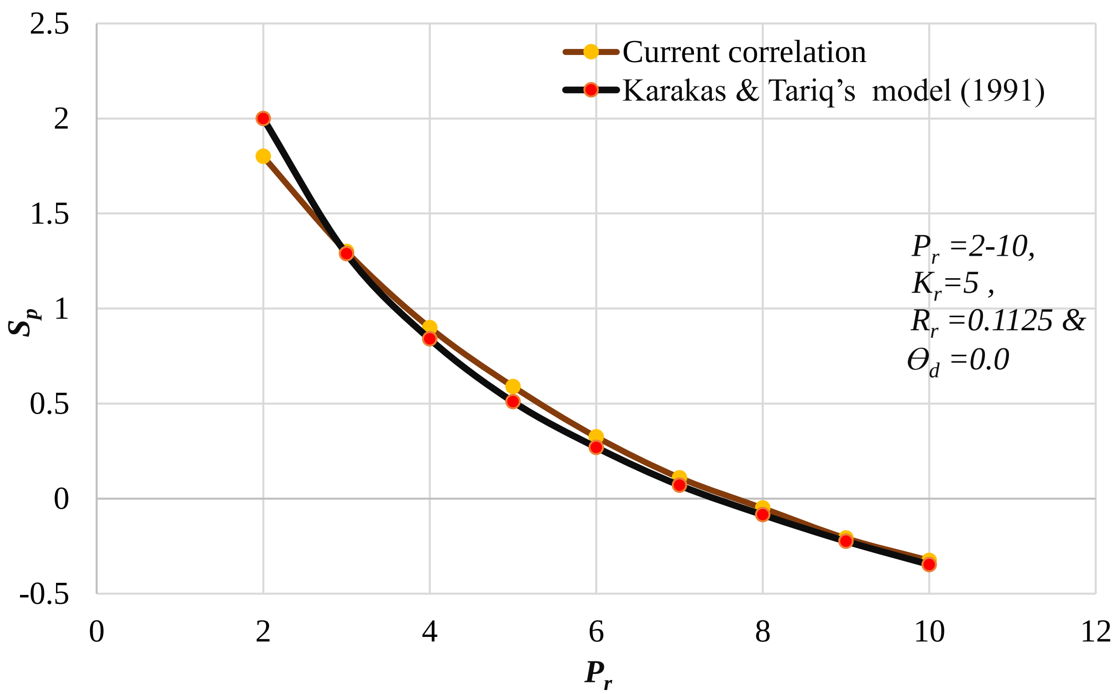

Figure 4.12: The comparison between Karakas and Tariq's model and the obtained correlation results of increasing the penetration ratio (P_r) on the perforation skin factor at perforation angle 360°

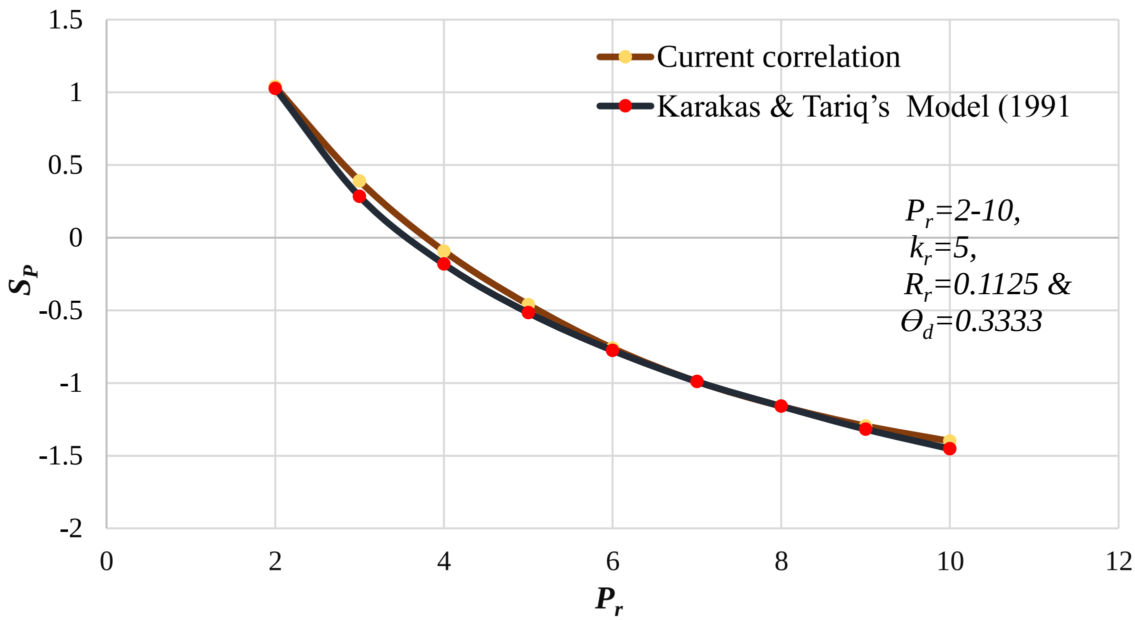

Figure 4.13: The comparison between Karakas & Tariq's model and the obtained correlation results of increasing the penetration ratio (P_r) on the perforation skin factor at perforation angle 60°.

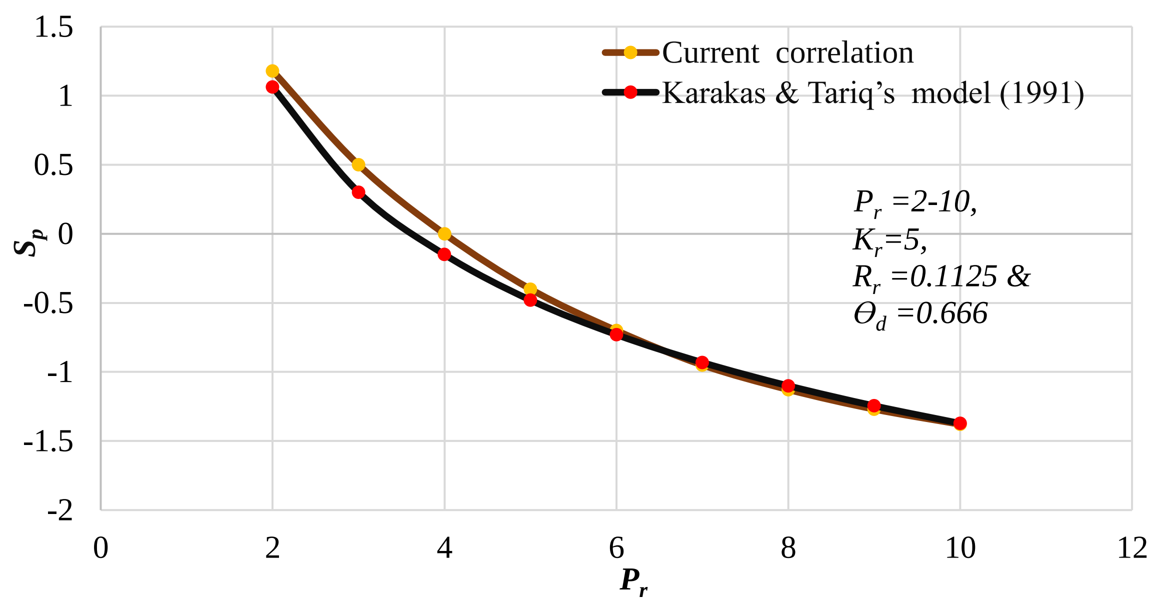

Figure 4.14: The comparison between Karakas & Tariq's model and the obtained correlation results of increasing the penetration ratio (P_r) on the perforation skin factor at perforation angle 120°

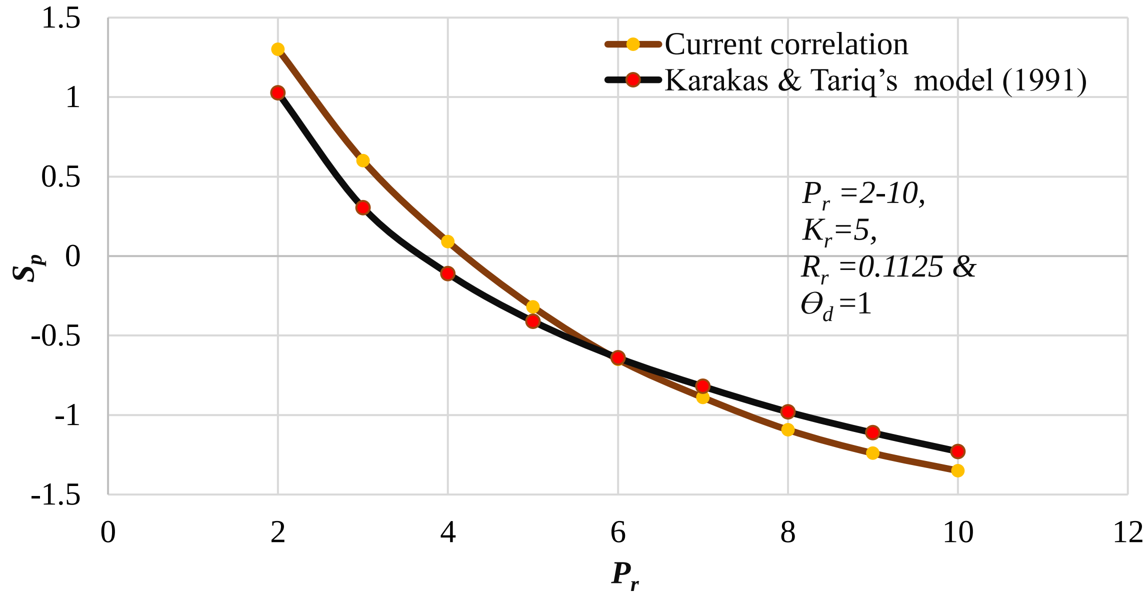

Figure 4.15: The comparison between Karakas & Tariq's model and the obtained correlation results of increasing the penetration ratio (P_r) on the perforation skin factor at perforation angle 180°

The productivity ratio (PR) is a function of perforation length to penetration space or perforation shot densities. The productivity improvements are shown by increasing the perforation's depth or using high perforation densities, as illustrated in Figure 16. Also, the results showed a slight improvement for productivity by increasing the ratio of perforation radius to wellbore radius (R_r) while increasing the permeability ratio (K_r) leads to reduced productivity, as shown in Figures 4.17 and 4.18. Additionally, the results demonstrated high productivity by decreasing the perforation angle. The pressure drop in the near-wellbore region decreases at the small perforation angle cases due to the addition of flow conduits from multiple directions. The maximum production rate was found for perforation angles of 60° degrees, likely due to the suitability of the flow convergence.

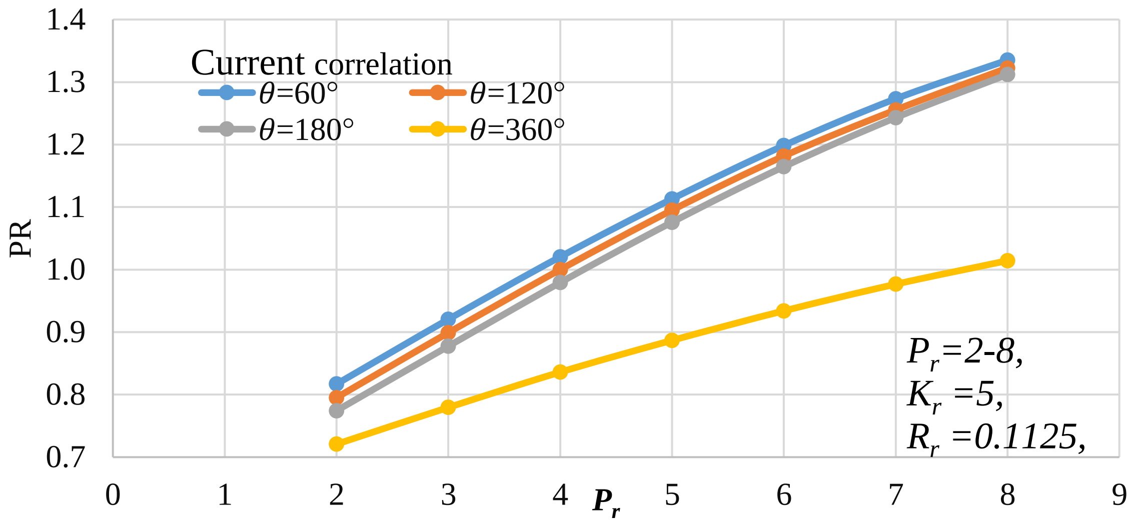

Figure 4.16: Effect of penetration ratio (P_r) on productivity ration PR at different perforation angles (60°-360°

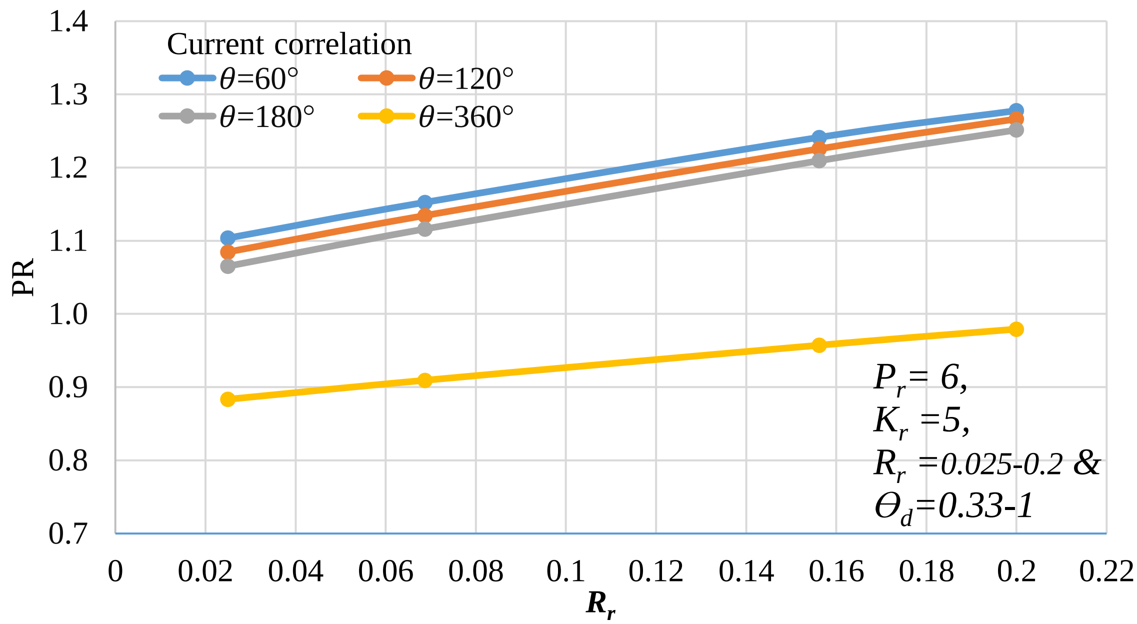

Figure 4.17: Effect of ratio of perforation radius to wellbore radius (R_r) on productivity ration PR at different perforation angles (60°-360°)

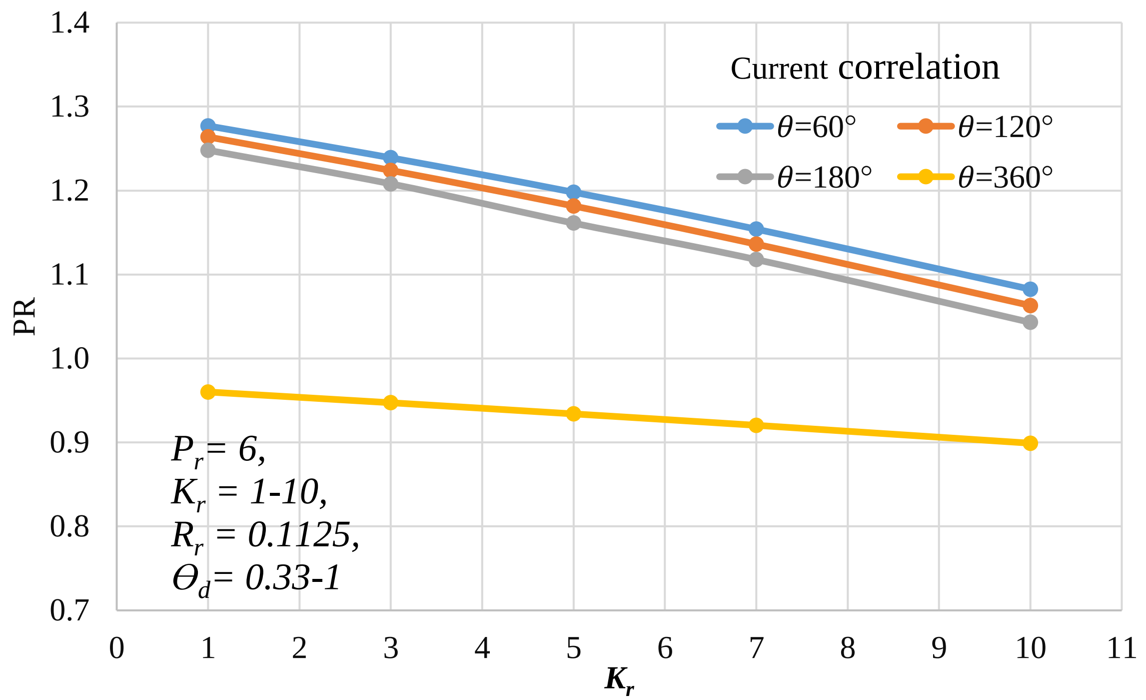

Figure 4.18: Effect of permeability ratio (K_r) on productivity ration PR at different perforation angles (60°-360°)

4.4. Conclusion

This work was conducted in order to expand the knowledge regarding the effect of perforated wells on the perforation skin factor and pressure gradient in a near-wellbore region. Based on experimental and numerical investigations, the following conclusions can be drawn:

1. The experimental data validated the numerical results; the validation showed a good agreement between the experimental data and numerical results.
2. This work presented a novel experimental and numerical approach for studying the effect of perforated casing completion on the perforation skin factor in the vertical near-wellbore region by creating a prototype representing the near-

wellbore region. The results showed that the penetration ratio significantly affects the perforation skin factor and pressure gradient in the near-wellbore region. In addition, the ratio of perforation radius to wellbore radius, and permeability ratio have a moderate effect, while the perforation angle has a low impact on the perforation skin factor value. Based on these results, choosing the optimal perforation parameters can be achieved, along with ways to boost productivity.

3. Two novel correlations have been produced from the current study that simplify the estimation of the perforation skin factor in the perforated casing completion. Compared to the available model:
    a) The comparison demonstrated good agreement between the current correlations and available model results within the range of the study's dimensionless parameters.
    b) The novel correlations work well by providing an accurate estimation for the perforation skin factor without using a lengthy procedure that includes many tables and equations.

References

Abobaker, E., Elsanoose, A., Khan, F., Rahman, M. A., Aborig, A., & Butt, S. (2021B). Comparison of Crushed-zone skin factor for cased and perforated wells calculated with and without including a Tip-Crushed Zone effect. *Geofluids, 2021*, 1-13. doi:10.1155/2021/3689964

Abobaker, E., Elsanoose, A., Khan, F., Rahman, M., Aborig, A., & Noah, K. (2021A). Quantifying the partial penetration skin factor for evaluating the completion efficiency of vertical oil wells. *Journal of Petroleum Exploration and Production Technology, 11*(7), 3031-3043. doi:10.1007/s13202-021-01229-8

Ahammad, M. J., Rahman, M. A., Butt, S. D., & Alam, J. M. (2019a). An experimental development to characterise the flow phenomena at the near-wellbore region. *ASME 2019 38th International Conference on Ocean, Offshore and Arctic Engineering.* Glasgow, Scotland, UK: Volume 8: Polar and Arctic Sciences and Technology; Petroleum Technology.

Ahammad, M., Rahman, M., Zheng, L., Alam, J., & Butt, S. (2018). Numerical investigation of Two-phase fluid flow in a perforation tunnel. *Journal of Natural Gas Science and Engineering, 55*, 606-611.

Behrmann, L., Hughes, K., Johnson, A., & Walton, I. (2002). New underbalanced perforating technique increases completion efficiency and eliminates costlyacid stimulation. *The SPE Annual Technical Conference and Exhibition.* Texas.

Butt, S. (1999). Development of an apparatus to study the gas permeability and acoustic emission characteristics of an outburst-prone sandstone as a function of stress. *International Journal of Rock Mechanics and Mining Sciences, 36*(8), 1079-1085.

Byrne, M. T., Jimenez, M. A., & Chavez, J. C. (2009). Predicting well inflow using computational fluid dynamics - closer to the truth? *the 8th European Formation Damage Conference.* Scheveningen- Netherlands.

Byrne, M. T., Jimenez, M. A., Rojas, E. A., & Chavez, J. C. (2010). Modelling well Inflow potential in three dimensions using computational fluid dynamics. *the SPE International Symposium and Exhibition on Formation Damage Control.* Louisiana, USA.

Byrne, M., Djayapertapa, L., Watson, K., & Goodin, B. (2014). Complex completion design and Inflow Prediction enabled by detailed numerical well modeling. *the SPE International Symposium and Exhibition on Formation Damage Control.* Lafayette, Louisiana, USA.

Byrne, M., Jimenez, M. A., Rojas, E., & Castillo, E. (2011). Computational fluid dynamics for reservoir and Well fluid Flow Performance Modelling. *the SPE European Formation Damage Conference.* Noordwijk-Netherlands.

Economides, M. J. (2013). *Petroleum production systems.* Upper Saddle River, NJ: Prentice Hall.

Economides, M. J., & Nolte, K. G. (2000). *Reservoir stimulation.* Chichester: Wiley.

Giesche, H. (2006). Mercury porosimetry: A general (practical) overview. *Particle & Particle Systems Characterization, 23*(1), 9-19. doi:10.1002/ppsc.200601009.

Harris, M. (1966). The effect Of perfforating oil well productivity. *Journal of Petroleum Technology, 18*(04), 518-528.

Holt, R., Brignoli, M., & Kenter, C. (2000). Core quality: Quantification of coring-induced rock alteration. *International Journal of Rock Mechanics and Mining Sciences, 37*(6), 889-907.

Karakas, M., & Tariq, S. (1991). Semianalytical productivity models for perforated completions. *SPE Production Engineering, 6*(01), 73-82.

Klotz, J., Krueger, R., & Pye, D. (1974). Effect of perforation damage on well productivity. *Journal of Petroleum Technology, 26*(11), 1303-1314.

Locke, S. (1981). An advanced method for predicting the productivity ratio of a perforated well. *Journal of Petroleum Technology, 33*(12), 2481-2488.

Molina, O., & Tyagi, M. (2015). A computational fluid dynamics approach to predict pressure drop and flow behavior in the near wellbore region of a frac-packed gas well. *ASME 2015 34th International Conference on Ocean, Offshore and Arctic Engineering, 10.* St. John's, Newfoundland, Canada.

Rahman, M. A. (2008). Scale-up of perforation process from laboratory model to bottom hole dimensions. *Journal of Porous Media, 11*(1), 19-34.

Rahman, M. A., Heidrick, T., Fleck, B., & Koksal, M. (2006). Enhancement of the completion efficiency of perforation tunnels in petroleum wells. *ASME 2006 2nd Joint U.S.-European Fluids Engineering Summer Meeting Collocated With the 14th International Conference on Nuclear Engineering.* Miami, Florida, USA.

Rahman, M., Mustafiz, S., Biazar, J., Koksal, M., & Islam, M. (2007). Investigation of a novel perforation technique in petroleum wells—perforation by drilling. *Journal of the Franklin Institute, 344*(5), 777-789.

Rahman, M., Mustafiz, S., Koksal, M., & Islam, M. (2007). Quantifying the skin factor for estimating the completion efficiency of perforation tunnels in petroleum wells. *Journal of Petroleum Science and Engineering, 58*(1-2), 99-110.

Renpu, W. (2011). Basis of Well Completion engineering. *Advanced Well Completion Engineering*, 1-74.

Wood, B. D., He, X., & Apte, S. V. (2020). Modeling turbulent flows in porous media. *Annual Review of Fluid Mechanics, 52*(01), 171-203.

Yildiz, T. (2006). Assessment of total skin factor in perforated wells. *SPE Reservoir Evaluation & Engineering, 9*(1), 61-76. doi:10.2118/82249-pa

Yuan, B., & Wood, D. A. (2018). A comprehensive review of formation damage during enhanced oil recovery. *Journal of Petroleum Science and Engineering, 167*, 287-299.

Zheng, L., Rahman, M. A., Ahammad, M. J., Butt, S. D., & Alam, J. M. (2016). Experimental and numerical investigation of a novel technique for perforation in petroleum reservoir. *the SPE International Conference and Exhibition on Formation Damage Control*. Lafayette, Louisiana, USA.

Chapter 5

5. Comparison of crushed-zone skin factor for cased and perforated wells calculated with and without including a tip-crushed zone effect

Comparison of crushed-zone skin factor for cased and perforated wells calculated with and without including a tip-crushed zone effect

Ekhwaiter Abobaker[1], Abadelhalim Elsanoose[1], Faisal Khan[1], Mohammad Azizur Rahman[2], Amer Aborig[1], Stephen Butt[1]

Corresponding author: Ekhwaiter Abobaker[1]; email: *eera48@mun.ca*

Geofluids Journal, 2021

Abstract: A number of different factors can affect flow performance in perforated completions, such as perforation density, perforation damage, and tunnel geometry. In perforation damage, any compaction at the perforation tunnels will lead to reduced permeability, more significant pressure drop, and lower productivity of the reservoir. The reduced permeability of the crushed zone around the perforation can be formulated as a crushed-zone skin factor. For reservoir flow, earlier research studies show how crushed (compacted) zones cause heightened resistance in radially converging vertical and horizontal flow entering perforations. However, the effects related to crushed zones on the total skin factor are still a moot point, especially for horizontal flows in perforations. Therefore, the present study will look into the varied effects occurring in the crushed zone in relation to vertical and horizontal flow. The experimental test was carried out using a geotechnical radial flow set-up to measure the differential pressure in the perforation tunnel with a crushed zone. Computational fluid dynamics (CFD) software was used for simulating pressure gradient in a cylindrical perforation tunnel. The single-

---

[1] Faculty of Engineering and Applied Science, Memorial University of Newfoundland, St. John's, NL, A1C 5S7, Canada

[2] Petroleum Engineering, Texas A&M University at Qatar, Doha, 23874, Qatar.

phase water was radially injected into the core sample with the same flow boundary conditions in the experimental and numerical procedures. In this work, two crushed zone configuration scenarios were applied in conjunction with different perforation parameters, perforation length, crushed zone radius, and crushed zone permeability. In the initial scenario, the crushed zone is assumed to be located at the perforation tunnel's side only, while in the second scenario, the crushed zone is assumed to be located at a side and the tip of perforation (a tip-crushed zone). The simulated results indicate a good comparison with regard to the two scenarios' pressure gradients. Furthermore, the simulations' comparison reveals another pressure drop caused by the tip crushed zone related to the horizontal or plane flow in the perforations. The differences between the two simulations' results show that currently available models for estimating the skin factor for vertical perforated completions need to be improved based on which of the two cases is closer to reality. This study has presented a better understanding of crushed zone characteristics by applying a different assumption about the composition and shape of the crushed zone and permeability reduction levels for the crushed zone in the axial direction of the perforation.

Keywords: Near-wellbore region, Crushed skin factor, Cased and perforated wells, Computational fluid dynamics

5.1. Introduction

For cased hole completions, the well needs to be perforated in order for communication to be enabled between the formation and wellbore. This is because perforations enhance flow convergence at the near-wellbore region. In comparison with ideal open-hole wells, perforated wells can undergo added pressure gains and losses. Especially when a well has a short length of perforations with lower density, it may lead to a greater drop in pressure at the near-wellbore region, which will lower the overall well productivity. Moreover, when wells are perforated by deep penetrating tunnels, there may be a more expansive communication area between the formation and the perforated wells. When this occurs, the perforations might enhance well productivity due to less pressure drop.

Any added pressure gain or drop that is due to ideal perforation may be formulated as a perforation skin factor. In this case, this skin factor is related to parameters like wellbore diameter, perforation length, shot density, phasing angle, and so on. Note that during the perforation process, rocks at the perforation tunnels' sites are crushed. However, the perforation skin factor measures flow convergence at perforations in ideal perforated wells, neglecting the effect of the crushed (compacted) zone encircling the perforation tunnels. Experimental data indicate that the greatest contribution to total skin is the crushed zone, whereas formation damage skin and perforation skin make less contribution overall. Furthermore, based on studies (i.e., field and experimental) conducted over the past half-century, a major factor adversely affecting productivity is deficiencies either in perforating procedures, perforator design, or both. For example, some studies on perforation damage showed that productivity declined in a gun-perforated hole formation when shots were fired into solid-containing fluid, such as drilling muds. There was also decreased productivity in cases where wellbore pressure exceeded formation pressure. In a typical process of perforation, a low-conductivity hole is created in the damaged formation. Post-perforation, the crushed damage expands around the perforation radially from the center of the perforation tunnel. In this evolution, compacted and pulverized rock and other debris from a barrier block the formation's natural pore spaces. Figure 5.1 illustrates this process (Alle and Worzel, 1956; Krueger, 1956, 1988).

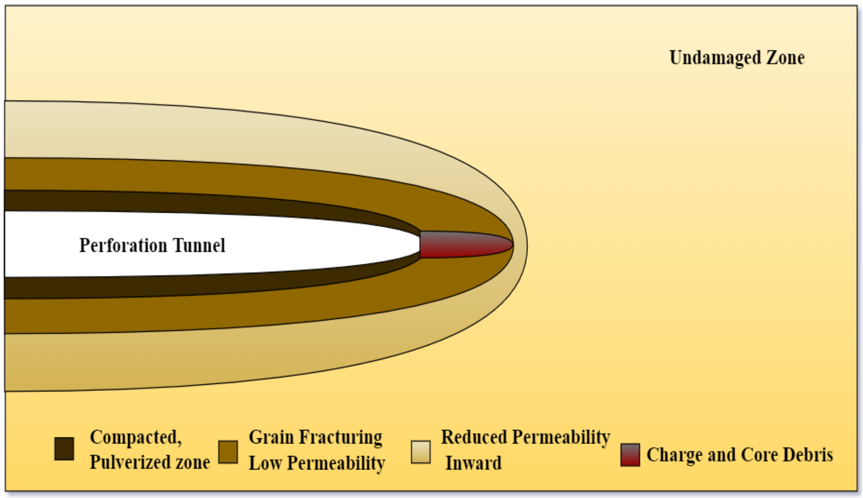

Figure 5.1: Schematic diagram of the crushed zone around the perforation.

The earlier studies mentioned above showed the importance of clearing perforating debris away from perforations to optimize the flow capacity. Debris removal, whether of some or most of the damaged material, enables the perforation tunnel to better perform its role as the wellbore's fluid conduit. One highly efficient way to remove the debris is through underbalanced perforating, although the precise underbalance degree required for generating effective perforations is still a topic of debate. The underbalance is usually calculated by considering the matrix permeability, along with tunnel parameters and fluid, as described by Tariq (1990), Walton (2000) and Grove et. al. (2013). More recent research has looked into various aspects of cleanup and productivity mechanisms in relation to perforation tunnels. Several studies have used computational analysis, due to a lack of experimental data, to explore a number of different challenges, such as isolating the competing effects of debris cleanup and dealing with the heterogeneity that often characterizes analog cores. One of the research teams who used the computational approach is Satti et al. (2015, 2016 and 2018), they proposed a 3-D flow model to determine flow impediments based on characteristics of perforation damage, debris and blockages, and tunnel geometry. The authors used the latest micro-CT methods as well as simulations to determine the most viable cleanup strategies for optimal productivity.

Interactions between formation damage, flow convergence near perforation tunnels, and rock compaction needs to be carefully formulated; rock compaction and formation damage can create a higher degree of dynamic interaction between plane flow and flow convergence at the perforations. The effects of rock compaction and formation damage should thus be included in any perforation model that is developed. However, these interactions can be extremely complex in nature, particularly when including parameters such as mechanical skin factor (formation damage), ideal perforation skin factor, and crushed-zone skin factor. Overall, perforation total skin factor (S_{pdc}) can be used to represent the combined impacts of reductions in compaction zone permeability near perforation tunnels, ideal perforations, and formation damage caused by drilling and other production operations near wellbores. In the Darcy flow case, any other pressure changes caused by these impacts in combination may be written as:

$$\Delta p_{pdc} = \frac{Q\mu}{2\pi k_f\, h} S_{pdc} \qquad (5.1)$$

A wide range of models (empirical, numerical, experimental, semi-analytical, etc.) have been developed over the past several decades for predicting perforated total skin and for determining the effects of the crushed zone. For example, Klotz et al. (1974) employed a 2-D finite element model to examine how perforations and formation damage at the crushed zone affect well productivity, while Locke (1981) looked at a novel way (nomograph) to estimate skin for perforated completions. Nomographs can take skin factor into account by considering rock compaction and formation damage at perforation tunnels. The nomograph results can be integrated into models that measure well performance. A decade later, in a study conducted by Thomas et al. (1991), a table look-up procedure was used for combining the results of Locke's nomograph and software developed for well performance. McLeod (1983) suggested that the combined effects of rock compaction, formation damage and perforation skin at perforation tunnels could be captured in Equation (5.1), as written below:

$$S_{pdc} = s_d + s_p + s_{cz} \tag{5.2}$$

The crushed-zone skin factor is expressed in Equation:

$$s_{cz} = \frac{h}{L_p n}\left(\frac{k_f}{k_{cz}} - \frac{k_f}{k_d}\right) ln\left(r_{cz}/r_p\right) \tag{5.3}$$

Using a finite element simulator, Karakas and Tariq (1991) formulated several empirical equations for predicting total skin factor at fully perforated vertical wells. One example of their formulations was an equation that predicted perforation skin in cases where there was no drilling damage.

$$S_{pdc} = s_h + s_v + s_{wb} + s_{cz} \tag{5.4}$$

In this equation, the initial term indicates flow convergence in the horizontal plane; the second term denotes flow convergence in the vertical plane; and the third term describes the effect of the wellbore geometry. The researchers also employed a formulation somewhat like Eq. 5.3 above to express the crushed-zone skin factor S_{cz} . This formulation is written as Equation (5) below:

$$s_{cz} = \frac{h}{L_p n}\left(\frac{k_f}{k_{cz}} - 1\right) ln\left(r_{cz}/r_p\right) \tag{5.5}$$

In other related research, Bell et al. (1995) formulated a skin-factor equation to account for perforations that ended within the confines of drill-damaged zones. This formula was based on the previous Karakas and Tariq model (1991) mentioned earlier and considered formation damage and crushed zone effects in combination. In 2006, Yildiz proposed a novel way to assess total skin factor that accounted for a large number of other factors, including compaction zone skin, perforation skin, drill-damaged skin, and the impact of partial formation perforation. However, despite their achievements, the effects related to crushed zones on the total skin factor are still a moot point, especially for horizontal flows in perforations. As well, computational fluid dynamics (CFD) investigations have been conducted by Sun. et al. (2013) for a perforated vertical well with different crushed zone scenarios. Their results showed an apparent discrepancy between the supposed crushed zone scenarios and available models.

All the preceding has derived several models based on the assumption that a crushed zone is uniform and cylindrical and has a homogeneous permeability and porosity. At the same time, recent studies using modern techniques computerized tomography (CT) and a scanning electron microscope (SEM)) have shown a different perception of the composition and shape of the crushed zone, especially in the axial direction of the perforation tunnel. In recent studies, the researchers have analyzed the results obtained based on the perforation process's effect. The process of perforation involves shooting a perforation agent into the near-wellbore formation to make holes. However, during this process, the affected rock could experience grain bond breakages in addition to micro-fractures caused by shock waves (Yew et al., 1993). Four levels of damage (i.e., four permeability and porosity change zones) were found in each of the simulated cases when permeability changes, porosity, and bond breakage in the axial direction and vicinity of the perforation tunnel. In Zone 1, there was a significant and rapid decrease in porosity after the minimum value was achieved. The force of the shock wave in this zone was sufficient to sever every bond between particles. The rocks typically had numerous micro-cracks, which became angular fragments during backward grain displacement. The result of this process was a major reduction in permeability due to the closing of pore throats. Zone 2 featured less variation in porosity compared to Zone 1. Even though most of the particle bonds in Zone 2 broke, a small portion of the grains did stay intact. Furthermore, after achieving a minimum value, both permeability and porosity saw slower increases in Zone 2 in comparison with Zone 1. In Zone 3, there were overall fewer decreases in permeability and porosity compared to Zones 1 and 2. Also, in Zone 3, the permeability and porosity generally stayed constant post-perforation. The reason for these differences between Zone 3 and Zones 1 and 2 is that the force of the shock wave was attenuated prior to arriving at Zone 3. Moreover, even though many bonds broke in Zone 3, the grains stayed intact. From this, we can see that the porosity decrease in Zone 3 was likely caused by particle adjustment, where the particles stay constant due to forces from particles situated around them. In Zone 4, no bond breakage or porosity damage was detectable, as this zone is too far away for the shock wave to reach, leaving the rock matrix intact. Figure 5.2 illustrates the four mentioned crushed change zones described by Sarmadivaleh. et al. (2010), Pucknell and Behrmann. (1991), Nabipour. et al. (2010) and Craddock. et al. (2018).

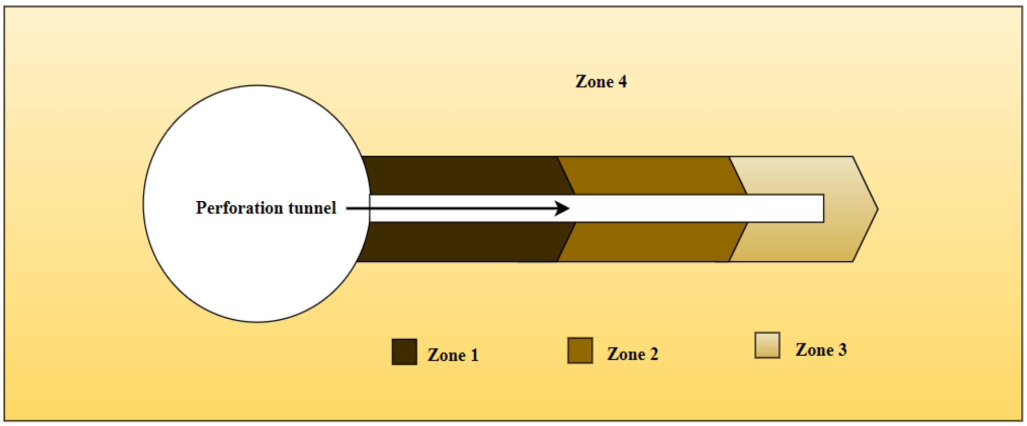

Figure 5.2: Schematic of four different zones of crushed change zones in the axial direction of the perforation tunnel.

In addition, Xue et al. (2016) developed a mechanical model to describe influences of perforating damage, especially with regard to perforations caused by explosions affecting the permeability and porosity of sandstone at the compaction zone. Their study results indicated that there was a notable decrease in damage, particularly to the thickness of the sandstone, when the load and pressure decreased in the axial direction of perforation tunnel, and these results confirm Sarmadivaleh. et al. (2010) and others' conclusions.

In addressing this research gap, the present study was conducted experimental and numerical investigations by employing a different approach to the composition and shape of the crushed zone and permeability reduction levels for the crushed zone in the axial direction of the perforation. The two crushed zone configuration scenarios were applied in conjunction with different perforation parameters, perforation length, crushed zone radius, and crushed zone permeability. In the initial scenario, the perforation zone's tip is assumed to be too far away for the shock wave to reach, leaving the rock matrix intact, so the crushed zone is located at the perforation tunnel's side. In the second scenario, the force of the shock wave in the perforation zone's tip is considered to be sufficient to sever every bond between particles, so the crushed area is located at a side and tip of perforation. The two scenarios were applied in conjunction with different perforation parameters, perforation length, crushed zone radius, and a permeability ratio. In additional investigations, the effect of permeability anisotropy in crushed zones on the crushed skin factor has been studied considering these scenarios.

5.2. Methodology

5.2.1. Experimental procedure

The experimental study was used to validate the numerical model for single-phase flow through the perforation tunnel that includes two different permeability zones. The first region surrounds the perforations and represents the crushed zone with low permeability; the second region exemplifies the formation region with high permeability. Statistical analysis was coupled with numerical simulation to expand the investigation of fluid flow in the near-wellbore region due to the limitations of the experimental setup, especially the small sample size. In the study, two crushed zone configuration scenarios are conducted in conjunction with different perforation parameters, perforation length, crushed zone, and permeability ratio, as shown in Figure 5.3.

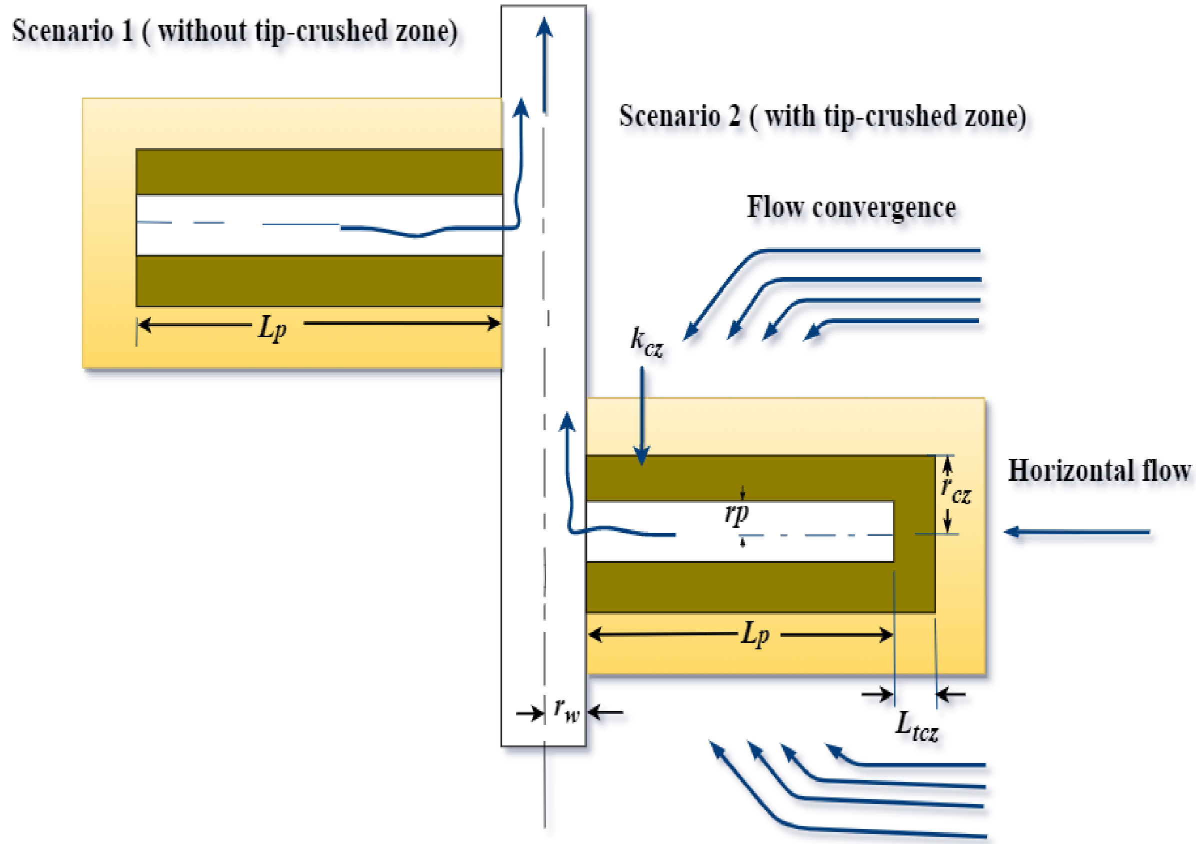

Figure 5.3: The Schematic diagram shows the two scenarios.

In the experimental work, we injected a measured volume of water into core sample. As well, we used a geotechnical radial flow test set-up to measure the differential pressure and single-phase flow rate of our synthetic sandstone sample, with water being radially injected into core sample within Darcy flow and flow boundary conditions (Q = 1 l/min, υ = 0. 95 mPa.s). Figure 6.4 shows the set-up, which features the three following main sections: flow lines extending from inlet to outlet; an inner chamber for holding samples with axial loads; and a Data Acquisition (DAQ) system.

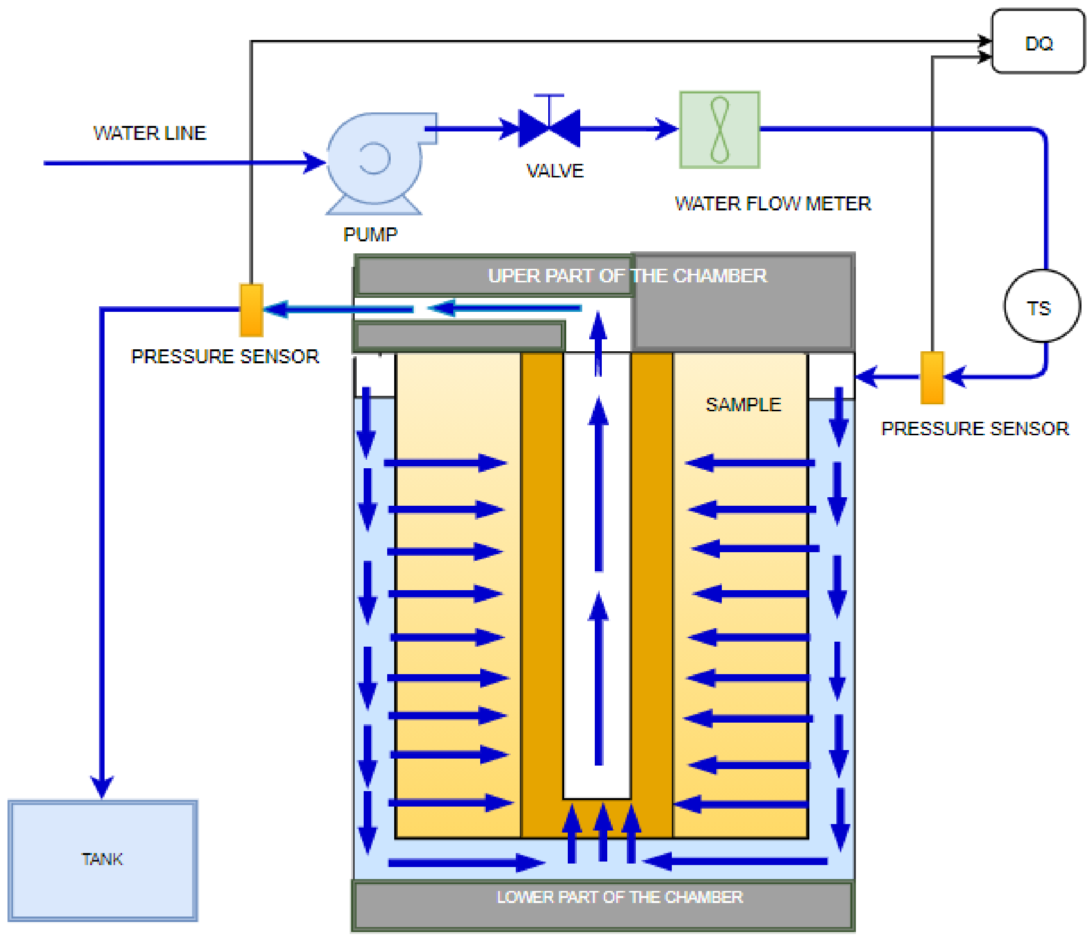

Figure 5.4: Schematic diagram of the experiment: Water flow meter; Inlet and outlet pressure sensors; TS: Temperature sensor; and DAQ: Data Acquisition system.

In the laboratory experiments, a highly permeable synthetic sandstone sample was prepared. The cylindrical sample was made of sand particles measuring 0.18 to 0.85 mm. The synthetic sample has been created from two different sandstone grain sizes. The fine grain size used to create a crushed zone around the perforation and the coarse grain size used to create a formation reservoir zone as demonstrated in Figure 5.5. The dimensions and the index properties of the sample included permeability and porosity, as shown in Table 5.1.

Table 5.1: The dimensions and the index properties of the sample.

Dimensions and properties the sample	**Values (units)**
Sample height (H)	30.48 cm
Sample radius (R)	7.62 cm
Perforation tunnel radius (r_p)	1.27 cm
Crushed zone radius (r_{cz})	5.08 cm
Perforation length (L_p)	25.4 cm
Permeability of crushed zone (k_{cz})	6.218×10^{-12} m^2
Porosity of skin zone (γ_s)	26 %
Permeability of formation zone (k_f)	2.625×10^{-11} m^2
Porosity of formation zone (γ_f)	21 %

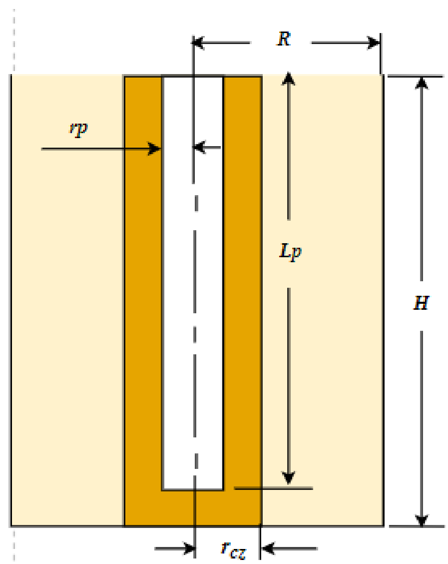

Figure 5.5: The dimensions of synthetic sandstone sample

5.2.2. Numerical procedure

In the present work, we used ANSYS FLUENT 18.1 for our computational fluid dynamics (CFD) model. Our aim was to present a single-phase fluid flow simulation for a reservoir described as three-dimensional, vertical, and cylindrically layered. The crushed skin has been considered in the present research. Other skin factors and effects of perforations angle, formation permeability anisotropy, and wellbore radius were neglected. The crushed skin factor is affected by crushed zone parameters and the permeability anisotropy of the crushed zone. In contrast, the perforation skin factor is more affected by perforation angle, formation permeability anisotropy, and the wellbore radius. Therefore, additional CFD investigations analyzed the effect of permeability anisotropy in crushed zones on the crushed skin factor, considering the study's two mentioned scenarios.

Uniform mesh and cut mesh method (Figure 5.6) were used to generate high-quality mesh. This configuration helped to predict a good quality, and high density mesh close to perforation borders.

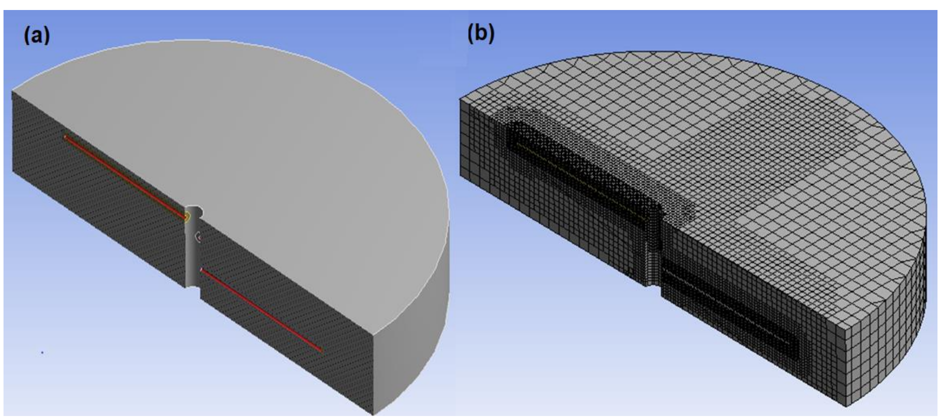

Figure 5.6: Vertical section shows: (a) The outlet; (b) The shape of uniform configuration mesh.

5.2.3. Statistical procedure

In statistical procedure, three dimensionless parameters were investigated, including the ratio of penetration space to perforation length P_r, the ratio of crushed radius to perforation radius R_r, and the crushed-zone damage permeability ratio K_r:

$$P_r = \frac{h}{L_p n}$$
$$R_r = \frac{r_{cz}}{r_p} \qquad (5.6)$$
$$K_r = \frac{k_f}{k_{cz}}$$

Two boundary points were then selected, and one midpoint was determined by BBD for the intervals of the parameters, as presented in Table 5.2.

Table 5.2: The range of dimensionless parameters.

Dimensionless parameters and index properties	Values
Penetration ratio (P_r)	0.125- 0.5
Ratio of crushed zone radius to perforation radius (R_r)	2 – 4
The crushed-zone damage permeability ratio (K_r)	10 – 100
Porosity of skin zone (γ_s)	20 %
Porosity of formation zone (γ_f)	25 %

5.3. Results and discussion

The comparison between the experimental and numerical results of the pressure buildup with the same flow boundary conditions is shown in Figure 5.7. The dimensions of the perforation geometry and the index properties are the same as those used in the experimental procedure (see Table 5.1). This research investigates a specific water flow rate (1 l/min) that was injected into the sample to determine the differential pressure. The experimental data and numerical results are in good agreement.

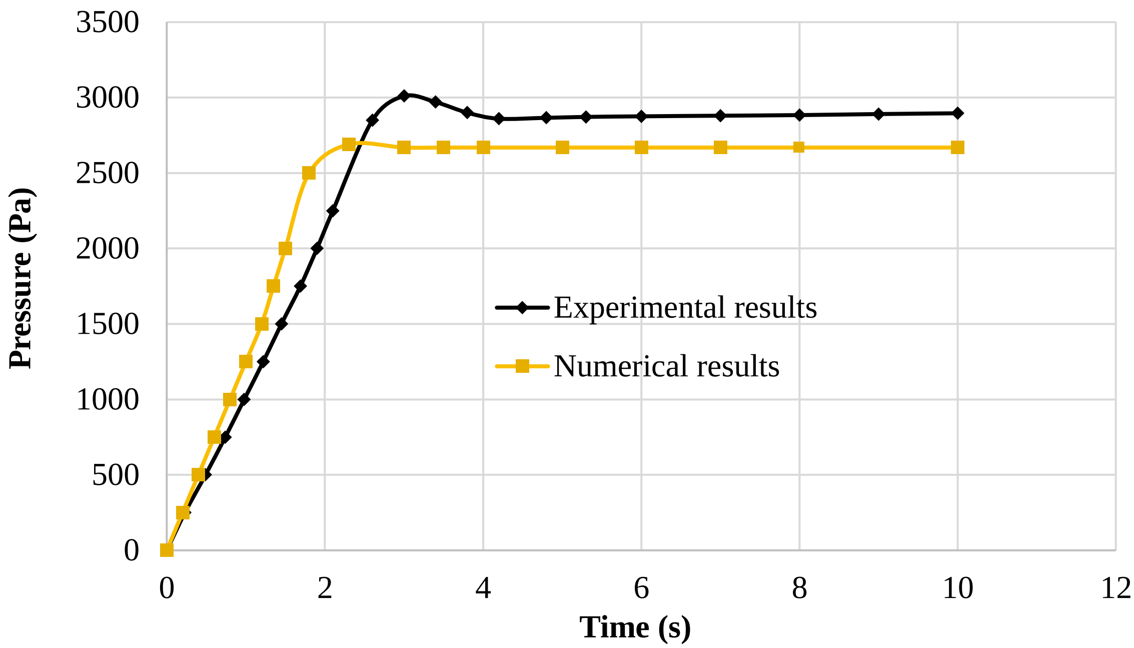

Figure 5.7: Comparison between experimental data, and numerical results of the pressure buildup at the same flow boundary conditions (Q = 1 *l/min*, υ = 0. 95 *mPa.s*)

The validation of numerical results with experimental ones has given full confidence in using the numerical model to conduct huge investigations by creating a crushed zone with different crushed perforation parameters, perforation length, and crushed zone radius. The relative effect of three dimensionless parameters on the crushed skin factor was investigated before conducting statistical analysis. The numerical results showed that the ratio of penetration space to perforation length P_r and the crushed-zone damage permeability ratio K_r significantly affect the crushed skin factor. In contrast, the ratio of crushed radius to perforation radius R_r has a moderate effect on the crushed skin factor, as shown in Table 5.3.

Table 5.3: The relative effect of three dimensionless parameters on the crushed skin factor.

P_r ($R_r = 3, K_r = 55$)	S_{wt}	R_r ($P_r = 0.3125, K_r = 55$)	S_{wt}	K_r ($P_r = 0.3125, R_r = 3$)	S_{wt}
0.125	7.27	2	10.6	10	2.2
0.3125	16.4	3	16.4	55	16.4
0.5	27.8	4	21.6	100	30.6

Twelve numerical runs were performed and analyzed to obtain a suitable statistical analysis using the ANOVA analysis with the BBD model (Table 5.4).

Table 5.4: Twelve numerical runs.

No	P_r	R_r	K_r	S_{wt}	S_{wot}	$\Delta P_{wt}(Pa)$	$\Delta P_{wot}(Pa)$	$\Delta P_{woc}(Pa)$
1	0.3125	2	100	20.01	9.52	2032	1082	211
2	0.125	3	10	1.23	1.14	217	208	104
3	0.125	2	55	4.68	3.64	532	437	104
4	0.5	2	55	18.08	8.78	1929	1079	276
5	0.5	4	55	34.13	11.86	3351	1361	276
6	0.5	3	100	51.31	13.28	4968	1491	276
7	0.125	4	55	9.045	6.06	931	658	104
8	0.5	3	10	4.63	3.62	799.6	607	276
9	0.3125	4	10	3.77	2.18	550	395	221
10	0.3125	2	10	1.74	1.68	370	365	211
11	0.125	3	100	13.33	7.7	1323	808	104
12	0.3125	4	100	40.77	9.4	3938	1071	211

Therefore, crushed perforation parameters were analyzed by using statistical analysis coupled with numerical simulation model. This study provided two correlations from the statistical analysis, based on the numerical results. These correlations were used to determine the relative impact of each factor for the two scenarios on the crushed skin factor.

$$S_{wot} = -4.3 + 12.67P_r + 0.673R_r + 0.088K_r \tag{5.7}$$

$$S_{wt} = 15.7 - 48.18P_r - 5R_r - 0.317K_r + 14.9\,P_r * R_r + P_r * K_r + 0.1076R_r * K_r \tag{5.8}$$

The results clearly indicate the crushed perforation parameters effects on both the crushed skin factor and pressure gradient values. The results show that crushed skin increases the pressure drop and thus contributes to a reduction in the productivity index. As illustrated in Figure 5.8, the value of crushed skin factor increases with the increase of the penetration ratio (P_r), the ratio of the crushed zone to perforation radius (R_r) and crushed-zone damage permeability ratio (K_r). From this, we can surmise that the interaction among these parameters has a marked effect on the crushed skin factor value, whereas the perforations without a crushed zone represent an ideal case that may or may not be reproducible in practice.

Furthermore, based on the results, we can see that the pressure gradient is more affected by a high ratio for the three parameters. The perforation length makes a more significant contribution to pressure drop decreasing, and the higher crushed-zone damage permeability ratio with short perforations leads to pressure drop increases around the perforations, as shown in Figure 5.9. Also, the results show the significant effect of a large thickness of crushed zone with a high crushed-zone damage permeability ratio on the pressure gradient due to the frame's resistance around the perforations with a significantly high reduction in the permeability.

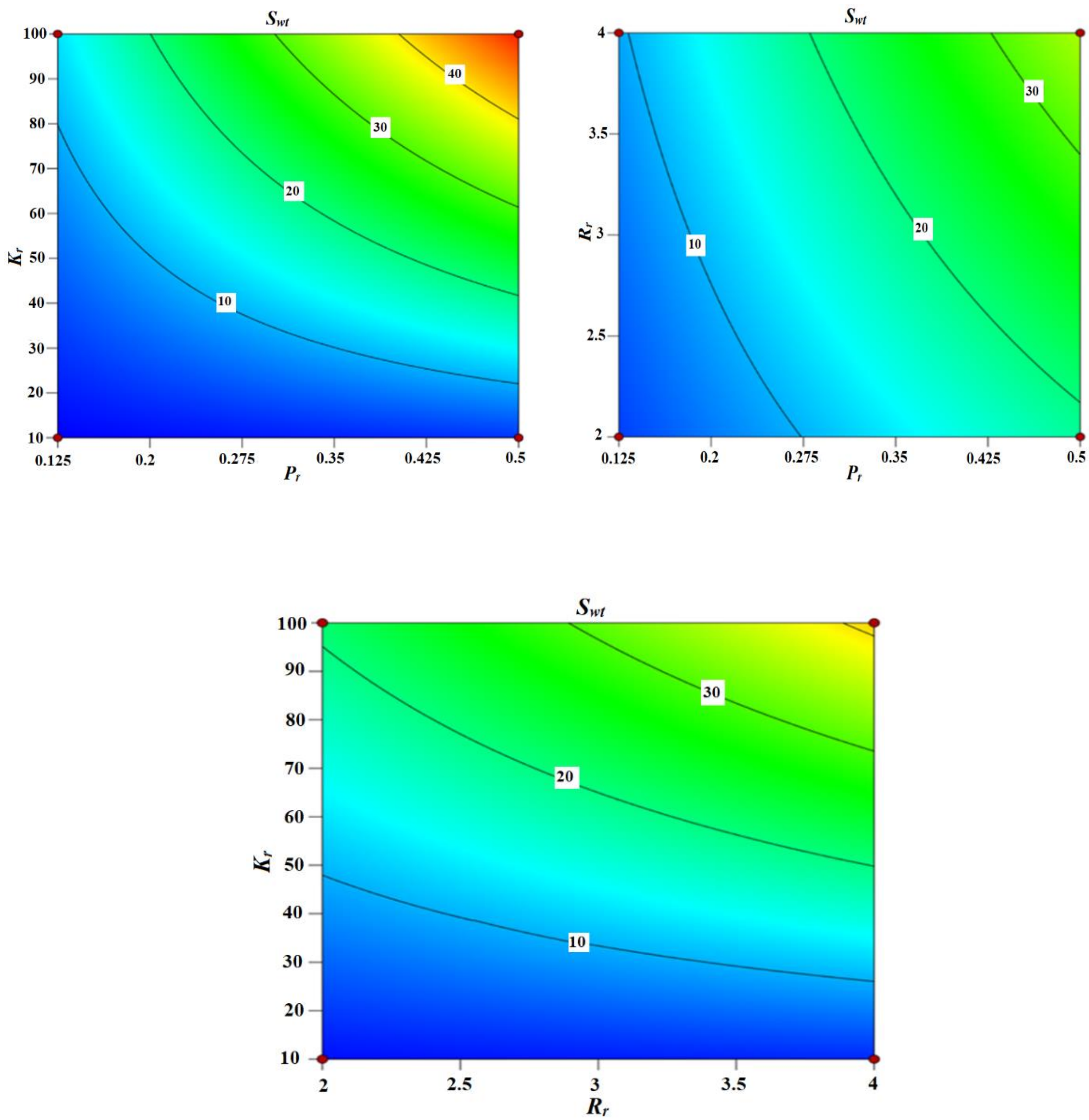

Figure 5.8: The dimensionless parameters (P_r , K_r and R_r), interactions with each other and their effect on crushed skin factor.

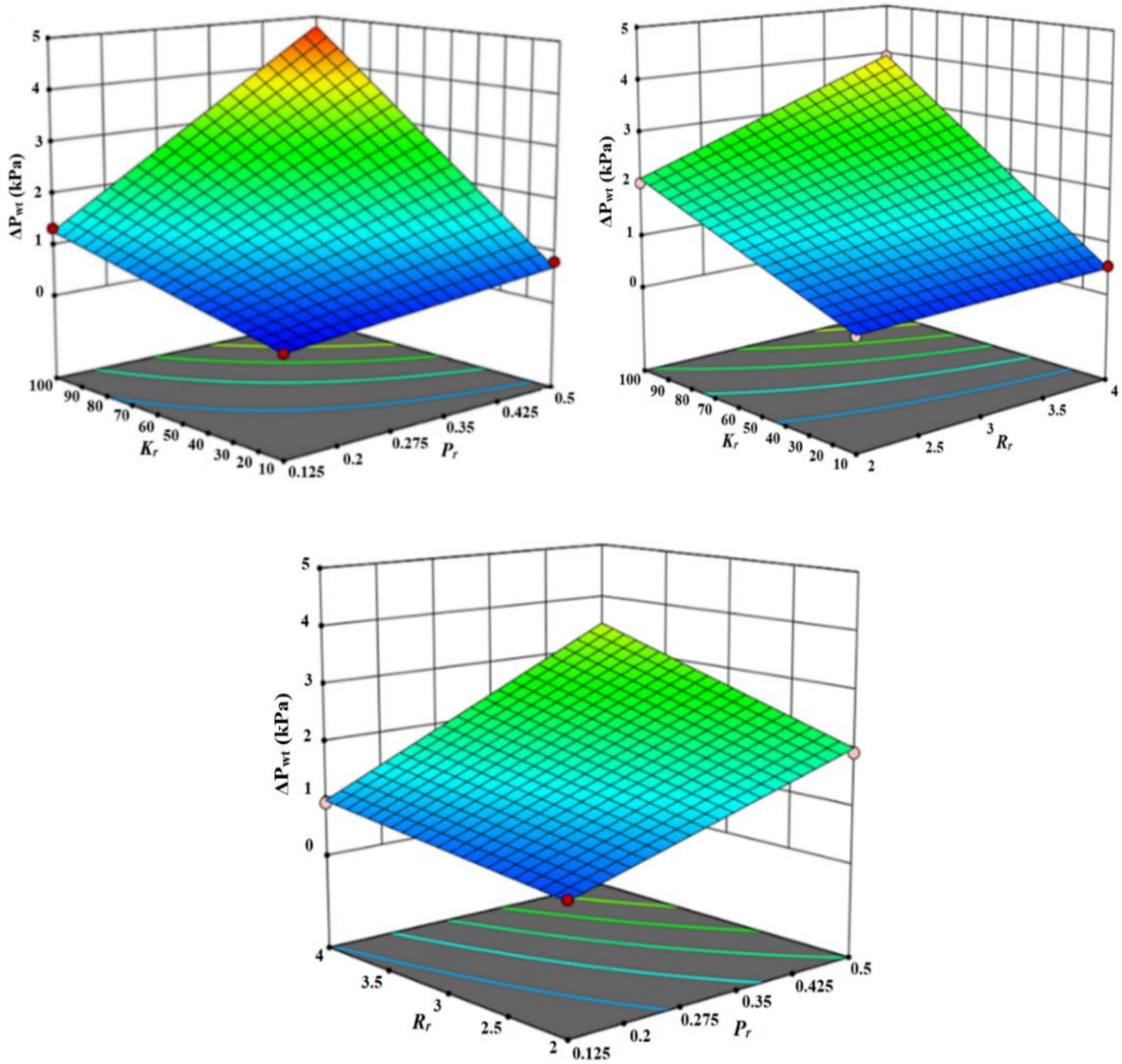

Figure 5.9: The dimensionless parameters' (P_r , K_r and R_r) interactions with each other and their effect on the pressure gradient for second scenario (with crushed tip) at boundary conditions of $Q = 1\frac{l}{min}$,= 0.001003 *kg/m-s*, r_e= 91.44 cm,$r_w = 3.81\ cm$,$r_p = 0.635\ cm$, $r_{cz} = 1.27 - 2.54\ cm$, $L_p = 15.24 - 60.96\ cm$, $h = 30.48\ cm$, $n = 2 - 8$, Θ = 90°, $k_f = 10^{-10}\ m^2$, $k_{cz} = 10^{-11} - 10^{-12}\ m^2$, γ_s=*20 %, and* γ_f=*25 %.*

Moreover, the numerical results show a clear view of pressure distribution for the perforation with a crushed tip, without a crushed tip, and ideal perforations cases. For example, the pressure gradient for the three cases at dimensions' parameters values (P_r = 0.125, R_r=3 and K_r= 100) is shown in Figure 5.10.

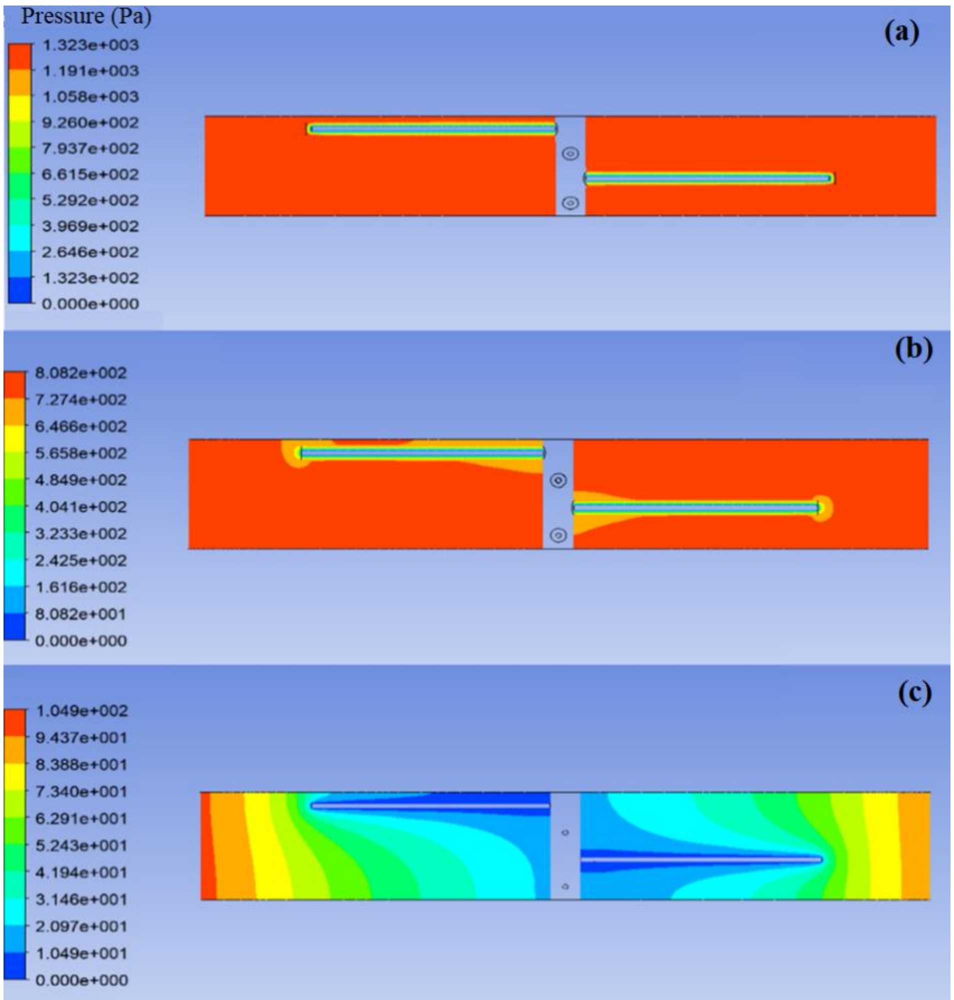

Figure 5.10: The distribution of the pressure gradient for three cases: (a) Perforations with crushed tip; (b) Perforations without crushed tip; (c) Ideal perforations without crushed zone at boundary conditions of $Q = 1 \frac{L}{min}$,=0.001003 kg/m-s, r_e= 91.44 cm, r_w = 3.81 cm, $r_p = 0.635\ cm$, $r_{cz} = 1.905\ cm$, $L_p = 60.96\ cm$, $h = 30.48\ cm$, $n = 4$, $\Theta = 90°$, $k_f = 10^{-10}\ m^2$, $k_{cz} = 10^{-12}\ m^2$, γ_s=20 %, and γ_f=25 % .

In order to compare and discuss the accuracy of the common models, Karakas and Tariq (1991) model was selected and used to calculate the case of the crushed skin factor without formation damage. The model was compared with two novel correlations for two scenarios. The comparison results show a comprehensive realization of the effect of three dimensionless parameters (P_r K_r and R_r) on the crushed skin value and the deviation between Karakas and Tariq (1991) (Karakas & Tariq, 1991) model and novel correlation for two scenarios.

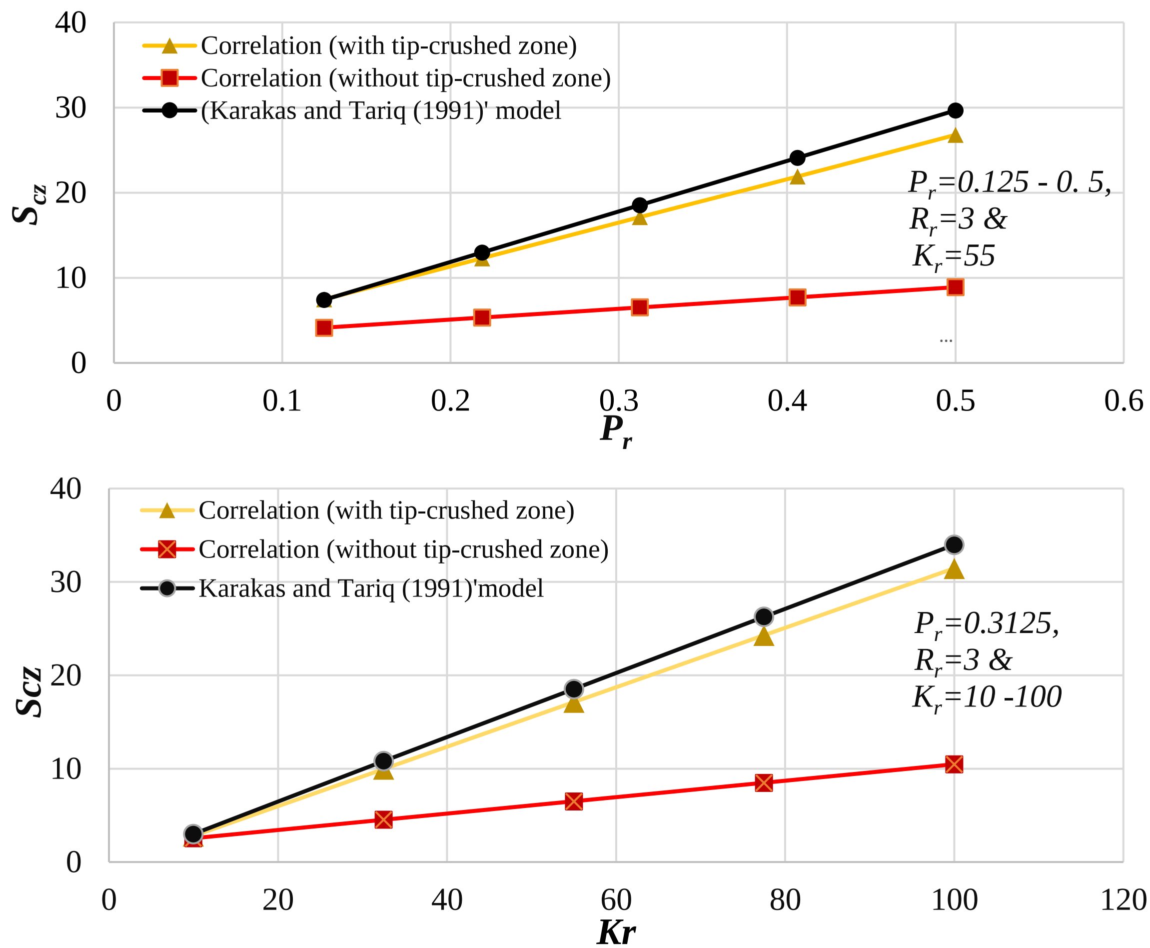

Figure 5.11: The comparison between the crushed skin factor results of two scenario correlations and the model of Karakas and Tariq (1991).

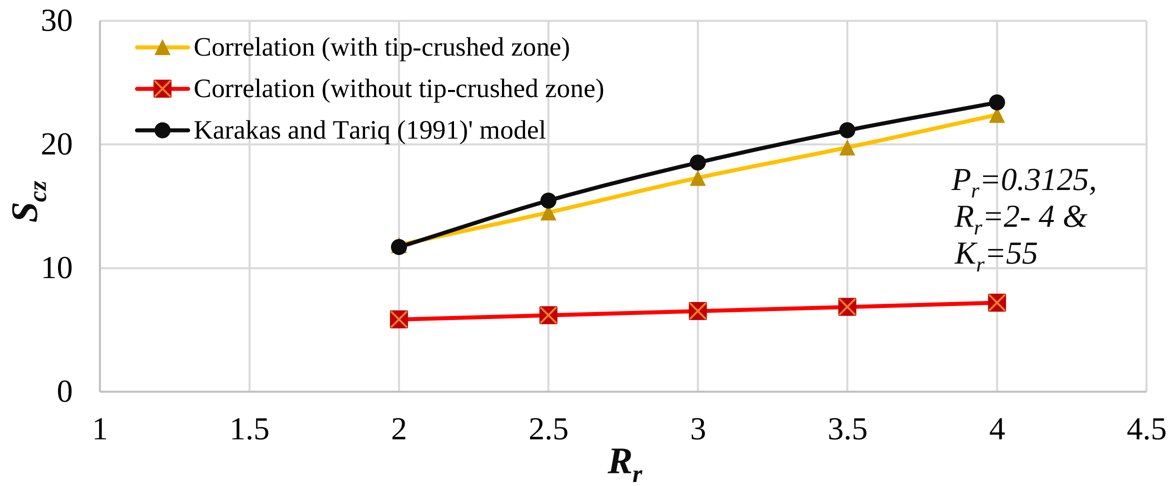

Figure 5.12: The comparison between the crushed skin factor results of two scenario correlations and the model of Karakas and Tariq (1991).

The crushed skin factor results of the second correlation with a tip-crushed zone (S_{wt}) showed a slight deviation with the previous model of Karakas and Tariq (1991) while the crushed skin results of the first correlation without a tip-crushed zone (S_{wot}) demonstrated a large deviation for three dimensionless parameters, as shown in Figure 5.11. In general, the Karakas and Tariq (1991) model applied to calculate the crushed skin factor shows a good convergence with the second scenario, so the model takes into consideration the effect of all frame resistance around the perforations. However, our CFD model gave almost identical results to the model if we assumed the length of the perforations was shorter than their length by a thickness of the crushed zone.

Also, the present study looked at the effect of permeability anisotropy in crushed zones on the skin factor with regard to the study's two scenarios. In the CFD simulations, the interaction effect between permeability anisotropy $(k_{ch}/k_{cv} = 1 - 10)$ in the crushed zone and the crushed-zone damage permeability ratio $(K_r = 1 - 100)$ has been investigated. As illustrated in Figure 5.12 and 5.13, there is a seeming increase in crushed skin factor when permeability anisotropy in the crushed zone is assumed. It is plausible that this rise's mechanism is related to non-radial flow near the perforation tunnel caused by permeability anisotropy at the crushed zone, particularly in cases of increased crushed zone thickness and perforation length. The results showed that the anisotropy in the crushed zone between $k_{ch}/k_{cv} = 1 - 7.75$ has a significant effect on the crushed skin factor, and then its effect decreases, due to the domination of the horizontal flow. These outcomes showed that a better understanding of crushed zone anisotropy is needed, using the improvement of techniques for determining which factors affect perforated completions and to what extent.

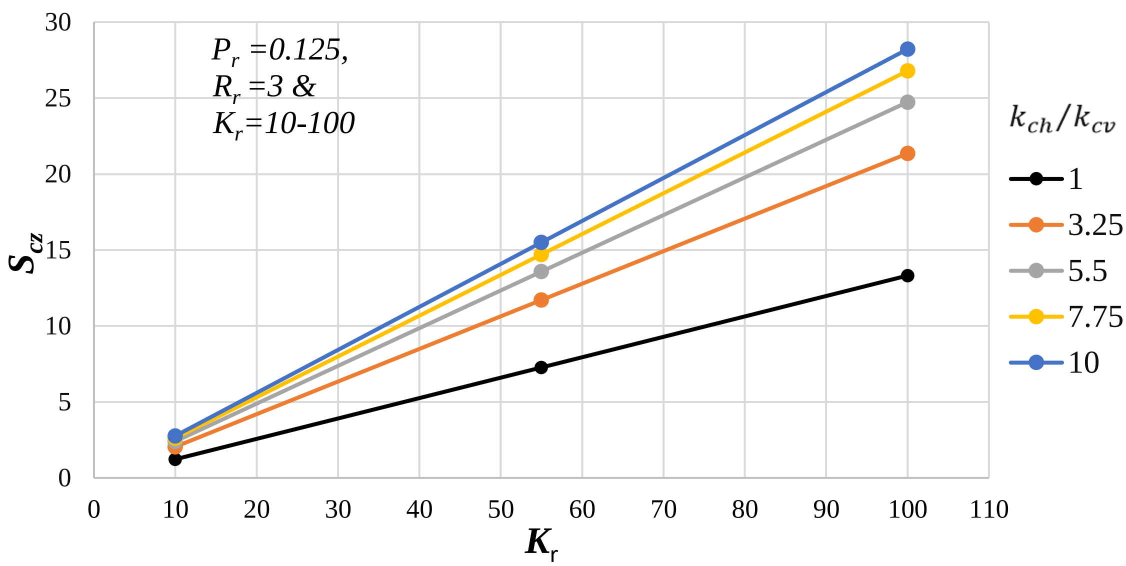

Figure 5.13: CFD results of crushed skin factor under the effect of permeability-anisotropy ($k_{ch}/k_{cv} = 1 - 10$) at the crushed zone for perforation with crushed tip scenario.

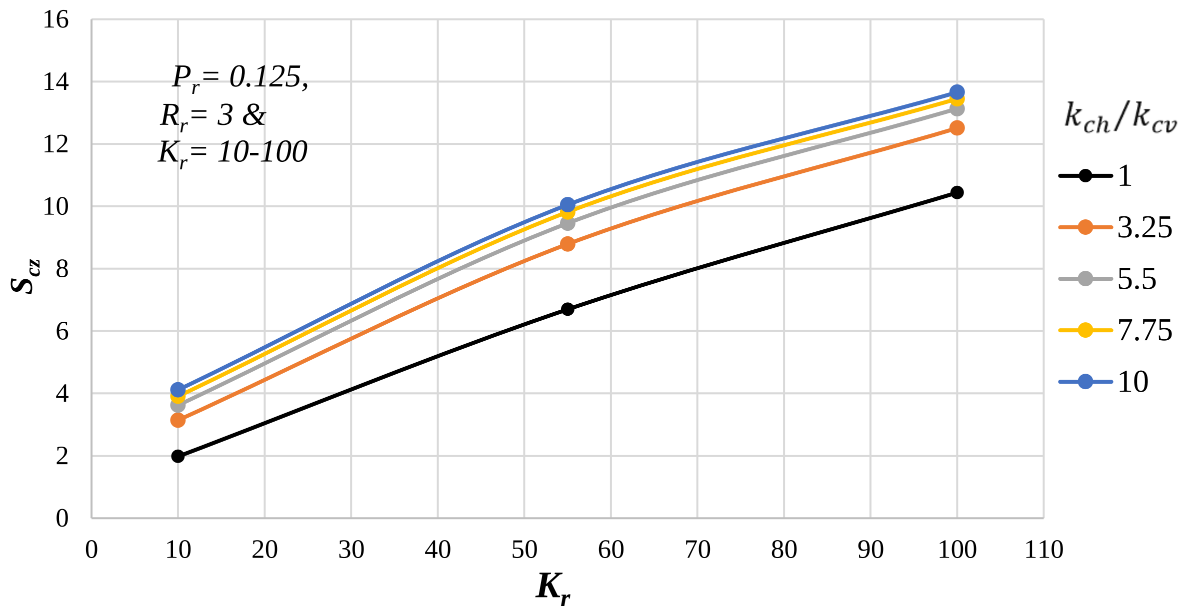

Figure 5.14: CFD results of crushed skin factor under the effect of permeability-anisotropy ($k_{ch}/k_{cv} = 1 - 10$) at the crushed zone for perforation without crushed tip scenario.

5.4. Conclusions

The study has conducted in order to further investigate the accuracy of Karakas and Tariq's (1991) model for crushed skin factor as well as to obtain new correlations which may be closer to reality, established on some assumptions. Based on the results of this investigations' analysis, the following conclusions can be summarized:

1) The experimental data showed good agreement with the numerical model results used in this work to conduct more investigations.

2) The study showed a clear view of the effect of the three dimensionless parameters (P_r K_r and R_r) on the crushed skin factor and pressure gradient.

3) The comparison of the simulations reveals that there is a significant difference between each of the two tip-crushed zone scenarios.

4) The numerical model gave almost identical results as for Karakas and Tariq (1991) model, if the length of the perforations was assumed to be shorter than their real length by a thickness of crushed zone.

5) The differences between the two simulations' results show that the currently available model (Karakas and Tariq (1991) for estimating the skin factor for vertical perforated completions needs to be improved, based on which of the two cases is closer to reality.

6) The study presented two novel correlations that give more than one option to calculate the crushed skin factor.

7) The outcomes of this study underscore the need to include the crushed zone anisotropy effect through the improvement of available models for determining the crushed skin factor.

References

Alle, T., & Worzel, H. (1956). Productivity Method of Evaluating Gun Perforating. *Paper presented at the Drilling and Production Practice* (pp. 112-125). New York: OnePetro.

Bell, T. W., Tariq, S. M., & Sukup, R. A. (1995). *Perforating.* Richardson: Henry L. Doherty memorial fund of AIME, Society of petroleum engineers.

Craddock, G. G., Smith, J., & Haggerty, D. (2018). Perforation crushed Zone characteristics in a Subsurface Sandstone. *the SPE International Conference and Exhibition on Formation Damage Control* . Lafayette, Louisiana, USA: OnePetro. doi:10.2118/189483-ms

Grove, B., Harvey, J., & Zhan, L. (2013). Perforation Cleanup by Means of Dynamic Underbalance: New Understanding. *SPE Drilling & Completion, 28*(1), 11-20. doi:10.2118/143997-pa

Karakas, M., & Tariq, S. (1991). Semianalytical productivity models for perforated completions. *SPE Production Engineering, 6*(01), 73-82.

Klotz, J., Krueger, R., & Pye, D. (1974). Effect of perforation damage on well productivity. *Journal of Petroleum Technology, 26*(11), 1303-1314.

Krueger, R. (1956). Joint Bullet and Jet Perforation Tests (Progress Report). *Paper presented at the Drilling and Production Practice.* New York: OnePetro.

Krueger, R. (1988). An Overview of Formation Damage and Well Productivity in Oilfield Operations. *An Update." Paper presented at the SPE California Regional Meeting 1988.* Long Beach, California. doi:https://doi.org/10.2118/17459-MS

Locke, S. (1981). An advanced method for predicting the productivity ratio of a perforated well. *Journal of Petroleum Technology, 33*(12), 2481-2488.

McLeod, H. (1983). The effect of perforating conditions on well performance. *Journal of Petroleum Technology, 35*(01), 31-39. doi:10.2118/10649-pa

Nabipour, A., Sarmadivaleh, M., Asadi, M. S., Sabogal Polania, J. M., Evans, B., & Rasouli, V. (2010). Evaluation of discrete element method for realistic modeling of reservoir rock. *the SPE Asia Pacific Oil and Gas Conference and Exhibition, Brisbane.* Queensland, Australia: OnePetro. doi:10.2118/132861-ms

Pucknell, J. K., & Behrmann, L. A. (1991). An investigation of the Damaged zone created by Perforating. *the SPE Annual Technical Conference and Exhibition.* Dallas, Texas: OnePetro. doi:doi.org/10.2118/22811-MS

Sarmadivaleh, M., Nabipour, A., Asadi, M. S., Sabogal Polania, J. M., & Rasouli, V. (2010). Identification Of Porosity Damaged Zones Around A Perforation Tunnel Based On Dem Simulation. *the ISRM International Symposium - 6th Asian Rock Mechanics Symposium.* New Delhi, India: OnePetro.

Satti, R. P., White, R., Ochsner, D., Osarumwense, O., Zuklic, S. N., & Sampson, T. (2015). From Computerized Tomography to CFD: Production Flow Prediction in Realistic Perforation Tunnels. *Paper presented at the SPE European Formation Damage Conference and Exhibition.* Budapest, Hungary. doi:10.2118/178935-ms

Satti, R. P., White, R., Ochsner, D., Osarumwense, O., Zuklic, S. N., & Sampson, T. (2016). New Insights into Optimizing Perforation Clean Up and Enhancing Productivity with Zinc-Case Shaped Charges. *Paper presented at the SPE International Conference and Exhibition on Formation Damage Control.*

Lafayette, Louisiana, USA: Paper Number: SPE-178935-MS. doi:10.2118/178935-ms

Satti, R., Zuklic, S. N., Bale, D., Koliha, N., Fager, A., Balasubramanian, G., Freed, D. (2018). Advanced Analysis of Clean-Up and Productivity from Perforated Rocks. *Paper presented at the SPE Western Regional Meeting*, *Paper Number: SPE-190113-MS.* Garden Grove, California, USA. doi:10.2118/190113-MS

Sun, D., Li, B., Gladkikh, M., Satti, R., & Evans, R. (2013). Comparison of skin factors for perforated completions calculated with computational-fluid-dynamics software and the karakas-tariq semianalytical model. *SPE Drilling & Completion, 28*(01), 21-33. doi:10.2118/143663-pa

Tariq, S. (1990). New, Generalized Criteria for Determining the Level of Underbalance for Obtaining Clean Perforations. *Paper presented at the SPE Annual Technical Conference and Exhibition.* New Orleans, Louisiana. doi:https://doi.org/10.2118/20636-MS

Thomas, L. K., Evans, C. E., Pierson, R. G., & Scott, S. L. (1991). Well performance model. *Journal of Petroleum Technology*, *44*(02), 220-229. doi:10.2118/20723-pa

Walton, I. (2000). Optimum Underbalance for the Removal of Perforation Damage. *Paper presented at the SPE Annual Technical Conference and Exhibition.* Dallas, Texas. doi:https://doi.org/10.2118/63108-MS

Xue, S., Zhu, X., Zhang, L., Zhu, S., & Ye, G. (2016). Research on the Damage of Porosityand Permeabilitydue to Perforation on Sandstone in the Compaction Zone. *Computers, Materials & Continua, 51*(1), 21-42. doi:10.3970/cmc.2016.051.021

Yew, C. H., & Zhang, X. (1993). A Study of the Damage Zone Created by Shaped-Charge Perforating . *the Low Permeability Reservoirs Symposium.* Denver, Colorado: OnePetro. doi:10.2118/25902-ms

Yildiz, T. (2006). Assessment of total skin factor in perforated wells. *SPE Reservoir Evaluation & Engineering, 9*(1), 61-76. doi:10.2118/82249-pa

Chapter 6

6. Quantifying the partial-penetration skin factor for evaluating the completion efficiency of vertical oil wells

Quantifying the partial-penetration skin factor for evaluating the completion efficiency of vertical oil wells

Ekhwaiter Abobaker[1], Abadelhalim Elsanoose[1], Faisal Khan[1], Mohammad Azizur Rahman[2], Amer Aborig[1], Khalid Noah[3]

Corresponding author: *Ekhwaiter Abobaker; email: eera48@mun.ca*

Journal of Petroleum Exploration and Production Technology, 2021

Abstract: An oil well's productivity is generally considered the standard measure of the well's performance. However, productivity depends on several factors, including fluid characteristics, formation damage, the reservoir's formation, and the kind of completion the well undergoes. How a partial completion can affect a well's performance will be investigated in detail in this study, as nearly every vertical well is only partially completed as a result of gas cap or water coning issues. Partially penetrated wells typically experience a larger pressure drop of fluid flow caused by restricted regions, thus increasing the skin factor. A major challenge for engineers when developing completion designs or optimizing skin factor variables is devising and testing suitable partial-penetration skin and comparing completion options. Several researchers have studied and calculated a partial-penetration skin factor, but some of their results tend to be inaccurate and cause excessive errors. The present work proposes experimental work and a numerical simulation model for accurate estimation of the skin factor for partially

[1] Faculty of Engineering and Applied Science, Memorial University of Newfoundland, St. John's, NL, A1C 5S7, Canada
[2] Petroleum Engineering, Texas A&M University at Qatar, Doha, 23874, Qatar.
[3] Faculty of Engineering, University of Tobruk, Tobruk, Libya.

penetrated wells. The work developed a simple correlation for predicting the partial-penetration skin factor for perforated vertical wells. The work also compared the results from available models that are widely accepted by the industry as a basis for gauging the accuracy of the new correlation in estimating the skin factor. Compared to other approaches, the novel correlation performs well by providing estimates for the partial-penetration skin factor that are relatively close to those obtained by the tested models. This work's main contribution is the presentation of a novel correlation that simplifies the estimation of the partial-penetration skin factor in partially completed vertical wells.

6.1. Introduction

In near-wellbore regions, fluid flow can be significantly affected by the type of well completion applied. There are several different kinds of well completion. For example, open-hole completion creates a radial flow pattern surrounding the wellbore, leaving a normal trajectory. However, this form of well completion may not in itself be sufficient, in which case other well completion approaches may be necessary. Other methods may be used for preventing water and gas coning, isolating or controlling wellbore fluid entry, or reducing sand production. Well completion applied on the part of a well is called a partially penetrated or restricted well. Unlike fully penetrated wells, the flow lines of partially completed wells proceed towards the wellbores perpendicularly, while flow pattern distortion due to partially penetrated completion increases pressure loss. Determining if stimulation of a partially penetrated well is warranted requires quantitatively calculating the various components in the total skin factor. For wells that are partially penetrated, the skin factor needs to be evaluated as a primary component of the total skin. Furthermore, partially penetrated wells may have a one-dimensional radial flow that is more deeply formed at a distance from a wellbore. In this case, as the fluid nears the wellbore, there is a fluid convergence in the area immediately surrounding the open well. As shown in Figure 6.1, partial penetration causes a field of flow surrounding the near-wellbore area that is two-dimensional. As a result of the fluid convergence along with the two-dimensional flow, the fluid at the wellbore region flows with higher velocity.

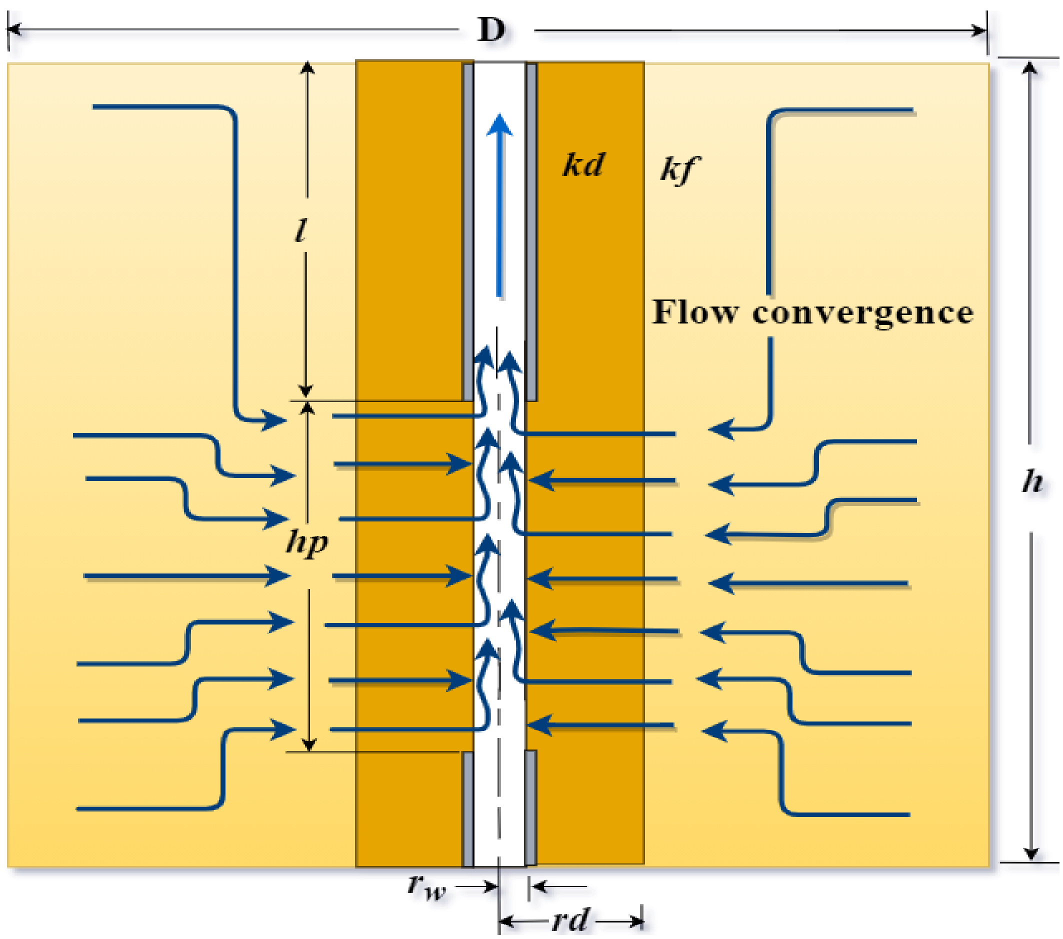

Figure 6.1: Schematic of partially penetrated well with formation damage

Overall, partial penetration leads to increased pressure drop at near-wellbore regions. It also causes lower well productivity. Several researchers (e.g., Muskat, 1949; Muskat & Boston, 1982; Nisle, 1958; Brons and Marting, 1961; Odeh, 1968, 1980 Gringarten and Ramey, 1975; Jones and Watts 1971; Saidikowski, 1979; Streltsova-Adams, 1979; Apatzacos, 1987; Yeh and Reynolds, 1989; Vrbik, 1991) have investigated how partial penetration at the wellbore affects pressure behaviour as well as productivity. Their studies have yielded a number of analytical models that simulate flow in partially penetrating wells. Some of these models are generally quite complex and are based on many functions, for instance, infinite series and Bessel functions.

In two-dimensional analytical solutions, the models have been developed to calculate partial-penetration skin using simpler and more straight forward approaches. The strategies presented by Odeh (1980), Papatzacos (1987) and Vrbik (1991) are especially popular due to their inherent ease of application. Also, analytical expressions pertaining to the skin factor were developed by Gomes and Ambastha (1993) for multi-layered reservoirs featuring closed-bottom/-top boundaries in addition to bottom-water zones and gas caps. A year later, Ding and Reynolds (1994) expanded on Papatzacos's (1987) research by modifying it and applying it to a multi-layered reservoir, giving good results in simulations. Lee and Kyonggi (2001) proposed a novel approach for generating a skin factor. The work is based on partial penetration of reservoirs that are either multi-layered or single-layered at the cross-flow between layers.

Many different techniques and models have been used for calculating the partial penetration skin factor. However, the results of some of these approaches tend to be inaccurate. The present study proposes experimental work, a numerical simulation model and statistical analysis for more accurate estimation of the skin factor for partially penetrated wells.

6.2. Methodology

6.2.1. Mathematical model

In porous media, fluid flow at low velocities typically obeys Darcy's law. As the flow velocity increases, however, a non-Darcy flow regime begins to develop, caused by the increasingly non-linear relationship between the local pressure gradient and in-situ fluid velocity. Open-hole well completion is both the simplest and most popular completion strategy used in the oil and gas hydrocarbon industry today. Constructing a productivity model of vertical open holes is also relatively straightforward. Through integrating the relevant data with Darcy's equation, a well-productivity model can be built that describes open-hole well production in steady-state flows.

$$q = \frac{2\,\pi k_f\, h\, \Delta_p}{\mu \ln(r_e/r_w)} \tag{6.1}$$

The productivity index is known as the ratio of flow rate to the pressure gradient.

$$J_o = \frac{q}{\Delta p} = \frac{2\,\pi k_f h}{\mu \ln(r_e/r_w)} \tag{6.2}$$

Hydrocarbon wells can be affected by a number of skin factors. These effects include mechanical skin as well as both geometrical and completion skins. In other words, any difference between an actual well's performances compared to that of an ideal vertical open hole is expressed as the total skin factor. In the literature, some studies calculate the total skin factor by adding together all of the above-mentioned skin factors, as in the eq below Yildiz (2006):

$$S_t = s_d + s_{pp} + s_p + s_{cz} + s_\theta + s_{df} \tag{6.3}$$

To better understand how skin factors can affect the productivity of a well, the productivity index for an ideal open hole is compared to that for a well with skin factors.

$$q = \frac{2\,\pi K_f h\ \ \Delta p}{\mu[\ln(r_e/r_w)+S_t]} \tag{6.4}$$

$$J_d = \frac{q}{\Delta p} = \frac{2\,\pi K_f h}{\mu\,[\ln(r_e/r_w)+S_t]} \tag{6.5}$$

To quantify the comparison, the productivity ratio (PR) is applied, as expressed in eq:

$$PR = \frac{J_d}{J_o} = \frac{\ln(r_e/r_w)}{\ln(r_e/r_w)+S_t} \tag{6.6}$$

Using previous research as a foundation and reference point, the present study aims to compare and extend the investigations of near-wellbore region flow. This study is an extended work, conducting three investigative procedures of experimental, numerical, and statistical analysis for more accurate estimation of the skin factor for partially penetrated wells. In some publications, a list of the partial penetration skin equations is given in Table 6.1.

Table 6.1: Summary of some studies' models that were conducted on partial completion wells.

Author(s)	Equations
(Brons & Marting, 1961)	$S_{pp} = \frac{1-b}{b}\left(ln\frac{h}{r_w} - G(b)\right)$ $b = \frac{h_p}{h}$
(Odeh, 1980)	$S_{pp} = 1.35\left(\left(h/h_p - 1\right)^{0.825}\left\{ln\left(h\sqrt{\frac{k_h}{k_v}} + 7\right) - \left[0.49 + 0.1ln\left(h\sqrt{\frac{k_h}{k_v}}\right)\right].lnr_{wc} - 1.95\right\}\right),$ $r_{wc} = r_w e^{0.2126(z_m/h+2.753)}$ $, \quad z_m = l + h_p/2$
(Papatzacos, 1987)	$S_{pp} = (1/b - 1)\ \ln\ (\pi/2r_D + 1/b\ ln\left[\frac{b}{2+b}\left(\frac{A-1}{B-1}\right)^{\frac{1}{2}}\right]$ $r_D = r_w/h, h_{1D} = l/h, \quad A = 1/\left(h_{1D} + \frac{b}{4}\right), \quad B = 1/\left(h_{1D} + \frac{3b}{4}\right)$
(Yeh & Reynolds, 1989)	$S_{pp} = \left[\frac{(1-b)}{b}\right]\{ln[2b(1-b)h_{wD1}] - C_1\}$ $h_{wD1} = \left(h_p/r_w\right)\sqrt{k_h/k_v}, \quad C_1 = 0.481 + 1.01b - 0.838b^2$
(Vrbik J. , 1991)	$S_{pp} = \left[\frac{(1-b)}{b}\right][1.2704 - ln(R)] - \left\{f(0) - f(b) + f(1-2D) - \left[\frac{f(1-2D+b)}{2}\right] - \left[\frac{f(1-2D-b)}{2}\right]\right\}b^2$ $f(y) = y\ ln(y) + (2-y)\ \ln(2-y) + R\ \ln\left[sin^2\left(\frac{\pi y}{2}\right) + 0.1053R^2\right]/\pi$ $D = \frac{d}{h}\ , \qquad R = r_w\ \sqrt{k_v/k_h}/h$

The experimental approach was used to validate the numerical model results for single-phase flow through the perforation tunnel. Statistical analysis was coupled with numerical simulation to expand the investigation of fluid flow in the near-wellbore region that cannot be obtained experimentally, due to the limitations of the experimental setup, especially the small sample size.

6.2.2. Experimental procedure

In the experimental portion of our work, we injected a measured volume of water into core sample. As well, we used a geotechnical radial flow test set-up to measure the differential pressure and single-phase flow rate of the perforated sample, with water being radially injected into the core sample within Darcy flow and the following boundary conditions: The outer side of the sample is considered an inlet while the perforation surface is an outlet. Furthermore, both inlet/outlet pressures were measured for our cylindrical samples using specified water flow rate.

Figure 6.2 shows the set-up, which features the three following main sections: flow lines extending from inlet to outlet; an inner chamber for holding samples with axial loads; and a Data Acquisition (DQ) system. Preparation of perforation tunnel was conducted by cutting a carbonate core sample from a rock from Nova Scotia, Canada. The geometry of the sample is cylindrical with a hole at the center as shown in Figure 6.3. The dimensions of the geometry and the sample properties are listed in Table 6.2.

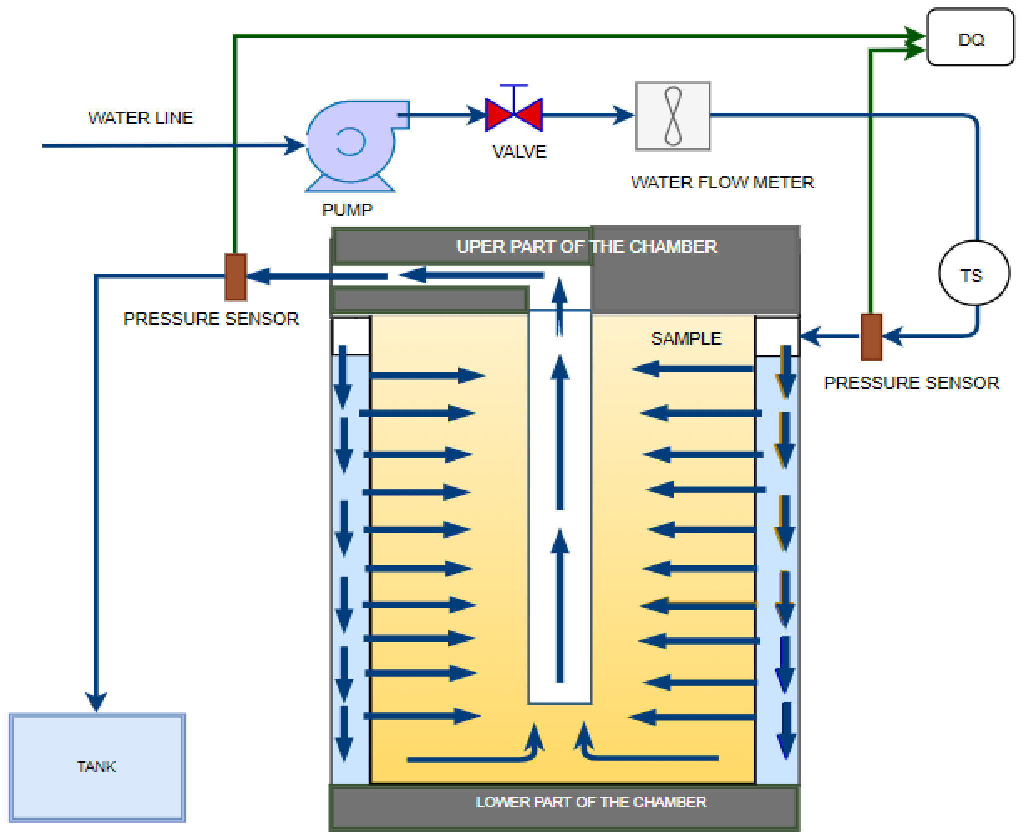

Figure 6.2: Schematic diagram of the experiment: Water flow meter; Inlet and outlet pressure sensors; TS: Temperature sensor; and DAQ: Data Acquisition system

Table 6.2: The dimensions and properties of the carbonate sample that used in the experimental procedure.

Sample Dimensions and Properties	**Values (units)**
Sample height (H)	30.48 cm
Radius of sample (R)	7.62 cm
Radius of perforation tunnel (r_p)	1.27 cm
Depth of perforation (L_p)	25.4 cm
Permeability (k_f)	6.27 × 10^{-15} m^2
Porosity (γ)	13.5 %

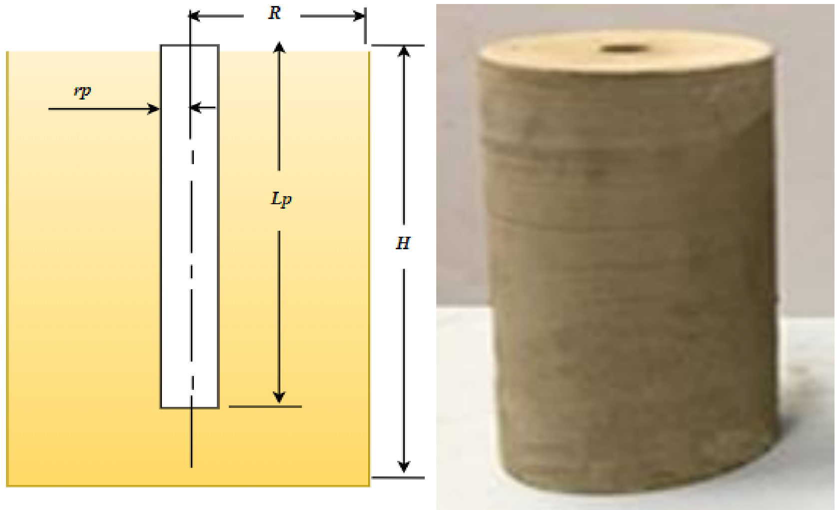

Figure 6.3: The dimensions and shape of carbonate sample used in the experimental work

6.2.3. Numerical procedure

In the present work, we used ANSYS FLUENT 18.1 for our computational fluid dynamics (CFD) model. Our aim was to present a single-phase fluid flow simulation for a reservoir described as three-dimensional, vertical, and cylindrically layered. We created a sample that is vertical with a single layer of uniform thickness (h), and we assumed the well was centrally located and cast radius (r_w) throughout the formation. Further, the well was partially completed at an open interval length h_p , in addition to the distance spanning the open interval's top to the formation's top (l); it also had vertical-to-horizontal permeability ratio (k_v/k_h). Although partial penetration skin has been considered in the present research, other skin factors have not.

Uniform mesh and cut mesh method (Figure 6.4) were used to generate high-quality mesh. This configuration helped to predict a good quality, high density mesh close to perforation borders.

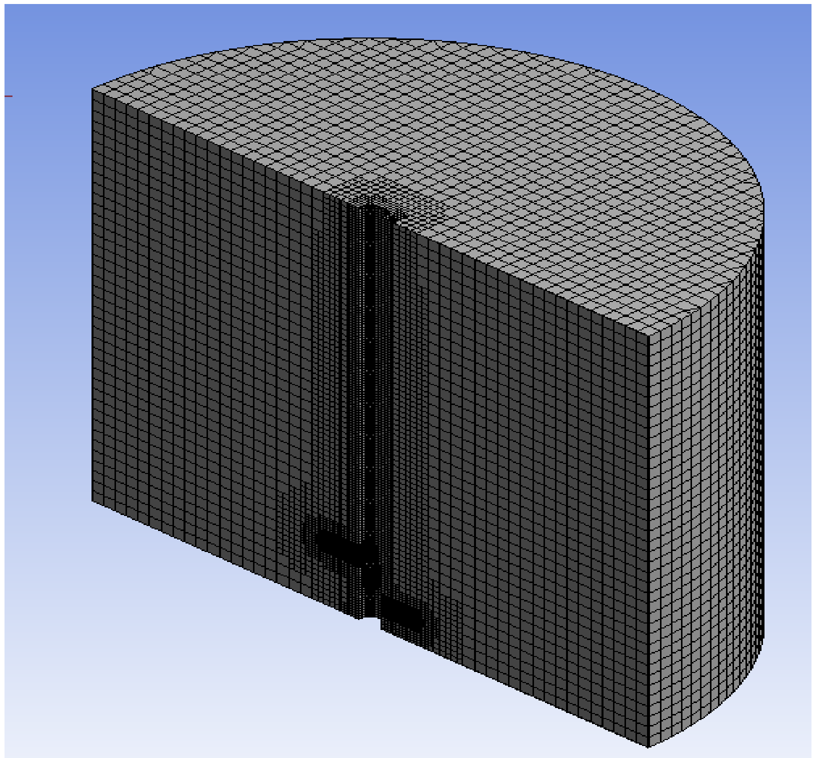

Figure 6.4: The shape of uniform configuration mesh that used in CFD simulations.

6.2.4. Statistical procedure

In statistical procedure, four parameters were investigated, including the length of the completed open interval (h_p), wellbore radius (r_w), and the distance from the top of the open interval to the top of the formation (l) divided each one on the formation's thickness (h) to make them dimensionless parameters as well as permeability ratio (k_r):

$$h_d = \frac{h_p}{h} \tag{6.7}$$

$$r_d = \frac{r_w}{h} \tag{6.8}$$

$$l_d = \frac{l}{h} \tag{6.9}$$

$$k_r = \frac{k_v}{k_h} \tag{6.10}$$

Two boundary points were selected, and one midpoint was determined by BBD for the intervals of the parameters as presented in Table 6.3. Twenty-five numerical runs were performed and analyzed to obtain a suitable statistical analysis using the ANOVA analysis with the BBD model.

Table 6.3: The dimensionless parameters of the near-wellbore region.

Dimensionless parameters	**Range**
Partially completed at an open interval length / formation thickness h_d	0.2-0.4
Wellbore radius / formation thickness r_d	0.00083-0.0025
The distance spanning the open interval's top to the formation's top / formation thickness l_d	0.1-0.6
Permeability Ratio (k_r)	0.1-1

6.3. Results and discussion

This study investigates specific water flow rate Q_w=2 cm^3/s with viscosity μ = 0. 95 mPa.s that was injected into the sample to determine the differential pressure. The dimensions and properties of the perforation tunnel sample in the numerical model are the same as those used in the experimental procedure (see Table 6.1). The comparison between the experimental and numerical results of the pressure buildup with the same flow boundary conditions is shown in Figure 6.5. The experimental data and numerical results are in good agreement.

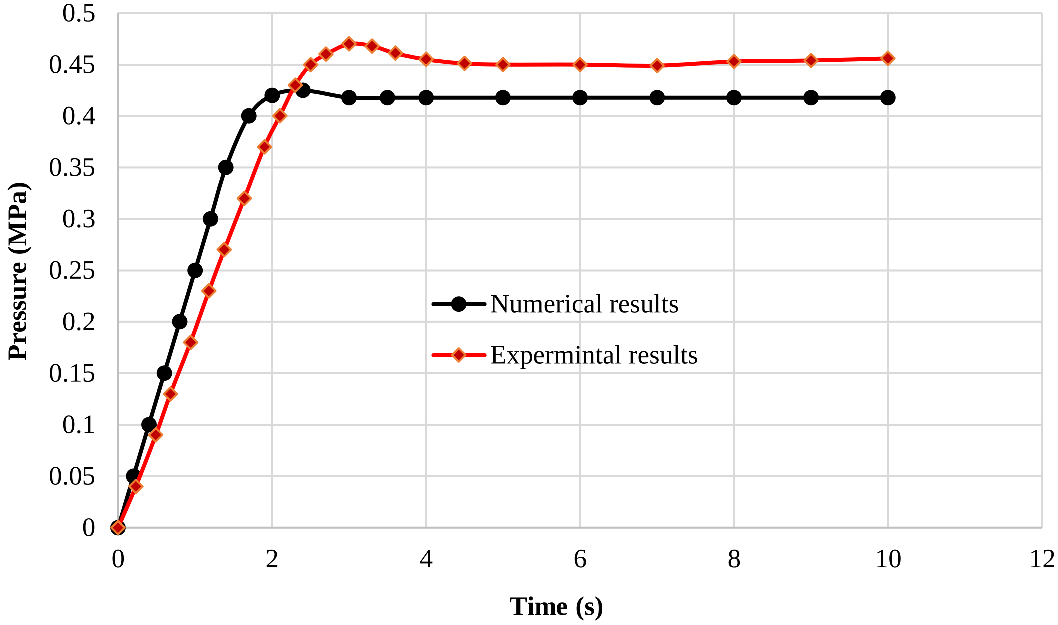

Figure 6.5: The comparison between experimental data, numerical results at the same flow boundary condition

The validation of numerical results with experimental ones has resulted in full confidence in using the numerical model to conduct huge investigations by creating the near-wellbore region with different dimensions. Therefore, partially penetrated well parameters were analyzed using statistical analysis coupled with the numerical simulation model. The statistical analysis results show that partial-penetration completion increases the pressure drop and thus contributes to a reduction in the productivity index.

This research investigated a specific water volume that was injected into the samples to determine the differential pressure of these samples. Table 6.4 presents the results of 25 numerical runs that were analyzed with ANOVA and the BBD model; the partial-penetration skin factor results are shown in the last column.

The primary assumption in using the DoE model was the normal distribution of numerical data with a constant variance of features. In looking at the residuals' normal plot in Figure 6.6, we can see that the numerical data follows a normal distribution pattern. Additionally, our results show that the predicted values derived from the model share strong similarities with the actual values derived numerically.

This study provided correlation from the statistical analysis based on the numerical results. This correlation used to determine the relative impact of each factor for different scenarios on the partial-penetration skin factor.

$$Spp = \ e^{(4-3.65h_d-135r_d-0.26k_r+0.125l_d)} \qquad (6.11)$$

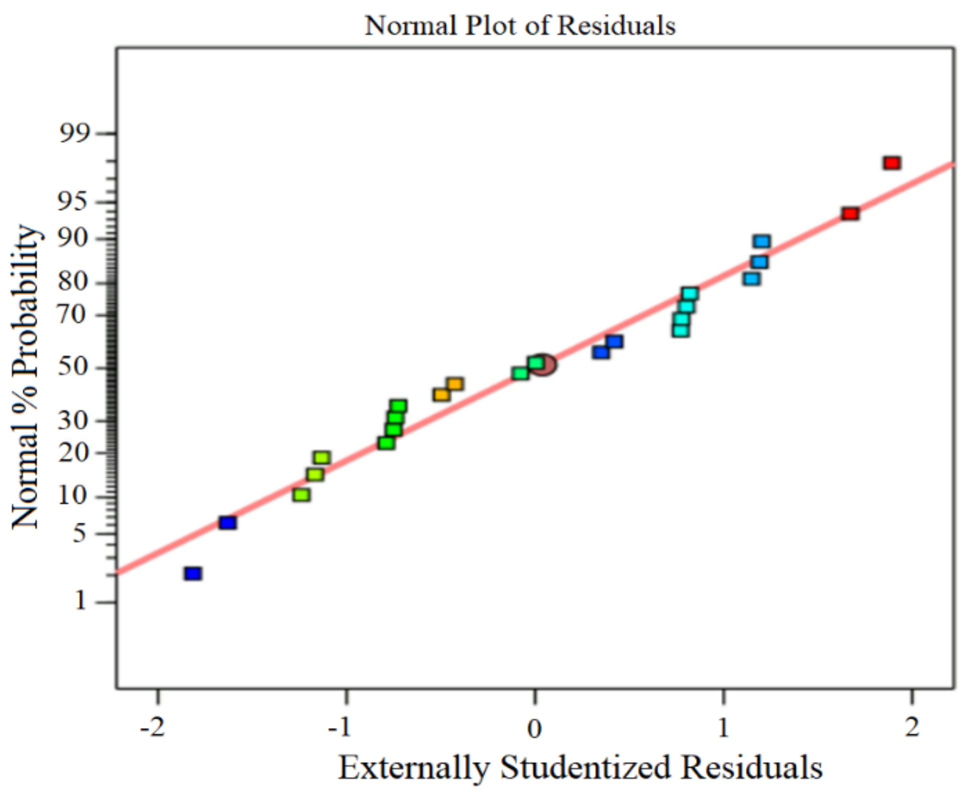

Figure 6.6: Normal plot of residuals

Table 6.4: Twenty-five numerical runs

No	h_d	r_d	k_r	l_d	S_{pp}
1	0.4	0.0016665	0.55	0.6	9.15
2	0.2	0.000833	0.55	0.35	20.85
3	0.2	0.0016665	0.1	0.35	21.11
4	0.2	0.0016665	1	0.35	16.73
5	0.4	0.0016665	0.55	0.1	8.91
6	0.4	0.000833	0.55	0.35	10.15
7	0.2	0.0025	0.55	0.35	16.74
8	0.3	0.0016665	1	0.6	11.81
9	0.4	0.0016665	0.1	0.35	10.12
10	0.3	0.0025	0.55	0.6	11.78
11	0.2	0.0016665	0.55	0.6	18.83
12	0.3	0.000833	0.55	0.6	14.67
13	0.3	0.0025	0.55	0.1	11.42
14	0.3	0.0016665	1	0.1	11.34
15	0.3	0.000833	0.1	0.35	16.31
16	0.3	0.000833	1	0.35	12.75
17	0.4	0.0016665	1	0.35	8.02
18	0.4	0.0025	0.55	0.35	7.45
19	0.3	0.000833	0.55	0.1	14.28
20	0.2	0.0016665	0.55	0.1	18.38
21	0.3	0.0016665	0.1	0.1	14.27
22	0.3	0.0025	0.1	0.35	13.05
23	0.3	0.0025	1	0.35	10.31
24	0.3	0.0016665	0.55	0.35	12.97
25	0.3	0.0016665	0.1	0.6	15.3

For example (numerical run), the partial-penetration skin factor can be calculated from the difference in the pressure drop between open hole completion and two partial completion ceases with isotropic permeability and anisotropic permeability ($k_r = 1$ and $k_r = 0.1$) at the same geometry dimensions and flow boundary conditions (Table 6.5).

Table 6.5: The dimensions, dimensionless parameters of two partial completion cases, and flow boundary conditions

Sample Dimensions and Properties	**Values (units)**
Reservoir thickness (h)	6.096 m
Reservoir radius (r_e)	3.6576 m
Wellbore radius (r_w)	1.27 cm
Partially completed at an open interval length / Formation thickness h_d	0.2
The distance spanning the open interval's top to the formation's top / Formation thickness l_d	0.4
Wellbore radius / Formation thickness r_d	0.002083
Horizontal permeability (k_h)	10^{-13} m^2
Vertical permeability (k_v)	10^{-14} m^2
Porosity (γ)	25%
Water flow rate (Q_w)	1.5 L/min
Water viscosity (μ)	0.001003 kg/m-s

The numerical results showed the pressure distribution and increased pressure drop for partially penetrated cases compared to open hole completion and illustrated the anisotropic permeability effect on flow converging, as shown in Figure 6.7 and 6.8. The fluid flow lines are started in the radial directions until the wellbore boundaries are reached; the spherical flow regime appears after that due to the flow convergence effect.

A low vertical-to-horizontal permeability ratio creates a high-pressure drop and affects spherical flow shape due to the vertical resistance. Also, the numerical results showed the gradation in the pressure and flow shape from spherical to elliptical with decreasing the permeability ratio.

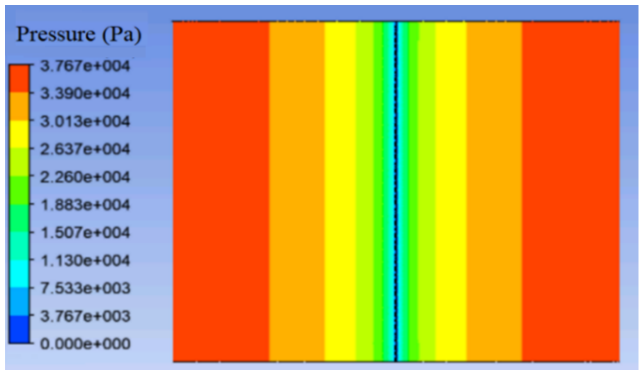

Figure 6.7: The pressure gradient for open hole completion case

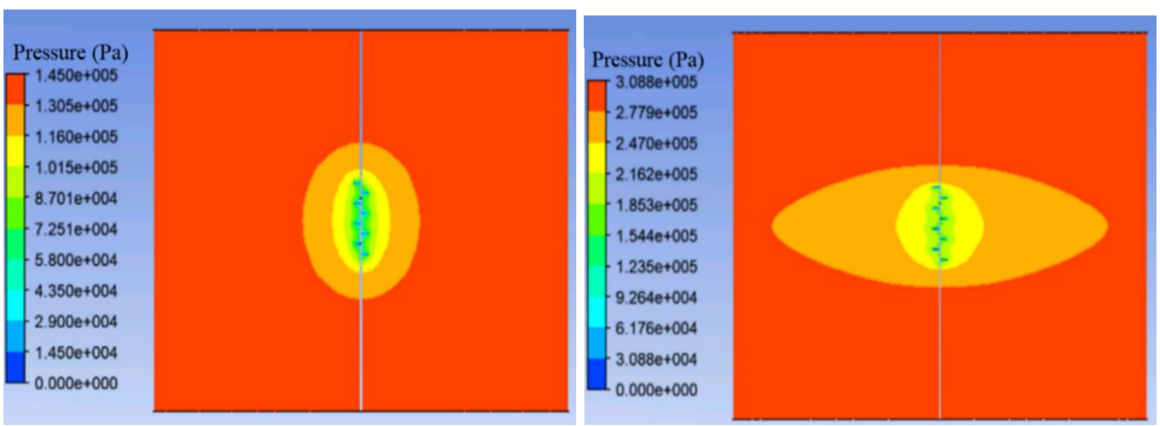

Figure 6.8: The pressure gradient for the two partial completion case with isotropic permeability ($k_r = 1$) and with anisotropic permeability ($k_r = 0.1$)

Based on the statistical analysis results, the partial-penetration skin factor value increase with decreases the dimensionless parameter(h_d). The pressure drop is more affected by a smaller area of perforation intervals; the smaller area makes a larger contribution to pressure drop; the higher inflow rate leads to energy consumption increases for accelerating the flow. In contrast, open-hole or fully completed perforation interval, this effect does not exist. However, we must note that this represents an ideal case that may or may not be reproducible in practice. Also, the results showed the interaction effect of the two dimensionless parameters (h_d and r_d) on the partial-penetration skin factor, as illustrated in Figure 6.9. The results indicated that the wellbore radius has a significant impact on partial- penetration skin factor.

The results also showed a similar effect for the dimensionless parameter (k_r) on the partial-penetration skin factor. Analyses of the impact of vertical-to-horizontal permeability ratio on partial-penetration skin factor indicate productivity's dependence on the permeability ratio. As shown in Figure 6.10, the impact of the permeability ratio on the partial-penetration skin factor is revealed by the positive slope curve. The reduction of productivity results from higher resistance to converging flow in very low vertical permeability cases, compared with horizontal permeability. Hence, we can assert that the permeability ratio is directly proportionate to the productivity ratio. In contrast, the dimensionless parameter (l_d) has less effect on the partial-penetration skin factor, whereas the maximum value for skin is achieved at a low and high value due to the flow convergence effect in the top or bottom of the reservoir, while the middle values do not have any effect, as illustrated in Figure 6.11. From these results, we can learn the effect of each parameter and, based on the results, choose a completion design that is optimal.

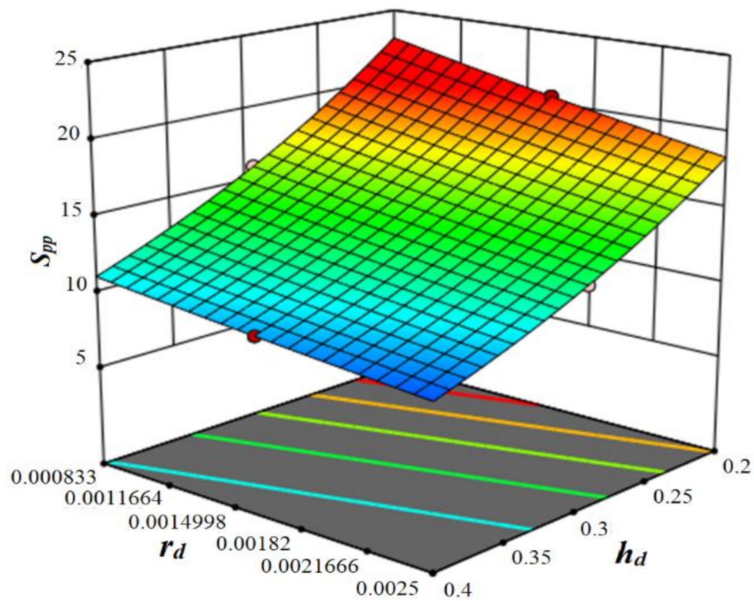

Figure 6.9: The interaction between the dimensionless parameters (h_d and r_d) and their effect on partial-penetration skin factor with constant values for the two dimensionless parameters ($l_d = 0.35$ and $k_r = 0.1$)

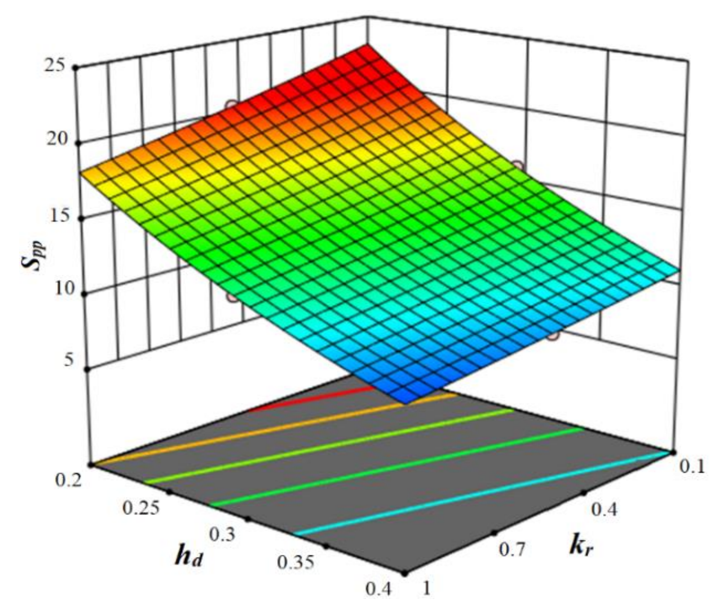

Figure 6.10: The interaction between the dimensionless parameters (h_d and k_r) and their effect on partial-penetration skin factor with constant values for the two dimensionless parameters ($l_d = 0.35$ and $r_d = 0.000833$)

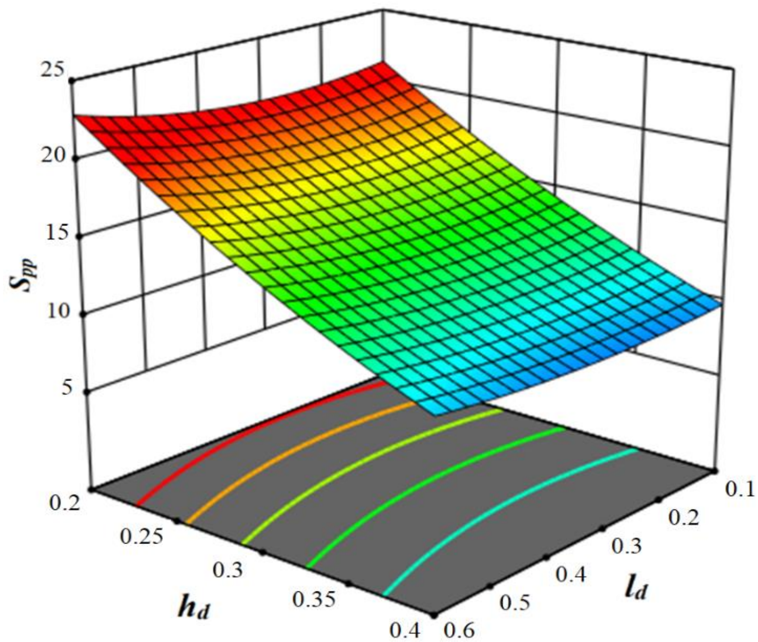

Figure 6.11: The interaction between the dimensionless parameters (h_d and l_d) and their effect on partial-penetration skin factor with constant values for the two dimensionless parameters ($r_d = 0.000833$ and $k_r = 0.1$)

The optimal completion design led to a reduction in the pressure drop as a result of reduced resistance coupled with an enhanced inflow rate. This means choosing the best dimensions of parameter that will lead to a high flow rate and accelerate radial inflow. The overall outcome of these informed choices is an increase in the productivity index. The effects of the four dimensionless parameters (h_d, k_r , r_d and l_d) on the productivity ratio are shown in Figures 6.12-6.15.

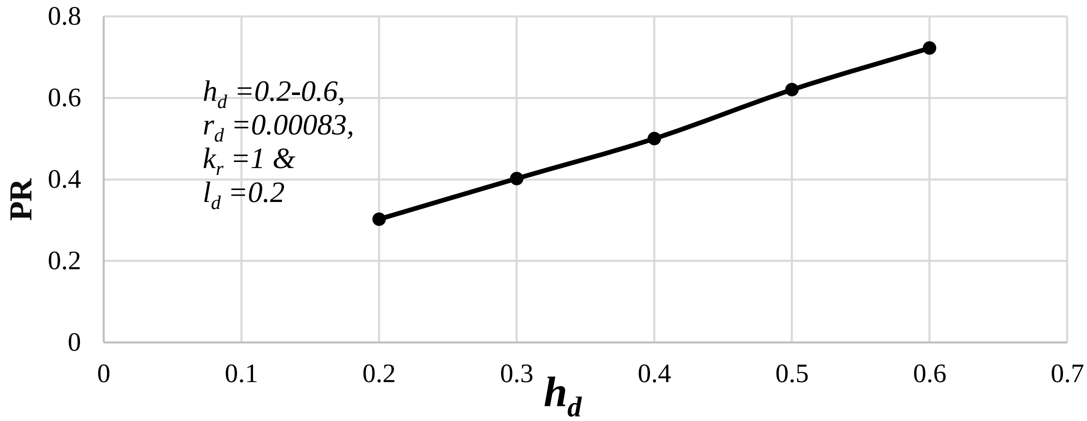

Figure 6.12: Effect of the dimensionless parameter (h_d) on productivity ratio PR

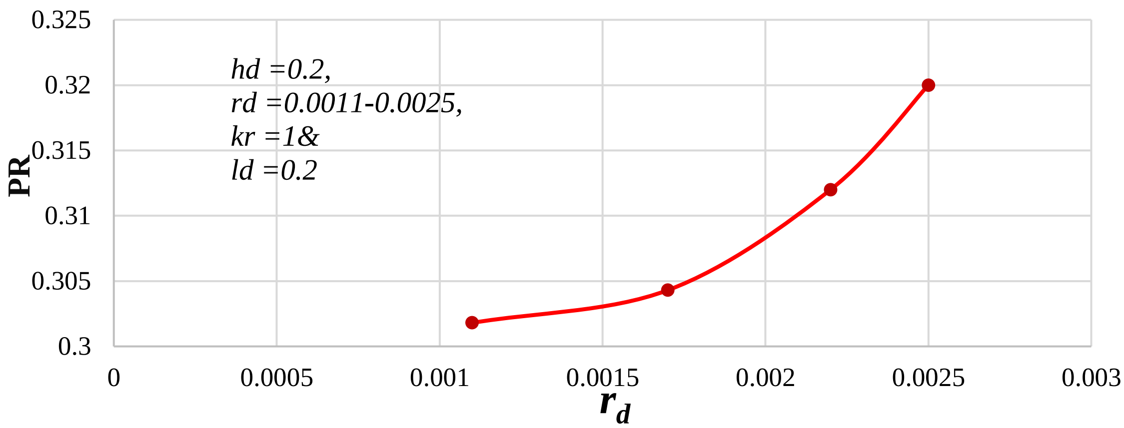

Figure 6.13: Effect of the dimensionless parameter (r_d) on productivity ratio PR

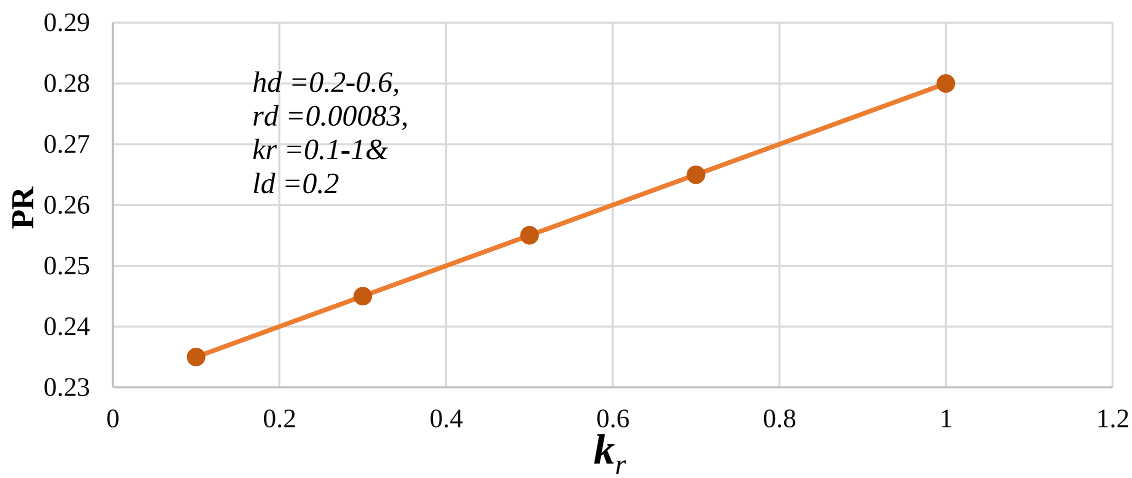

Figure 6.14: Effect of the dimensionless parameter (k_r) on productivity ratio PR

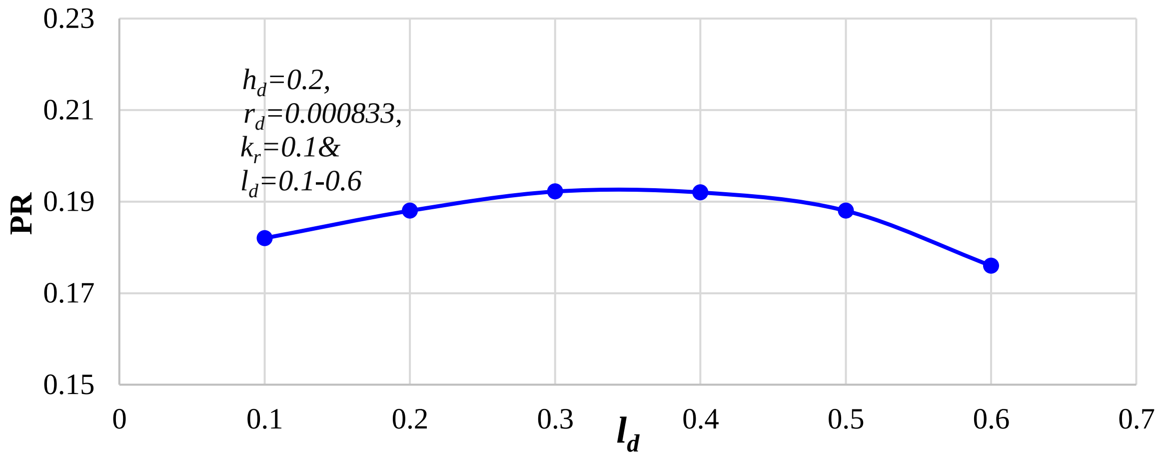

Figure 6.15: Effect of the dimensionless parameter (l_d) on productivity ratio PR

In order to compare the accuracy of our correlation, five models (Brons and Marting, 1961; Odeh, 1980; Vrbik, 1991; Papatzacos, 1987; Yeh and Reynolds, 1989) were selected and used to calculate the partial-penetration skin factor. The five models were compared to the proposed correlation. To perform a comprehensive test, the effects of three-dimensional parameters for h_d=*0.2-0.6*, r_d= 0.00083-0.0025, k_v/k_h= 0.1-1, and l_d = 0.2 on partial-penetration skin factor were compared. The proposed correlation performs well by providing estimates for the skin factor that are relatively close to those obtained by the tested models, as shown in Figures 6.16, 6.17 and 6.18. In general, analytical solutions applied to partially penetrating wells take into consideration that fluid is admitted at each point along the surface of the open interval. In other words, existing models neglect to include any additional fluid convergence caused by perforations. However, our CFD model did consider the effect of this convergence. In the high length of the completed perforation cases, the proposed correlation showed little deviation compared to other models, due to local fluid convergence caused by perforations. However, this deviation does not appear in the short length of the completed perforation cases.

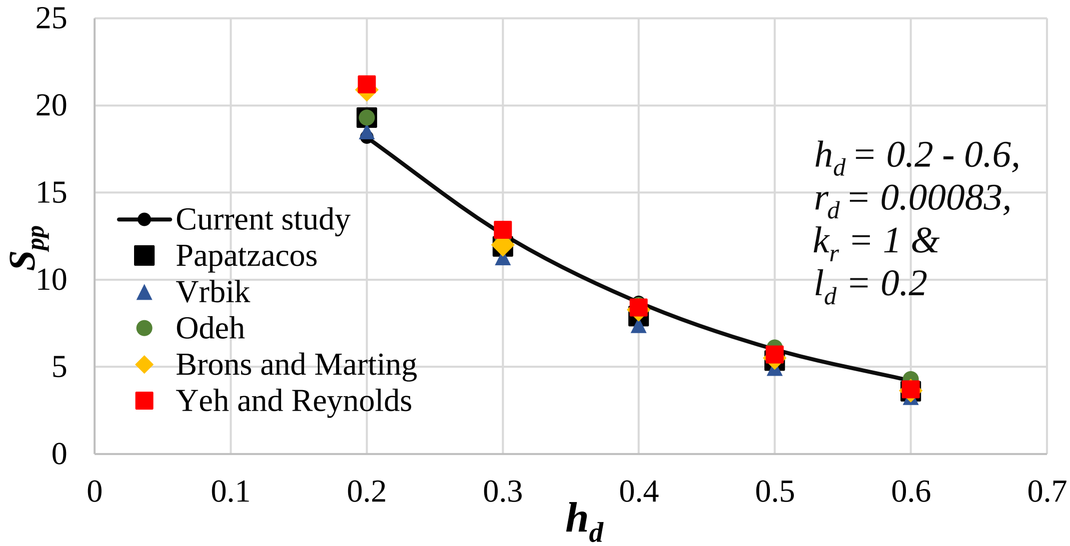

Figure 6.16: The comparison of the five models and the proposed correlation results for the effect of dimensionless open interval length (h_d) on the partial skin factor

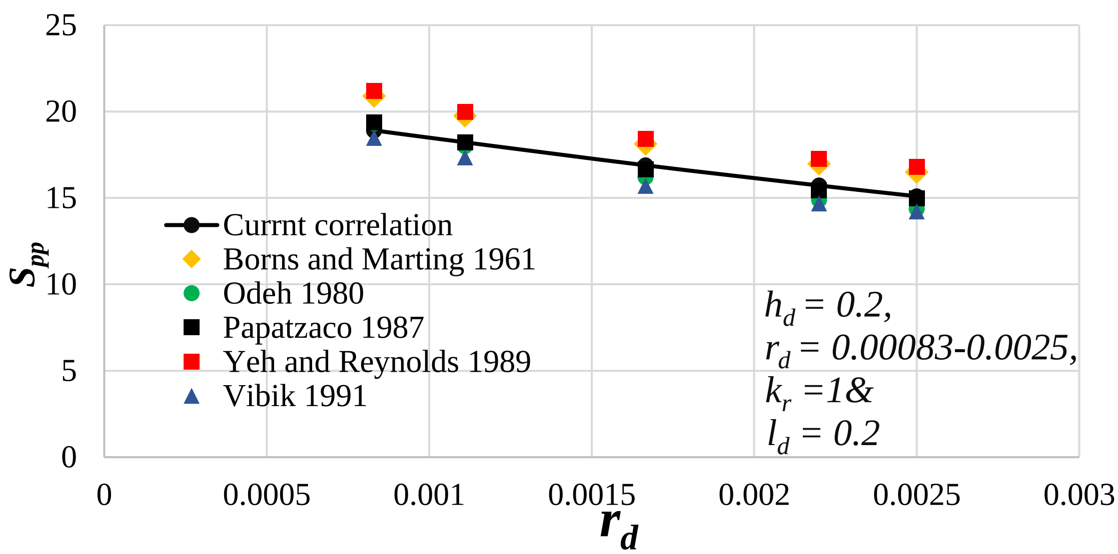

Figure 6.17: The comparison of the five models and the proposed correlation results for the effect of dimensionless wellbore radius (r_d) on the partial skin factor

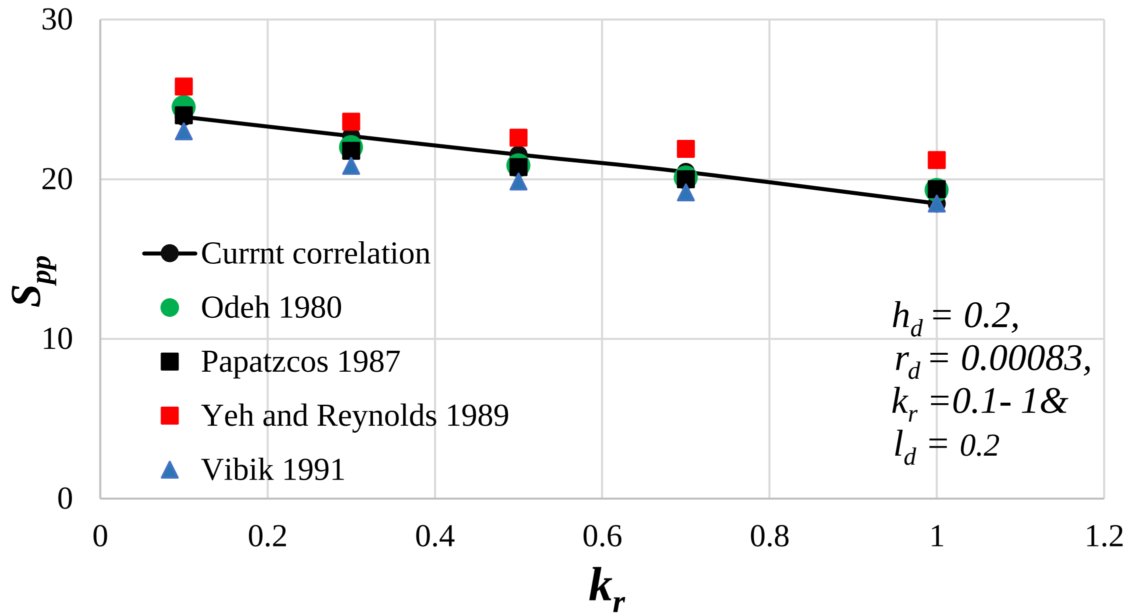

Figure 6.18: The comparison of the five models and the proposed correlation results for the effect of permeabilty ratio (k_r) on the partial skin factor

6.4. Conclusions

The study has been conducted to expand the investigation on partially completed vertical wells, understand its effects on partial penetration skin factor, and choose the optimal dimensions and distribution of partial penetration parameters. Based on the results of investigative analysis, the following conclusions can be summarized:

1) The study showed a clear view of the effect of each penetration parameter on the partial penetration skin factor and productivity index.

  a) The results showed that perforated/completion interval, wellbore radius and permeability ratio have a significant effect on the partial penetration skin factor and productivity index.

  b) The results indicated the distance spanning the open interval's top to the formation's top has less effect on the partial penetration skin factor.

2) The novel correlation has been produced from the current study that simplifies the estimation of the skin factor in partially completed vertical wells for different dimensions and distributions of the completion parameters.

3) Compared to other approaches, the novel correlation performs well by providing estimates for the partial penetration skin factor that are relatively close to previous models.

References

Brons, F., & Marting, V. (1961). The effect of restricted fluid entry on well productivity. *Journal of Petroleum Technology, 13*(2), 172-174. doi:10.2118/1322-g-pa

Ding, W., & Reynolds, A. (1994). Computation of THE Pseudoskin factor for a restricted-entry well. *SPE Formation Evaluation, 0*(01), 9-14.

Gomes, E., & Ambastha, A. (1993). Analytical expressions for Pseudoskin for Partially Penetrating Wells under various Reservoir Conditions. *the SPE Annual Technical Conference and Exhibition, Houston.* Texas: OnePetro. doi:10.2118/26484-ms

Gringarten, A. C., & Ramey, H. J. (1975). An approximate infinite conductivity solution for a partially penetrating line-source well. *Society of Petroleum Engineers Journal, 15*(2), 140-148. doi:10.2118/4733-pa

Jones, L., & Watts, J. (1971). Estimating skin effect in a partially completed damaged well. *Journal of Petroleum Technology, 23*(2), 249-252. doi:10.2118/2616-pa

Karakas, M., & Tariq, S. (1991). Semianalytical productivity models for perforated completions. *SPE Production Engineering, 6*(01), 73-82.

Lee, K. (2001). A New Method for Computing Pseudoskin Factor for a Partially-Penetrating Well. *the SPE Asia Pacific Oil and Gas Conference and Exhibition,.* Jakarta, Indonesia: OnePetro Journals. doi: https://doi.org/10.2118/68698-MS

Muskat, M. (1949). Calculation of initial fluid distributions in oil reservoirs. *Transactions of the AIME*, 119-127. doi:10.2118/949119-g

Muskat, M., & Boston, M. (1982). *The Flow of Homogeneous Fluids Through Porous Media.* New York: International Human Resources Development Corporation.

Nisle, R. G. (1958). The effect of Partial penetration on pressure build-up in oil wells. *Transactions of the AIME, 213*(1), 85-90. doi:10.2118/971-g

Odeh, A. (1968). Steady-State flow capacity of wells with limited entry to flow. *Society of Petroleum Engineers Journal, 8*(01), 43-51. doi:10.2118/1797-pa

Odeh, A. (1980). An equation for calculating skin factor due to restricted entry. *Journal of Petroleum Technology*, 964-965. doi:10.2118/8879-pa

Papatzacos, P. (1987). Approximate Partial-Penetration Pseudo-siKin for Infinite conductivity wells. *SPE Reservoir eng, 2*(02), 222-234. doi:10.2118/13956-pa

Saidikowski, R. M. (1979). Numerical Simulations Of The Combined Effects Of Wellbore Damage And Partial Penetration. *the SPE Annual Technical Conference and Exhibition.* Las Vegas, Nevada: OnePetro. doi:https://doi.org/10.2118/8204-MS

Streltsova-Adams, T. (1979). Pressure drawdown in a well with limited flow entry. *Journal of Petroleum Technology, 31*(11), 1469-1476. doi:10.2118/7486-pa

Vrbik, J. (1986). Calculating The Pseudo-Skin Factor Due To Partial Well Completion. *Journal of Canadian Petroleum Technology, 25*. doi:10.2118/86-05-07

Vrbik, J. (1991). A simple approximation to the pseudoskin factor resulting from restricted entry. *SPE Formation Evaluation, 6*(4), 444-446. doi:10.2118/21469-pa

Yeh, N., & Reynolds, A. (1989). Computation of the Pseudoskin factor caused by a restricted-entry Well completed in a Multilayer Reservoir. *SPE Formation Evaluation, 4*(2), 253-263. doi:10.2118/15793-pa

Yildiz, T. (2006). Assessment of total skin factor in perforated wells. *SPE Reservoir Evaluation & Engineering, 9*(1), 61-76. doi:10.2118/82249-pa

Chapter 7

7. A New evaluation of skin factor in inclined wells with anisotropic permeability

A new evaluation of skin factor in inclined wells with anisotropic permeability

Ekhwaiter Abobaker[1], Abadelhalim Elsanoose[1], Faisal Khan[1], Mohammad Azizur Rahman[2], Amer Aborig[1], Khalid Noah[3]

Corresponding author: Ekhwaiter Abobaker[1]; email: *eera48@mun.ca*

Energies Journal, 2021

Abstract: Oil and gas well productivity can be affected by a number of different skin factors, the combined influences of which contribute to a well's total skin factor. The skin caused by deviated wells is one such well-known factor. The present study aimed to investigate skin effects caused by deviated well slants when considering vertical-to-horizontal permeability anisotropy. The research employed computational fluid dynamics (CFD) software to simulate fluid flows in inclined wells through the injection of water with Darcy flow using 3D geometric formations. The present work investigated the effects of four main characteristics—namely, the permeability anisotropy, wellbore radius, reservoir thickness, and deviation angle—of open-hole inclined wells. Additional investigations sought to verify the effect of the direction of perforations on the skin factor or pressure drop in perforated inclined wells. In the case of an inclined open hole well, the novel correlation produced in the current study simplifies the estimation of the skin

1 Faculty of Engineering and Applied Science, Memorial University of Newfoundland, St. John's, NL, A1C 5S7, Canada
2 Petroleum Engineering, Texas A&M University at Qatar, Doha, 23874, Qatar.
3 Faculty of Engineering, University of Tobruk, Tobruk, Libya.

factor of inclined wells at different inclination angles. Our comparison indicates good agreement between the proposed correlation and available models. Furthermore, the results demonstrated a deviation in the skin factor estimation results for perforated inclined wells in different perforation orientation scenarios; therefore, existing models must be improved in light of this variance. This work contributes to the understanding and simulation of the effects of well inclination on skin factor in the near-wellbore region.

Keywords: skin factor; inclined wells; anisotropic permeability; CFD

7.1 Introduction

To a great extent, a well's geometry may determine its production performance. Common geometrical shapes of wells include inclined, undulating, multi-branched, horizontal, and vertical. Both the increasing complexity of sites as a result of drilling in non-traditional locations and the geological condition of the reservoir increase the overall complexity. To overcome these potential challenges, technology developed for inclined wells is beginning to be used during the extraction stage. The extent to which inclination affects an inclined open-hole well may be quantified using the inclination skin factor. Investigations of transient inclined well solutions show radial flows around the length of the inclined well, which can be applied when determining the effects of combined well deviation and formation damage. In the damaged zones, flow convergence caused by well deviation typically occurs close to the near-wellbore region prior to the entry of the fluid into the damaged zone. Figure 7.1 presents a schematic of flow convergence at a formation-damaged deviated well.

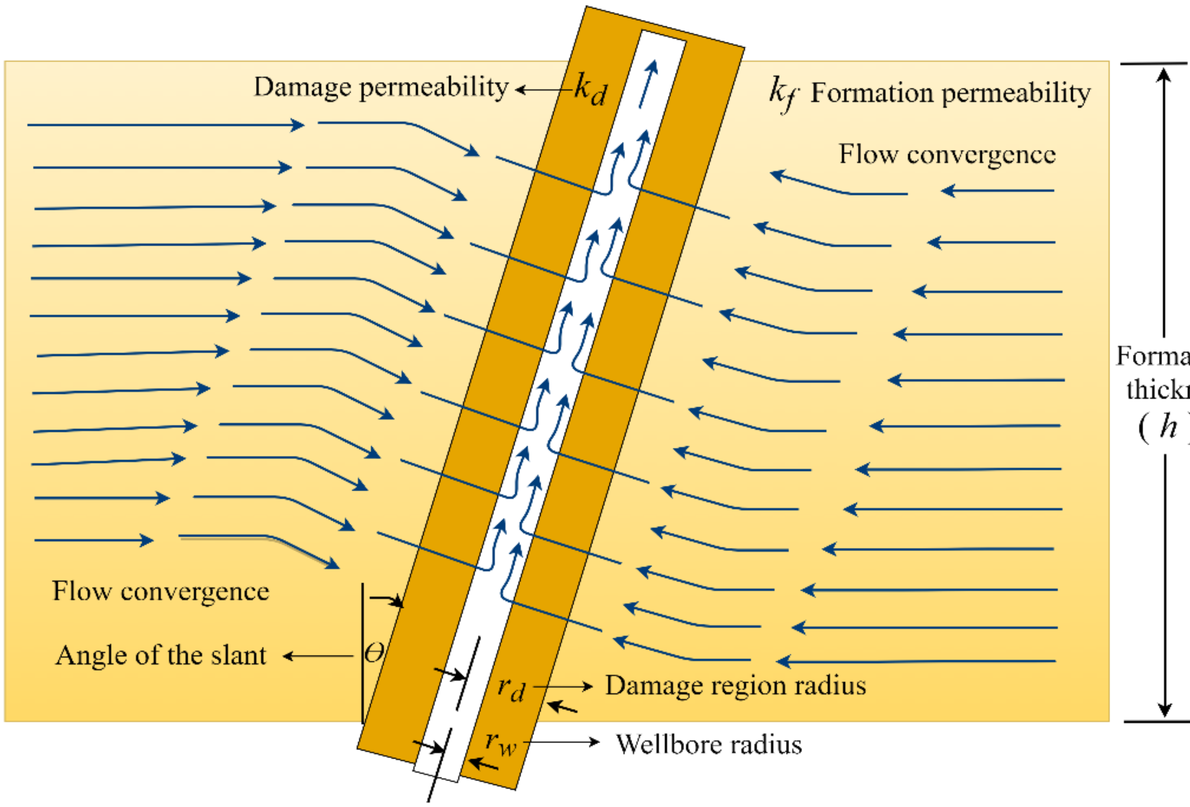

Figure 7. 1: Schematic of inclined open-hole well flow with formation damage.

In the case of completely or partially perforated wells where the flow is located far from a wellbore, fluid typically moves along a radial-like flow in the general direction of the wellbore. This flow type usually occurs in cases of wells designated as partially perforated vertical structures. In such cases, well inclination and perforations have little impact on fluid streamlines. Instead, as the fluid nears the wellbore, the streamlines slowly converge until they are perpendicular in relation to the axis of the wellbore. This results in a pseudo-radial flow that surrounds the inclined wellbore prior to arrival at the perforated well. When the fluid streamlines finally do reach the near-wellbore region, they are redirected due to perforations and formation damage, as shown in Figure 7.2.

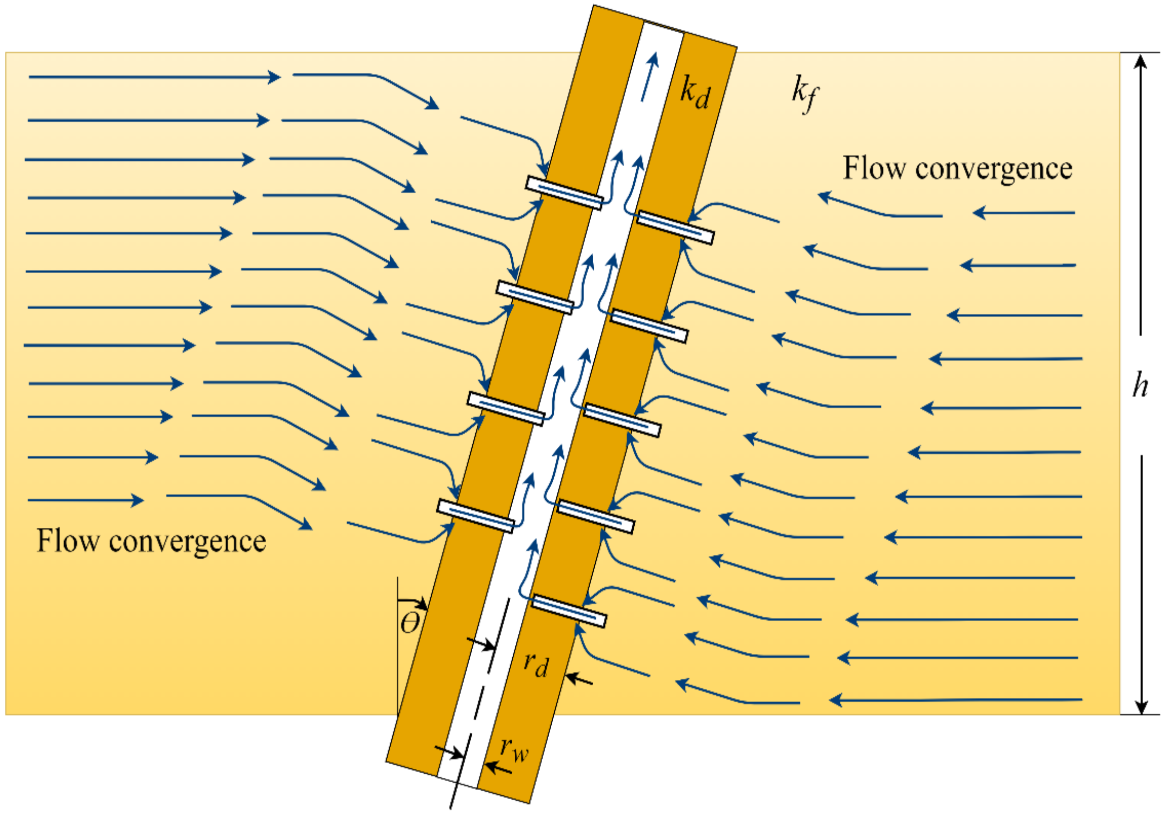

Figure 7.2: Schematic of inclined and completely perforated well with perforations perpendicular to well and formation damage

In inclined wells, the pressure transient behavior needs to be determined with mathematical models. Many models have been developed over the past several decades for the prediction of perforated skin for inclined wells; Cinco et al. (1975) described analytical solutions for inclined wells that take into account pseudo-radial flow periods for relatively large time values. The slant skin equation of Cinco et al. (1975) is commonly applied when estimating how a well's productivity is influenced by inclination. After determining the skin's inclination, the additional pressure change caused by well deviation can be expressed as follows:

$$S_\theta(\dot{\theta}, h_D) = -\left(\frac{\dot{\theta}}{41}\right)^{2.06} - \left(\frac{\dot{\theta}}{56}\right)^{1.865} \times \log\left(\frac{h_D}{100}\right) \tag{7.1}$$

$$h_D = \frac{h}{r_w}\sqrt{\frac{k_h}{k_v}} \tag{7.2}$$

$$\text{For } 0^\circ \leq \theta \leq 75^\circ, \dot{\theta} = tan^{-1}\left(\sqrt{\frac{k_v}{k_h}} \times \tan(\theta)\right) \tag{7.3}$$

Later, (Besson 1990) employed a semi-analytical simulator to determine pressure decline curves in slant horizontal wells located within an isotropic, infinite, and homogeneous formation.

$$S_\theta = ln\left(\frac{4\,r_w}{L}\right) + \frac{h}{L}\ln\left(\frac{\sqrt{Lh}}{4\,r_w}\right) \tag{7.4}$$

This formula can then be changed to accommodate an anisotropic reservoir via spatial transformation (i.e., real medium to isotropic medium) (Besson 1990), as shown in Equation (5) below:

$$S_\theta = \ln\left(\frac{4\,r_w}{L}\,\frac{1}{I_{ani}\,\gamma}\right) + \frac{h}{\gamma L}\ln\left(\frac{\sqrt{Lh}}{4\,r_w}\,\frac{2\,I_{ani}\sqrt{\gamma}}{1+\frac{1}{\gamma}}\right) \tag{7.5}$$

$$\gamma = \sqrt{cos^2\theta + \frac{1}{{I_{ani}}^2}sin^2\theta} \tag{7.6}$$

$$I_{ani} = \sqrt{\frac{k_h}{k_v}} \tag{7.8}$$

Rogers and Economides (1996) later developed a correlation that involved the skin's complete penetration of deviated wells located in anisotropic reservoirs. The researchers employed a semi-analytical productivity index model proposed previously by Besson (1990). The model was intended to be applied in horizontal wells as a means of taking well deviation into account. To measure the effect of anisotropy, Rogers and Economides (1996) applied the transformation used in the experiments of Besson (1990).

$$\text{For } I_{ani} < 1,\ S_\theta = -1.64\,\frac{sin\theta^{1.77}{h_d}^{0.184}}{{I_{ani}}^{0.821}} \tag{7.9}$$

$$\text{For } I_{ani} \geq 1,\ S_\theta = -2.48\,\frac{sin\theta^{5.87}{h_d}^{0.152}}{{I_{ani}}^{0.964}} \tag{7.10}$$

In related works, Yildiz and Ozkan (1998)], Ozkan, Yildiz, and Raghavan, (1999), and Ozkan and Raghavan (2000) investigated rate distribution and transient pressure behavior in perforated and slanted wells. Their applied calculation strategies for these types of wells were shown to boost both computational accuracy and efficiency. Sensitivity studies were also carried out by Suk Kyoon et al. (2008) to determine analytical correlations that could be used to calculate deviated well productivity. The researchers found that the available semi-analytical correlations appeared to be unsuitable when applied to wells that had a deviation angle of 75° or greater. Semi-analytical correlations also did not appear to be suitable in calculations for partially penetrating deviated wells. Additionally, they reviewed several different analytical solutions for the inflow performance relationship (IPR) and productivity index (PI). Their extensive review of the literature was augmented with case studies that compared correlations in similar categories as a means of building selection guidelines. Numerous empirical and theoretical models and correlations of variable reservoir parameters have been devised since Darcy's law was first proposed in 1856. These parameters include elements such as area, reservoir shape, time independence, well trajectory, and fluid phases.

In recent studies conducted by Wang et al. (2012), a highly deviated well inflow model for an anisotropic reservoir was tested. Their results indicated that an increase in the anisotropy index effectively boosted the deviation angle effect on well productivity. In the same year, Ghahri and Jamiolahmady (2012) conducted a sensitivity study that reviewed skin values from the work of Rogers and Economides (1996). They proposed that these values had been underestimated by the researchers and thus differed significantly in comparison to those produced by the models of Cinco et al. (1975) and Besson (1990) when applying the same or similar transformation models in isotropic media.

In a subsequent study, Feng and Liu (2014) developed a mathematical model for testing inclined wells that featured impermeable faults using point source theory. Recently, Dong et al. (2018) proposed a model for the skin factor of wells that were directionally drilled and partially penetrated in anisotropic reservoirs. Their aim was to simulate how slants were affected by flow and drilling. There are several drawbacks and limitations in the current models. For example, one limitation of the current models concerns perforation orientation with regard to top and bottom reservoir boundaries. In this situation, the perforations and bedding planes must be parallel. For perforated inclined wells, however, perforations typically deviate from the horizontal plane at angle θ. In fact, some completion designs, such as the one presented in Figure 7.3, show perforations of inclined wells being forced into an orientation parallel to the bedding plane.

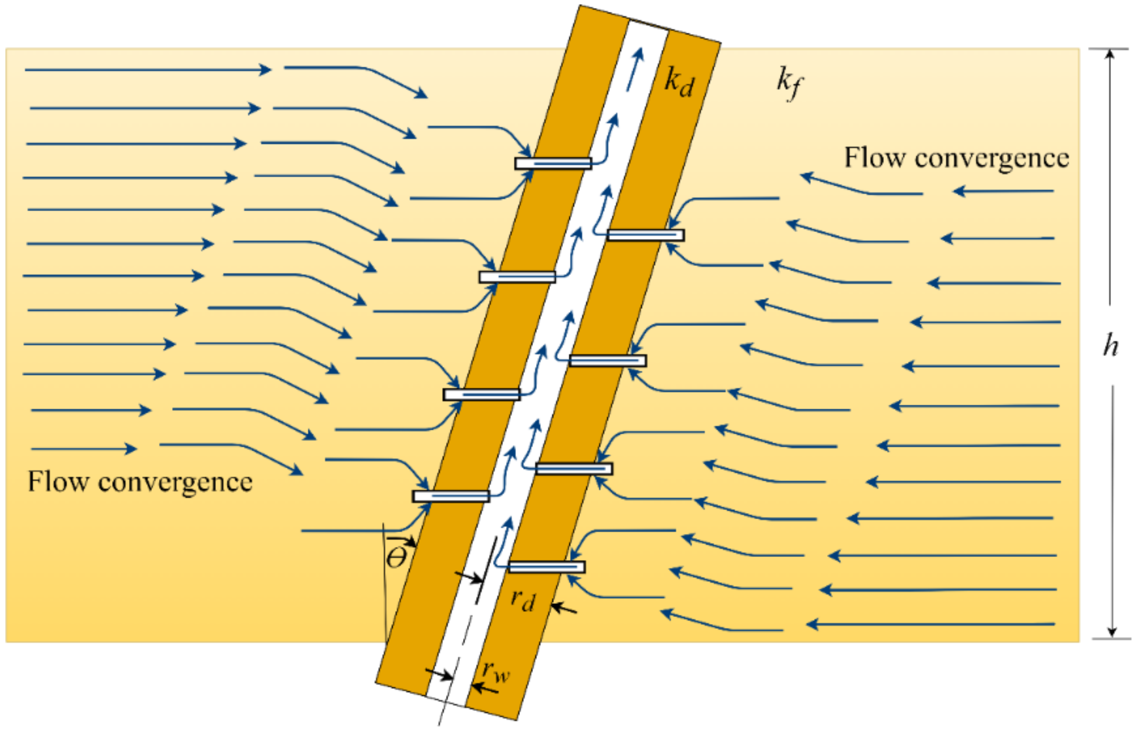

Figure 7.3: Schematic of inclined and completely perforated well with perforations parallel to radial flow direction and formation damage.

Earlier techniques to predict the skin factor remain relatively impractical from an applicability perspective when considered for use in different reservoir types. This lack of practical applicability is caused by issues pertaining to computational accuracy and geometrical effects. More specifically, these aspects have persistently lacked sufficient accuracy and/or need to be processed through an elaborate transient numerical simulator. Accordingly, the primary aim of the present work is to present a numerical model that can simulate the real conditions of fluid flows in inclined wells. In order to compare and discuss the accuracy of the proposed model, the analytical model of Cinco et al. (1975) and the Besson (1990) anisotropic formulations were utilized as a basis for the comparison of numerical simulations of slant skin. This was accomplished by determining the differences between cases of vertical open-hole and inclined-well pressure drops.

7.2 Methodology

This study is an extension of the work of Abobaker et al. (2021A, 2021B), which conducts the two main investigative procedures of numerical and statistical analysis for more accurate estimation of the skin factor of inclined wells with anisotropic permeability. Abobaker et al. (2021A, 2021B) used the experimental schemes (Ahammad et al., 2018, 2019a) as a radial flow cell (RFC). Their experiments carried out on fluid flows through the perforation samples primarily relied on rather simplistic assumptions, such as those presented by Rahman et al. (2006, 2007a, 2007b, 2008, and 2016). The results of numerical model used in this study were validated with the experimental data of studies' Abobaker et al. (2021A, 2021B). In this study, statistical analysis was coupled with numerical simulation to expand the investigation of fluid flow in the near-wellbore region by producing data that cannot be obtained experimentally due to limitations in the experimental setup and, especially, the small sample size.

7.2.1 Numerical simulation procedure

ANSYS (ANSYS Inc., PA, USA) fluent (3D) 18.1 was used for numerical simulations of fluid flow through a near-wellbore region. The cylindrical geometry—including permeability anisotropy, wellbore radius, reservoir thickness, and deviation angle—were used to represent near-wellbore conditions in inclined wells. The single phase (water) was injected radially through the cylindrical near-wellbore region. In the case of an open-hole well, the inlet was specified as the outer formation zone surface, and the outlet was specified as the interior surface of the wellbore, as exhibited in Figure 7.4. The pressure at the outlet was set as equal to atmospheric pressure.

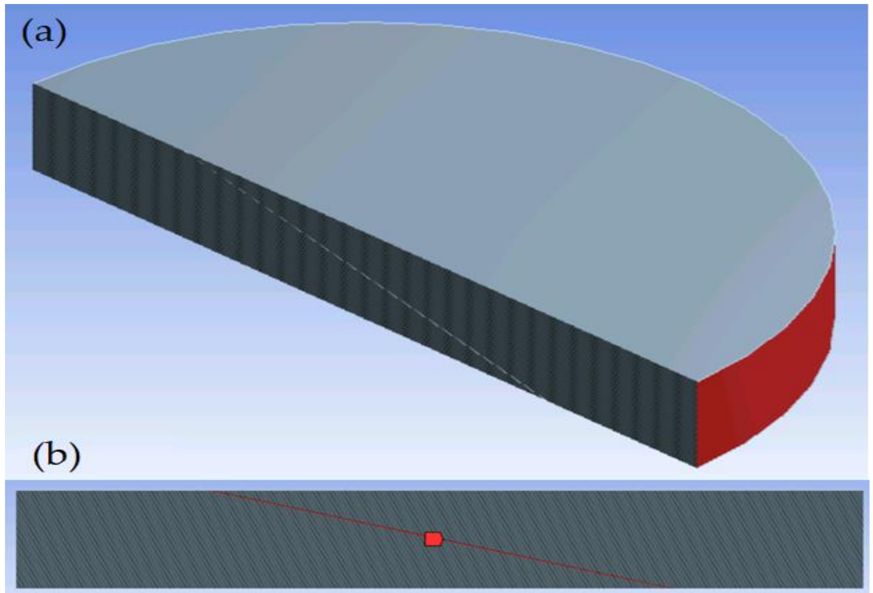

Figure 7.4. Vertical section for inlet (**a**) and outlet (**b**).

In the case of inclined wells with completely or partially perforated completions, two scenarios were suggested to verify the effect of perforation direction on the skin factor or pressure drop in inclined wells, as shown in Figure 7.5. In the first scenario, the direction of perforations was perpendicular to the wellbore with a perforation angle of 180° in the direction of the well inclination. In the second, the direction of perforations was parallel to radial flow direction with the same perforation angle. The effect of increasing the three factors (perforation depth L_p, perforation diameter r_p, and penetration space n_p) on the skin factor was analyzed, as shown in Table 7.1.

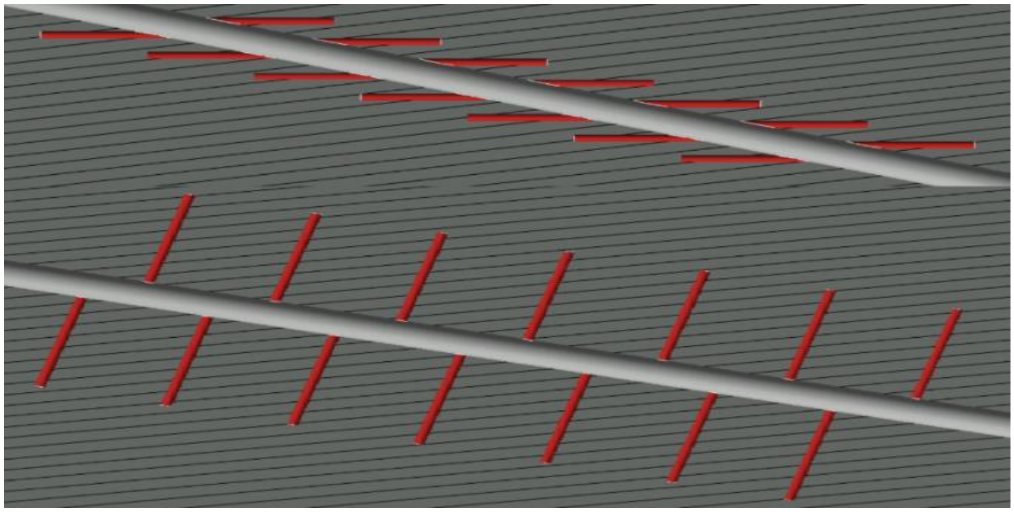

Figure 7.5: Schematic of inclined and completely perforated well with perforations parallel or perpendicular to well and formation damage.

The uniform mesh and cut mesh methods were used to generate high quality mesh, as shown in Figure 7.6. This configuration contributed to the production of a high mesh density to capture the significant pressure gradients in the border regions.

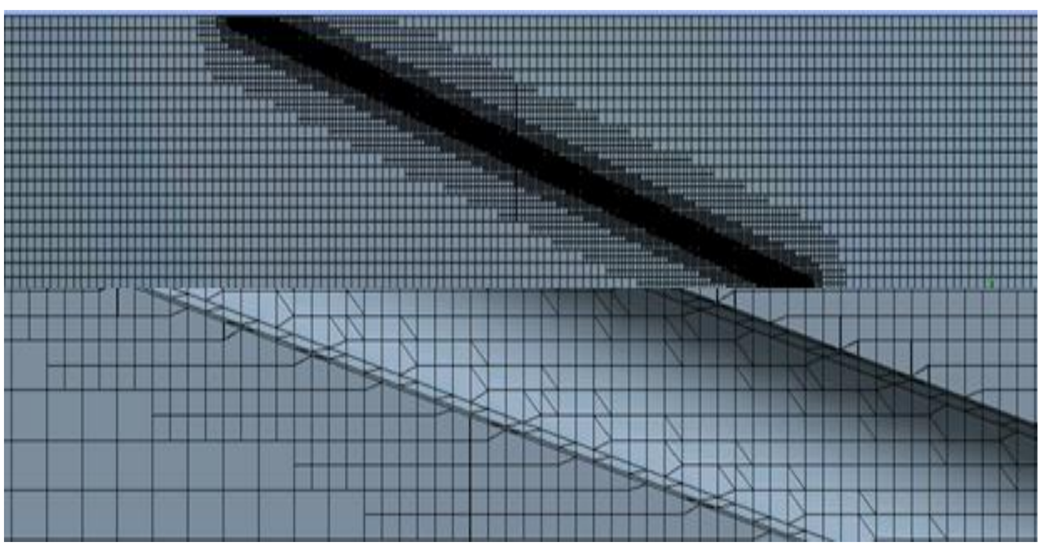

Figure 7.6: The shape of the uniform configuration mesh used in CFD simulations.

Table 7.1. Dimensions and properties of the vertical near-wellbore region and the ranges of three investigated parameters.

Dimensions and Properties of the Sample	Values (Units)
Reservoir or pay zone thickness (h)	2.66 m
Reservoir radius (r_e)	10 m
Formation permeability (k_f)	10^{-14} m^2
Porosity ($\emptyset$)	20%
Flow rate (Q)	2 L/min
Viscosity of water (μ)	0.00103 kg/(m·s)
Perforation depth (L_p)	30.48–91.44 cm
Perforation diameter (r_p)	1–2.5 cm
Penetration space (n_p)	1–5 perforations/30.48 cm

7.2.2 Statistical procedure

Various strategies for investigating how several parameters or variables may affect experimental data were applied by utilizing the design of experiments (DoE) software. The first step in DoE is the determination of independent parameters and/or variables that may affect the experimental results. The second step includes determining the dependent variables (Davim, 2016). The experiments generally run based on different parameter values, such that each run presents a combination associated with the specific variable value(s) being investigated. In this study, we used DoE with Box–Behnken design (BBD) to design the runs required for statistical analysis. The BBD, described as a design of response surface methodology, needs only three levels of parameters and/or variables in its experimental runs (Box & Cox, 1964). Then, the analysis of variance (ANOVA) was used to validate the proposed model statistically (Box & Behnken, 1960; Ferreira, et al., 2007). The three dimensionless parameters investigated included the ratio of reservoir thickness to wellbore radius, the permeability ratio, and the ratio of the well inclination angle to the maximum inclination angle ($\theta_m = 75^o$).

$$h_d = \frac{h}{r_w} \tag{7.11}$$

$$k_r = \frac{k_h}{k_v} \tag{7.12}$$

$$\theta_d = \frac{\theta}{\theta_m} \tag{7.13}$$

The ranges of the three dimensionless parameters for the inclined near-wellbore region are presented in Table 7.2.

Table 7.2. The ranges of the three dimensionless parameters.

Dimensions and Properties of the Sample	Values (Units)
Ratio of reservoir thickness to wellbore radius (h_d)	80–540
Range of permeability ratio (k_r)	1–10
Range angle of the slant (θ)	10°–75°

The flow rate for vertical wells in cylindrical near-wellbore regions with anisotropy permeability and Darcy flow perpendicular to the wellbore is expressed as:

$$Q = \frac{2\pi k_f h(p_e - p_{wf})}{\mu\left[ln\left(\frac{r_e}{r_w}\right) + S_\theta\right]} \tag{7.14}$$

The skin factor can be obtained after the pressure drop is calculated from the simulation using:

$$s_\theta = \frac{2\pi k_f h(p_e - p_{wf})}{Q\mu} - \ln\left(\frac{r_e}{r_w}\right) \tag{7.15}$$

7.3 Results and discussion

For the present work, a three-dimensional simulation model was built to investigate Darcy flow conditions for single-phase flow in a deviated well. The simulation results generated an extensive pressure gradient data bank covering the near-wellbore region, including variations for relevant parameters. The skin effect was quantified here by taking into account vertical-to-horizontal permeability anisotropy in the deviated wells. The results of numerical investigations showed that CFD simulation was able to predict the effect of an inclined well on the pressure gradient in the near-wellbore region, as shown in Figure 7.7. Based on these outcomes, our numerical model presents a streamlined method that significantly outperforms the requirements of 3D simulation as used in previously developed simulations. In fact, the simulation results agree with the actual flow performance by utilizing the skin effect applied to inclined wells.

Geometric skin essentially determines how geometry affects flow in a deviated wellbore. In Equation (7.14), the skin is utilized to determine the equivalent open-hole productivity and shows a flow rate that is nearly the same as that of the deviated wells. To construct the formula, a data bank was generated that includes geometrical parameter variations such as reservoir thickness, wellbore radius, deviation angle, formation properties, and anisotropy. A deviated well's flow regime can be divided into two regions to provide a deeper perspective. In such a division, one region represents the flow regime near the deviated well and is primarily affected by geometrical parameters. The other region is only slightly affected by geometrical parameters as the flow regime proceeds in a mostly radial pattern.

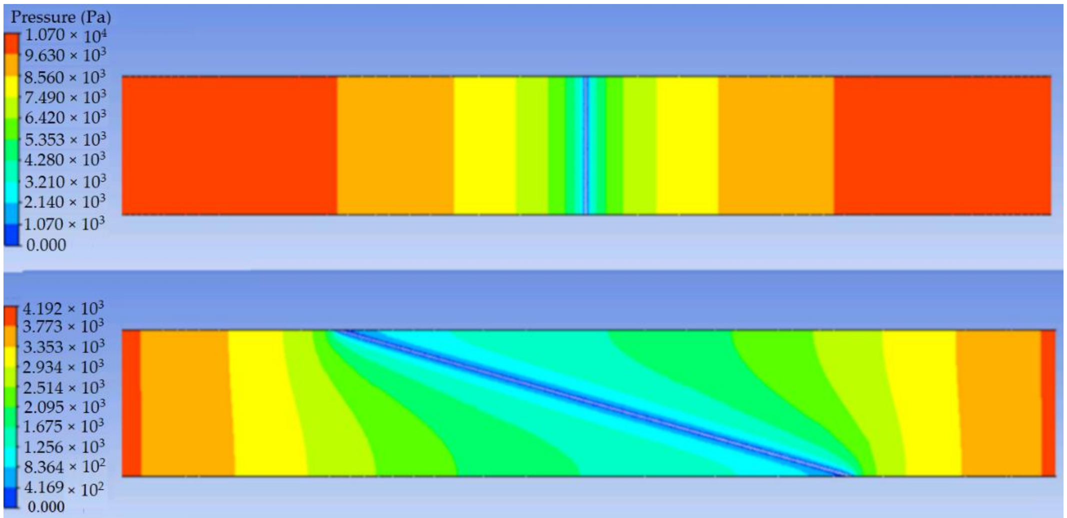

Figure 7.7: Numerical results of the pressure gradient through the near-wellbore region for vertical angle 90° and inclination angle 75° with two dimensionless parameters (h_d = 108.267, k_r = 1) and flow rate (Q = 2 l/min).

Twelve numerical runs were performed to obtain a statistical model deemed suitable via ANOVA analysis with the BBD model; the results of skin factor values for twelve numerical runs are shown in Table 7.3.

Table 7.3. Twelve numerical runs and the results of skin factor.

Runs	h_d	θ_d	k_r	S_θ
1	180	0.566665	10	−0.35
2	180	0.13333	5.5	−0.0010
3	180	1	5.5	−2.9
4	360	0.13333	10	−0.02
5	180	0.566665	1	−1.32
6	360	0.13333	1	−0.1
7	360	1	1	−4.2
8	360	1	10	−2.22
9	540	1	5.5	–3.1
10	540	0.566665	10	−0.41
11	540	0.13333	5.5	−0.06
12	540	0.566665	1	−1.8

The main assumption of the DoE model was the normal distribution of numerical data with a constant variance of features. Inspection of the normal plot of residuals in Figure 7.8 emphasizes the significant correlation between a normal distribution and the obtained data. Additionally, our results demonstrate that the predicted values derived from the statistical model share strong similarities with the actual values derived numerically.

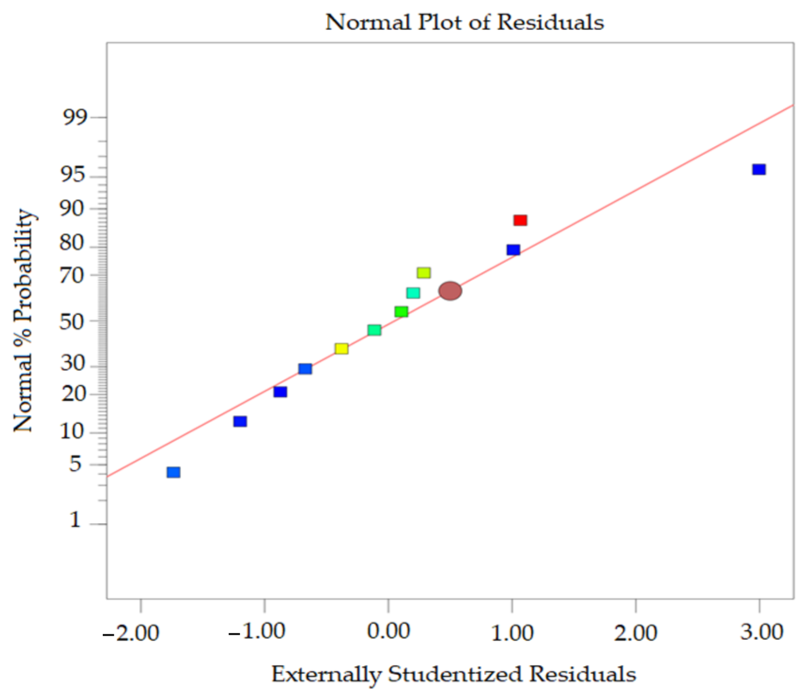

Figure 7.8: Normal plot of residuals.

The results reveal the interaction effect among the three dimensionless parameters (h_d, θ_d, and k_r). The two dimensionless parameters (the ratio of the angle of the slant to the maximum inclination angle and the permeability ratio) demonstrated a significant effect on the skin factor. The angle of the slant has significant effect on the reduction in pressure drop in the near-wellbore region due to the increase in the contact area between the well and the reservoir resulting from the increase in the angle of inclination, as exhibited in Figure 7.9. Additionally, anisotropy is a crucial parameter affecting deviated well productivity; the ratio of horizontal permeability to vertical permeability has a great effect on the skin factor with regard to the well productivity, by increasing the resistance of flow convergence and decreasing the performance of deviated wells, as exhibited in Figure 7.10. The study findings indicate that any reduction in vertical-to-horizontal permeability subsequently reduces deviated well performance. As a vector, permeability depends heavily on its measured direction and typically shows high levels of anisotropy. The index of anisotropy is critically important, and the calculated skin effects appear to differ significantly from calculations in the literature that were based on the assumption of complete isotropy. Hence, most common assumptions pertaining to permeability isotropy are unfounded.

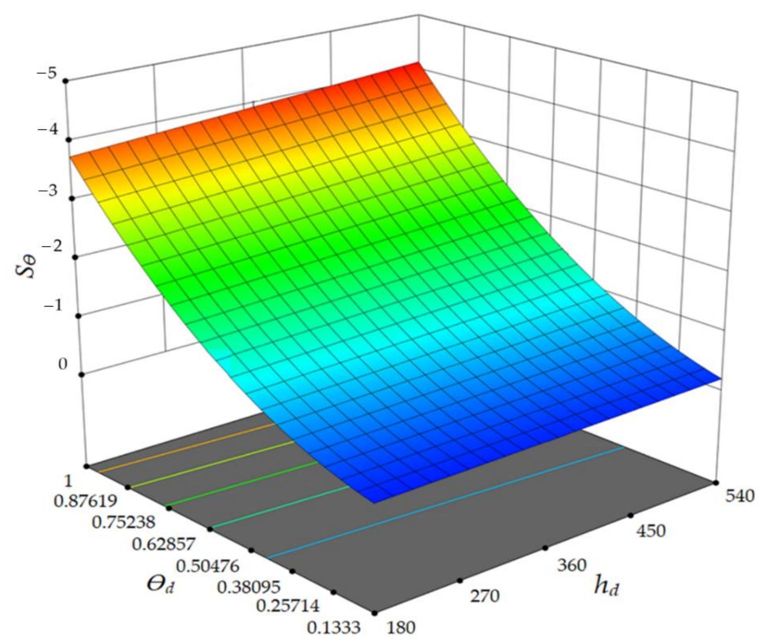

Figure 7.9: Effect of interaction between the two dimensionless parameters Θ_d and h_d on skin factor with constant value for the third dimensionless parameter ($k_r = 1$).

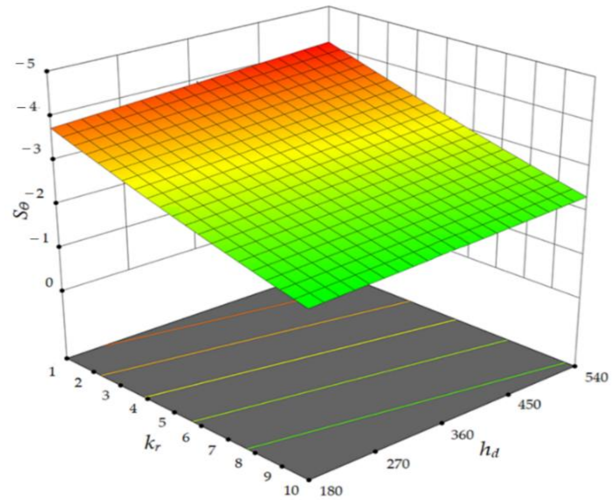

Figure 7.10: Effect of interaction between the dimensionless parameters h_d and k_r on skin factor with constant value for the third dimensionless parameter ($\theta_d = 1$).

The strategy applied in this study can be used to estimate the productivity of deviated wells and to optimize the angle and length of wells. Such optimization can be performed with a simple correlation alone, making it practical for application to a variety of purposes. Therefore, this study provides a correlation from the statistical analysis based on numerical results. This correlation utilized to determine the effect of the ratio of reservoir thickness to wellbore radius, and inclination angle on the skin factor value, taking the anisotropy into account, is as follows:

$$S_\theta = -(0.1 + 0.00025 * h_d + 1.852 * \theta_d - 0.056 * k_r)^2 \tag{7.16}$$

The proposed correlation can be applied in deviation angles between 10° and 75°. The resulting formula is highly efficient compared with those presented in the recent literature. A comparison between the current correlation and the slant skin models of Cinco et al. (1975) and Besson (1990) provides results for skin factors of highly deviated wells that produce at a constant flow rate. In the comparison, the effects of increasing the deviation angle and permeability ratio were investigated by assuming the impermeable top and bottom boundaries of the reservoir and the ratio of reservoir thickness to wellbore radius ($h_d = 180$). The comparison results indicate that, under conditions of weak anisotropy, the impact of the deviation angle on inflow performance is moderate. However, as anisotropy increases, the impact of the deviation angle increases. The comparison results demonstrate good agreement between the proposed correlation and the slant skin model results of Cinco et al. (1975) and Besson (1990), as shown in Figures 7.11 and 7.12. The results of the numerical model used in this study were validated with the experimental data, giving the advantage of new correlation compared to old correlations and providing a new option to calculate the inclined skin factor. Additionally, the accuracy of the results of the proposed correlation was verified in numerous cases under constant flow conditions via comparison with available models. Overall, this approach presents a highly efficient method for the quantification of the skin factor of deviated wells.

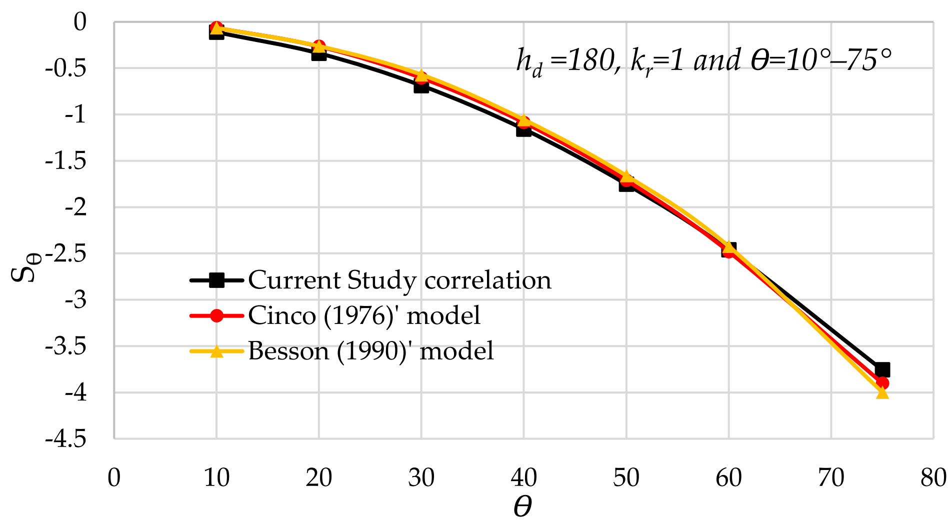

Figure 7.11: Comparison between the current correlation and the slant skin model results of Cinco et al. (1975) and Besson (1990) for increasing the angle of the slant (10°–75°).

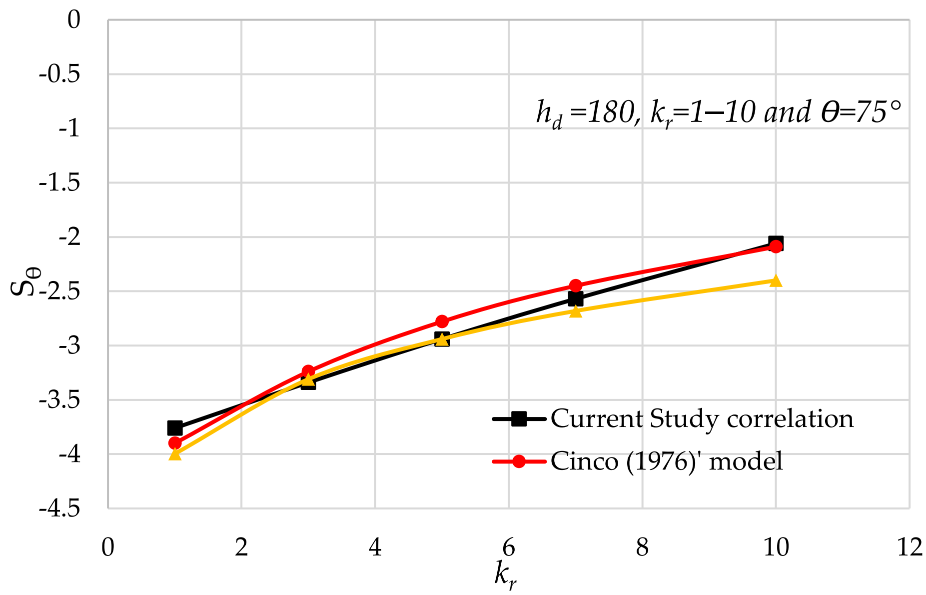

Figure 7.12: Comparison between the current correlation and the slant skin model results of Cinco et al. (1975) and Besson (1990) for increasing permeability ratio (1–10).

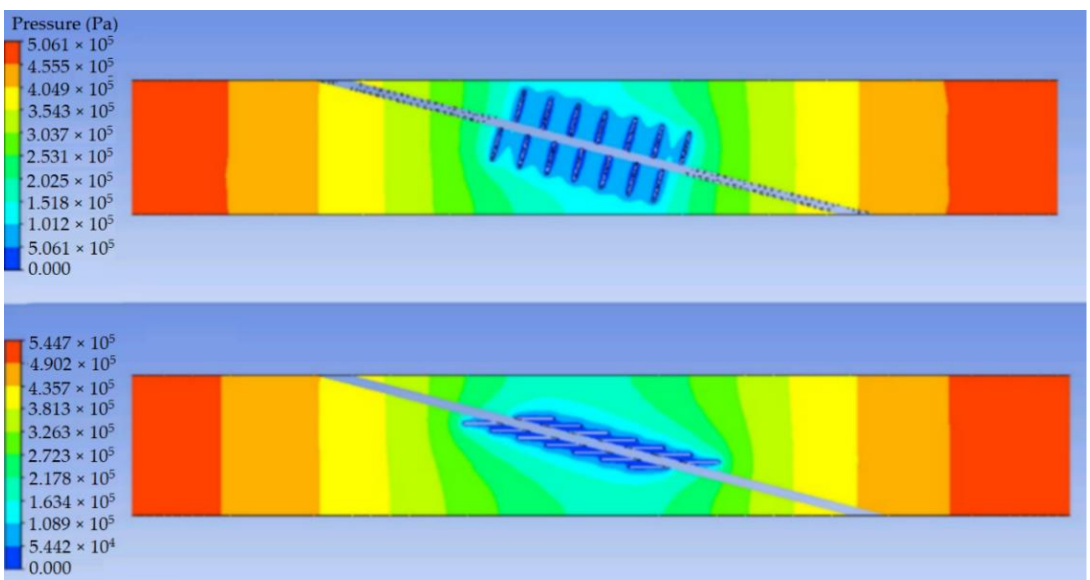

Figure 7.13: Numerical results for the pressure gradient through the near-wellbore region for two scenarios with maximum inclination angle 75°, Q = 2 l/min, L_p = 60.96 cm, and n_p = 1 perforation/30.48 cm).

In inclined perforated well cases, when the direction of perforations is perpendicular to the wellbore or parallel to the radial flow direction, the results of numerical investigations reveal different pressure gradients for these two scenarios in the near-wellbore region, as shown in Figure 7.13. The results demonstrate the difference in skin factor (S_D) or pressure gradient that result from the different directions of perforations in relation to the wellbore. This contrast increases with an increase in the depth and diameter of the perforations and penetration space to reach a maximum value at critical values of the three parameters (L_p = 60.96 cm, r_p = 2 cm, and n_p = 4 perforations/30.48 cm), after which it begins to decrease, as shown in Figures 7.14–7.16. Simultaneously, the increase in flow rate during the Darcy flow range does not show any effect on the variance in skin factor. The variance between the two scenarios results from an increase in the cross-area in the radial flow direction combined with a decrease in the flow convergence effect in the first scenario. Meanwhile, the perforation tips are subject to radial flow with increasing flow convergence in the second. This difference in the computation of pressure drop and the calculation of the skin factor depends on a complex interaction between several factors, including the depth and diameter of perforation, penetration space, perforation angle, and the inclination of the well. In this study, the variance between the two scenarios, including the effects of the indicated parameters, was investigated in the case of perforation direction at the same inclination as the well angle with a perforation angle of 180°. The interaction effect of other perforation angles with different configurations on the skin factor warrants further investigation.

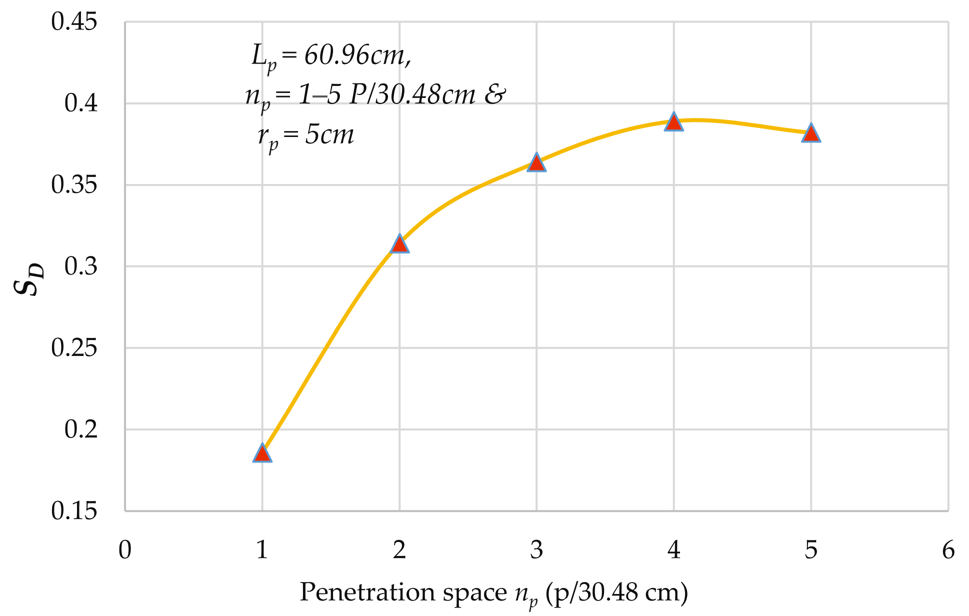

Figure 7.14: Difference in skin factor values for two perforation orientations with increasing penetration space n_p (1–5 perforations/30.48 cm).

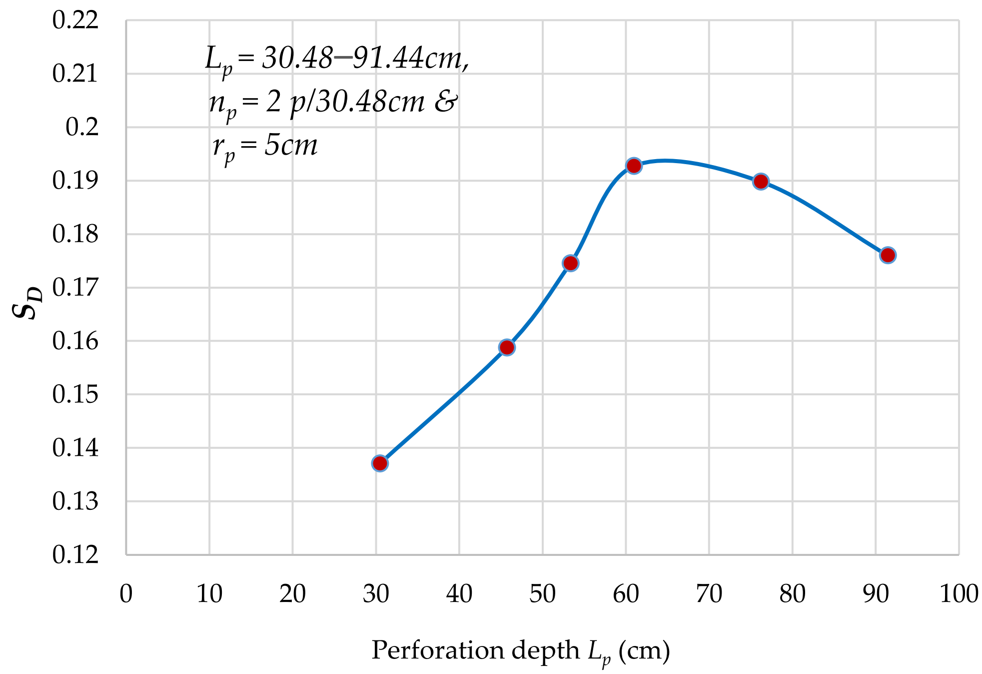

Figure 7.15: Difference in skin factor values for two perforation orientations with increasing perforation depth L_p (30.48–91.44 cm).

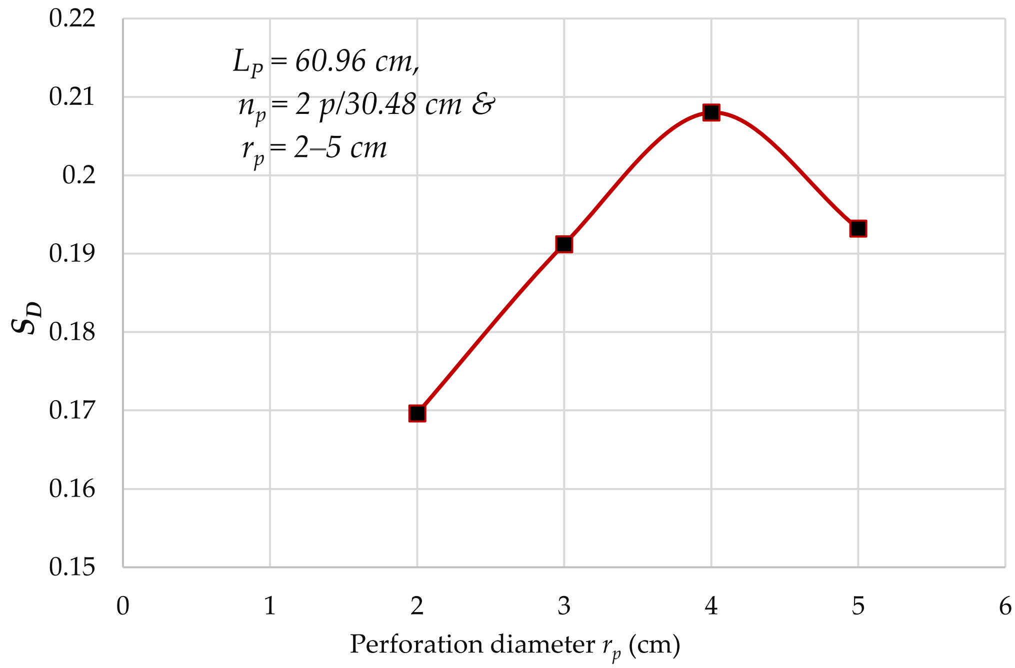

Figure 7.16: Difference in skin factor values of two perforation orientations with increasing perforation diameter r_p (2–5 cm).

7.4 Conclusions

This work was conducted in order to expand the knowledge regarding the effect of inclined wells on the skin factor and pressure gradient in a near-wellbore region. Based on numerical investigations, the following conclusions can be drawn:

1. Numerical investigations clearly indicated the effect of three dimensionless parameters (h_d, Θ_d, and k_r) on the skin factor due to inclination in the vertical wells. The results demonstrate that the ratio of inclination angle to the maximum inclination angle (75°) and the permeability ratio significantly affect the skin factor and pressure drop in the near-wellbore region. In contrast, the ratio of reservoir thickness to wellbore radius ($\mathrm{h_d}$) has a more negligible effect.

2. In the case of an inclined open hole well, the novel correlation presented in the current study simplifies the estimation of the skin factor of inclined wells at different inclination angles. Compared with other approaches, the novel correlation performs well by providing estimates of the skin factor that are relatively close to those of previous models.
3. In the case of an inclined perforated well, the results demonstrate the variance in skin factor and pressure gradient that result from the direction of perforations in relation to the wellbore:
    a. This difference in the computation of pressure drop and the calculation of the skin factor depends on the complex interaction between several factors, including depth and diameter of perforation, penetration space, perforation angle, and the inclination of the well.
    b. The difference between the results for the two scenarios indicates that currently available models for evaluating the skin factor of inclined perforated wells need to be improved in light of this variance.

References

Abobaker, E., Elsanoose, A., Khan, F., Rahman, M. A., Aborig, A., & Butt, S. (2021B). Comparison of crushed-zone skin factor for cased and perforated wells calculated with and without including a Tip-Crushed Zone effect. *Geofluids, 2021*, 1-13. doi:10.1155/2021/3689964

Abobaker, E., Elsanoose, A., Khan, F., Rahman, M., Aborig, A., & Noah, K. (2021(A)). Quantifying the partial penetration skin factor for evaluating the completion efficiency of vertical oil wells. *Journal of Petroleum Exploration and Production Technology, 11*(7), 3031-3043. doi:10.1007/s13202-021-01229-8

Ahammad, M. J., Rahman, M. A., Butt, S. D., & Alam, J. M. (2019a). An experimental development to characterise the flow phenomena at the near-wellbore region. *ASME 2019 38th International Conference on Ocean, Offshore and Arctic Engineering.* Glasgow, Scotland, UK: Volume 8: Polar and Arctic Sciences and Technology; Petroleum Technology.

Ahammad, M., Rahman, M., Zheng, L., Alam, J., & Butt, S. (2018). Numerical investigation of Two-phase fluid flow in a perforation tunnel. *Journal of Natural Gas Science and Engineering, 55*, 606-611.

Besson, J. (1990). Performance of slanted and horizontal wells on an anisotropic medium. *the European Petroleum Conference.* Hague, Netherlands: OnePetro. doi:https://doi.org/10.2118/20965-MS

Box, G. E., & Behnken, D. W. (1960). Some new three level designs for the study of quantitative variables. *Technometrics, 2*(4), 455-475.

Box, G. E., & Cox, D. R. (1964). An analysis of transformations. *Journal of the Royal Statistical Society: Series B (Methodological), 26*(2), 211-243.

Cinco, H., Miller, F., & Ramey, H. (1975). Unsteady-state pressure distribution created by a directionally drilled well. *27*(11), 1392-1400. doi:10.2118/5131-pa

Darcy, H. (1956). Les Fontaines Publiques de la Ville de Dijon: Exposition et Application des Principes a Suivre et des Formulesa Employer dans les Questions de Distribution d'Eau.

Davim, j. P. (2016). *Design of experiments in production engineering.* Cham: Springer.

Dong, W., Wang, X., & Wang, J. (2018). A new skin factor model for partially penetrated directionally-drilled wells in anisotropic reservoirs. *Journal of Petroleum Science and Engineering, 161*, 334-348. doi:10.1016/j.petrol.2017.11.062

Feng, G.-q., & Liu, Q.-g. (2014). Pressure transient behavior of a slanted well with an impermeable fault. *Journal of Hydrodynamics, 26*(6), 980-985.

Ferreira, S., Bruns, R., Ferreira, H., Matos, G., David, J., Brandão, G., dos Santos, W. (2007). Box-Behnken design: An alternative for the optimization of analytical methods. *Analytica Chimica Acta, 597*(2), 179-186.

Ghahri, P., & Jamiolahmady, M. (2012). A new, accurate and simple model for calculation of productivity of deviated and highly deviated well – part i: Single-phase incompressible and compressible fluid. *Fuel, 97*, 24-37. doi:10.1016/j.fuel.2012.03.030

Ozkan, E., & Raghavan, R. (2000). A computationally efficient, transient-pressure solution for inclined wells. *SPE Reservoir Evaluation & Engineering, 3*(05), 414-425. doi:10.2118/66206-pa

Ozkan, E., Yildiz, T., & Raghavan, R. (1999). Pressure-Transient analysis of Perforated slant and horizontal wells. *the SPE Annual Technical Conference and Exhibition.* Houston, Texas: Oneoetro. doi:10.2118/56421-ms

Rahman, M. A. (2008). Scale-up of perforation process from laboratory model to bottom hole dimensions. *Journal of Porous Media*, *11*(1), 19-34.

Rahman, M. A., Heidrick, T., Fleck, B., & Koksal, M. (2006). Enhancement of the completion efficiency of perforation tunnels in petroleum wells. *ASME 2006 2nd Joint U.S.-European Fluids Engineering Summer Meeting Collocated With the 14th International Conference on Nuclear Engineering.* Miami, Florida, USA.

Rahman, M., Mustafiz, S., Biazar, J., Koksal, M., & Islam, M. (2007a). Investigation of a novel perforation technique in petroleum wells—perforation by drilling. *Journal of the Franklin Institute*, *344*(5), 777-789.

Rahman, M., Mustafiz, S., Koksal, M., & Islam, M. (2007). Quantifying the skin factor for estimating the completion efficiency of perforation tunnels in petroleum wells. *Journal of Petroleum Science and Engineering*, *58*(1-2), 99-110.

Rogers, E. J., & Economides, M. J. (1996). The skin due to slant of deviated wells in Permeability-Anisotropic reservoirs. *the International Conference on Horizontal Well Technology.* Calgary, Alberta, Canada: Openpetro. doi:10.2118/37068-ms

Suk Kyoon, C., Ouyang, L.-B., & Huang, W. B. (2008). A comprehensive comparative study on analytical pi/ipr correlations. *the SPE Annual Technical Conference and Exhibition.* Denver, Colorado, USA: OnePetro. doi:10.2118/116580-ms

Wang, H., Xue, S., Gao, C., & Tong, X. (2012). Inflow performance for highly deviated wells in anisotropic reservoirs. *Petroleum Exploration and Development, 39*(2), 239-244.

Yildiz, T., & Ozkan, E. (1998). Pressure-transient analysis for perforated wells. *the SPE Annual Technical Conference and Exhibition.* New Orleans, Louisiana: Openpetro. doi:10.2118/49138-ms

Zheng, L., Rahman, M. A., Ahammad, M. J., Butt, S. D., & Alam, J. M. (2016). Experimental and numerical investigation of a novel technique for perforation in petroleum reservoir. *the SPE International Conference and Exhibition on Formation Damage Control*. Lafayette, Louisiana, USA.

Chapter 8

8. Experimental, numerical, and statistical investigation of two-phase flow in a cylindrical perforation tunnel

Experimental, numerical, and statistical investigation of two-phase flow in a cylindrical perforation tunnel

Ekhwaiter Abobaker[1], Abadelhalim Elsanoose[1], Faisal Khan[1], Mohammad Azizur Rahman[2], Amer Aborig[1], Stephen Butt[1]

Corresponding author: Ekhwaiter Abobaker[1]; email: *eera48@mun.ca*

40th International Conference on Ocean, Offshore and Arctic Engineering

OMAE2021

Abstract: Perforation is the final stage in well completion that helps to connect reservoir formations to wellbores during hydrocarbon production. The drilling perforation technique maximizes the reservoir productivity index by minimizing damage. This can be best accomplished by attaining a better understanding of fluid flows that occur in the near-wellbore region during oil and gas operations. The present work aims to enhance oil recovery by modelling a two-phase flow through the near-wellbore region, thereby expanding industry knowledge about well performance. An experimental procedure was conducted to investigate the behaviour of two-phase flow through a cylindrical perforation tunnel. Statistical analysis was coupled with numerical simulation to expand the investigation of fluid flow in the near-wellbore region that cannot be obtained

[1] Faculty of Engineering and Applied Science, Memorial University of Newfoundland, St. John's, NL, A1C 5S7, Canada

[2] Petroleum Engineering, Texas A&M University at Qatar, Doha, 23874, Qatar.

experimentally. The statistical analysis investigated the effect of several parameters, including the liquid and gas flow rate, liquid viscosity, permeability, and porosity, on the injection build-up pressure and the time needed to reach a steady-state flow condition. Design-Expert® Design of Experiments (DoE) software was used to determine the numerical simulation runs using the ANOVA analysis with a Box-Behnken Design (BBD) model. ANSYS-FLUENT was used to analyses the numerical simulation of the porous media tunnel by applying the volume of fluid method (VOF). The numerical results were validated with the experimental data and the comparison of results was in good agreement. The numerical and statistical analysis demonstrated each investigated parameter's effect. The permeability, flow rate, and viscosity of the liquid significantly affect the injection pressure build-up profile, and porosity and gas flow rate substantially affect the time required to attain steady-state conditions. In addition, two correlations obtained from the statistical analysis can be used to predict the injection build-up pressure and the required time to reach steady state for different scenarios. This work will contribute to the clarification and understanding of the behaviour of multiphase flow in the near-wellbore region.

Key Words: Experimental, numerical, statistical, two-phase flows, perforation tunnel.

8.1. Introduction

An emerging trend in the hydrocarbon industry is to boost production rates at wells instead of exploring for new ones, as new wells are becoming scarcer. The majority of formation damage occur during one or more of the perforation procedures, so the present work focuses on optimizing the productivity index and the life of the well through cylindrical perforation tunnel. Using pressure build-up tests, the performance of the perforation technique can be measured. Pressure drop can take a number of forms, namely friction, gravity, mixing and acceleration. Studies on horizontal well pressure drop have thus far mainly focused on acceleration and friction pressure drop in variable mass flows of horizontal wellbores (Stone et al., 1989; Novy, 1995; Landman & Goldthorpe, 1991; Marett & Landman, 1993; Ozkan et al., 1995; Sarica et al., 1994; Suzuki, 1997) without considering how radial inflow affects wellbore flow. In 1993, Su and Gudmundsson investigated how friction changes variable mass flow through perforated pipelines. Their study looked at injection as well as non-injection conditions, using water for their fluid medium. Su et al. (1993, 94) found that horizontal wellbore pressure drop could be divided into four components: mixed, acceleration, wall friction, and perforation roughness. Using these categories, the researchers first calculated the empirical formula for mixed pressure drop and then determined the other three based on experimental data. Around the same time, Ihara et al. (1992, 1994 and 1995) carried out simulation experiments using liquid-gas two-phase flow through horizontal wellbores. The flow simulations were created using injections along various points of the wellbore test area. The original simulation model used for low liquid-gas injection ratios was adjusted to take into account how fluid injection impacts pressure drop. The new model, however, was relatively inaccurate under high injection ratios.

Yuan et al. (1998 and 1999) subsequently carried out simulations on single-phase single-hole injections using water as the fluid medium. The researchers formulated pressure loss caused by hole injections using an integrated resistance factor. The factor represented hole injections, acceleration pressure drop, wall friction, among others.

Additionally, the researchers performed tests on single-phase flow using perforation injection to determine how perforation density affected flow features. The formula for the integrated resistance factor was based on perforation density. Nghiem et al. (1991), then studied the productivity of horizontal wells using simulated flows in different wellbores. Based on the assumption that the well block was porous, the researchers proposed a number of different approaches to deal with ultra-permeable wellbores and reservoirs. By applying mixed grid system parameters, the simulator calculated the flow using Darcy’s law. The resulting simulation model was able to determine the distributions of saturation and pressure simultaneously, yet could not provide information for wellbore fluid flow.

An ongoing issue that occurs across the various branches of the hydrocarbon industry is formation damage (Civan, 2015). This type of damage typically takes place during production (e.g., drilling, completion, or workover operations) or reservoir engineering (VasheghaniFarahani et al., 2014). Formation damage can impact the near-wellbore region as well as further down the formation itself. In the drilling and completion stages, the damage usually results from fluids entering the pay zone or perforations causing rock compaction (Ezeakacha et al., 2017). Perforation is used to connect reservoir formations to wellbores during hydrocarbon production stages. Although the primary purpose of using perforation is to boost production, its application can also cause issues with virgin reservoirs (Renpu, 2011).

Perforation can be created using a variety of methods (Behrmann et al., 2002), and its success is related to any number of characteristics, including radius, phasing angle, density and length (Economides et al., 2013). Rahman et al. (2006, 2007a, 2007b and

2008) investigated perforation in single-phase flow through comparing a drilling method to perforation with a shooting technique. These authors also examined how the skin effect impacts the permeability of the near-wellbore region under these techniques, finding that during the shooting method, there was a redistribution of fine particles throughout the perforation tunnel. Such redistribution shrinks the size of the pore throat, leading to substantially reduced permeability. When this occurs, there is a reduction in flow rates similar to that caused by differential pressure. Note that no studies have investigated decreased permeability caused by common perforation methods in multiphase flows with regard to petroleum production engineering, particularly those in gas reservoirs.

Intense pressure drop can also cause damage in the form of severe asphalting close to perforated intervals (Joonaki et al., 2017). However, because near-wellbore permeability reduction affects well productivity, any kind of formation damage could negatively impact the overall success of the drill project. Therefore, to reduce any formation damage effects on the productivity of the well, damage mechanisms must be mitigated. This can be best accomplished by attaining a better understanding of fluid flows that occur in wellbores during hydrocarbon operations (Soleimani et al., 2018). Figure 8.1 schematically illustrates a horizontal near-wellbore region as well as a vertical perforation tunnel. Here, a flow path is generated between the wellbore and pay zone that impacts the efficiency of the well's operation (Economides & Nolte, 2000). Several recent studies have focused on fluid flow near the wellbore, especially near perforation tunnels (Yildiz, 2002; Abdulwahid et al., 2014). For instance, Li et al. (2012) used a two-dimensional analytical model to understand single-phase fluid flow passing through an ideal perforation set-up under steady-state conditions. The authors studied how diverse boundary conditions affected core flow efficiency, measuring the model's accuracy through comparisons of their results with those generated by FLUENT software.

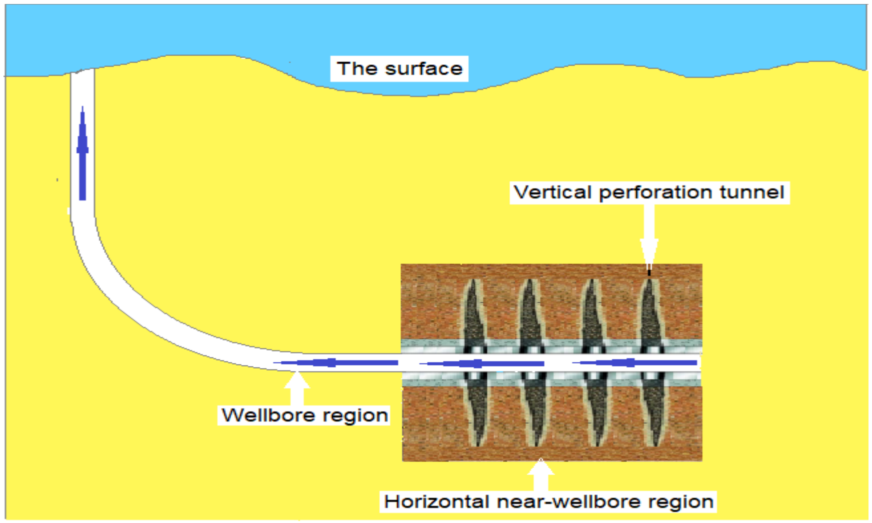

Figure 8.1: Schematic of the horizontal near-wellbore region and vertical perforation tunnel.

Because fluid flow near perforations is relatively complicated, researchers have used several different numerical approaches and some have also applied the finite difference method (FDM) when examining fluid flow in perforations. In the hydrocarbon industry, the use of CFD (computational fluid dynamics) for simulating multiphase flows in porous media, especially near perforations and the wellbore region is becoming more widespread due in large part to improvements in computer technology. For example, CFD can predict velocity, pressure, and flow patterns within specific boundary conditions (Movahedi et al., 2019), a numerical study by Wijeratne and Halvorsen (2015) examined heavy oil reservoir flow by applying the volume of fluid (VOF) approach, verifying their model with experimental data .Finally, Zheng et al. (2016) experimentally investigated and numerically simulated two-phase fluid flows occurring in perforated porous substances.

The researchers' model predicted the pressure gradients of petrophysical characteristics within perforation tunnels.

Using previous research as a foundation and reference point, the present study aims to enhance oil recovery by employing two-phase flow mechanisms, thereby expanding industry knowledge about well performance. This study is a continuous work and extension of Ahammad et al., (2018) by conducting the three main investigative procedures of experimental, numerical, and statistical analysis to investigate the effect of two-phase flows on pressure build-up and the time required to reach steady-state conditions in a cylinder perforation tunnel

8.2. Methodology

8.2.1. Experimental procedure

In the experimental work, the experimental facility at Memorial University has been updated to be able to inject three-phase oil, gas, and water rather than just two-phase water and air into the sample via flow lines. However, in the present study, only two lines (water/air) were used.

Figure 8.2 shows the set-up, which features the three following main sections: flow lines extending from inlet to outlet; an inner chamber for holding samples with axial loads; and a Data Acquisition (DQ) system. In the experimental portion of our work, we injected a measured air/water volume into the core sample. As well, we used a geotechnical radial flow test set-up to measure the differential pressure and two-phase flow rate of the perforated sample. Both air and water being radially injected into the core sample in the two-phase flow within the following boundary conditions: The outer side of the sample is considered an inlet while the perforation surface is an outlet. Furthermore, both inlet/outlet pressures were measured for the cylindrical samples using specified air and water flow rates. The numerical results were validated with the experimental data for two-phase flows under the same boundary conditions.

Preparation of perforation tunnel was conducted by cutting a carbonate core sample from rocks from Nova Scotia, Canada. The geometry of the carbonate sample is cylindrical with a hole at the center that made by drilling technique. The dimensions of the geometry and the sample properties are listed in Table 8.1.

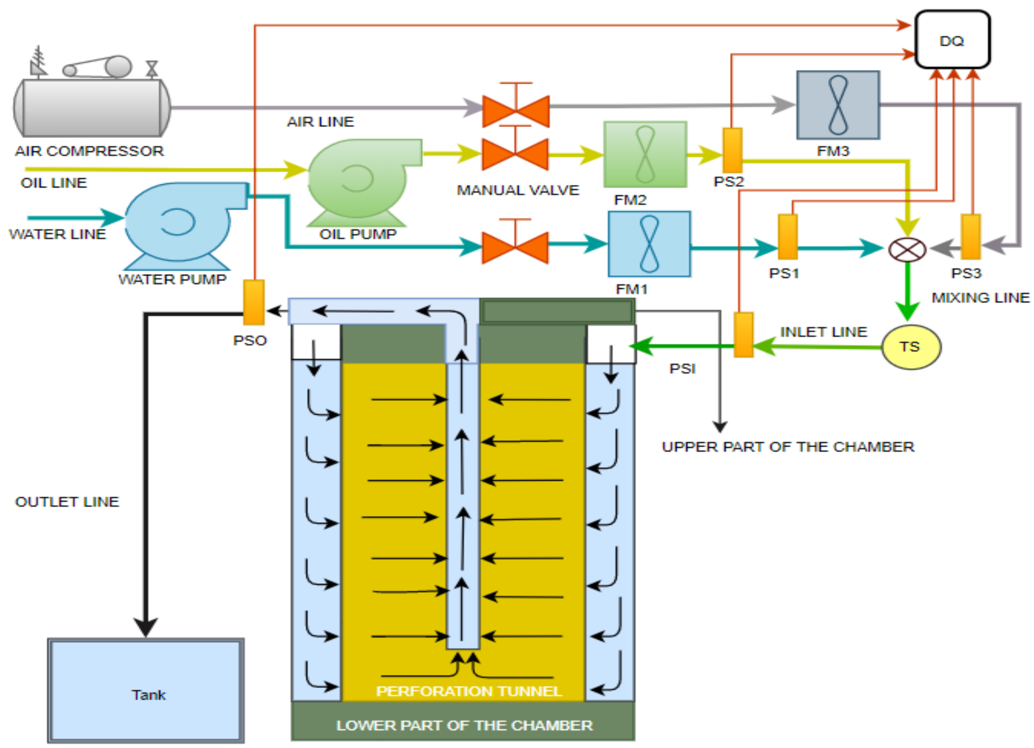

Figure 8.2: The Schematic diagram of the experiment. FM1, FM2 and FM3: Water flow meter, oil flow meter, and air flow meter. PS1, PS2 and PS3: 3 pressure sensors before mixing point, PSI and PSO Inlet and outlet pressure sensors, TS Temperature sensor, DQ Data Acquisition.

Table 8.1: The dimensions of the geometry and the sample properties

Dimensions and properties the sample	Values (units)
Sample height (H)	30.48 cm
Diameter of sample (D)	15.24 cm
Perforation diameter (d)	2.54 cm
Depth of perforation (P_d)	25.4 cm
Permeability (K)	6.3 mD
Porosity (γ)	13.5 %

8.2.2. Numerical simulation procedure

8.2.2.1. Mathematical model

In the porous media tunnel, a physical velocity porous formulation has been utilized for simulating two-phase flows. The two distinct characterizations of superficial and physical velocity formulation have been used to define multiphase flow modelling velocity. The main difference between these two formulations is that physical velocity includes porosity as part of the calculation by incorporating valuation for momentum and continuity equations. For porous regions in multiphase flow, ANSYS FLUENT calculations rely on volumetric flow rate. If we then assume isotropic porosity and multiphase flow, momentum and continuity equations describing two-phase flow in a porous region could be expressed, respectively, as:

$$\frac{\partial}{\partial t}(\gamma \alpha_q \rho_q) + \nabla \cdot \left(\gamma \alpha_q \rho_q \vec{v}_q\right) = \gamma \sum_{p=1}^{n}(\dot{m}_{pq} - \dot{m}_{qp}) + \gamma S_q \qquad (8.1)$$

and

$$\frac{\partial}{\partial t}\left(\gamma\alpha_q\,\rho_q\vec{v}_q\right)+\nabla\cdot\left(\gamma\alpha_q\,\rho_q\vec{v}_q\vec{v}_q\right)=-\,\gamma\alpha_q\,\nabla_{(p-p_c)}+\nabla\cdot\left(\gamma\,\bar{\bar{\tau}}_q\right)+\gamma\,\alpha_q\,\rho_q\vec{B}_f-\left(\alpha_q^2\gamma^2\frac{\mu_q\,\vec{v}_q}{KK_{r,q}}+\alpha_q^3\gamma^3\frac{C_{2\rho}|\vec{v}_q|\vec{v}_q}{2}\right)+\ \gamma\ \sum_{p=1}^{n}(\vec{F}_{pq}^{D}+\vec{F}_{pq}^{TD}+\dot{m}_{pq}\vec{v}_{pq}-\ \dot{m}_{qp}\vec{v}_{qp})+\gamma(\ \vec{F}_q+\vec{F}_q^{L}+\vec{F}_q^{vm}) \tag{8.2}$$

8.2.2.2. Computational technique

As a simulation tool, ANSYS FLUENT can be used for accurately solving flow problems across a broad field (Wood et al., 2020). The present study employed ANSYS FLUENT 18.1 in numerical simulations of a reservoir well's perforated tunnel. In the two-phase flow model, we utilized the volume of fluid (VOF) approach for solving porous media air-water flow. The VOF method is ideal for predicting the interface condition between immiscible fluids throughout the flow time

Figure 8.3 illustrates the cut mesh and uniform mesh strategies used for generating high-quality mesh. As shown, the presented configuration was effective in helping predict high-density and good quality mesh that was located near the perforation borders. As a means to verify the solution mesh's independence in relation to the boundary conditions, we employed six standard mesh numbers, as shown in Table 8.2. The comparison reveals the independence of the injection pressure and steady state time solution from increasing mesh elements' number.

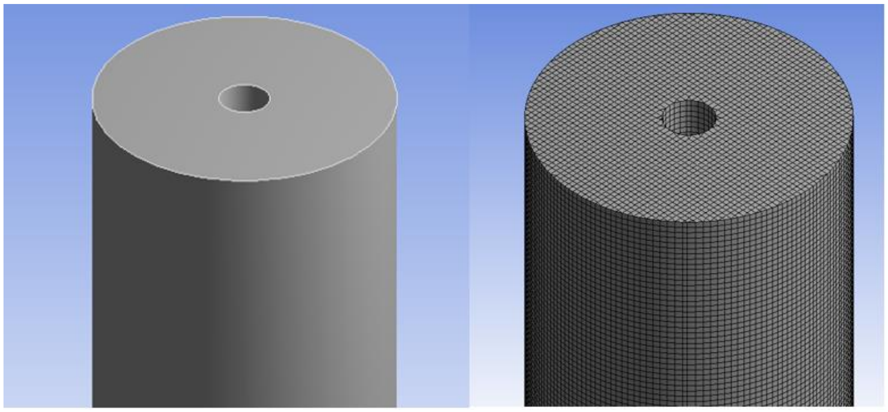

Figure 8.3: The shape of uniform configuration mesh that used in CFD simulations of two-phase flow.

Table 8.2: Mesh dependency

Mesh cases (22)	Number of elements	Inject pressure (MPa)	Steady state time (s)
Mesh 1	67184	0.438105	39
Mesh 2	112240	0.4371e5	38.5
Mesh 3	177192	0.4364e5	38
Mesh 4	254826	0.4361e5	38
Mesh 5	369489	0.4358e5	38
Mesh 6	467115	0.4356e5	38

8.2.3. Statistical Analysis procedure

The proposed study adopted Design-Expert® DoE software with BBD for designing statistical analysis runs. To statistically validate the model, we used analysis of variance (ANOVA) (Box & Behnken, 1960; Ferreira, 2007). The two-phase flow's main parameters were chosen, including water viscosity, porosity, permeability, air flow rate, and water flow rate. In choosing these parameters, we assumed air density, air viscosity, and water density remained constant. Next, we choose two boundary points for the intervals of the parameters and one midpoint determined by BBD, as shown in Table 8.3.

Table 8.3: Boundary conditions Range.

Boundary conditions	**Values**	**Units**
Water flow rate ($\boldsymbol{Q_w}$)	5, 10 and 15	cm^3/s
Air flow rate ($\boldsymbol{Q_a}$)	5, 15 and 25	cm^3/s
Permeability ($\boldsymbol{K}$ **)**	0.011, 0.0225 and 0.034	Darcy
Porosity ($\boldsymbol{\gamma}$ **)**	15, 21.5 and 28	%
Water viscosity ($\boldsymbol{\upsilon}$)	0.89, 1.1 and 1.31	mPa.s
Pressure outlet (g)	0	Pa

8.3. Results and discussion

This research investigated a specific liquid and gas volume that was injected into the samples to determine the differential pressure of these samples as well as the time need to achieve a steady state under a variety of tested boundary conditions. Table 8.4 presents the results from 41 numerical runs that were analyzed with ANOVA and the BBD model. The steady-state time and injection build-up pressure results of the analysis are showed in the last two columns. In looking at the residuals' normal plot in Figure 8.4a, we can see that the numerical data follows a normal distribution pattern. Additionally, the results show that the predicted values derived from the model share strong similarities with the actual values derived numerically.

Table 8.4: The forty-one numerical runs of the Design-Expert® analyses and the numerical results.

Run No	Water flow rate (cm^3/s)	Air flow rate (cm^3/s)	Permeability (Darcy)	Porosity (%)	Viscosity (mPa.s)	Pressure (Pa)	Time (s)
1	15	15	0.034	0.215	1.1	677400	56
2	15	25	0.0225	0.215	1.1	1.048E+06	46
3	5	5	0.0225	0.215	1.1	377100	128
4	15	15	0.011	0.215	1.1	2.096E+06	65
5	10	15	0.011	0.15	1.1	1.208E+06	39
6	15	15	0.0225	0.15	1.1	1.001E+06	35
7	5	15	0.0225	0.215	0.89	318900	70
8	5	15	0.034	0.215	1.1	233800	68
9	10	5	0.034	0.215	1.1	429100	96
10	10	5	0.0225	0.28	1.1	678700	122
11	10	25	0.0225	0.215	1.31	837300	53
12	5	15	0.0225	0.15	1.1	386400	48
13	10	15	0.0225	0.28	1.31	822900	86
14	15	5	0.0225	0.215	1.1	1.027E+06	86
15	5	25	0.0225	0.215	1.1	397500	48
16	10	5	0.011	0.215	1.1	1.353E+06	102
17	10	15	0.011	0.215	1.31	1.47E+06	64
18	10	15	0.0225	0.215	1.1	697500	70
19	10	25	0.0225	0.15	1.1	707300	32
20	10	5	0.0225	0.215	1.31	817700	90
21	15	15	0.0225	0.215	1.31	1.232E+06	56
22	10	15	0.034	0.15	1.1	436000	38
23	10	15	0.0225	0.15	1.31	825400	38
24	10	15	0.0225	0.15	0.89	565300	38
25	10	15	0.034	0.215	0.89	360600	58
26	15	15	0.0225	0.28	1.1	1.032E+06	70
27	10	15	0.034	0.215	1.31	527500	68
28	10	15	0.034	0.28	1.1	425400	88
29	5	15	0.0225	0.28	1.1	376000	90
30	10	25	0.034	0.215	1.1	443000	46
31	5	15	0.0225	0.215	1.31	459500	70
32	15	15	0.0225	0.215	0.89	921100	48
33	10	15	0.011	0.28	1.1	1.21E+06	80
34	10	15	0.011	0.215	0.89	1.145E+06	56
35	10	25	0.0225	0.215	0.89	575900	46
36	5	15	0.011	0.215	1.1	715700	68
37	10	25	0.011	0.215	1.1	1.228E+06	40
38	10	25	0.0225	0.28	1.1	707000	64
39	10	5	0.0225	0.215	0.89	546200	90
40	10	15	0.0225	0.28	0.89	563200	70
41	10	5	0.0225	0.15	1.1	682900	70

In the literature, numerous researchers have applied the Box-Cox normality plot to DoE models (Box & Cox, 1964). As in the proposed study, the majority of the statistical tests in the literature also assumed normal distribution of the sample. This approach makes DoE testing substantially more powerful than nonparametric tests. If the results fail to satisfy the assumption of normality, dataset transformation with the Box-Cox plot may be utilized. Figure 8.4b illustrates the Box-Cox plot of power transformation, with lambda = 0 located between the lambda confidence interval (CI), giving (- 0.5, 0.5). As can be seen, the developed model has been transformed, resulting in a residual (7.55) maximum-to-minimum rate, which is under the threshold (here, set at 10). According to the ANOVA analysis, the design model provides the outcomes desired.

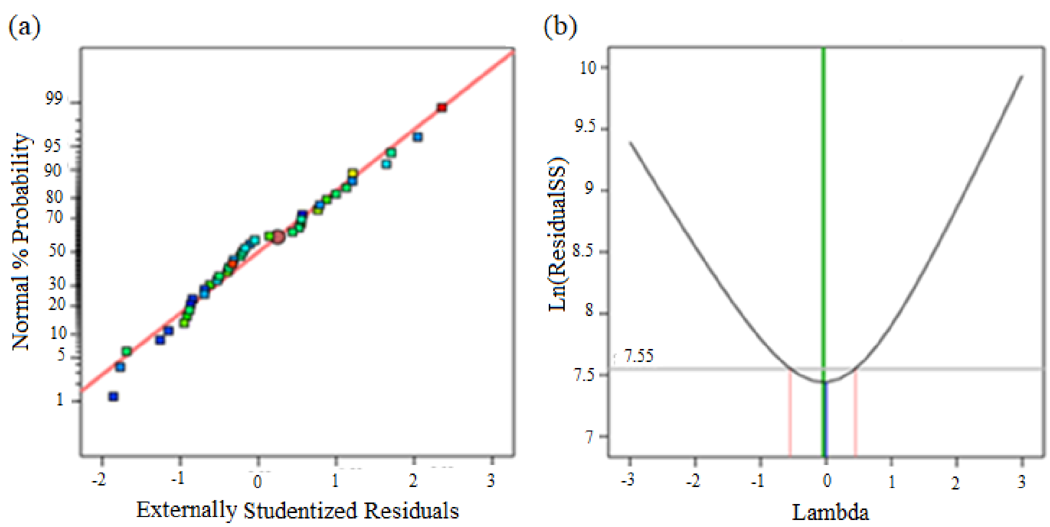

Figure 8.4: Normal plot of residuals (A) and Box-Cox plot for power transformations (B).

More specifically, using the Design-Expert® DoE software and based on numerical results, two correlations from the statistical analysis were provided. By applying the same geometry used for the experimental procedure, these two correlations may then be utilized for predicting the time required to reach steady-state or the injection build-up pressure for the values of investigated parameters, as follows:

$$P(Pa) = e^{(12.552+b*Q_w+c*Q_a+d*K-0.034*\gamma+f*\upsilon)} \tag{8.3}$$

$$t(s) = e^{(3.54107+n*Q_w+r*Q_a+s*K+5.34261*\gamma+z*\upsilon)} \tag{8.4}$$

The first correlation predicts the injection build-up pressure through the available sample under different boundary conditions, this correlation includes four constants ($b = 0.1015\, s/cm^3, c = 0.001\, s/cm^3, d = -47.054/Darcy,\ and\ f = 0.84/mPa.s$). The second correlation predicts the required time to reach steady state under different boundary conditions; this correlation includes four constants ($n = -0.025823\ s/cm^3, r = -0.036918\, s/cm^3,\ s = -0.671396/Darcy, and\ z = 0.236384/mPa.s$). These correlations can be used to predict the injection build-up pressure and the time required to reach the steady-state flow condition, as long as using the same sample geometry and the units of the parameters that used in this study.

The CFD simulation results were validated using the experimental data. The dimensions of the perforation geometry are the same as that used in the experimental procedure (see Table 8.1). The distribution of the injection build-up pressure for the two-phase flow through the perforation tunnel is shown in Figure 8.5. The comparison between the experimental, numerical and two correlations results with the same flow boundary conditions is shown in Figure 8.6. The experimental data and numerical results are in a good agreement.

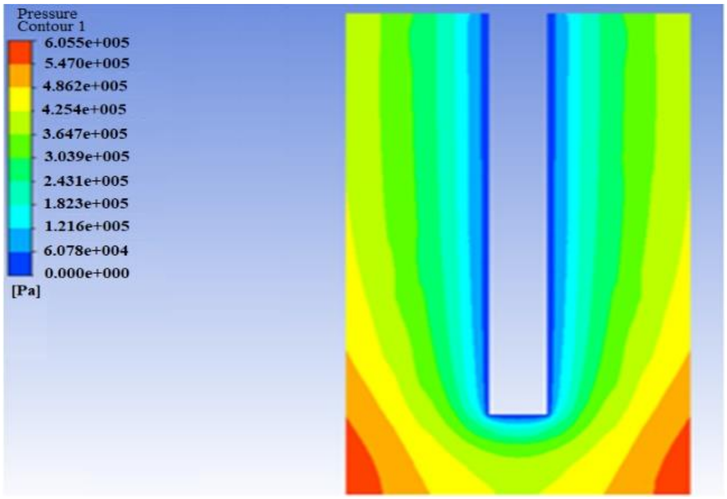

Figure 8.5: Numerical results of the pressure gradient for air-water two-phase flow through the perforation tunnel with the flow boundary conditions (Qa = 66 cm3/s, Qw = 2 cm3/s, υ = 0. 95 mPa.s, K = 0.0063 Darcy, and γ =13.5 %).

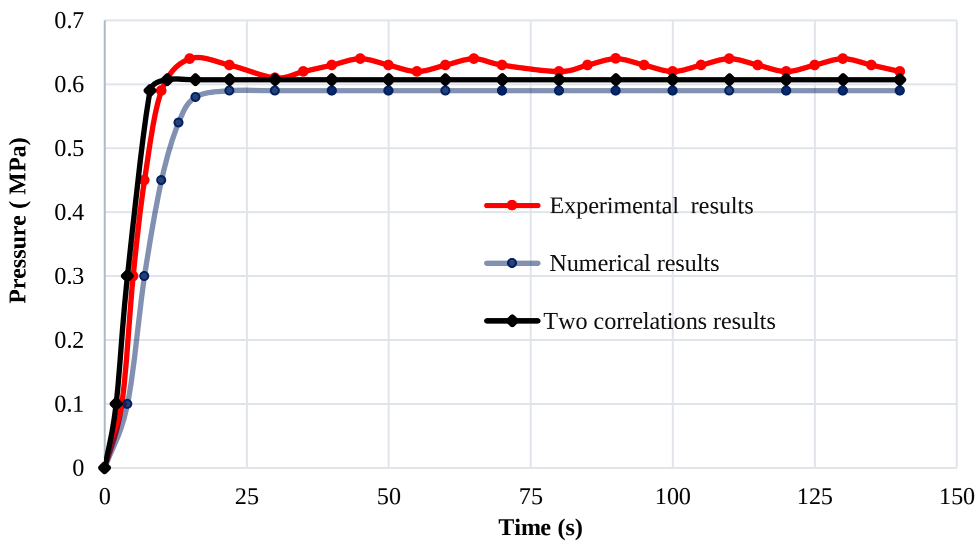

Figure 8.6: The comparison between experimental, numerical, and two correlations results with the same flow boundary conditions (Qa = 66 cm3/s, Qw = 2 cm3/s, υ = 0. 95 mPa.s, K = 0.0063 Darcy, and γ =13.5 %).

The calculated P and t from the two correlations are in a good agreement with numerical results as shown in figure 8.7, under the same boundary flow conditions.

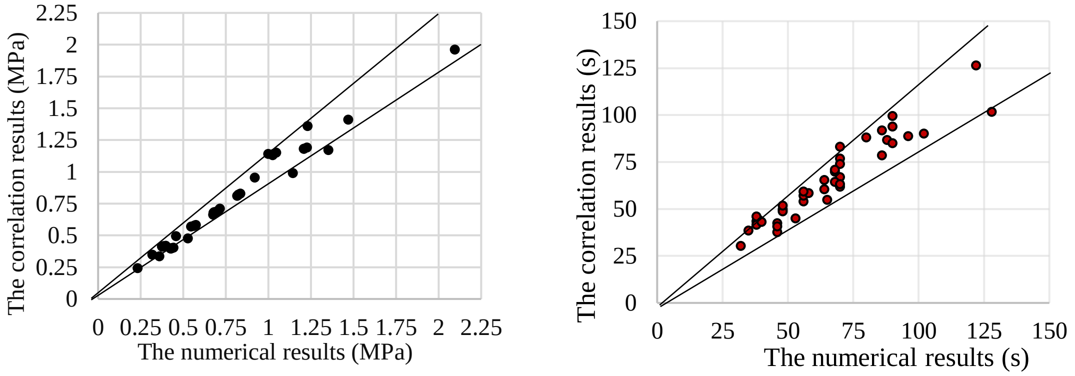

Figure 8.7: Comparison of the numerical and correlation results for the injection build-up pressure (pa) and the required time to reach steady state (s).

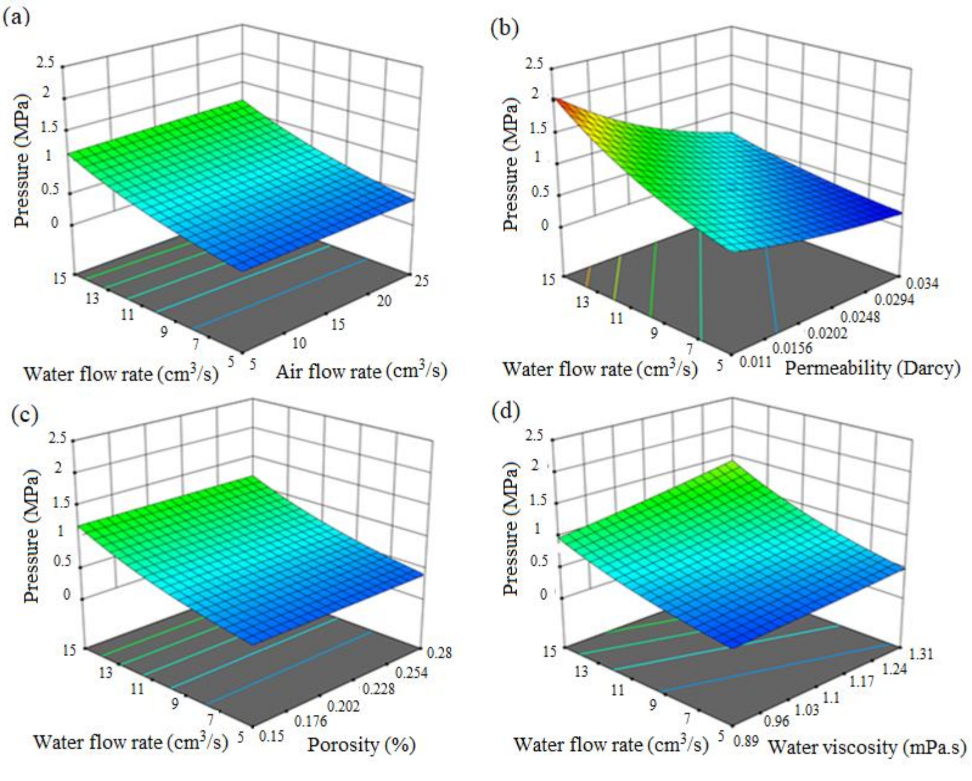

Figure 8.8: The resulting of the injection build-up pressure (Pa) through the vertical perforation tunnel by interacting the water flow rate with (a) air flow rate, (b) permeability, (c) porosity, and (d) water viscosity.

The statistical analysis identified the effect of each parameter on the pressure build-up as well as the steady-state time. Specifically, permeability, water flow rate, and water viscosity have a very strong effect on the injection pressure build-up as shown in Figure 8.8.

Moreover, the results indicate that porosity and air flow rate have a substantial effect on the time required to reach steady-state conditions, as illustrated in Figure 8.9. According to the results, increasing the water flow rate causes a substantial rise in injection pressure, as air flows more easily compared to water. Thus, if both air and water are injected into a sample, the air flow will be hindered, which will lead to a rise in the injection pressure.

The addition of more water will eventually result in the formation of bubbles. This causes an intensification of the Jamin effect, where capillary pressure hinders the flow of bubbles and droplets past the narrow throat. The Jamin effect can critically impact two-phase flows occurring in reservoir porous substances at specific velocities. Meanwhile, higher air flow rates hasten the time required to reach steady-state conditions, as faster air flows serve to fill the sample's pores more quickly. If permeability is low, the rise in injection pressure will be higher. In this case, due to high resistance, higher injection pressure would be necessary to inject the required volume into the core sample. This is accomplished through gradual reduction of the sample's absolute permeability, as illustrated by Figure 8.9b.

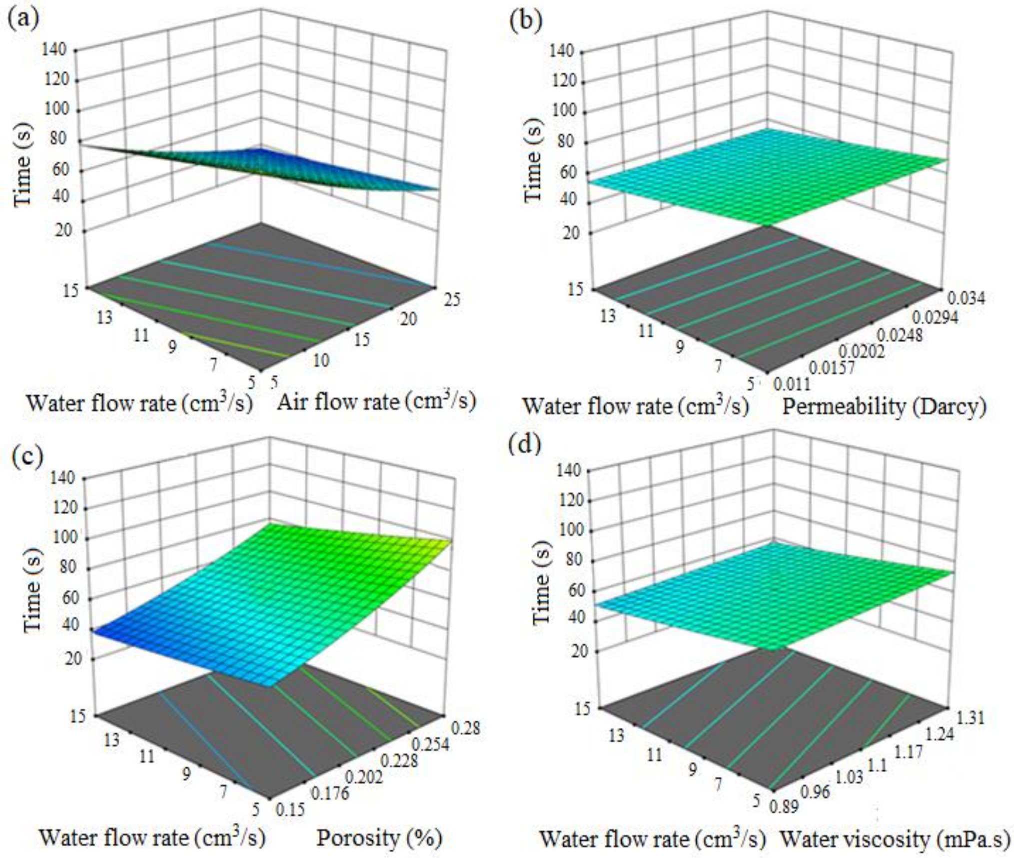

Figure 8.9: The interaction of time and water flow rate with (a) air flow rate, (b) permeability, (c) porosity, and (d) viscosity and their effect on the time required to reaching steady-state (s) in the vertical perforation tunnel.

Greater porosity of the media results in a longer time required to reach steady-state conditions as a result of the increase in the sample's storage capacity. Specifically, a portion of the liquid will pass through the substance, whereas another portion will be stored within the pores, as illustrated in Figure 8.9c. Moreover, in comparison to porosity or gas flow rate, the viscosity of the liquid in a sample is a key factor affecting the behavior of pressure gradients in two-phase flows as shown in Figure 8.9d. Nonetheless, we can readily predict the impact of each parameter (the injection build-up pressure and the required time to reach steady-state) through employing the sample geometry from the resulting correlation.

8.4. Conclusions

The study has expanded the investigation of gas-liquid two-phase flow at the near-wellbore region. Based on the three main investigative procedures of experimental, numerical, and statistical analysis, the following conclusions can be summarized:

1) The numerical results were validated with experimental data, and the comparison of results were in good agreement.
2) The numerical and statistical analyses showed a clear view of the effect of each investigated parameter on the injection build-up pressure and time required to reach the steady-state flow condition. Specifically:
    a) The results show that the permeability, flow rate, and viscosity of the liquid have a significant effect on the injection pressure buildup profile.
    b) The results indicated that porosity and gas flow rate have a substantial effect on the time required to attain steady-state conditions.
3) Two correlations have been produced from the statistical analysis that can be used to predict the injection build-up pressure and the time required to reach the steady-state flow condition for a given value of each investigated parameter through the study's sample geometry.

References

Abdulwahid, M. A., Niranjan Kumar, I. N., & Dakhil, S. F. (2014). Influence of radial flux inflow profile on pressure drop of perforated horizontal wellbore. *Journal of Energy Resources Technology, 136*(4), 042907. doi:10.1115/1.4028770

Ahammad, M., Rahman, M., Zheng, L., Alam, J., & Butt, S. (2018). Numerical investigation of Two-phase fluid flow in a perforation tunnel. *Journal of Natural Gas Science and Engineering, 55*, 606-611.

Behrmann, L., Hughes, K., Johnson, A., & Walton, I. (2002). New underbalanced perforating Technique INCREASES Completion efficiency and eliminates

Costly Acid Stimulation. *The SPE Annual Technical Conference and Exhibition.* Texas.

Box, G. E., & Behnken, D. W. (1960). Some new three level designs for the study of quantitative variables. *Technometrics, 2*(4), 455-475.

Box, G. E., & Cox, D. R. (1964). An analysis of transformations. *Journal of the Royal Statistical Society: Series B (Methodological), 26*(2), 211-243.

Civan, F. (2015). *Reservoir formation damage.* Gulf Professional Publishing.

Economides, M. J., & Nolte, K. G. (2000). *Reservoir stimulation.* Chichester: Wiley.

Ezeakacha, C. P., Salehi, S., & Hayatdavoudi, A. (2017). Experimental study of drilling fluid's filtration and mud cake evolution in sandstone formations. *Journal of Energy Resources Technology, 139*(2), 1-8.

Ferreira, S., Bruns, R., Ferreira, H., Matos, G., David, J., Brandão, G., . . . dos Santos, W. (2007). Box-Behnken design: An alternative for the optimization of analytical methods. *Analytica Chimica Acta, 597*(2), 179-186.

Ihara, M., Brill, J., & Shoham, O. (1992). Experimental and theoretical investigation of two-phase flow in horizontal wells. *Paper presented at the SPE Annual Technical Conference and Exhibition* . Washington. doi:10.2118/24766-ms

Ihara, M., Kikuyama, K., & Mizuguchi, K. (1994). Flow in horizontal wellbores with influx through porous walls. *Paper presented at the SPE Annual Technical Conference and Exhibition.* New Orleans, Louisiana. doi:10.2118/28485-ms

Ihara, M., Yanai, K., & Shingo, T. (1995). Two-Phase Flow in Horizontal Wells. *SPE Prod & Fac, 10*, 249–256.

Joonaki, E., Burgass, R., Hassanpouryouzband, A., & Tohidi, B. (2017). Comparison of experimental techniques for evaluation of chemistries against asphaltene aggregation and deposition: New application of high-pressure and high-temperature quartz crystal microbalance. *Energy & Fuels, 32*(3), 2712-2721. doi:10.1021/acs.energyfuels.7b02773

Landman, M., & Goldthorpe, W. (1991). Optimization of perforation distribution for horizontal wells. *Paper presented at the SPE Asia-Pacific Conference.* Perth. Australia. doi:10.2118/23005-ms

Li, B., Sun, D., Gladkikh, M., & Wu, J. (2012). 2D analytical solution of ideal perforation flow. *SPE Journal, 17*(2), 631-652. doi:10.2118/128021-pa

Marett, B., & Landman, M. (1993). Optimal perforation design for horizontal wells in reservoirs with boundaries. *Paper presented at the SPE Asia Pacific Oil and Gas Conference.* Singapore.

Movahedi, H., Vasheghani Farahani, M., & Masihi, M. (2019). Development of a numerical model for single- and two-phase flow simulation in perforated porous media. *Journal of Energy Resources Technology, 142*(4), 042901. doi:10.1115/1.4044574

Nghiem, L., Collins, D., & Sharma, R. (1991). Seventh Spe Comparative Solution Project: Modelling of Horizontal Wells in reservoir simulation. *Paper presented at the SPE Symposium on Reservoir Simulation.* Anaheim, California. doi:10.2118/21221-ms

Novy, R. (1995). Pressure drops in horizontal wells: When can they be ignored? *SPE Reservoir Engineering, 10*, 29-35. doi:10.2118/24941-pa

Ozkan, E., & Raghavan, R. (2000). A computationally efficient, transient-pressure solution for inclined wells. *SPE Reservoir Evaluation & Engineering, 3*(05), 414-425. doi:10.2118/66206-pa

Rahman, M. A. (2008). Scale-up of perforation process from laboratory model to bottom hole dimensions. *Journal of Porous Media, 11*(1), 19-34.

Rahman, M. A., Heidrick, T., Fleck, B., & Koksal, M. (2006). Enhancement of the completion efficiency of perforation tunnels in petroleum wells. *ASME 2006 2nd Joint U.S.-European Fluids Engineering Summer Meeting Collocated With the 14th International Conference on Nuclear Engineering.* Miami, Florida, USA.

Rahman, M., Mustafiz, S., Biazar, J., Koksal, M., & Islam, M. (2007a). Investigation of a novel perforation technique in petroleum wells—perforation by drilling. *Journal of the Franklin Institute, 344*(5), 777-789.

Rahman, M., Mustafiz, S., Koksal, M., & Islam, M. (2007b). Quantifying the skin factor for estimating the completion efficiency of perforation tunnels in petroleum wells. *Journal of Petroleum Science and Engineering, 58*(1-2), 99-110.

Renpu, W. (2011). Basis of Well Completion engineering. *Advanced Well Completion Engineering*, 1-74.

Sarica, C., Haciislamoglu, M., Raghavan, R., & Brill, J. (1994). Influence of wellbore hydraulics on pressure behavior and productivity of horizontal gas wells. *Paper presented at the SPE Annual Technical Conference and Exhibition.* New Orleans, Louisiana. doi:10.2118/28486-ms

Soleimani, R., Jahanpeyma, Y., & Salehian, M. (2018). Analysis of horizontal well productivity in tight gas formations and its sensitivity to reservoir properties. *Journal of Petroleum Exploration and Production Technology, 9*(2), 1237-1244. doi:10.1007/s13202-018-0546-0

Stone, T., Edmunds, N., & Kristoff, B. (1989). A comprehensive wellbore/reservoir simulator. *Paper presented at the SPE Symposium on Reservoir Simulation.* Houston, Texas. doi:10.2118/18419-ms

Su, Z., & Gudmundsson, J. (1993). Friction factor of perforation roughness in pipes. *Paper presented at the SPE Annual Technical Conference and Exhibition.* Houston, Texas. doi:10.2118/26521-ms

Su, Z., & Gudmundsson, J. (1994). Pressure drop in perforated pipes: Experiments and analysis. *Paper presented at the SPE Asia Pacific Oil and Gas Conference.* Melbourne, Australia. doi:10.2118/28800-ms

Suzuki, K. (1997). Influence of wellbore hydraulics on horizontal well pressure transient behavior. *SPE Formation Evaluation*, *12*, pp. 175-181. doi:10.2118/24684-pa

Well. *Journal of Petroleum Technology, 5*(6), 171-176. doi:10.2118/203-g

VasheghaniFarahani, M., Soleimani, R., Jamshidi, S., & Salehi, S. (2014). Development of a dynamic model for drilling fluid's filtration: Implications to prevent formation damage. *Paper presented at the SPE International Symposium and Exhibition on Formation Damage Control.* Lafayette, Louisiana, USA. doi:https://doi.org/10.2118/168151-MS

Wijeratne, D. E., & Halvorsen, B. M. (2015). Computational study of fingering phenomenon in heavy oil reservoir with Water Drive. *Fuel*, *158*, 306-314. doi:10.1016/j.fuel.2015.05.052

Wood, B. D., He, X., & Apte, S. V. (2020). Modeling turbulent flows in porous media. *Annual Review of Fluid Mechanics, 52*(01), 171-203.

Yildiz, T. (2002). Impact of perforating on well performance and cumulative production. *Journal of Energy Resources Technology, 124*(3), 163-172. doi:10.1115/1.1487879

Yuan, H., Sarica, C., & Brill, J. (1998). Effect of completion geometry and phasing on single-phase liquid flow behavior in Horizontal Wells. *Paper presented at the SPE Annual Technical Conference and Exhibition.* New Orleans, Louisiana.

Yuan, H., Sarica, C., & Brill, J. (1999). Effect of perforation density on single phase liquid flow behavior in Horizontal Wells. *SPE Prod & Fac, 14*, pp. 203–209.

Zheng, L., Rahman, M. A., Ahammad, M. J., Butt, S. D., & Alam, J. M. (2016). Experimental and numerical investigation of a novel technique for perforation in petroleum reservoir. *the SPE International Conference and Exhibition on Formation Damage Control.* Lafayette, Louisiana, USA.

Chapter 9

Conclusion and future work

This study's overall objective is to present a better understanding of the fluid flow behavior in the near-wellbore region by evaluating the well completion effects on pressure gradient as a function of single and two-phase flow rate conditions. Therefore, the work was assessed how different damage, well geometry, completion configurations and other perforation characteristics impact the total skin factor by creating a prototype representing the near-wellbore region conditions. The four main investigative procedures of the sample's preparation, experimental, numerical, and statistical analysis, were used in this study to investigate the effects of the skin zone (damaged region), perforation parameters, the crushed zone around the perforation, partial completion, inclination of wells and two-phase flow behavior on the pressure gradient and skin factor in the near-wellbore region.

A new technique has been presented to prepare homogenous artificial sandstone samples that were used in this study and can be applied in hydrocarbon recovery projects. Mercury intrusion porosimetry (MIP) and scanning electron microscopy (SEM) have been used to first characterize and then analyze the pore morphology and index properties for the synthetic sandstone samples. The experimental results indicated that weak solidified sandstone index characteristics are strongly affected by both mixing and grain size. In addition, SEM map images revealing pore morphologies and homogenous grain distribution of the tested samples indicate that grains that undergo reductions in size require additional epoxy glue content, likely due to binder distribution of glue among the small grains.

Numerical study was presented to investigate the effect of damaged zone parameters on the mechanical skin factor value in the vertical open hole well and investigate how skin zone characteristics affect both the cross-flow and pressure distribution of a dual-layer reservoir vertical well. The results showed the numerical model's ability to simulate real conditions of the near-wellbore region, and the comparison results demonstrated good agreement between the numerical model and Hawkins (1956) equation results. In addition, the cross-flow and pressure distribution appear to be affected by interactions occurring between the various characteristics of the skin zone and the reservoir layers.

Experimental and numerical investigations have been conducted to determine the effect of the perforated casing completion on the perforation skin factor of oil production by conducting a single flow through the vertical near wellbore region. This work presented a novel experimental approach for studying the effect of well perforation on hydrocarbon production by creating a prototype representing the near-wellbore region. The experimental data validated the numerical results; the validation showed a good agreement between the experimental results and numerical data. The study provided an in-depth analysis of perforated well completion productivity. As part of the analysis, dimensionless groups were identified that control flows around the perforations, along with the effects of these groups on wells' productivity. Furthermore, using numerical and statistical analyses, a series of results were obtained that highlight the examined well's perforation skin factor. The statistical analysis results showed a clear view of the interaction effect among the four dimensionless parameters (P_r, R_r, K_r and Θ_d) on the perforation skin factor (S_p) for two perforation angle cases (360° and 60°- 180°).

The experimental work and a numerical simulation model have conducted in order to further investigate the accuracy of Karakas and Tariq’s (1991) (Karakas & Tariq, 1991) model for crushed skin factor as well as to obtain new correlations which may be closer to reality, established on some assumptions. In the initial scenario, the crushed zone is assumed to be located at the perforation tunnel's side only, while in the second scenario, the crushed zone is assumed to be located at a side and the tip of perforation (a tip-crushed zone). The simulated results indicate a good comparison with regard to the two scenarios' pressure gradients. Furthermore, the simulations' comparison reveals another pressure drop caused by the tip crushed zone related to the horizontal or plane flow in the perforations. The differences between the two simulations' results show that currently available models for estimating the skin factor for vertical perforated completions need to be improved based on which of the two cases is closer to reality. This study has presented a better understanding of crushed zone characteristics by employing a different approach to the composition and shape of the crushed zone and permeability reduction levels for the crushed zone in the axial direction of the perforation.

The experimental work and a numerical simulation model were conducted for accurate estimation of the skin factor for partially penetrated wells. The partially penetrated well parameters were analyzed using statistical analysis coupled with the numerical simulation model. The statistical analysis results show that partial-penetration completion increases the pressure drop and thus contributes to a reduction in the productivity index. The pressure drop is more affected by a smaller area of perforation intervals; the smaller area makes a larger contribution to pressure drop; the higher inflow rate leads to energy consumption increases for accelerating the flow. A low vertical-to-horizontal permeability ratio creates a high-pressure drop and affects spherical flow shape due to the vertical resistance. Also, the numerical results showed the gradation in the pressure and flow shape from spherical to elliptical with decreasing the permeability ratio. In contrast, the distance spanning the open interval’s top to the formation’s top has less effect on the partial-penetration skin factor, whereas maximum value for skin is achieved at a low and high value, while the middle values do not have any effect.

The work was investigated the effects of four main characteristics—namely, the permeability anisotropy, wellbore radius, reservoir thickness, and deviation angle—of open-hole inclined wells. Additional investigations sought to verify the effect of the direction of perforations on the skin factor or pressure drop in perforated inclined wells. The two dimensionless parameters (the ratio of the angle of the slant to the maximum inclination angle and the permeability ratio) demonstrated a significant effect on the skin factor. The angle of the slant has a significant effect on the reduction in pressure drop in the near-wellbore region due to the increase in the contact area between the well and the reservoir resulting from the increase in the angle of inclination. Additionally, anisotropy is a crucial parameter affecting deviated well productivity; the ratio of horizontal permeability to vertical permeability has a great effect on the skin factor with regard to the well productivity, by increasing the resistance of flow convergence and decreasing the performance of deviated wells. Furthermore, the results demonstrated a deviation in the skin factor estimation results for perforated inclined wells in different perforation orientation scenarios; therefore, existing models must be improved in light of this variance. This work contributes to the understanding and simulation of the effects of well inclination on skin factor in the near-wellbore region.

The study also aimed to enhance oil recovery by modelling a two-phase flow through the near-wellbore region, thereby expanding industry knowledge about well performance. An experimental procedure was conducted to investigate the behavior of two-phase flow through a cylindrical perforation tunnel. The experimental data were validated to the numerical results, and the comparison of results was in good agreement. The numerical and statistical analysis demonstrated each investigated parameter's effect. The permeability, flow rate, and viscosity of the liquid significantly affect the injection pressure build-up profile, and porosity and gas flow rate substantially affect the time required to attain steady-state conditions.

In addition, the novel correlations have been produced from statistical analysis that simplify the estimation of the skin factor in the four well completion cases. The work also compared the results from available models that are widely accepted by the industry as a basis for gauging the accuracy of the novel correlations in estimating the skin factor and their results showed a good agreement with the available models results.

In future work, the set-up has been appropriately updated to target the monitoring of interaction flows for both well, and near-well areas, including axial well and radial near-well flows. However, the scope of the current research can be extended by including and coupling radial and axial flows in the near-wellbore and wellbore regions. This complex combination of components of physical properties of the reservoir, well completion method, and well geometry have a significant impact on the productivity of wells, which prompts many researchers to conduct further investigations.

In the crushed perforation zone case, the present study was conducted to investigate two scenarios for permeability reduction levels for the crushed zone in the axial direction of the perforation. The same procedure can be repeated in future works, including permeability reduction levels for the crushed zone in the radial direction of the perforation and the crushed zone anisotropy effect.

In inclined wells, the variance between the two scenarios for skin factor, including the effects of the indicated parameters, was investigated in the case of perforation direction at the same inclination as the well angle with a perforation angle of 180°. In future works, further investigations can be conducted to find the variance between the two scenarios for other perforation angles (60°, 90°, 120°, 360°) with different parameters configurations.

List of Appendices:

Appendix I - Design of experiments techniques used in this study:

Two-level factorial designs change factor levels during the process of determining each factors relative importance in as few runs as possible. The factors are changed at two levels – low and high – in order to gauge their experimental significance. For designs involving full factorial parameters, every combination of factors is run to determine its potential impact. In cases where a numerical simulation or experiment results in a nonlinear response, different strategies called response surface methodologies (RSM) can be applied. RSM may be loosely defined as techniques employed in empirical studies of relationships occurring between responses and groups of variables.

An example of a statistical analysis in this study, partially penetrated well parameters were analyzed using statistical analysis coupled with the numerical simulation. The design of the experiment's software is provided several useful statistical tables and various graphs that can use to identify which best model can be used to determine the relative impact of each factor for different scenarios on the partial-penetration skin factor.

The first part of the analysis includes determining the order of the model considered appropriate to match the response. A fit summary of available model types is shown in Table 1. Two coefficients of determination (P-value and R-squared) values are presented to determine the adequacy of the match.

Table 1. fit summary of available models

Source	**Sequential P-value**	**Adjusted R²**	Program recommendation
Linear	< 0.0001	0.99	Suggested
2FI	0.9813	0.99	
Quadratic	0.0002	0.99	Suggested
Cubic	0.4134	0.99	Aliased

The next step of the analysis includes using an ANOVA to determine which variables or factors, corresponding interactions, and higher-order terms contribute to the response. The F-value and P-value are checked for each model term to determine whether factor is significant or not. The results of the ANOVA are shown in Table 2.

Table 2. The response results of the ANOVA

Source	**Sum of Squares**	**Degrees of freedom**	**Mean Square**	**F-value**	**P-value**	**Program recommendation**
Model	1.92	4	0.4788	4.698E+07	< 0.0001	significant
h_d	1.60	1	1.60	1.569E+08	< 0.0001	
r_d	0.1519	1	0.1519	1.491E+07	< 0.0001	
k_r	0.1643	1	0.1643	1.612E+07	< 0.0001	
l_d	0.0001	1	0.0001	11318.64	< 0.0001	
Residual	2.039E-07	20	1.019E-08			
Cor Total	1.92	24				

The Box-Cox plot is a tool to help us determine the most suitable power transformation (square root, natural log, base 10 log, Inverse square root, etc.) to apply to response data. The power function can describe most data transformations.

The natural log was applied because it was an appropriate power transformation for this study.

We confirm ANOVA results by running general diagnostic tests for normality, constant variance and randomness of residuals to ensure that no ANOVA assumptions are violated. Figure 1 shows the test results. As can be seen in the graph (1A), the residuals' normal probability plot indicates that the data follow a straight line, which represents normal distribution. In the next graph (1B), we see a comparison of residuals and predicted values based on the regression equation. The data show that the residuals are mostly evenly distributed, indicating that the normality and constant variance assumptions are correct. The third graph (1C) shows a comparison of run number and residuals. Unlike with many numerical simulations, there is no trend indicating the presence of any systemic error, thus verifying that the residual randomness assumption has been satisfied. Overall, the three mentioned assumptions have been satisfied, which means we can trust the results.

The diagnostic plot test results validate that no ANOVA assumptions are violated here. Specifically, the normal probability plot has all points occurring in a straight line, which is normal distribution. The data comparing predicted and residual values shows a constant variance that falls well within the necessary limits. The data comparing run number and residuals shows no indication of systematic trends, validating the presence of randomness. In comparing actual and predicted values shows a comparison of run number and residuals. Unlike with many numerical simulations, there is no trend indicating the presence of any systemic error, thus verifying that the residual randomness assumption has been satisfied; the graphs show a good match between predicted and actual values. The ANOVA and model can therefore be considered an accurate representation of numerical results.

(A)

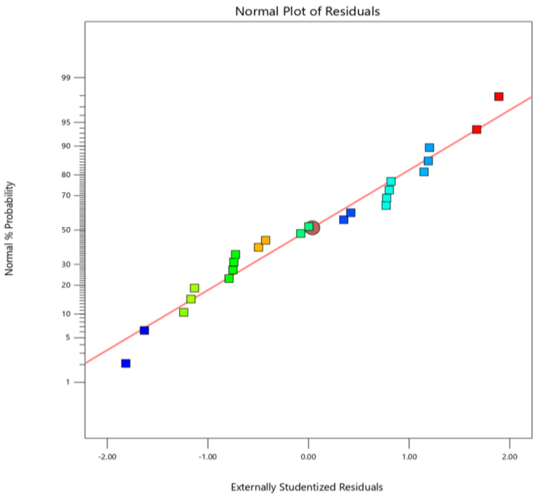

(B)

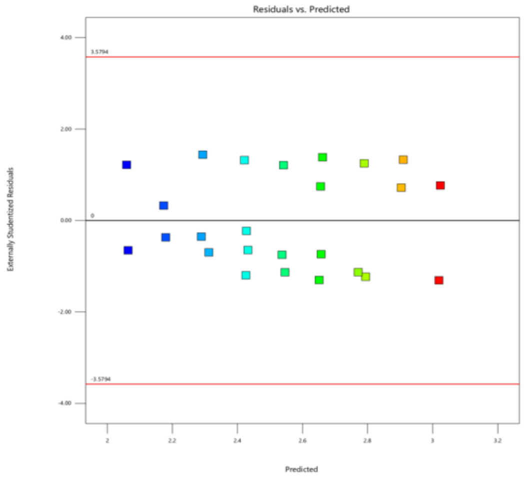

(C)

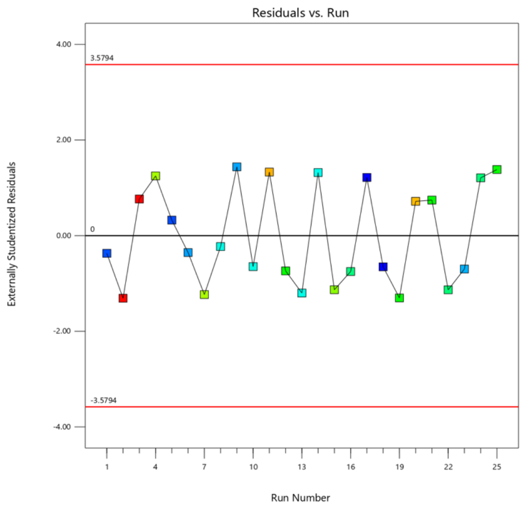

(D)

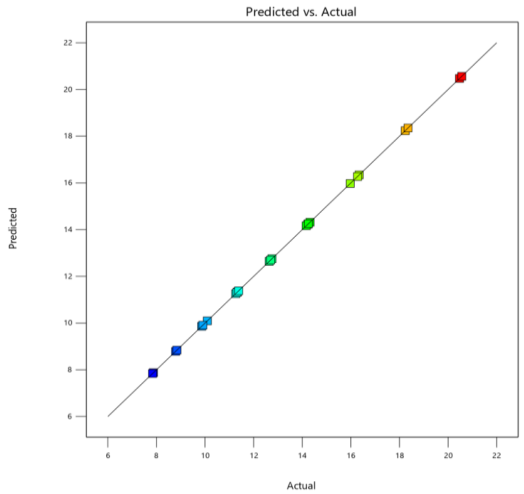

Figure 1: Model Graphs that provide interpret the response of the model selected

Appendix II - Basics of estimating measurement uncertainty:

Systematic Error: We applied two strategies to ensure our flow rate meters and pressure sensors work well. The first strategy involved replacing our sensor with a trusted and more accurate one, after which we checked the measurement readings at the same flow boundary conditions and compared them against earlier readings. In the second strategy, we employed both manual and theoretical calculations. Manual calculations were obtained by collecting and then measuring liquid quantities at the outlet and calculating the time needed to do it. The calculated flow rate results were then compared against the meter readings for the flow rates.

Random Errors (Repeatability): We conducted approximately ten quantity measurements in order first to describe and then to determine any measurement variations that were taken under the same conditions. In other words, we compared differences in the same variables when using the same location, the same instruments, the same procedures, etc., with the comparisons made within a short period of time of each other. Obtaining replicate measurements of the same quantity helps to improve measurement reliability. In these cases, measurement results are often given as a replicate measurement's mean value *V*m.

$$V_m = \frac{V_1+V_2+V_3+\cdots+V_n}{n} = \frac{\sum_{i=1}^{n} V_i}{n} \tag{1}$$

Next, we formulated standard deviations (SD) for the obtained mean values:

$$SD = \sqrt{\frac{\sum_{i=1}^{n}(V_i-V_m)^2}{n-1}} \tag{2}$$

Most of the dispersion of the results (imprecision) falls under the category of the normal probability distribution for nearly 95% of our obtained results.

Appendix III - Darcy's law holds for an upper limit Reynolds number:

The present research conducted the modeling technique under the Darcy flow conditions. However, for validity purposes, the flow in the reservoir medium has to stay laminar. Porous media high-velocity flows typically have local nonlinear interactions that occur between viscous, pressure, and inertial forces. Although there is no consensus yet among researchers to determine the exact range of Darcy or linear flow in porous media, but there is a consensus that Darcy's law still holds in cases where there is an upper limit Reynolds number value of 1 to 10, based on average velocity and grain size. Any flows that are less than this limit tend to be dominated by viscosity and are deemed laminar, in which case Darcy's law also applies. However, in cases where flows above the stated limit are turbulent or non-laminar, Darcy's law cannot be used. The Reynolds number may be formulated as follows:

$$R_e = \frac{\rho v D}{\mu} \tag{3}$$

where v is the average flow velocity (m/s), D is the mean grain diameter (m), and μ is the kinematic viscosity coefficient (m^2/s).